

Aleksander Lovrić

Finite Element Framework for Phase-Field Modelling of Multiphase Flows



Swansea University
Prifysgol Abertawe

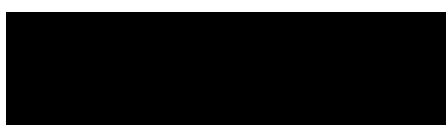
A thesis submitted to Swansea University in candidature for the degree of Doctor of
Philosophy

College of Engineering
Swansea University
Swansea, Wales, UK
December 2019

Declaration

Statement 1

This work has not previously been accepted in substance for any degree and is not being concurrently submitted in candidature for any degree.



Signed: 

Date January 10, 2020

Statement 2

This thesis is the result of my own investigations, except where otherwise stated. Any sources used in this work are acknowledged by references. A reference list is appended.



Signed: 

Date January 10, 2020

Statement 3

I hereby give consent for my thesis, if accepted, to be available for photocopying and for inter-library loan, and for the title and summary to be made available to outside organisations.



Signed: 

Date January 10, 2020

Acknowledgements

I am deeply grateful to the friends, colleges and family who have supported me through the years of my PhD research. Particularly I would like to express my gratitude to Prof. Wulf G Dettmer, and Prof. Djordje Perić for their enthusiasm, encouragement and dedication to the project. Of course, the PhD project would not have come to fruition without Schaeffler Group, who sponsored the project together with the College of Engineering at Swansea University. I would also like to thank Swansea University for their continual support and for providing an ideal research environment. Finally, I could not have accomplished what I have without my parents, Zoran and Mirjana, and my brother, Vladimir, for their continuous support over the years.

Summary

This thesis is concerned with the simulation of multiphase systems and phase transition. Specifically of interest is the modelling of liquid-vapour systems, usually in the presence of surface tension, using diffuse-interface methods. An emphasis is placed on increasing computational efficiency with order reduction and segregation strategies. The thesis opens with the modelling of phase-transition phenomena using a non-conservative low order formulation of the Navier-Stokes-Korteweg equations: a diffuse-interface model for simulating compressible single-component fluid systems. Of particular interest is the simulation of temperature induced cavitation, which is successfully demonstrated with the numerical simulation of nucleate boiling. The focus is turned to binary fluid systems with the introduction of a classical phase dynamics model: The Cahn-Hilliard equation. The inherent physical phenomena associated with the Cahn-Hilliard equation are investigated, and strategies are proposed to reduce their contributions, which are demonstrated with a selection of numerical examples. The Cahn-Hilliard equation is coupled with the incompressible Navier-Stokes equations. A computationally efficient, low order finite element formulation is presented for modelling the coupled Navier-Stokes-Cahn-Hilliard equations: a diffuse-interface model for the simulation of immiscible multiphase flows. The present work suggests that traditional Navier-Stokes-Cahn-Hilliard models do not allow for surface tension effects to be neglected due to the presence of the surface tension parameter in the Cahn-Hilliard equation. This motivates the proposed formulation, which allows surface tension effects to be changed without affecting the behaviour of the phase transport. The proposed models are demonstrated with surface tension dominated problems, as well as problems where surface tension effects are negligible. All results obtained agree very well with reference solutions. As a final contribution of the thesis an effort is placed on increasing computational efficiency by implementing projection-type decoupling strategies. Two new families of projection schemes are proposed which are based on the generalised midpoint rule and the generalised- method, respectively, and allow control over high-frequency damping. Both schemes are investigated in detail on the basis of a spatially discrete model problem and subsequently implemented in the context of a finite element formulation for the incompressible Navier-Stokes equations. Comprehensive numerical studies are presented, and importantly the observations made are in agreement with the conclusions drawn from the model problem. The present work suggests that it is not possible to formulate a second order accurate projection scheme which possesses any high-frequency damping.

Contents

1	Introduction	1
1.1	Motivation	1
1.2	Diffuse-interface methods	2
1.2.1	Binary fluid systems	3
1.2.2	Single-component fluid systems	4
1.3	Contributions of the thesis	7
1.4	Layout of the thesis	9
2	Single-Component Fluid Systems: The Navier-Stokes-Korteweg Equations	11
2.1	Thermodynamics of a van der Waals fluid	12
2.1.1	Maxwell states for the van der Waals fluid model	15
2.2	Governing equations	16
2.2.1	Conservation laws	16
2.2.2	The Navier-Stokes-Korteweg equations	18
2.2.3	Order reduction with auxiliary variable	19
2.2.4	Dimensionless form	20
2.2.5	Isothermal case	20
2.2.6	Boundary conditions	21
2.2.7	Physical relevance of parameters	21
2.3	Numerical Formulation	22
2.3.1	Spatial semi-discrete weak form	23
2.3.2	Temporal discretisation	23
2.3.3	Solution strategy	24
2.3.4	Adaptive time stepping	24
2.4	Isothermal numerical examples	24
2.4.1	Reproducing the $\theta - \rho$ phase diagram	25
2.4.2	Coalescence of two vapour bubbles	25
2.4.3	Evolution of three vapour bubbles	29
2.4.4	Sessile drop	31
2.4.5	Falling liquid drop	32
2.5	Non-isothermal numerical examples	33
2.5.1	Evaporation/Condensation	33
2.5.2	Nucleate boiling	34
2.5.3	Temperature driven rising bubble	43
2.6	Concluding remarks	43

3	Binary Fluid Systems: The Cahn-Hilliard Equation	47
3.1	Model derivation and thermodynamics	49
3.2	The Cahn-Hilliard equation	50
3.2.1	Exact solution of the one-dimensional Cahn-Hilliard equation	52
3.2.2	Relating well height and interface thickness	53
3.2.3	Choosing the mobility function	53
3.3	Numerical formulation	54
3.3.1	Spatial semi-discrete weak forms	54
3.3.2	Temporal discretisation and solution strategy	55
3.4	Numerical examples	55
3.4.1	Evolution to static of two bubbles	55
3.4.2	Coalescence of two bubbles	56
3.4.3	Spinodal decomposition of a randomly perturbed initial condition	58
3.4.4	Vortex induced flow	58
3.5	Investigation into coarsening	62
3.5.1	Time scaling and setting the mobility	63
3.5.2	Reduction of coarsening through modification	65
3.5.3	Numerical examples	67
3.6	Investigation into shrinkage	72
3.6.1	Evaluation of non-critical shrinkage	72
3.6.2	Evaluation of critical volume fraction	73
3.6.3	Suggestions for double well potentials	75
3.6.4	Initial conditions to account for sub-critical volume fractions	78
3.7	Concluding remarks	80
4	Binary Fluid Systems: The Navier-Stokes-Cahn-Hilliard Equations	83
4.1	The Navier-Stokes-Cahn-Hilliard equations	84
4.2	Numerical formulation	85
4.2.1	Mixed Taylor-Hood formulation	85
4.2.2	Stabilised formulation	86
4.2.3	Temporal discretisation and solution strategy	87
4.3	Numerical Examples	87
4.3.1	Static bubble	88
4.3.2	Small amplitude oscillations of a two-dimensional drop . . .	88
4.3.3	Large amplitude oscillation of a two-dimensional drop	90
4.3.4	Capillary rise	90
4.3.5	Sessile drop	95
4.3.6	Pendant drop	96
4.3.7	Rising bubble	98
4.3.8	Faucet leak in two dimensions	99
4.3.9	Faucet leak in three dimensions	100
4.3.10	Broken dam	102
4.3.11	Slushing tank	106
4.3.12	Rayleigh-Taylor instability	107

4.3.13	Industrial case study: Flow splitting device	110
4.4	Concluding remarks	118
5	Increasing Computational Efficiency: Segregation Strategies	119
5.1	Analysis of projection schemes	121
5.1.1	1D model problem with analytical solution	121
5.1.2	Time integration schemes	123
5.1.3	Projection schemes	125
5.1.4	Comparison of schemes	128
5.1.5	Conclusions drawn from model problem analysis	132
5.2	Formulations for incompressible fluid flow	134
5.2.1	Projection schemes: time discretisation	134
5.2.2	Finite element method: spatial discretisation	136
5.2.3	Stable velocity-pressure interpolations	137
5.3	Numerical examples	138
5.3.1	Lid-driven cavity	138
5.3.2	Lid-driven cavity with dynamic boundary conditions	139
5.3.3	Flow around a cylinder	142
5.4	Concluding remarks	144
6	Conclusions and Future Work	147
6.1	Conclusions	147
6.2	Suggested future research	148
	References	149
	Appendices	165
A	Formulation and Solution Strategies	167
A.1	Linearisation and Newton-Raphson procedure	167
A.2	Power expenditure term	172
A.3	Non-conservative Korteweg stress term	173

Chapter 1

Introduction

1.1 Motivation

Every day we encounter natural and industrial processes involving multiphase flows and phase transition. The boiling of water in a kettle for instance, involves the formation of a liquid-vapour system through phase transition. In this case a system consisting of water and water vapour. Multiphase flows can be observed in countless industrial applications, including but not limited to: emulsification, bubble driven circulation systems used for metal processing, fluidised beds, combustion reactors, gas-liquid pipeline flows, etc. Similarly numerous natural applications spring to mind, such as: rain, fog, volcanic eruptions, etc.

In classical fluid mechanics, these types of problems are referred to as free or moving boundary problems. They are characterised by having an interface between two or more fluid bodies, modelled as a free boundary that evolves with time. Traditionally the mathematical description of a free boundary problem involves partial differential equations (PDEs) that hold in each fluid body and are coupled by boundary conditions placed on the separating interface. Mathematically speaking, these types of problems are notoriously difficult to solve. Not only are the PDEs representing each component highly nonlinear, but the liquid-vapour systems in question are often subject to a high degree of topological change, making interface tracking difficult, if not impossible. Analytical solutions to liquid-vapour multiphase flows are limited to trivial problems, such as Stokes flow or linear inviscid waves [1]. Experimental investigations are also few and far between, with limitations placed on the length and time scales used as well as visual access. As a result, numerical approaches have been propelled to the forefront of multiphase analysis.

Developing numerical models for simulating free boundary problems has for a long period of time been the subject of scientific investigation. Strategies for simulating such flows can be categorised as either interface-tracking or interface-capturing methods. The more traditional interface-tracking methods require updating the computational mesh continuously in order to resolve the interface which is aligned with it. Some examples of interface-tracking approaches include arbitrary Lagrangian-Eulerian (ALE) [2, 3, 4, 5] or purely Lagrangian finite element formulations [6, 7, 8, 9, 10]. Interface-capturing methods introduce additional

variables in order to represent the interface implicitly. Interface-capturing methods include: volume-of-fluid (VOF) [11, 1], level-set [12] and diffuse-interface (or phase-field) methods [13, 14, 15], to name a few. These methods possess several advantages over more classical interface-tracking methods. For instance their ability to handle topological changes is significantly improved, and the necessity for mesh updating is reduced if not removed. These along with other benefits to be discussed later on have resulted in interface-capturing methods, such as VOF and level-set methods, being widely adopted in commercial software.

Many recent advances in computational power, numerical methods and mathematical models have brought attention to diffuse-interface methods as a means of interface-capturing. The present work focusses on using exclusively diffuse-interface methods to model multiphase/multicomponent flows and phase transition. The methods are categorised according to whether they consider single-component or binary fluid systems. Single-component fluid models are those which simulate multiple phases of the same component, and are typically associated with phase transition. Binary fluid models are those which simulate mixtures consisting of two different components, which are not necessarily of the same family. A brief history of these methods is now presented.

1.2 Diffuse-interface methods

The concept of having an interface separating phases has been investigated for centuries. The earliest multiphase models, studied by the likes of Young, Laplace and Gauss, involved an interface of zero thickness between phases, and are hence known as *sharp-interface* methods. Here the interface would include physical properties such as surface tension, and all the physical quantities, i.e. density, viscosity, heat conductivity etc. would be discontinuous across it. Physicists quickly recognised that the interface could represent a smooth transition of quantities and interfacial forces between the distinct bulk phases. With advances in the theory of capillarity pioneered by Lord Rayleigh [16, 17] and van der Waals [18], the concept of continuous variation of density was created. This coupled with the introduction of a capillary stress tensor expressed in terms of the density and its gradients by Korteweg [19], constitutes the foundation of diffuse-interface methods.

The advantages of the diffuse-interface approach become apparent when considering the classical interface-tracking free boundary methods. While classical free-boundary methods typically require adaptive grids, diffuse-interface methods simply require fixed grids through which interfaces can propagate. Importantly, this allows them to conveniently deal with a high degree of topological and morphological change, which is a crucial proponent for their increasing popularity in recent years. A further hindrance of classical free-boundary methods is evident when considering mixtures near the critical point. Classical physics dictates that the interface thickness diverges as the temperature approaches the critical point [20], and hence a sharp interface assumption does not hold.

To fully appreciate the benefits of diffuse-interface methods, consider the example of modelling the formation and growth of a solid dendrite submerged in a liquid. To model the dendrites evolution, described by the local normal velocity

of a dendrite stem, one needs to impose appropriate boundary conditions on the interface. Here the velocities can be computed from the temperature gradients, which are obtained from solving a heat diffusion equation. However imposing the required temperature boundary conditions requires knowing where to apply them. This proves challenging since the interface is constantly evolving in space, and since the velocity is required to track the position of the interface, one ends up in a vicious loop. Such is often the predicament of classical free-boundary problems. Additionally the complex topology of the dendrite results in a highly nonlinear problem as a result of having to resolve the curvature term in each iteration. As pointed out earlier diffuse-interface methods do not face these problems since they are able to represent complex interface topologies and dynamics using just fixed grids. The mechanisms behind this will be explored shortly. Diffuse-interface methods are successfully implemented to model dendritic growth in the context of binary alloys in for instance [21, 22, 23]. Binary fluid systems such as this and their simulation will now be discussed.

1.2.1 Binary fluid systems

One of the most popular diffuse-interface models for the simulation of two component immiscible phase dynamics is the Cahn-Hilliard equation. Cahn and Hilliard [24, 25] propose a time dependant extension of van der Waal's hypothesis, which itself suggests that equilibrium interface profiles are obtained from minimising a Helmholtz free energy functional [26]. In essence, the Cahn-Hilliard equation is a mass conserving transport equation wherein the dissipation of the mixing energy, in combination with some external advection, drives the motion of the interface and localises the individual phases. In order to represent a mixture continuously, the Cahn-Hilliard equation introduces an auxiliary field variable, typically called the *phase-field variable* or *order parameter*, which varies quantities and forces across the interface between two distinct bulk phases. The Cahn-Hilliard equation has been extensively reviewed from a physical and mathematical perspective in [27, 28, 29], and has been demonstrated in numerous numerical simulations (see, for instance [30, 31, 32]). Alternatively, the non-conservative counterpart, the Allen-Cahn equation [33] is sometimes considered at the expense of having an additional constraint to enforce mass conservation.

Coupling the Cahn-Hilliard equation with hydrodynamic Navier-Stokes equations results in the Navier-Stokes-Cahn-Hilliard equations, which have been extensively researched from a mathematical and numerical perspective in for instance [34, 35, 26, 28, 36]. These types of equations were utilised as early as the 1970's [37], with the so-called Model H. This model combines the phase dynamics of the Cahn-Hilliard equation with the hydrodynamics of the Navier-Stokes equation for the purpose of modelling immiscible, incompressible two-component flows. The drawback of the Model H is that it assumes that the mixture is comprised of constant matching densities, and is hence severely restricted in its application. The difficulty with considering non-matching densities is that the macroscopic description of the density differs from the direct average of the microscopic descriptions, meaning that even if the individual components are incompressible, the mixture

may not be.

Typically models proposed for mixtures of non-matching densities are characterised as either: incompressible - where the volume averaged velocity field is divergence-free (*i.e.* satisfies incompressibility), or quasi-incompressible - where the mass-averaged velocity field satisfies mass conservation only, resulting in a slight compressibility in the interface region. A quasi-incompressible modification of the Model H by Lowengrub and Truskinovsky [28] allows for the use of non-matching densities in the bulk regions. However, as mentioned the definition of the average velocity results in the loss of the divergence-free velocity field. Furthermore, a stronger coupling is present since the pressure from the momentum equation of the Navier-Stokes equations is present in the Cahn-Hilliard part of the equations. More recently, another quasi-incompressible form of the equations is proposed in [38], where notably a linear method is used which satisfies discrete energy dissipation unconditionally. On the other hand, models by Boyer [15] and Ding et al. [39] present appealing formulations with divergence-free velocity fields; however the energy inequalities are unknown for the model. Shen et al. [36] propose a physically consistent model for incompressible mixtures with non-matching densities, implementing energy stable, accurate time integration schemes. More recently, Abels et al. [14] derived a variable density variation of the Model H which is thermodynamically consistent. The model is shown to recover sharp interfaces when the interface thickness tends to zero. The Abels et al. model has been effectively used in numerous numerical studies, and is chosen as the base model of this paper. The Allen-Cahn equation has also been successfully coupled with the Navier-Stokes equations in [40, 41, 42]. Though contrary to the name, the theory behind binary fluids extends to systems involving more than two components. In [43], Boyer et al. construct a Navier-Stokes-Cahn-Hilliard model to simulate incompressible flow of three immiscible components, without complication.

In addition to modelling dendrite growth (as previously discussed), diffuse-interface methods for binary fluid systems are largely represented in the simulation of numerous industrial and natural processes, for instance: emulsification, tumour growth [44, 45], crystallisation [46], hydraulic fracturing [47, 48], phase-change-driven implosion [49] etc.

1.2.2 Single-component fluid systems

Single-component fluid based diffuse-interface models are constructed primarily from the point of modelling critical phenomena [29]. These models describe viscous, compressible flows either of a non-isothermal or isothermal nature. Much like the binary-fluid models, these type of models consider a Helmholtz free energy functional consisting of a bulk free energy and surface free energy or free energy excess square gradient term associated with density variations. The bulk free energy component associated with free energy functional is represented by a double well potential for subcritical temperatures, and a single well potential supercritical temperatures. The Navier-Stokes-Korteweg model is an example of a widely implemented single-component model used primarily to model two-phase (liquid-vapour) systems. The model results primarily from concepts developed by

Korteweg [19] and van der Waals [18]. One cannot however contribute all the progress made in developing these models to just these authors. Some important contributions and reviews from mathematical and physical standpoints are made by Langer and Turski [50], Dunn and Serrin [51], Truskinovsky [52], Antanovskii [34, 53], Jacqmin [54], and Anderson and McFadden [55].

Probably the most important aspect of single-component fluid models is their ability to represent phase transition. For instance, recall the example of boiling water in a kettle, in which liquid water transforms into gaseous water vapour. Liquid-vapour phase transitions of this kind are synonymous with the phenomenon of cavitation.

Cavitation occurs when the local pressure in a liquid falls below its vapour pressure resulting in the formation of vapour bubbles, or cavities. When these bubbles enter regions of higher pressure they implode, and the micro-jets resulting from repeated implosions cause cyclic stress to nearby surfaces. This is an ever present concern for engineers, specifically in the design of propeller and impeller blades. Affected blades can undergo significant wear over time, rendering them ineffective. Damage of this nature was observed as early as the 19th century on steam ship propellers. It is not surprising therefore, that cavitation has been studied for centuries by the likes of Euler, Besant, Stokes, and Rayleigh [56]. The prediction and reduction of impeller/propeller cavitation is still a relevant research topic (see for instance [57, 58]). Needless to say there is substantial industrial interest in multiphase flow and cavitation research. Some topics of interest include:

- *Mechanical engineering.* In addition to the aforementioned impeller/propeller cavitation encountered in pumps and ships, it is not uncommon for diesel engines to experience cavitation erosion on the exterior walls of cylinder liners. Here cavitation occurs when harmonic vibrations on the cylinder walls give rise to fluctuating pressures in the surrounding coolant, see [59]. Typically the combination of excessive vibrations and loose fitting cylinder liners, induce low enough pressures such that vapour bubbles form in the coolant. Shock waves from collapsing bubbles impact the surface with immense force, causing damage over time and potentially a leak in the cylinder.
- *Biomedical engineering.* Mechanical heart valves experience cavitation on the edges of the valve stops and leaflet tips as a result of high frequency pressure fluctuations [60]. Not related but also of significance is the emergence of thousands of air bubbles into cerebral circulation during cardiac surgery. Here larger bubbles run the risk of developing into air embolisms, which could prevent oxygenated blood from reaching targeted organs. Acoustic cavitation occurs when liquids are subjected to a high intensity ultrasound. This is particularly useful in biomedical applications, for instance in non-invasive therapy and drug delivery [61].
- *Geology.* Coastal erosion occurs when air pockets carried by incoming waves are thrust into coastal surfaces, compressing them until they implode, causing erosion over time. Explosive volcano eruptions are also attributed to a form of cavitation. Gas bubbles form from supersaturated magma during

eruption under a decompression wave. The high viscosity of the magma limits the expansion of the gas thereby increases the pressure inside the bubbles. The bubbles eventually burst causing liquid magma to fragment into clots.

Now that the concepts behind diffuse-interface methods have been introduced, their benefits and limitations compared to classical free boundary or sharp interface methods are summarised as follows. The benefits include, but are not limited to:

- Extraordinarily easy to add physics to, be it coupling with hydrodynamics, thermodynamics, solid mechanics, etc.
- Require no interface tracking unlike sharp-interface methods.
- Able to capture phenomena and morphology changes such as coalescence and spinodal decomposition.
- Capable of modelling near-critical phenomena.
- Capable of being derived directly from free-energy functionals using classical thermodynamics.
- Suitable for visualisation of microstructural development.

Though there is obviously an attractive element to these methods, there are several drawbacks as well:

- Choosing the parameters such as interface thickness, double well height, is non-trivial and may be problem dependant. In many cases the interface thickness is chosen much larger than the real thickness to make the methods more computationally attractive.
- Limited selection of comparisons with real physical phenomena.
- Often dense meshes are required to capture interfaces and the associated steep gradients, and large computational domains become expensive to compute.
- Inherent physical effects of phase transport equations such as the Cahn-Hilliard equation. This aspect is explored in Chapter 3 of this thesis.
- There is no clarity to where the assumption of irreversible thermodynamics would fail.

Although there are clearly difficulties associated with diffuse-interface methods, they do constitute the only feasible way of modelling highly complex multiphase flows which undergo a large degree of topological change or even phase transition. In the following section the underlying achievements and contributions of the thesis are summarised.

1.3 Contributions of the thesis

The novel contributions and primary results of the thesis are presented here. The structure is such that an aim is first identified, followed by an associated list of contributions.

Low order strategies for modelling phase transition: A study is undertaken into single-component fluid models capable of phase transition. The contributions are as follows:

1. A low order, computationally efficient Navier-Stokes-Korteweg model is presented for simulating phase transition problems, with particular interest in cavitation. Typically capturing such phenomena is achieved through highly expensive strategies, such as Isogeometric Analysis (IGA) approaches involving very dense meshes of higher order b-splines which are at least C_1 continuous (see, for instance [62]). In the present work a finite element formulation for non-isothermal and isothermal variations of the Navier-Stokes-Korteweg equations is introduced non-conservatively, and with a reduced system order, allowing for linear elements to be used.
2. A number of benchmark problems are demonstrated with the presented model, including temperature induced nucleate boiling, which clearly demonstrates the models ability to capture complex phenomena.

Phenomena associated with phase transport: The coarsening and shrinking effects inherently present with the Cahn-Hilliard equation are investigated. The contributions are as follows:

1. A modification of the Cahn-Hilliard equation is proposed which reduces the effects of grain coarsening, an inherent property of the equation. This involves modifying the diffusive component of the Cahn-Hilliard equation such that the surface rounding is reduced. Moreover relationships are developed between the mobility function, interface thickness and effective radius of a bubble.
2. A suggested initial condition is proposed to allow for a significant improvement in mass conservation of individual phases, i.e. reduction of drop shrinkage, another inherent property of the Cahn-Hilliard equation. Although there have been guidelines presented in [26, 63] on how to reduce shrinkage, these do not remove the problems all together, but merely suggest how to delay them.

Several findings from this research have been presented at the IGA conference 2018: Integrating Design and Analysis.

Low order strategies for modelling binary fluid systems: An investigation is made into efficiently modelling immiscible two-component flows with particular focus on physical relevance and surface tension control. The contributions are as follows:

1. A novel Navier-Stokes-Cahn-Hilliard model is proposed that allows for activation/deactivation of surface tension effects. The present work suggests that traditional Navier-Stokes-Cahn-Hilliard models do not allow for surface tension effects to be neglected due to the presence of the surface tension parameter in the Cahn-Hilliard equation. This motivates the proposed formulation, which allows surface tension effects to be changed without affecting the behaviour of the phase transport.
2. Formulation and implementation of computationally efficient, low order finite element methods for the Navier-Stokes-Cahn-Hilliard equations based on both stabilised SUPG/PSPG elements and mixed Taylor-Hood elements.
3. The proposed models (contribution 2) are applied to an extensive set of benchmark and example problems, including both capillary regime in which surface tension effects are dominant, and inertial regime in which surface tension effects are negligibly small. All results obtained agree very well with reference solutions. At the time this writing and to the best of the author's knowledge, the comparison of the numerical solution of the Navier-Stokes-Cahn-Hilliard equations with realistic physical processes, such as capillary rise or faucet leak, has not been reported elsewhere in literature.

The findings resulting from this work were submitted as an article for publication to the journal of *Computer Methods in Applied Mechanics and Engineering*, which at the time of this writing, is under review. An *arXiv.org* version of the article can be accessed in [64].

Increasing computational efficiency with decoupling strategies: The focus here is on exploring various decoupling strategies to efficiently model single and multi-phase fluid flow. The contributions are as follows:

1. Presentation of a model problem for assessment of projection schemes including numerical damping. A simple spatially discrete model problem consisting of mass points and dash-pots is presented which allows for the assessment of the properties of different projection schemes for the solution of the incompressible Navier-Stokes equations. In particular, the temporal accuracy, the stability and the numerical damping are investigated with the model problem.
2. Assertion: Second order accurate projection schemes do not possess high frequency damping. An investigation using the model problem suggests that it is not possible to formulate a second order accurate projection/pressure-correction scheme which possesses any high-frequency damping.
3. Presentation of two new methodologies for the model problem and for the incompressible Navier-Stokes equations. Motivated by contribution 2, two new families of projection schemes, developed from the generalised midpoint rule and the generalised- α method respectively, are proposed. Notably the schemes offer control over high-frequency damping. Both schemes are investigated in detail on the basis of the model problem and subsequently

implemented in the context of a finite element formulation for the incompressible Navier-Stokes equations. It is found that the proposed schemes offer a compromise between accuracy and high-frequency damping. This is confirmed with comprehensive numerical studies of the flow in a lid-driven cavity and the flow around a cylinder problems. The observations made are in agreement with the conclusions drawn from the model problem.

These findings were published in the journal of *Computer Methods in Applied Mechanics and Engineering* [65].

1.4 Layout of the thesis

The thesis is arranged as follows:

Chapter 2 describes single-component fluid models for simulating multiphase flows and phase transition. The fundamental van der Waals thermodynamics and Navier-Stokes conservation laws are explored. The Navier-Stokes-Korteweg equations are constructed in a low order, non-conservative manner for modelling both non-isothermal and isothermal flows. Finite element formulations, as well as solution strategies are presented for the models. A number of isothermal and non-isothermal benchmark problems are simulated, including a demonstration of phase transition with nucleate boiling.

Chapter 3 introduces the Chan-Hilliard phase transport equation. The derivation and thermodynamic concepts are briefly explained. A finite element formulation and solution strategy is introduced. Various numerical benchmark problems are presented to showcase the inherent physical behaviour of the model. Investigations are carried out into the inherent effects of grain coarsening and drop shrinkage, and strategies are proposed for reducing them. This chapter provides the preliminaries for Chapter 4, which couples the Cahn-Hilliard equation with the Navier-Stokes equation.

Chapter 4 introduces the Navier-Stokes-Cahn-Hilliard equations for the purpose of modelling immiscible binary fluids with and without the effects of surface tension. Two finite element formulations are proposed: A stabilised SUPG/PSPG formulation, and a mixed Taylor-Hood formulation. The formulations are demonstrated with a number of numerical benchmark problems; These are categorised into both problems which are dominated by surface tension effects, and those which have no surface tension effects. The results are compared with analytical models, experimental data, and other numerical approaches.

Chapter 5 opens with a review on decoupling strategies for modelling fluid flow efficiently. A discrete model problem is introduced for the purpose of studying various projection schemes, which are analysed in terms of accuracy and stability. The Navier-Stokes equations are formulated using the proposed projection schemes. Numerical examples, namely the lid driven cavity and flow around a cylinder problems, are demonstrated for the purpose of understanding the relationship between accuracy and high frequency damping.

Chapter 6 summarises the achievements of the thesis. Conclusions are drawn and potential future work is suggested.

Chapter 2

Single-Component Fluid Systems: The Navier-Stokes-Korteweg Equations

When considering a homogeneous system, phase transition occurs if the equilibrium state of the system changes from one phase to another as a result of changing thermodynamic variables, such as pressure or temperature. The simulation of complex phase transition, specifically for liquid-vapour systems, has been made possible with diffuse-interface methods. Recently, the Navier-Stokes-Korteweg equations have been shown effective at modelling single-component multiphase flows with possible phase transition, see for instance [66, 49, 62, 67, 68, 69]. In essence, the Navier-Stokes-Korteweg equations can be seen as an extension of the typical compressible Navier-Stokes equations, wherein the ideal fluid is replaced with a van der Waals fluid, and the Cauchy stress tensor is appropriately modified to include surface tension. Proposed by Korteweg [19], the so-called *Korteweg stress tensor* (or capillary tensor), $\boldsymbol{\kappa}$, is described in the form,

$$\boldsymbol{\kappa} = \lambda \left(\rho \Delta \rho + \frac{1}{2} |\nabla \rho|^2 \right) \mathbf{I} - \lambda \nabla \rho \otimes \nabla \rho, \quad (2.1)$$

where ρ denotes the density, Δ denotes the Laplacian, and λ denotes the capillary coefficient. Contrary to binary-fluid models, the order parameter is the density itself rather than an auxiliary phase-field variable. Similarly however it localises the phases in the bulk regions and smoothly transitions over the interface region.

In terms of numerical simulation, Isogeometric analysis (IGA) has been used effectively to model the isothermal case of the Navier-Stokes-Korteweg equations, in for instance [66, 70]. Similarly the full non-isothermal Navier-Stokes-Korteweg equations have been solved with IGA in Liu et al. [62], where the authors demonstrate the effectiveness of their conservative formulation by simulating a variety of boiling problems in multiple space dimensions. Introducing an auxiliary variable to represent the Laplacian of the density, Bueno et al. [49, 71] use IGA to simulate fluid structure interaction problems related to droplet dynamics. A local discontinuous Galerkin (LDG) method in combination with adaptive mesh refinement is used by Diehl et al. [69] to solve the non-conservative form of the isothermal

Navier-Stokes-Korteweg equations. A similar discretisation for the non-isothermal equations is found in Tian et al. [68]. Abels et al. [72] investigate the sharp-interface limit of the Navier-Stokes-Korteweg equations, where they find that the solutions converge to the physically relevant free-boundary problem.

This chapter is arranged as follows: The thermodynamic concepts of a van der Waals fluid are introduced in Section 2.1. In Section 2.2, the governing equations for the Navier-Stokes-Korteweg equations are derived and presented in multiple forms. In Section 2.3 the variational forms are presented, as well as the spatial and temporal discretisations. In Sections 2.4 and 2.5, a selection of numerical examples are presented for the isothermal and non-isothermal cases of the Navier-Stokes-Korteweg Equations respectively.

2.1 Thermodynamics of a van der Waals fluid

The Helmholtz free energy measures the useful work obtainable from a closed thermodynamic system while the temperature and volume are constant. It can be expressed in the form,

$$\Psi = i - \theta s, \quad (2.2)$$

where i is the internal energy, θ is the temperature, s is the entropy. The following fundamental thermodynamic relation can be expressed,

$$d\Psi = -sd\theta - pdv + \eta dn, \quad (2.3)$$

where n is the number of particles, η is the chemical potential and p is the pressure. The necessary thermodynamic quantities can be recovered as

$$s = - \left(\frac{\partial \Psi}{\partial \theta} \right)_{v,n}, \quad p = - \left(\frac{\partial \Psi}{\partial v} \right)_{\theta,n}, \quad \eta = - \left(\frac{\partial \Psi}{\partial n} \right)_{\theta,v}. \quad (2.4)$$

In order to obtain the Helmholtz free energy, the pressure in (2.4) is replaced with the van der Waals equation of state, as follows

$$\left(\frac{\partial \Psi}{\partial v} \right)_{\theta,n} = -p = -\frac{nk\theta}{v - nb} + a\frac{n^2}{v^2}. \quad (2.5)$$

Integrating (2.5) yields the Helmholtz free energy,

$$\Psi = -nR\theta \ln(v - nb) - \frac{an^2}{v} + c(\theta), \quad (2.6)$$

where a , b are constants associated with the fluid properties, $c(\theta)$ is an arbitrary function of temperature, and R is the universal gas constant. If one considers Ψ as a function of density ρ and temperature θ , we can obtain the necessary thermodynamic quantities with the following relations:

$$p(\rho, \theta) = \rho^2 \frac{\partial \Psi(\rho, \theta)}{\partial \rho} \quad (2.7a)$$

$$i(\rho, \theta) = \Psi(\rho, \theta) - \theta \frac{\partial \Psi(\rho, \theta)}{\partial \theta} \quad (2.7b)$$

$$s(\rho, \theta) = -\frac{\partial \Psi(\rho, \theta)}{\partial \theta} \quad (2.7c)$$

$$\eta(\rho, \theta) = \frac{\partial (\rho \Psi(\rho, \theta))}{\partial \rho}, \quad (2.7d)$$

The typical description of the Helmholtz free energy functional [18, 29] is expressed in terms of ρ , θ , and $\nabla \rho$ as:

$$\mathcal{F} = \int_{\Omega} (\rho \Psi_b + \rho \Psi_s) d\Omega \quad (2.8)$$

where the bulk (or local) and surface free energy components are respectively given as

$$\Psi_b = \bar{R}\theta \log \left(\frac{\rho}{b-\rho} \right) - a\rho + c_v\theta \left(1 - \log \left(\frac{\theta}{\theta_0} \right) \right), \quad (2.9a)$$

$$\Psi_s = \frac{\lambda}{2\rho} |\nabla \rho|^2. \quad (2.9b)$$

Here c_v is the specific heat capacity at constant volume, θ_0 is the reference temperature, \bar{R} is the specific gas constant, and λ is again the capillarity coefficient which is related to the interface thickness and surface tension effects. The bulk free energy contribution $\rho \Psi_b$ is the nature of a hydrophobic double well when the temperature is below the critical temperature and a single well when it is above it. The surface free energy contribution $\rho \Psi_s$ is hydrophilic by nature and related to the change in density. The bulk thermodynamic quantities (2.7) are evaluated using Ψ_b as:

$$p = \bar{R}b \frac{\rho\theta}{b-\rho} - a\rho^2 \quad (2.10a)$$

$$i = c_v\theta - a\rho \quad (2.10b)$$

$$s = -\bar{R} \log \left(\frac{\rho}{b-\rho} \right) + c_v \log \left(\frac{\theta}{\theta_0} \right) \quad (2.10c)$$

$$\eta = \bar{R}\theta \left(\frac{b}{b-\rho} + \log \left(\frac{\rho}{b-\rho} \right) \right) + c_v\theta \left(1 - \log \left(\frac{\theta}{\theta_0} \right) \right) - 2a\rho. \quad (2.10d)$$

The extended internal energy and chemical potential are recovered using the combined contributions of Ψ_b and Ψ_s , which would imply:

$$i = c_v\theta - a\rho + \frac{\lambda}{2\rho} |\nabla \rho|^2 \quad (2.11a)$$

$$\eta = \bar{R}\theta \left(\frac{b}{b-\rho} + \log \left(\frac{\rho}{b-\rho} \right) \right) + c_v\theta \left(1 - \log \left(\frac{\theta}{\theta_0} \right) \right) - 2a\rho - \lambda \Delta \rho. \quad (2.11b)$$

Equation (2.11b) can be seen similarly to the chemical potential from binary-fluid systems, i.e. $\eta = f(\varphi) - \Delta \varphi$.

Dimensionless van der Waals fluid: The critical temperature, θ_c , can be defined as the maximum possible temperature at which two-phase flow is possible. The critical point is defined when

$$\frac{\partial p}{\partial \rho} = 0, \quad \frac{\partial^2 p}{\partial \rho^2} = 0, \quad (2.12)$$

from which the critical density, temperature and pressure are evaluated as

$$\rho_c = \frac{b}{3}, \quad \theta_c = \frac{8ab}{27\bar{R}}, \quad p_c = \frac{ab^2}{27}. \quad (2.13)$$

Following an $MLT\theta$ measurement scaling (see, for instance Gomez et al. [73]), if we scale the mass by bL^3 , length by L , time by L/\sqrt{ab} and temperature by θ_c , such that

$$\rho = b\hat{\rho}, \quad x = L\hat{x}, \quad t = \frac{L}{\sqrt{ab}}\hat{t}, \quad \theta = \theta_c\hat{\theta}. \quad (2.14)$$

The bulk and surface free energy densities are obtained in dimensionless form as

$$\hat{\Psi}_b = \frac{8}{27}\hat{\theta} \left(\log \left(\frac{\hat{\rho}}{1-\hat{\rho}} \right) + \frac{1}{\bar{\gamma}-1} \left(1 - \log(\hat{\theta}) \right) \right) - \hat{\rho}, \quad (2.15a)$$

$$\hat{\Psi}_s = \frac{1}{2\text{We}\hat{\rho}} |\hat{\nabla}\hat{\rho}|^2. \quad (2.15b)$$

where the Weber number is defined as

$$\text{We} = \frac{aL^2}{\lambda}. \quad (2.16)$$

The other bulk thermodynamic quantities are

$$\hat{p} = \frac{8}{27} \frac{\hat{\theta}\hat{\rho}}{1-\hat{\rho}} - \hat{\rho}^2 \quad (2.17a)$$

$$\hat{i} = \frac{8}{27} \frac{\hat{\theta}}{\bar{\gamma}-1} - \hat{\rho} + \frac{1}{2\text{We}\hat{\rho}} |\hat{\nabla}\hat{\rho}|^2 \quad (2.17b)$$

$$\hat{s} = \frac{8}{27} \left(\frac{1}{\bar{\gamma}-1} \log(\hat{\theta}) - \log \left(\frac{\hat{\rho}}{1-\hat{\rho}} \right) \right) \quad (2.17c)$$

$$\hat{\eta} = \frac{8}{27} \hat{\theta} \left(\frac{1}{1-\hat{\rho}} + \log \left(\frac{\hat{\rho}}{1-\hat{\rho}} \right) + \frac{1}{\bar{\gamma}-1} \left(1 - \log(\hat{\theta}) \right) \right) - 2\hat{\rho} - \frac{1}{\text{We}} \hat{\Delta}\hat{\rho}, \quad (2.17d)$$

where the heat capacity ratio, $\bar{\gamma}$, is introduced for simplicity, such that

$$c_v = \frac{\bar{R}}{\bar{\gamma}-1}. \quad (2.18)$$

The dimensionless van der Waals pressure and chemical potential are shown in Figure 2.1. Clearly when the temperature is below θ_c , the pressure and chemical potential are non-monotonic. Here the region between points a and b corresponds to the unstable region in which the mixture would decompose into separate phases.

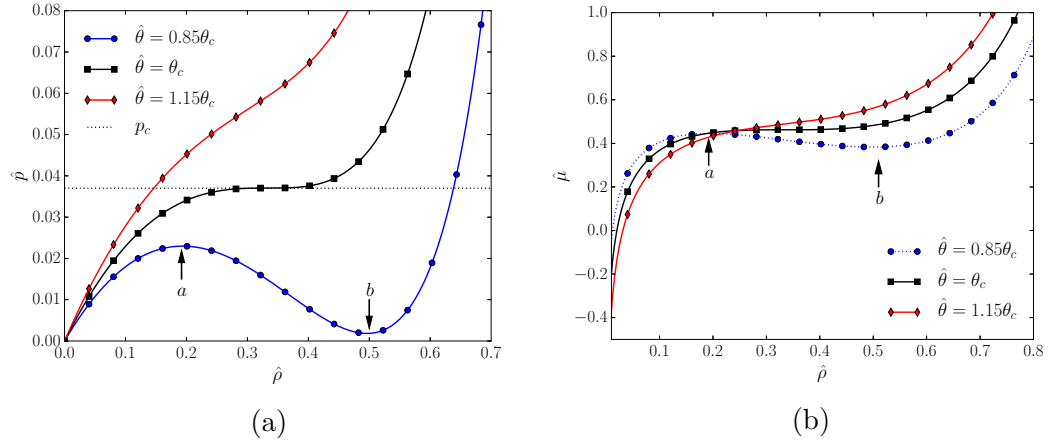


Figure 2.1: Van der Waals fluid: Dimensionless (a) pressure vs. density, (b) chemical potential vs. density.

2.1.1 Maxwell states for the van der Waals fluid model

The Maxwell states represent the states at which the system is in chemical and mechanical equilibrium. The minimum energy principle would imply that a two-phase state is preferred by the system. This could be observed by drawing a common tangent line between the states on the free energy curve, since it falls below the free energy line, two phases are favourable. The equilibrium vapour and liquid states are evaluated at the points where

$$\begin{aligned} p(\rho_v^M) &= p(\rho_l^M) \\ \eta(\rho_v^M) &= \eta(\rho_l^M). \end{aligned}$$

The $\theta - \rho$ phase diagram for the van der Waals fluid at the Maxwell states is shown in the Figure 2.2. The outline of the elliptic region is referred to as the spinodal line. This line intersects with the Maxwell binodal line at the critical point, beyond

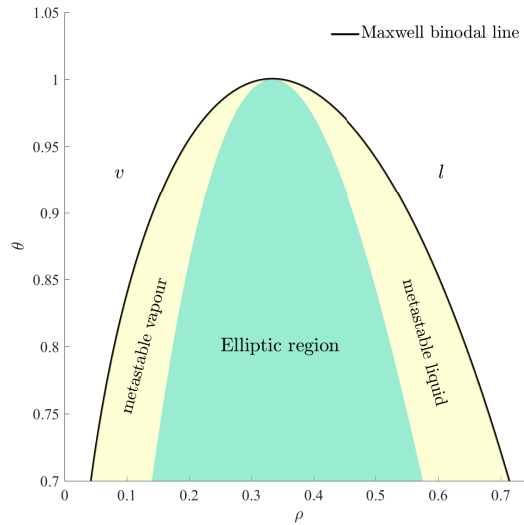


Figure 2.2: Liquid-vapour phase diagram depicting the Maxwell binodal line.

which fluid becomes supercritical (i.e. no definitive liquid and vapour states). The regions between the spinodal line and Maxwell binodal line correspond to metastable regions of liquid and vapour. These regions correspond to unstable energy states, which may be perturbed thermodynamically in order to overcome the energy barrier, moving them towards stable liquid and vapour states [62].

2.2 Governing equations

The thermodynamic concepts presented thus far will be instrumental in recovering the Navier-Stokes-Korteweg equations. First however, the conservation laws which constitute the Navier-Stokes equations will be constructed.

2.2.1 Conservation laws

Before describing the conservation laws, a few important assumptions will be mentioned:

- The fluids at the scale of interest are considered as a continuum.
- Long-ranged forces are neglected, e.g. Electromagnetic forces.
- The field variables are differentiable.

The Reynolds transport theorem states that the sum of the changes of a parameter α defined over a control volume Ω must be equal to what is gained or lost through the boundaries of the volume, plus what is created/consumed by a source/sink. This can be written as

$$\frac{d}{dt} \int_{\Omega} \alpha \, d\Omega = - \int_{\Gamma} \alpha \mathbf{u} \cdot \mathbf{n} \, d\Gamma - \int_{\Omega} Q \, d\Omega, \quad (2.19)$$

where Γ denotes the smooth boundary of Ω , and \mathbf{n} denotes the unit outward normal. By considering the divergence theorem and the Leibniz integral rule, the above expression is simplified to

$$\int_{\Omega} \frac{\partial \alpha}{\partial t} \, d\Omega = - \int_{\Omega} \nabla \cdot (\alpha \mathbf{u}) \, d\Omega - \int_{\Omega} Q \, d\Omega. \quad (2.20)$$

Since this holds for all Ω , the integral can be dropped,

$$\frac{\partial \alpha}{\partial t} = -\nabla \cdot (\alpha \mathbf{u}) - Q. \quad (2.21)$$

Conservation of mass

Applying the Reynolds transport theorem to the mass density ρ , without any sources/sinks, gives

$$\frac{d}{dt} \int_{\Omega} \rho \, d\Omega = - \int_{\Gamma} \rho \mathbf{u} \cdot \mathbf{n} \, d\Gamma. \quad (2.22)$$

The left-hand side of the equation represents the rate of changing mass in Ω , and the right-hand side represents the flow through boundary Γ . Thus the only way in which the mass inside Ω can change is if it flows in or out of Γ . Utilizing the divergence theorem, and taking into account that it holds for all Ω , gives

$$\frac{\partial \rho}{\partial t} + \nabla \cdot (\rho \mathbf{u}) = 0. \quad (2.23)$$

Introducing the material derivative as $\frac{D}{Dt} := \partial + \mathbf{u} \cdot \nabla$, the equation may be expressed as

$$\frac{D\rho}{Dt} + \rho \nabla \cdot \mathbf{u} = 0. \quad (2.24)$$

which suggests that the density can only change if the fluid is subjected to expansion or compression, i.e. $\nabla \cdot \mathbf{u} \neq 0$.

Conservation of momentum

Again using the Reynolds transport theorem, this time considering the momentum $\rho \mathbf{u}$, gives

$$\frac{d}{dt} \int_{\Omega} \rho \mathbf{u} \, d\Omega = - \int_{\Gamma} \rho \mathbf{u} (\mathbf{u} \cdot \mathbf{n}) \, d\Gamma + \int_{\Omega} \rho \mathbf{b} \, d\Omega, \quad (2.25)$$

where \mathbf{b} represents the body/external forces. With the total forces exerted by stress attributed to a symmetric stress tensor $\boldsymbol{\sigma}$, Equation 2.25 becomes

$$\frac{d}{dt} \int_{\Omega} \rho \mathbf{u} \, d\Omega = \int_{\Gamma} (\boldsymbol{\sigma} \mathbf{n} - \rho \mathbf{u} (\mathbf{u} \cdot \mathbf{n})) \, d\Gamma + \int_{\Omega} \rho \mathbf{b} \, d\Omega. \quad (2.26)$$

Using the divergence theorem and mass conservation, this is reduced to

$$\frac{\partial(\rho \mathbf{u})}{\partial t} + \nabla \cdot (\rho \mathbf{u} \otimes \mathbf{u}) - \nabla \cdot \boldsymbol{\sigma} - \rho \mathbf{b} = \mathbf{0}, \quad (2.27)$$

For Newtonian fluids, the stress term $\boldsymbol{\sigma}$ can be assumed as

$$\boldsymbol{\sigma} = \boldsymbol{\tau} - p \mathbf{I}, \quad (2.28)$$

where the viscous component is written as

$$\boldsymbol{\tau} = 2\mu \nabla^s \mathbf{u} + \zeta \nabla \cdot \mathbf{u} \mathbf{I}. \quad (2.29)$$

Here μ and ζ are coefficients of viscosity, and the symmetric gradient is $\nabla^s := \frac{1}{2}(\nabla + \nabla^T)$. For the remainder of this chapter the satisfaction of the Stokes hypothesis will be assumed, that is $\zeta = -\frac{2}{3}\mu$.

Conservation of energy

Considering the energy $\rho \mathcal{E}$ comprised of internal and kinetic energies, the conservation of energy as applied to Ω fixed in space is

$$\frac{d}{dt} \int_{\Omega} \rho \mathcal{E} \, d\Omega = \int_{\Gamma} (\boldsymbol{\sigma} \mathbf{u} - \rho \mathcal{E} \mathbf{u} - \mathbf{q}) \cdot \mathbf{n} \, d\Gamma + \int_{\Omega} \rho \mathbf{b} \cdot \mathbf{u} + \rho r \, d\Omega. \quad (2.30)$$

The heat flux is obtained from Fourier's law as

$$\mathbf{q} = -k\nabla\theta, \quad (2.31)$$

where k is the thermal conductivity, and r denotes a heat source. Appropriately applying the divergence theorem, gives

$$\frac{\partial(\rho\mathcal{E})}{\partial t} + \nabla \cdot (\rho\mathcal{E}\mathbf{u} - \boldsymbol{\sigma} \cdot \mathbf{u} + \mathbf{q}) - \rho\mathbf{b} \cdot \mathbf{u} - \rho r = 0, \quad (2.32)$$

2.2.2 The Navier-Stokes-Korteweg equations

The Navier-Stokes-Korteweg model modifies the Navier-Stokes equations, replacing the ideal fluid with a van der Waals fluid, and appropriately modifying the Cauchy stress tensor to account for interfacial stresses. This is better understood by considering the equilibrium conditions of the van der Waals fluid; Minimising Equation (2.8) under a mass conservation constraint yields,

$$\frac{\delta\mathcal{F}}{\delta\rho} = \frac{\partial(\rho\Psi_b)}{\partial\rho} - \lambda\Delta\rho + c = 0, \quad (2.33)$$

with the conservation of mass related Lagrange multiplier c . Noether's theorem [29] dictates there is a conservation law:

$$\nabla \cdot \mathbf{S} = 0, \quad (2.34)$$

where

$$\mathbf{S} = \mathcal{L}\mathbf{I} - \nabla\rho \otimes \frac{\partial\mathcal{L}}{\partial\nabla\rho}. \quad (2.35)$$

Here $\mathcal{L} = \rho(\Psi_b + \Psi_s - c)$. Substituting Equation (2.33) into Equation (2.34), and recalling from Equation (2.10a) that the thermodynamic pressure $p = \rho^2 \frac{\partial\Psi_b}{\partial\rho}$, yields

$$\nabla p - \nabla \cdot \lambda \left[\left(\rho\Delta\rho + \frac{1}{2}|\nabla\rho|^2 \right) \mathbf{I} - \nabla\rho \otimes \nabla\rho \right] = 0 \quad (2.36)$$

The first term here is the pressure gradient, and the second term is associated with the Korteweg or capillary stress. The reader is referred to [29] for a more detailed analysis into the derivation of the Navier-Stokes-Korteweg equations starting from the conservation of mass, momentum, internal energy and entropy.

Utilising the fundamental thermodynamic concepts from Section 2.1 and hydrodynamic conservation laws from Section 2.2.1, the full non-isothermal Navier-Stokes-Korteweg equations can now be presented for the purpose of studying liquid-vapour phase transition. The strong form of the Navier-Stokes-Korteweg equations may be written as follows.

Strong form: The boundary value problem, considering a sufficiently smooth domain $\Omega \subset \mathbb{R}^d$ (d is the number of spatial dimensions) bounded by Γ and for

the time interval $\mathcal{I} = (0, T)$, consists of finding the density ρ , velocity \mathbf{u} and temperature θ such that

$$\frac{\partial \rho}{\partial t} + \nabla \cdot (\rho \mathbf{u}) = 0 \quad \text{in } \Omega \times \mathcal{I} \quad (2.37a)$$

$$\frac{\partial (\rho \mathbf{u})}{\partial t} + \nabla \cdot (\rho \mathbf{u} \otimes \mathbf{u}) + \nabla p - \nabla \cdot (\boldsymbol{\tau} + \boldsymbol{\kappa}) - \rho \mathbf{b} = \mathbf{0} \quad \text{in } \Omega \times \mathcal{I} \quad (2.37b)$$

$$\frac{\partial (\rho \mathcal{E})}{\partial t} + \nabla \cdot ((\rho \mathcal{E} + p) \mathbf{u} - (\boldsymbol{\tau} + \boldsymbol{\kappa}) \mathbf{u} + \mathbf{q}) - \rho \mathbf{b} \cdot \mathbf{u} - \rho r = 0 \quad \text{in } \Omega \times \mathcal{I}. \quad (2.37c)$$

Here the thermodynamic pressure p is approximated with the van der Waals equation of state (2.10a). The viscous stress tensor $\boldsymbol{\tau}$ and Korteweg stress tensor are written as in Equations (2.29) and (2.1), respectively. The useful *non-conservative* identity $\nabla \cdot \boldsymbol{\kappa} = \lambda \rho \nabla \Delta \rho$ is often considered here. In the present study however, the full *conservative* form, i.e. Equation (2.1), is considered. It is not uncommon to include a term accounting for the power expenditure of the microstress (see, for instance [62]). The term $\nabla \cdot \boldsymbol{\Pi}$ is added to the energy equation (2.37c), where

$$\boldsymbol{\Pi} = \lambda \rho \nabla \cdot \mathbf{u} \nabla \rho. \quad (2.38)$$

Furthermore the total energy can be expressed as the sum of the internal and the kinetic energies,

$$\rho \mathcal{E} = \rho i + \frac{\rho}{2} |\mathbf{u}|^2, \quad (2.39)$$

where i is obtained from Equation (2.11a).

2.2.3 Order reduction with auxiliary variable

It is convenient to reduce the order of the PDEs to allow computationally efficient lower order elements to be used at the discrete level. Since the Korteweg stress term, $\nabla \cdot \boldsymbol{\kappa}$, carries the highest order partial derivative, a new variable $\Upsilon = \Delta \rho$ is introduced as an additional equation. The terms of the strong form can be rewritten as

$$\frac{\partial \rho}{\partial t} + \nabla \cdot (\rho \mathbf{u}) = 0 \quad (2.40a)$$

$$\frac{\partial (\rho \mathbf{u})}{\partial t} + \nabla \cdot (\rho \mathbf{u} \otimes \mathbf{u}) + \nabla p - \nabla \cdot (\boldsymbol{\tau} + \boldsymbol{\kappa}) - \rho \mathbf{b} = \mathbf{0} \quad (2.40b)$$

$$\frac{\partial (\rho \mathcal{E})}{\partial t} + \nabla \cdot ((\rho \mathcal{E} + p) \mathbf{u} - (\boldsymbol{\tau} + \boldsymbol{\kappa}) \mathbf{u} + \mathbf{q}) - \rho \mathbf{b} \cdot \mathbf{u} - \rho r = 0 \quad (2.40c)$$

$$\Upsilon - \Delta \rho = 0, \quad (2.40d)$$

where

$$\boldsymbol{\kappa} = \lambda \left(\rho \Upsilon + \frac{1}{2} |\nabla \rho|^2 \right) \mathbf{I} - \lambda \nabla \rho \otimes \nabla \rho. \quad (2.41)$$

2.2.4 Dimensionless form

This subsection describes the non-dimensional form of the Navier-Stokes-Korteweg equations with the additional auxiliary equation, as described in Section 2.2.3. The process would be identical with the standard Navier-Stokes-Korteweg equations from 2.2.2. As in Equation (2.14), the dimensionless quantities are expressed as $(\hat{\bullet})$, such that the governing equations become

$$\frac{\partial \hat{\rho}}{\partial \hat{t}} + \hat{\nabla} \cdot (\hat{\rho} \hat{\mathbf{u}}) = 0, \quad (2.42a)$$

$$\frac{\partial (\hat{\rho} \hat{\mathbf{u}})}{\partial \hat{t}} + \hat{\nabla} \cdot (\hat{\rho} \hat{\mathbf{u}} \otimes \hat{\mathbf{u}}) + \hat{\nabla} \hat{p} - \hat{\nabla} \cdot (\hat{\boldsymbol{\tau}} + \hat{\boldsymbol{\kappa}}) - \hat{\rho} \hat{\mathbf{b}} = \mathbf{0}, \quad (2.42b)$$

$$\frac{\partial (\hat{\rho} \hat{\mathcal{E}})}{\partial \hat{t}} + \hat{\nabla} \cdot \left((\hat{\rho} \hat{\mathcal{E}} + \hat{p}) \hat{\mathbf{u}} - (\hat{\boldsymbol{\tau}} - \hat{\boldsymbol{\kappa}}) \hat{\mathbf{u}} + \hat{\mathbf{q}} \right) - \hat{\rho} \hat{\mathbf{b}} \cdot \hat{\mathbf{u}} - \hat{\rho} \hat{r} = 0, \quad (2.42c)$$

$$\hat{\Upsilon} - \hat{\Delta} \hat{\rho} = 0, \quad (2.42d)$$

with

$$\hat{p} = \frac{8}{27} \frac{\hat{\theta} \hat{\rho}}{1 - \hat{\rho}} - \hat{\rho}^2, \quad (2.43a)$$

$$\hat{\boldsymbol{\tau}} = \frac{2}{\text{Re}} \left(\hat{\nabla}^s \hat{\mathbf{u}} - \frac{1}{3} \hat{\nabla} \cdot \hat{\mathbf{u}} \mathbf{I} \right), \quad (2.43b)$$

$$\hat{\boldsymbol{\kappa}} = \frac{1}{\text{We}} \left(\left(\hat{\rho} \hat{\Upsilon} + \frac{1}{2} |\hat{\nabla} \hat{\rho}|^2 \right) \mathbf{I} - \hat{\nabla} \hat{\rho} \otimes \hat{\nabla} \hat{\rho} \right), \quad (2.43c)$$

$$\hat{\mathbf{q}} = -\frac{8c_v}{27\bar{R}\text{RePr}} \hat{\nabla} \hat{\theta}. \quad (2.43d)$$

Here the Weber number We is as in Equation (2.16), and the Reynolds number and Prandtl number are respectively,

$$\text{Re} = \frac{Lb\sqrt{ab}}{\mu}, \quad \text{Pr} = \frac{c_p \mu}{k}, \quad (2.44)$$

where $c_p = \bar{\gamma} c_v$ and is the specific heat capacity at constant pressure. The total energy can be expressed as

$$\hat{\rho} \hat{\mathcal{E}} = \frac{8\hat{\rho} \hat{\theta}}{27(\bar{\gamma} - 1)} - \hat{\rho}^2 + \frac{1}{2\text{We}} |\hat{\nabla} \hat{\rho}|^2 + \frac{1}{2} \hat{\rho} |\hat{\mathbf{u}}|^2. \quad (2.45)$$

For the remainder of this chapter, the hat $(\hat{\bullet})$ will be omitted from the dimensionless equations.

2.2.5 Isothermal case

For the case of a constant temperature the system Equations (2.40a)-(2.40d) reduce to three equations.

$$\frac{\partial \rho}{\partial t} + \nabla \cdot (\rho \mathbf{u}) = 0 \quad (2.46a)$$

$$\frac{\partial \rho \mathbf{u}}{\partial t} + \nabla \cdot (\rho \mathbf{u} \otimes \mathbf{u}) + \nabla p(\rho) - \nabla \cdot (\boldsymbol{\tau} + \boldsymbol{\kappa}) - \rho \mathbf{b} = \mathbf{0} \quad (2.46b)$$

$$\Upsilon - \Delta \rho = 0, \quad (2.46c)$$

where $p(\rho)$, $\boldsymbol{\tau}$ and $\boldsymbol{\kappa}$ are respectively as written in Equations (2.10a), (2.29) and (2.41). The dimensionless form of the isothermal case is as written in Equations (2.42a)-(2.42c), with the pressure and stress terms defined as Equations (2.43a)-(2.43c).

2.2.6 Boundary conditions

The general contact angle boundary condition is as follows:

$$-\frac{\nabla \rho}{|\nabla \rho|} \cdot \mathbf{n} = \cos \alpha. \quad (2.47)$$

where $|\nabla \rho| = (\nabla \rho \cdot \nabla \rho)^{1/2}$. α is the three-phase contact angle at the boundary. For the special case of a 90° contact angle, i.e. $\alpha = \pi/2$, the boundary condition becomes

$$\nabla \rho \cdot \mathbf{n} = 0 \quad (2.48)$$

The boundary term which appends to the strong form description of the auxiliary equation 2.42d, and likewise its isothermal counterpart, is as follows:

$$\nabla \rho \cdot \mathbf{n} + |\nabla \rho| \cos(\alpha) = 0 \quad \text{on } \Gamma_q \times \mathcal{I}. \quad (2.49)$$

where Γ_q once more used to denotes the Neumann subset of Γ , the boundary of Ω .

For non-isothermal cases it is commonplace to prescribe a heat flux boundary condition as follows:

$$\mathbf{q} \cdot \mathbf{n} = 0 \quad \text{on } \Gamma_q \times \mathcal{I}. \quad (2.50)$$

2.2.7 Physical relevance of parameters

The capillary coefficient λ is related to both the physical surface tension and interface thickness of a liquid-vapour system. The surface tension coefficient γ , not to be confused with the heat capacity ratio, can be obtained by considering the expression of the surface/interfacial energy of an equilibrium density profile,

$$\gamma = \int_{x-}^{x+} \lambda \left(\frac{d\rho}{dx} \right)^2 dx \quad (2.51)$$

It is important that the interface thickness is set sufficiently large such that the diffuse interface can be resolved, and spurious oscillations avoided. It is suggested by Jamet et al. [74], that for temperatures slightly lower than the critical temperature, the interface associate with a liquid-vapour system is of the order of $1 \mu\text{m}$. This is a numerically viable length scale, and supports the overwhelming use of the Navier-Stokes-Korteweg equations to model critical phenomena. The

authors provide descriptions of the interface thickness and surface tension under assumptions that the temperature is close to critical,

$$\epsilon = \frac{4}{\rho_l - \rho_v} \sqrt{\frac{\lambda}{2A}}, \quad (2.52)$$

$$\gamma = \frac{(\rho_l - \rho_v)^3}{\sqrt{2A\lambda}}, \quad (2.53)$$

where ρ_l and ρ_v are the saturation densities and A is a constant. Combining the two yields the capillary coefficient as a function of interface thickness and surface tension coefficient [75],

$$\lambda = \frac{3}{2} \frac{\gamma \epsilon}{(\rho_l - \rho_v)^2} \quad (2.54)$$

2.3 Numerical Formulation

This section presents the variational form of the Navier-Stokes-Korteweg equations, as well as the discretisation in space and time.

The weak form of the continuous Navier-Stokes-Korteweg problem described in Equations (2.42a)-(2.42d) with appropriate integration by parts, reads: Find $(\rho, \mathbf{u}, \theta, \Upsilon) \in \mathcal{X}$, such that, for all $(q, \mathbf{w}, v, s) \in \mathcal{Y}$,

$$\int_{\Omega} q \frac{\partial \rho}{\partial t} - \nabla q \cdot \rho \mathbf{u} \, d\Omega = 0 \quad (2.55a)$$

$$\begin{aligned} \int_{\Omega} \mathbf{w} \cdot \left(\mathbf{u} \frac{\partial \rho}{\partial t} + \rho \frac{\partial \mathbf{u}}{\partial t} \right) - \nabla \mathbf{w} : (\rho \mathbf{u} \otimes \mathbf{u}) - (\nabla \cdot \mathbf{w}) p + \nabla \mathbf{w} : (\boldsymbol{\tau} + \boldsymbol{\kappa}) \\ - \mathbf{w} \cdot \rho \mathbf{b} \, d\Omega = 0 \end{aligned} \quad (2.55b)$$

$$\begin{aligned} \int_{\Omega} v \frac{\partial(\rho \mathcal{E})}{\partial t} - \nabla v \cdot (\rho \mathcal{E} + p) \mathbf{u} + \nabla v \cdot (\boldsymbol{\tau} + \boldsymbol{\kappa}) \mathbf{u} - \nabla v \cdot \mathbf{q} - v (\rho \mathbf{b} \cdot \mathbf{u}) \\ - v \rho r \, d\Omega = 0 \end{aligned} \quad (2.55c)$$

$$\int_{\Omega} s \Upsilon + \nabla s \cdot \nabla \rho \, d\Omega + \int_{\Gamma} s |\nabla \rho| \cos(\alpha) \, d\Gamma = 0, \quad (2.55d)$$

where \mathcal{X} and \mathcal{Y} denote the appropriate trial solution and weighting function spaces, respectively.

Considering Equation (2.45), and noting that $|\mathbf{A}|^2 = \mathbf{A} \cdot \mathbf{A}$,

$$\rho \mathcal{E} = \frac{8}{27} \frac{\theta \rho}{\bar{\gamma} - 1} - \rho^2 + \frac{1}{2} \rho \mathbf{u} \cdot \mathbf{u} + \frac{1}{2\text{We}} \nabla \rho \cdot \nabla \rho. \quad (2.56)$$

The other functions $p, \boldsymbol{\tau}, \boldsymbol{\kappa}, \mathbf{q}$ are given in Equations (2.43a)-(2.43d).

2.3.1 Spatial semi-discrete weak form

Considering the standard Galerkin method [76, 77], the following interpolations are defined:

$$\begin{aligned} \mathbf{u}^h &= \sum_{A \in \mathcal{N}} N_A \mathbf{u}_A, \quad \rho^h = \sum_{A \in \mathcal{N}} N_A \rho_A, \quad \theta^h = \sum_{A \in \mathcal{N}} N_A \theta_A, \quad \Upsilon^h = \sum_{A \in \mathcal{N}} N_A \Upsilon_A \\ \mathbf{w}^h &= \sum_{A \in \mathcal{N}} N_A \mathbf{w}_A, \quad q^h = \sum_{A \in \mathcal{N}} N_A q_A, \quad v^h = \sum_{A \in \mathcal{N}} N_A v_A, \quad s^h = \sum_{A \in \mathcal{N}} N_A s_A, \end{aligned} \quad (2.57)$$

where N_A denotes the shape functions, and \mathcal{N} denotes the sets of nodes. Discretising the weak form in Equations (2.55a)-(2.55d) and expanding the terms reads : Find $(\rho^h, \mathbf{u}^h, \theta^h, \Upsilon^h) \in \mathcal{X}^h$, such that, for all $(q^h, \mathbf{w}^h, v^h, s^h) \in \mathcal{Y}^h$,

$$\int_{\Omega} q^h \frac{\partial \rho^h}{\partial t} - \nabla q^h \cdot \rho^h \mathbf{u}^h \, d\Omega = 0 \quad (2.58a)$$

$$\begin{aligned} \int_{\Omega} \mathbf{w}^h \cdot \left(\mathbf{u}^h \frac{\partial \rho^h}{\partial t} + \rho^h \frac{\partial \mathbf{u}^h}{\partial t} - \rho^h \mathbf{b} \right) - \nabla \mathbf{w}^h : (\rho^h \mathbf{u}^h \otimes \mathbf{u}^h) \\ - \nabla \cdot \mathbf{w}^h \left(\frac{8}{27} \frac{\theta \rho^h}{1 - \rho^h} - (\rho^h)^2 \right) + \nabla \mathbf{w}^h : \frac{2}{\text{Re}} \left(\nabla^s \mathbf{u}^h - \frac{1}{3} \nabla \cdot \mathbf{u}^h \mathbf{I} \right) \\ + \nabla \cdot \mathbf{w}^h \frac{1}{\text{We}} \left(\rho^h \Upsilon^h + \frac{1}{2} \nabla \rho^h \cdot \nabla \rho^h \right) - \nabla \mathbf{w}^h : \frac{1}{\text{We}} \nabla \rho^h \otimes \nabla \rho^h \, d\Omega = 0 \end{aligned} \quad (2.58b)$$

$$\begin{aligned} \int_{\Omega} v^h \frac{\partial}{\partial t} \left(\frac{8}{27} \frac{\theta \rho^h}{\bar{\gamma} - 1} - (\rho^h)^2 + \frac{1}{2} \rho^h \mathbf{u}^h \cdot \mathbf{u}^h + \frac{1}{2\text{We}} \nabla \rho^h \cdot \nabla \rho^h \right) \\ - \nabla v^h \cdot \left(\frac{8}{27} \frac{\theta \rho^h}{1 - \rho^h} - 2(\rho^h)^2 \right) \mathbf{u}^h - \nabla v^h \cdot \left(\frac{8}{27} \frac{\theta \rho^h}{\bar{\gamma} - 1} + \frac{1}{2} \rho^h \mathbf{u}^h \cdot \mathbf{u}^h \right. \\ \left. + \frac{1}{2\text{We}} \nabla \rho^h \cdot \nabla \rho^h \right) \mathbf{u}^h + \nabla v^h \cdot \frac{2}{\text{Re}} \left(\nabla^s \mathbf{u}^h - \frac{1}{3} \nabla \cdot \mathbf{u}^h \mathbf{I} \right) \mathbf{u}^h \\ + \nabla v^h \cdot \frac{1}{\text{We}} \left(\left(\rho^h \Upsilon^h + \frac{1}{2} \nabla \rho^h \cdot \nabla \rho^h \right) \mathbf{I} - \nabla \rho^h \otimes \nabla \rho^h \right) \mathbf{u}^h \\ + \nabla v^h \cdot k \nabla \theta - v^h (\rho^h \mathbf{b} \cdot \mathbf{u}^h) \, d\Omega = 0 \end{aligned} \quad (2.58c)$$

$$\int_{\Omega} s \Upsilon^h + \nabla s^h \cdot \nabla \rho^h \, d\Omega + \int_{\Gamma} s^h |\nabla \rho^h| \cos(\alpha) \, d\Gamma = 0. \quad (2.58d)$$

where \mathcal{X}^h and \mathcal{Y}^h denote the appropriate trial solution and weighting function finite element spaces of piecewise continuous linear basis functions, respectively.

2.3.2 Temporal discretisation

The generalised- α method is employed for the temporal discretisation. This method is an unconditionally stable, implicit single-step time integration scheme (refer to [78, 79]). The scheme allows for high frequency damping to be controlled by without compromising the second order accuracy (see [80, 65]). Applying the generalised- α method to a generic first order problem gives

$$\dot{\mathbf{u}}^{n+\alpha_m} = \mathbf{f}(t^{n+\alpha_f}, \mathbf{u}^{n+\alpha_f}), \quad (2.59)$$

with

$$\dot{\mathbf{u}}^{n+\alpha_m} = (1 - \alpha_m) \dot{\mathbf{u}}^n + \alpha_m \dot{\mathbf{u}}^{n+1} \quad (2.60)$$

$$t^{n+\alpha_f} = (1 - \alpha_f) t^n + \alpha_f t^{n+1} \quad (2.61)$$

$$\mathbf{u}^{n+\alpha_f} = (1 - \alpha_f) \mathbf{u}^n + \alpha_f \mathbf{u}^{n+1} \quad (2.62)$$

$$\frac{\mathbf{u}^{n+1} - \mathbf{u}^n}{\Delta t} = (1 - \gamma) \dot{\mathbf{u}}^n + \gamma \dot{\mathbf{u}}^{n+1}, \quad (2.63)$$

and,

$$\alpha_m = \frac{1}{2} \frac{3 - \rho_\infty}{1 + \rho_\infty}, \quad \alpha_f = \frac{1}{1 + \rho_\infty}, \quad \gamma = \frac{1}{2} + \alpha_m - \alpha_f, \quad (2.64)$$

where γ must not be confused with the surface tension parameter. Note that α_m , α_f and γ are expressed in terms of the spectral radius ρ_∞ for an infinitely large time step size.

This scheme has been successfully employed in solution of a number of challenging coupled field problems [5, 81, 82, 83].

2.3.3 Solution strategy

The system described by Equations (2.55a)-(2.55d) is solved using the Newton-Raphson method. The Newton-Raphson procedure including the linearisation of the nonlinear terms is shown in Appendix A.1. A direct linear solver (PARDISO [84, 85, 86]) is used for smaller problems, whereas for larger scale problems, an iterative parallel solver (PETSC [87]) with a block Jacobi pre-conditioner is employed.

2.3.4 Adaptive time stepping

Several of the numerical examples in the following section implement an adaptive time stepping procedure, wherein the time step size Δt is modified in each time instance according to

$$\Delta t = (t^{n+1} - t^n) \theta^{(n_{\text{iter}} - n_{\text{opt}})}, \quad (2.65)$$

where n_{iter} and n_{opt} are respectively the number of Newton iteration steps required in the previous time step and the desired number of iteration steps. The constant θ is typically chosen between 0.5 and 1.

2.4 Isothermal numerical examples

The numerical examples to follow are set up with the following commonalities:

- *Time integration:* The generalised- α method is used in the time stepping algorithm with $\rho_\infty = 0.5$.
- *Dimensionless parameters:* Unless otherwise stated the dimensional parameters are set as follows:

$$\begin{aligned}
\text{Reynolds number: } \text{Re} &= 2/h, \\
\text{Weber number: } \text{We} &= 1/h^2, \\
\text{Temperature: } \theta &= 0.85.
\end{aligned}$$

Here h is the characteristic element size, which in this case is taken as the largest element size of the mesh used. The parameters Re and We are set based on scaling presented in [66].

2.4.1 Reproducing the $\theta - \rho$ phase diagram

This example involves numerically reproducing the Maxwell binodal line from the $\theta - \rho$ diagram in Figure 2.3. A square domain, $\Omega = [0, 1] \times [0, 1]$, is set up with a uniform initial density; This is chosen as the critical density at the specific temperature of analysis. A perturbation $\delta\rho = 0.01\rho_c$ is added in the domain centre at point $\mathbf{C} = [0.5, 0.5]$. A mesh consisting of 256×256 linear quadrilateral elements is chosen, and the time step size is fixed as $\Delta t = 0.5$. Periodic boundary conditions are set in all directions.

The density is allowed to evolve and decompose into vapour and liquid states as depicted in Figure 2.3. The resulting liquid and vapour densities are recorded in the bulk regions once a steady solution is reached. The points on the $\theta - \rho$ phase diagram in Figure 2.4 were obtained from running several dimensionless temperatures ranging between 0.7 and 1. Clearly a very close match is observed between the numerical points and the analytical Maxwell binodal line.

2.4.2 Coalescence of two vapour bubbles

Coalescence occurs when two or more droplets/bubbles merge to form a single larger droplet/bubble. Such a process frequently occurs in natural or industrial applications. The process is demonstrated visually in Figure 2.5, which depicts experimental results of a small water drop coalescing with a larger body of water [88]. In this numerical example, two vapour bubbles of different sizes are placed an order of magnitude of the interface thickness apart in order to observe their coalescence. This is a classical multiphase benchmark problem, and is constructed following a similar set up to Gomez et al. [66]. The larger bubble with a radius

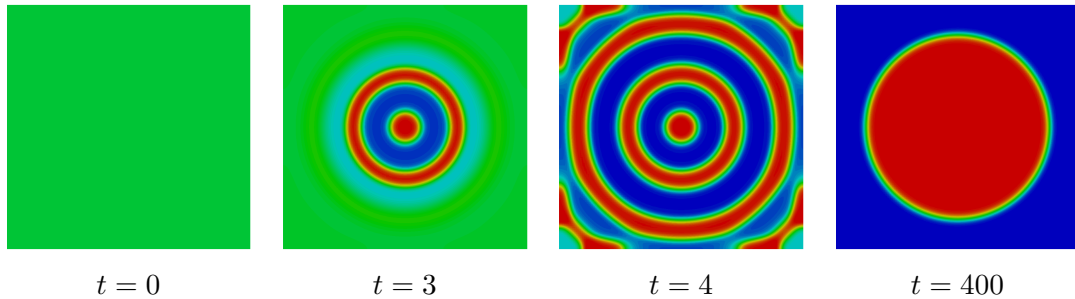


Figure 2.3: $\theta - \rho$ phase diagram: Evolution of critical density with 256×256 linear elements.

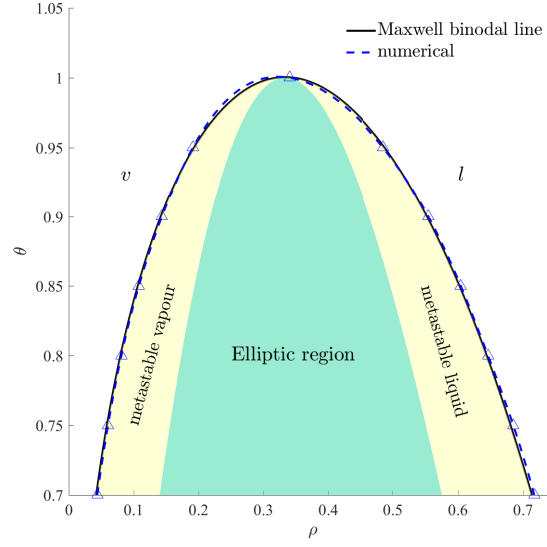


Figure 2.4: $\theta - \rho$ phase diagram: Comparison of the analytical van der Waals solution at the Maxwell states and the numerical solution.

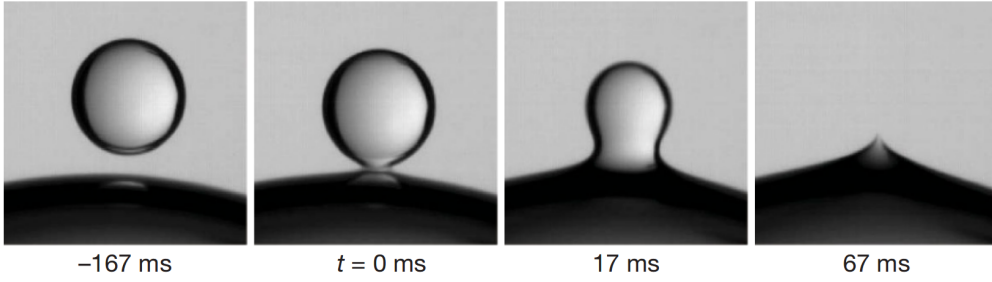


Figure 2.5: Drop coalescence experimental study by Ristenpart et al. [88]

of $R_1 = 0.25$ is placed at the coordinate $\mathbf{C}_1 = [0.4, 0.5]$, while the smaller bubble of radius $R_2 = 0.1$ is situated at $\mathbf{C}_2 = [0.78, 0.5]$. The computational domain considered is of size $\Omega = [0, 1] \times [0, 1]$. Periodic boundary conditions are considered in all directions. The initial conditions are set as:

$$\rho_0(\mathbf{x}) = 0.1 + 0.25 \left(\tanh \left(\frac{|\mathbf{x} - \mathbf{C}_1| - R_1}{2h} \right) + \tanh \left(\frac{|\mathbf{x} - \mathbf{C}_2| - R_2}{2h} \right) \right), \quad \mathbf{x} \in \Omega, \quad (2.66a)$$

$$\mathbf{u}_0(\mathbf{x}) = \mathbf{0}, \quad \mathbf{x} \in \Omega, \quad (2.66b)$$

$$\Upsilon_0(\mathbf{x}) = 0, \quad \mathbf{x} \in \Omega, \quad (2.66c)$$

Multiple uniform meshes consisting of 64×64 , 128×128 and 256×256 linear quadrilateral elements, are considered. A fixed time step size of $\Delta t = 0.1$ is used.

Figures 2.6, 2.7 and 2.8 show the time evolution of the density, auxiliary variable, and velocity streamlines respectively.

The total free energy is shown for element sizes $h = 1/64$ and $h = 1/256$ in Figure 2.9. Although in both cases there is an expected monotonic decrease in energy with time, it is clear that the mesh density has an effect. With $h = 1/256$,

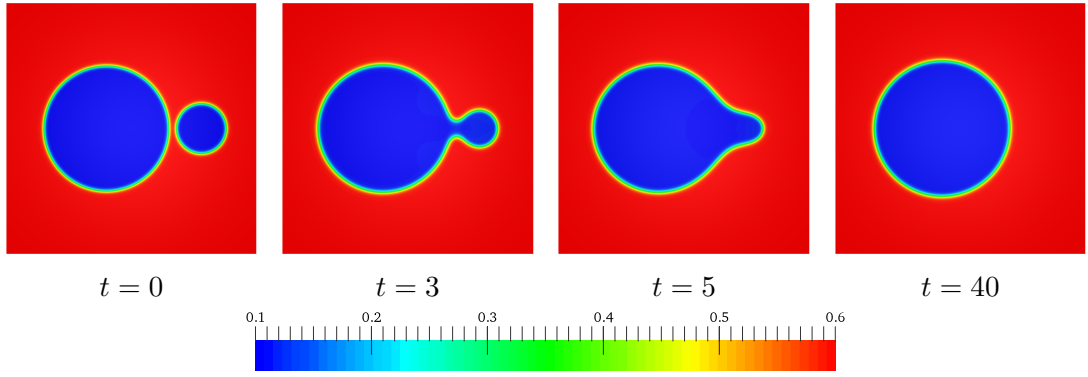


Figure 2.6: Coalescence of two vapour bubbles: Density field evolution, with 256×256 linear elements.

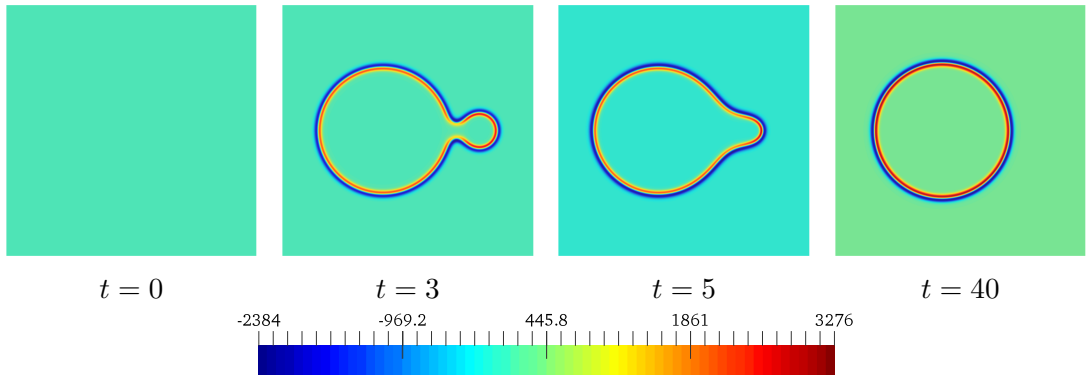


Figure 2.7: Coalescence of two vapour bubbles: Density field evolution, with 256×256 linear elements.

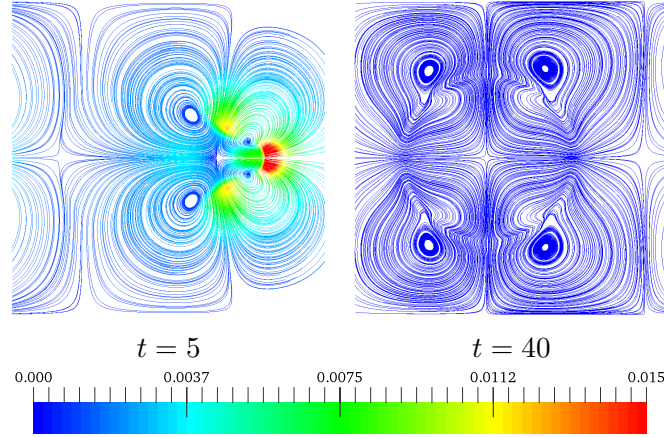


Figure 2.8: Coalescence of two vapour bubbles: Velocity field streamlines at (a) $t = 5$ and (c) $t = 40$, with 256×256 linear elements.

the interface is thin enough such that the bubbles are completely separated at the start of the simulation, and thus there is a notable variation in the energy at $t \approx 3$, where the bubbles coalesce. With the less dense mesh, the coalescence is immediate which explains the lack of energy variation.

An investigation is made into the effects of further refining the mesh, such that

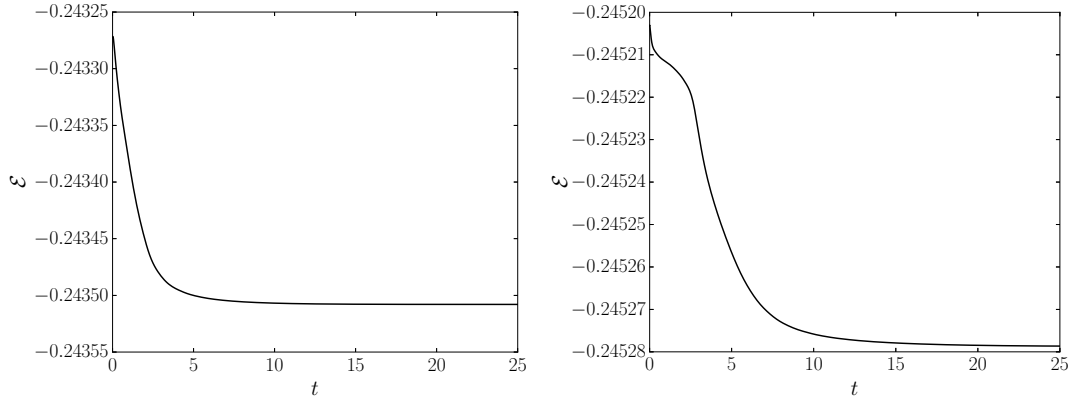


Figure 2.9: Coalescence of two vapour bubbles: Free energy evolution with $h = 1/64$ (left) and $h = 1/256$ (right).

there are 512×512 linear quadrilateral elements. The corresponding interface thickness is hence also reduced, since $We = 1/h^2$, while the geometry remains unchanged. Figure 2.10 shows the evolution of the density field with this denser mesh. It is observed that bubbles do not coalesce in this instance, but rather the larger bubble grows as the smaller one disappears. It may be said that under the equilibrium pressure set by the larger bubble, the smaller one becomes unstable and vanishes. This effect is explored further in the next example (Section 2.4.3).

Three-dimensional analysis: Considering now a computational domain $\Omega = [0, 1] \times [0, 1] \times [0, 1]$, and using the same dimensionless parameters as before, the larger bubble is now placed at position $\mathbf{C}_1 = (0.4, 0.5, 0.55)$ and the smaller one at $\mathbf{C}_2 = (0.75, 0.5, 0.4)$. The initial condition is as before, with the Euclidean distance $|\mathbf{x} - \mathbf{C}_i|$ being extended to three-dimensional space. A uniform mesh is used which consists of $100 \times 100 \times 100$ linear hexahedron elements. The density isolines are shown immersed in the fluid in Figure 2.11. It is observed that the bubbles coalesce similarly to the two-dimensional experiment. Significantly, the coalescence occurs at a faster rate, which is consistent with the observations in [66].

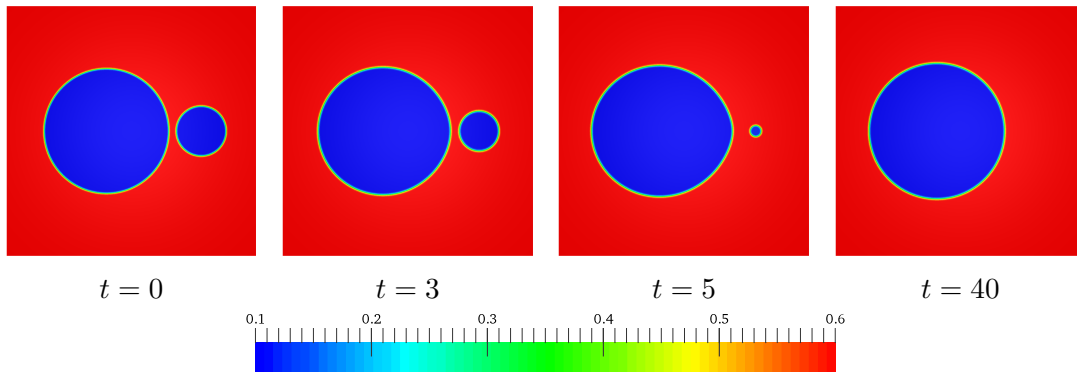


Figure 2.10: Coalescence of two vapour bubbles: Density field evolution, with 512×512 linear elements.

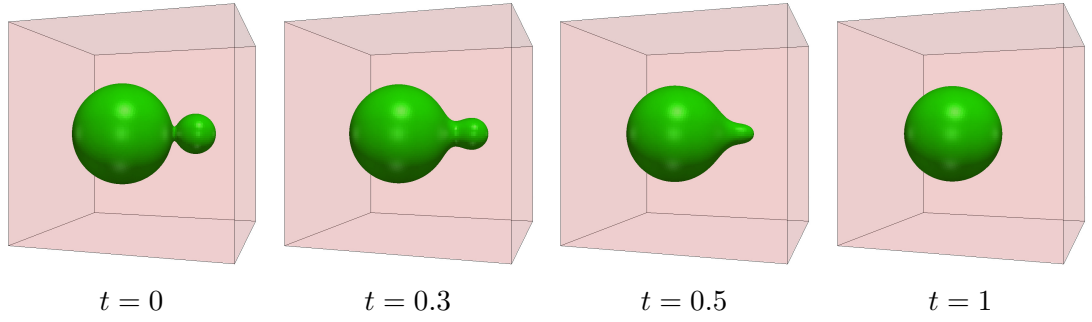


Figure 2.11: Three-dimensional coalescence of two vapour bubbles: Density field evolution, with $100 \times 100 \times 100$ linear elements.

2.4.3 Evolution of three vapour bubbles

This benchmark problem involves three vapour bubbles of different sizes placed at various positions in a square computational domain of size $\Omega = [0, 1] \times [0, 1]$. The three bubbles are placed at coordinates $\mathbf{C}_1 = [0.75, 0.5]$, $\mathbf{C}_2 = [0.25, 0.5]$, $\mathbf{C}_3 = [0.4, 0.75]$ with respective radius sizes of $R_1 = 0.1$, $R_2 = 0.15$ and $R_3 = 0.08$. Periodic boundary conditions are considered in all directions and the initial conditions are set as:

$$\rho_0(\mathbf{x}) = 0.1 + 0.25 \left(\tanh \left(\frac{|\mathbf{x} - \mathbf{C}_1| - R_1}{2h} \right) + \tanh \left(\frac{|\mathbf{x} - \mathbf{C}_2| - R_2}{2h} \right) + \tanh \left(\frac{|\mathbf{x} - \mathbf{C}_3| - R_3}{2h} \right) \right), \quad \mathbf{x} \in \Omega, \quad (2.67a)$$

$$\mathbf{u}_0(\mathbf{x}) = \mathbf{0}, \quad \mathbf{x} \in \Omega, \quad (2.67b)$$

$$\Upsilon_0(\mathbf{x}) = 0, \quad \mathbf{x} \in \Omega. \quad (2.67c)$$

A uniform mesh is chosen, consisting of 256×256 linear quadrilateral elements, and a fixed time step size of $\Delta t = 0.1$ is used.

It is expected from a physical standpoint that the larger bubble would set the equilibrium pressure, causing the smaller bubbles to disappear by inducing an instability at the equilibrium pressure. This behaviour is reflected in the Figures 2.12 and 2.13, which show the time evolution of the density and velocity fields.

The free energy evolution is shown in Figure 2.14, where the notable dips are associated with the disappearance of the smaller bubbles.

Comparison with IGA: To appreciate the results obtained using the low order model, a comparison is made using C_1 continuous b-splines. The IGA formulation is similar to what is presented in [66], where specifically a non-conservative Korteweg stress term is considered, i.e. $\nabla \cdot \boldsymbol{\kappa} = \frac{1}{\text{We}} \rho \nabla \Delta \rho$. Additionally no auxiliary variable is required since the C_1 continuous quadratic b-splines are sufficient to deal with the higher order spatial derivatives present in the Korteweg stress term. In this study the weak formulation is considered as in Equations (2.55a)-(2.55b), with the conservative Korteweg stress term replaced by its non-conservative coun-

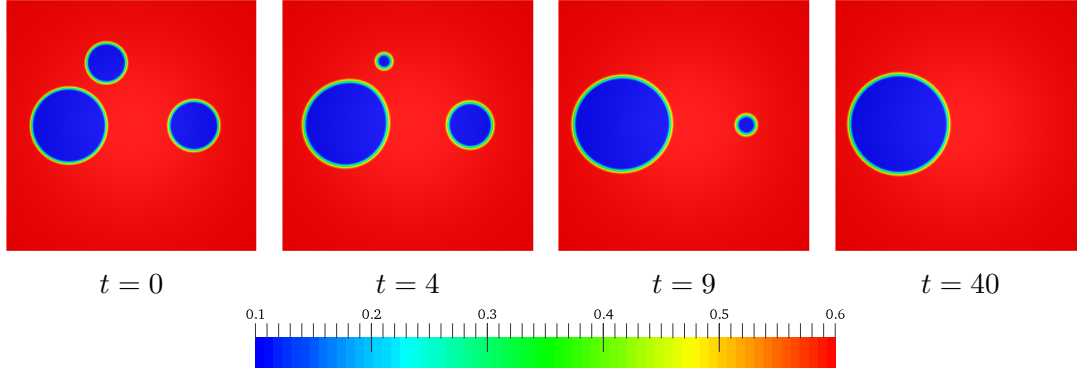


Figure 2.12: Evolution of three vapour bubbles: Density field evolution, with 256×256 linear elements.

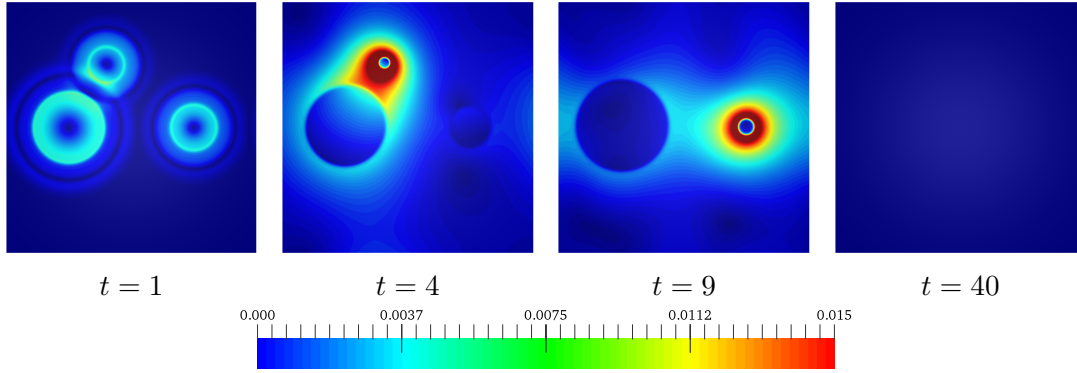


Figure 2.13: Evolution of three vapour bubbles: Density field evolution, with 256×256 linear elements.

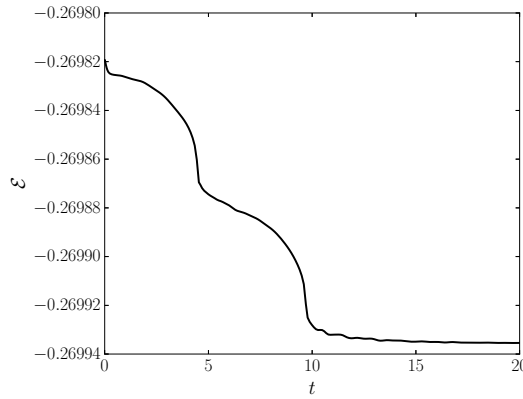


Figure 2.14: Evolution of three vapour bubbles: Free energy evolution.

terpart. The linearisation and discretisation of this non-conservative term is presented in Appendix A.3. Figure 2.15 shows the density field evolution using 256×256 quadratic b-splines. Notably the evolution of the three vapour bubbles is indistinguishable from the lower order simulation presented in Figure 2.13. The free energy evolution is shown in Figure 2.16. The time instances associated with the bubbles disappearing correspond to the observed variations in free energy.

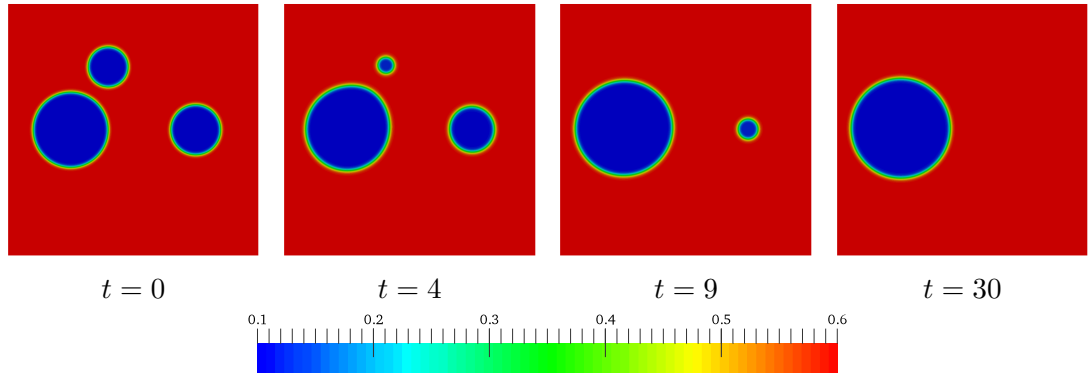


Figure 2.15: Evolution of three vapour bubbles: Density field evolution with IGA analysis, using 256×256 quadratic b-splines.

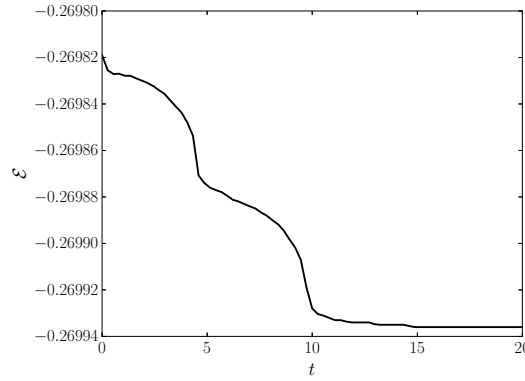


Figure 2.16: Evolution of three vapour bubbles: Free energy evolution with IGA analysis, using 256×256 quadratic b-splines.

The graph matches closely to the behaviour observed in Figure 2.12.

2.4.4 Sessile drop

This example involves obtaining the equilibrium configuration of a sessile drop resting on a rigid surface. The initial conditions are set as:

$$\rho_0(\mathbf{x}) = 0.3545 - 0.2479 \tanh\left(\frac{|\mathbf{x} - \mathbf{C}| - R}{2h}\right), \quad \mathbf{x} \in \Omega, \quad (2.68a)$$

$$\mathbf{u}_0(\mathbf{x}) = \mathbf{0}, \quad \mathbf{x} \in \Omega, \quad (2.68b)$$

$$\Upsilon_0(\mathbf{x}) = 0, \quad \mathbf{x} \in \Omega, \quad (2.68c)$$

where the position of the drop $\mathbf{C} = [0.75, 0]$. Slip velocity boundary conditions are applied to all surfaces. The body force is set as $b = [0, -0.01]^T$. The mesh is comprised of 96×64 linear quadrilateral elements. Adaptive time stepping is used with an initial time step size of $\Delta t = 0.1$.

Figure 2.17 shows the steady state density fields for contact angles 45° , 60° , 90° , 120° and 135° . It should be noted that the angles which are set on the contact boundary are in fact retrieved in the steady state configurations presented in the figures.

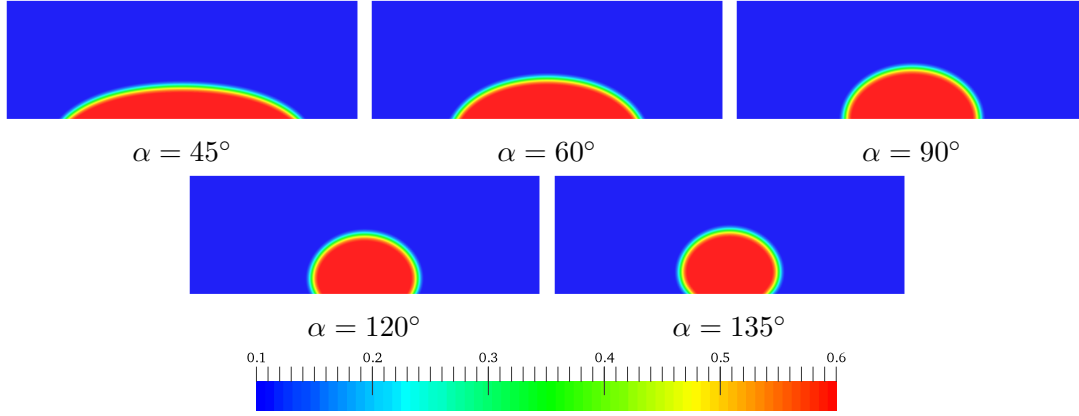


Figure 2.17: Sessile drop: Equilibrium configuration of density field, with 96×64 linear elements.

2.4.5 Falling liquid drop

A simple drop falling in a box, $\Omega = [0, 1] \times [0, 1]$, under the effects of gravity is demonstrated in this example. The gravitational force is set as $b = [0, -0.03]$. The initial conditions are set as:

$$\rho_0(\mathbf{x}) = 0.3545 - 0.2479 \tanh\left(\frac{|\mathbf{x} - \mathbf{C}| - R}{2h}\right), \quad \mathbf{x} \in \Omega, \quad (2.69a)$$

$$\mathbf{u}_0(\mathbf{x}) = \mathbf{0}, \quad \mathbf{x} \in \Omega, \quad (2.69b)$$

$$\Upsilon_0(\mathbf{x}) = 0, \quad \mathbf{x} \in \Omega, \quad (2.69c)$$

where the position of the drop $\mathbf{C} = [0.5, 1]$. Velocity slip boundary conditions are considered on all boundaries. A mesh consisting of 256×256 linear quadrilateral elements is chosen. Adaptive time stepping is used with an initial time step size of $\Delta t = 0.001$. Figure 2.18 shows the time evolution of the density field.

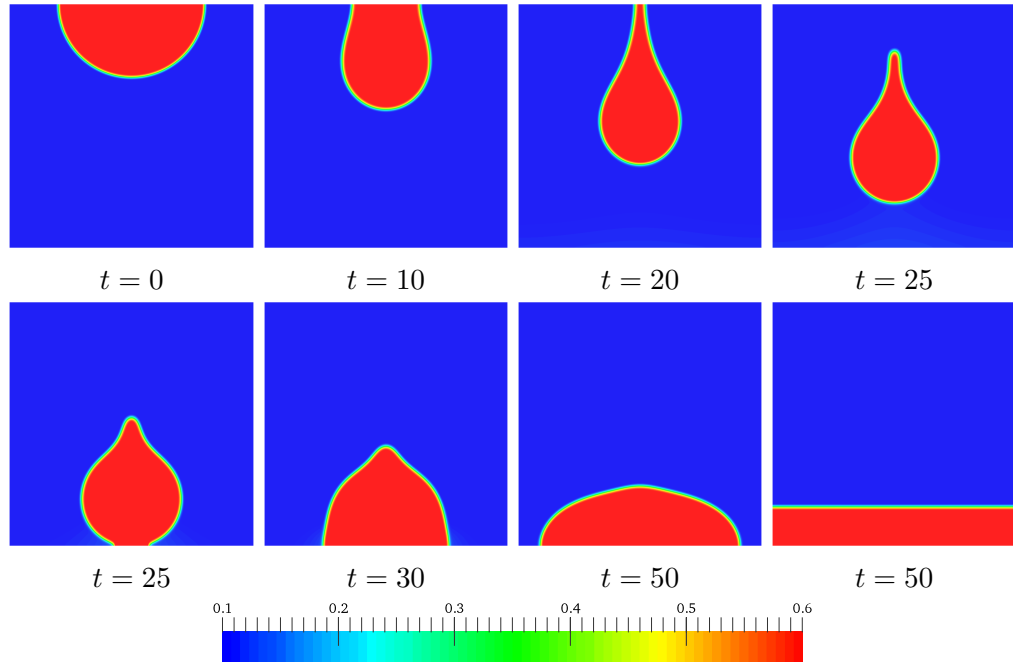


Figure 2.18: Falling liquid drop: Density field evolution, with 256×256 linear elements.

2.5 Non-isothermal numerical examples

As with the isothermal examples the generalised- α method with $\rho_\infty = 0.5$ is chosen. The heat capacity ratio is taken as $\bar{\gamma} = 1.333$ unless otherwise stated.

2.5.1 Evaporation/Condensation

In this demonstration, a vapour bubble of radius $R = 0.25$ is placed in the centre, $\mathbf{C} = [0.5, 0.5]$, of a square computational domain $\Omega = [0, 1] \times [0, 1]$, with the intention of observing the effect of increasing/decreasing the boundary temperature. The initial conditions are set as:

$$\rho_0(\mathbf{x}) = 0.3545 + 0.2479 \tanh\left(\frac{|\mathbf{x} - \mathbf{C}| - R}{2h}\right), \quad \mathbf{x} \in \Omega, \quad (2.70a)$$

$$\mathbf{u}_0(\mathbf{x}) = \mathbf{0}, \quad \mathbf{x} \in \Omega, \quad (2.70b)$$

$$\theta_0(\mathbf{x}) = 0.85, \quad \mathbf{x} \in \Omega, \quad (2.70c)$$

$$\Upsilon_0(\mathbf{x}) = 0, \quad \mathbf{x} \in \Omega, \quad (2.70d)$$

while the boundary conditions are taken as:

$$\mathbf{u} = \mathbf{0}, \quad \text{on } \Gamma, \quad (2.71a)$$

$$\theta = \theta_b, \quad \text{on } \Gamma, \quad (2.71b)$$

$$\nabla \rho \cdot \mathbf{n} = 0, \quad \text{on } \Gamma. \quad (2.71c)$$

Here the boundary temperature ranges from $\theta_b = 0.75$ to $\theta_b = 0.95$. The problem parameters are set as follows: $\text{Re} = 2/h$, $\text{We} = 2/h^2$, $k = 10^{-2}$, where h is the

element size. Two uniform linear quadrilateral meshes are considered: *mesh 1* consisting of 128×128 elements, and *mesh 2* consisting of 256×256 elements. Adaptive time stepping is used with an initial time step size of $\Delta t = 0.0005$. For comparison the analytical radius is obtained by considering the conservation of mass (as in [62]). Neglecting the volume occupied by the interface, the total mass in Ω is evaluated as

$$m = \rho_l V_l + \rho_v V_v = \rho_l(1^2 - \pi R^2) + \rho_v \pi R^2. \quad (2.72)$$

The values of ρ_l and ρ_v are the Maxwell states at the specific temperature of interest (refer to Figure 2.2). Considering (2.72) for $R = 0.25$, $\theta = 0.85$, and the respective Maxwell state densities $\rho_l = 0.6024$ and $\rho_v = 0.1066$, the mass is evaluated as $m = 0.505$. For the other temperatures considered R is solved for in Equation (2.72) given that the mass is conserved.

Figures 2.19 and 2.20 respectively show the steady state configurations of the density field for the boundary temperatures higher and lower than θ_0 . Figure 2.21 shows the comparison between the numerically obtained steady state radii and those obtained analytically from Equation (2.72) for the appropriate Maxwell states. The numerically obtained radii are recorded on the horizontal axis ($y = 0.5$) from the centre of the bubble to the interface centre. The radii are tabulated in Table 2.1 for the different temperatures considered. It is clear that the radii observed match well with the analytical radii. It is also evident that the observed radii approach the analytical radii with increasing mesh density, and consequently reducing the interface thickness.

2.5.2 Nucleate boiling

Boiling is one of the most commonly encountered examples of phase transition in our daily lives. The process involves a liquid rapidly vaporising as a result of the local temperature being raised beyond the saturation temperature. Nucleate boiling occurs when vapour bubbles emerge at discrete points on a surface, as a result of the temperature surpassing the saturation temperature. This could be

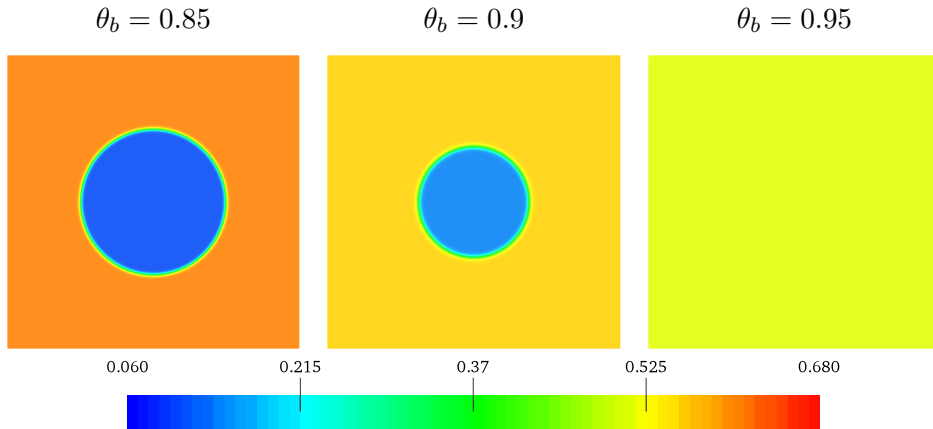


Figure 2.19: Evaporation: Steady state density field, with 256×256 linear elements.

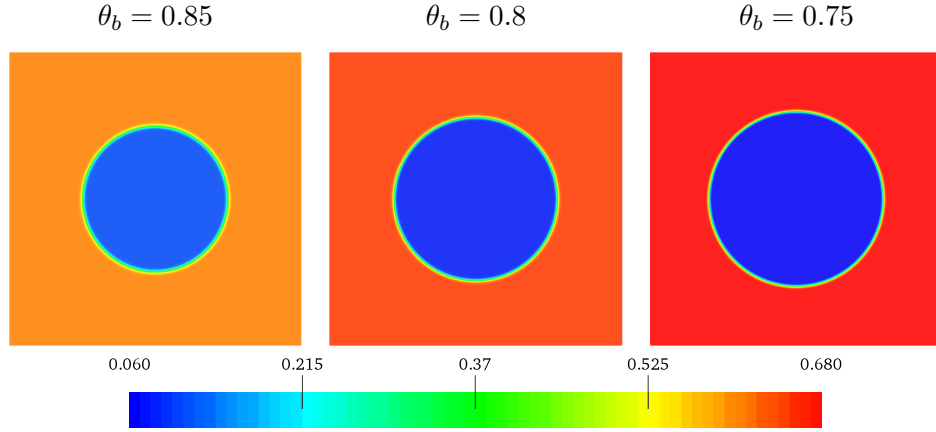


Figure 2.20: Condensation: Steady state density field, with 256×256 linear elements.

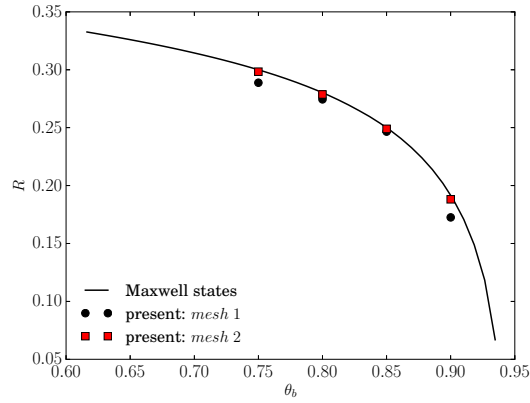


Figure 2.21: Evaporation/Condensation: Steady state radii comparison, with 256×256 linear quadrilateral elements.

Table 2.1: Evaporation/Condensation: Steady state bubble radii.

θ	R [<i>mesh 1</i>]	R [<i>mesh 2</i>]	R [<i>analytical</i>]
0.75	0.2888	0.2983	0.3000
0.8	0.2744	0.2787	0.2802
0.85	0.2466	0.2490	0.2500
0.9	0.1725	0.1881	0.1916
0.95	—	—	—

attributed to topological differences on the surface, for instance cavities on the surface of a cooking pot.

Following a similar setup to Liu et al. [62], this example considers a two-dimensional computational domain $[0, 1] \times [0, 0.5]$ for the simulation of nucleate boiling. The initial conditions are set as:

$$\rho_0(\mathbf{x}) = 0.366 + 0.297 \tanh\left(\frac{\sqrt{\text{We}}(y - 0.35)}{2}\right), \quad \mathbf{x} \in \Omega, \quad (2.73a)$$

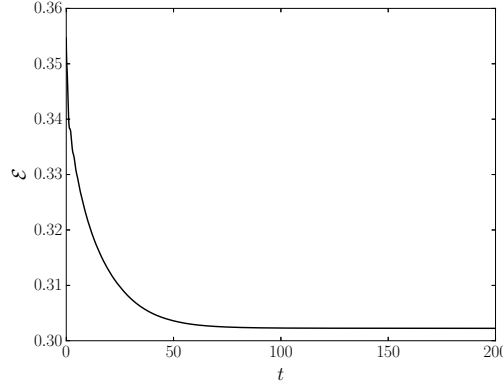


Figure 2.22: Condensation: Total energy evolution.

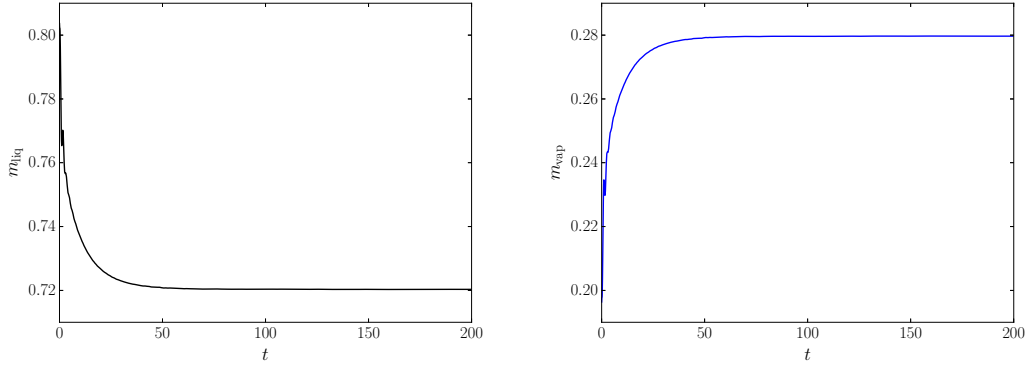


Figure 2.23: Condensation: Mass evolution for liquid (left) and vapour (right).

$$\mathbf{u}_0(\mathbf{x}) = \mathbf{0}, \quad \mathbf{x} \in \Omega, \quad (2.73b)$$

$$\theta_0(\mathbf{x}) = 0.775, \quad \mathbf{x} \in \Omega, \quad (2.73c)$$

$$\Upsilon_0(\mathbf{x}) = 0, \quad \mathbf{x} \in \Omega, \quad (2.73d)$$

and the boundary conditions are taken as:

$$\theta = \theta_c, \quad \text{on } \Gamma_u, \quad (2.74a)$$

$$\theta = \theta_h, \quad \text{on } \Gamma_l, \quad (2.74b)$$

$$\nabla \rho \cdot \mathbf{n} = 0, \quad \text{on } \Gamma, \quad (2.74c)$$

$$\mathbf{q} \cdot \mathbf{n} = 0, \quad \text{on } \Gamma. \quad (2.74d)$$

Here Γ_u , and Γ_l are the subsets of Γ corresponding to the upper and lower boundaries. For consistency the power expenditure term $\nabla \cdot \mathbf{\Pi}$ is added to the energy equation (2.40c). The weak form of this term, and its linearisation is shown in Appendix A.2. The dimensionless Weber number is set as $We = 2.103 \cdot 10^{-6}$. Following [62], the dimensionless thermal conductivity and viscosity are taken as functions of density, such as to vary the properties of the two phases; These parameters are set as $k = 3.448 \cdot 10^{-5} \rho$ and $\mu = 2.298 \cdot 10^{-4} \rho$, respectively.

Slip boundary conditions are prescribed for the velocity field on all boundaries. In order to represent the unevenness of the temperature distribution expected

from rough surfaces, i.e. on a cooking pot surface, the temperature on the bottom surface, θ_h and top surface, θ_c are set as:

$$\theta_h = 0.950 + \delta\theta_h \quad (2.75)$$

$$\theta_c = 0.775 + \delta\theta_c, \quad (2.76)$$

where the variations are randomly set in the ranges,

$$\delta\theta_h \in \{-4.3079 \cdot 10^{-2}, 4.7375 \cdot 10^{-2}\} \quad (2.77)$$

$$\delta\theta_c \in \{-2.9915 \cdot 10^{-3}, 3.0148 \cdot 10^{-3}\}. \quad (2.78)$$

Figures 2.24 and 2.25 show the time evolution of the density and temperature fields respectively. Figure 2.26 shows the time evolution of the velocity streamlines. From Figure 2.24, it can be seen that small vapour bubbles are generated at the early stages of the simulation. With the evolution of time, the bubbles grow and coalesce with other bubbles in close proximity. The growing bubbles gain a higher buoyancy and eventually detach from the lower surface. When the bubbles reach the surface and break through the liquid barrier, small droplets form which immediately return to the liquid. Similar observations are made by Liu et al. in [62]. A close-up of a collapsing bubble at the water level is shown in Figure 2.27. Notably a small droplet occurs when the bubble reaches the free surface.

Effect of viscosity: A demonstration is conducted into the effects of varying the viscosities of the liquid-vapour system. The viscosity used in the previous simulation is halved such that $\mu = 1.149 \cdot 10^{-4}\rho$, thereby doubling the Reynolds number throughout the mixture. Figure 2.28 shows the time evolution of the density field. It is clear that for the same instantaneous times, the bubbles are more evolved than with the larger viscosity (i.e. Figure 2.24). For instance at $t = 20.058$ two bubbles are clearly detached from the lower surface, whereas in Figure 2.24 at $t = 20.224$ this is not the case.

Effect of thermal conductivity: The effects of varying the thermal conductivity are examined. The thermal conductivity in the mixture is doubled, such that $k = 6.896 \cdot 10^{-5}\rho$. The same random distribution for the surface temperature is considered as before. Figure 2.29 shows the time evolution of the density field. Increasing the thermal conductivity, results in the bubbles rising faster than observed in both Figures 2.24 and 2.28. However the bubbles are smaller and thus produce longer stems before detaching.

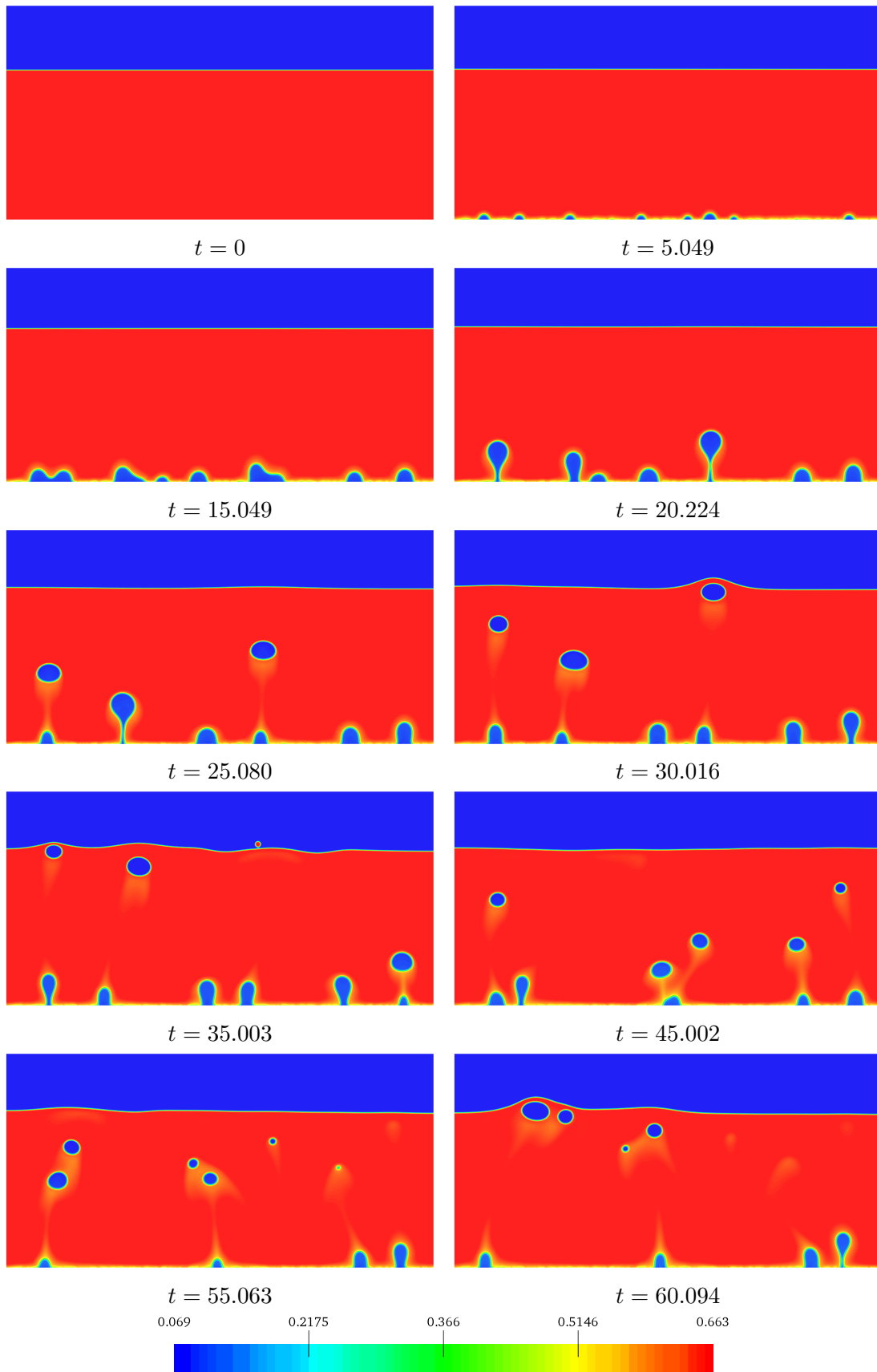


Figure 2.24: Nucleate boiling: Density field evolution, with 800×400 linear elements.

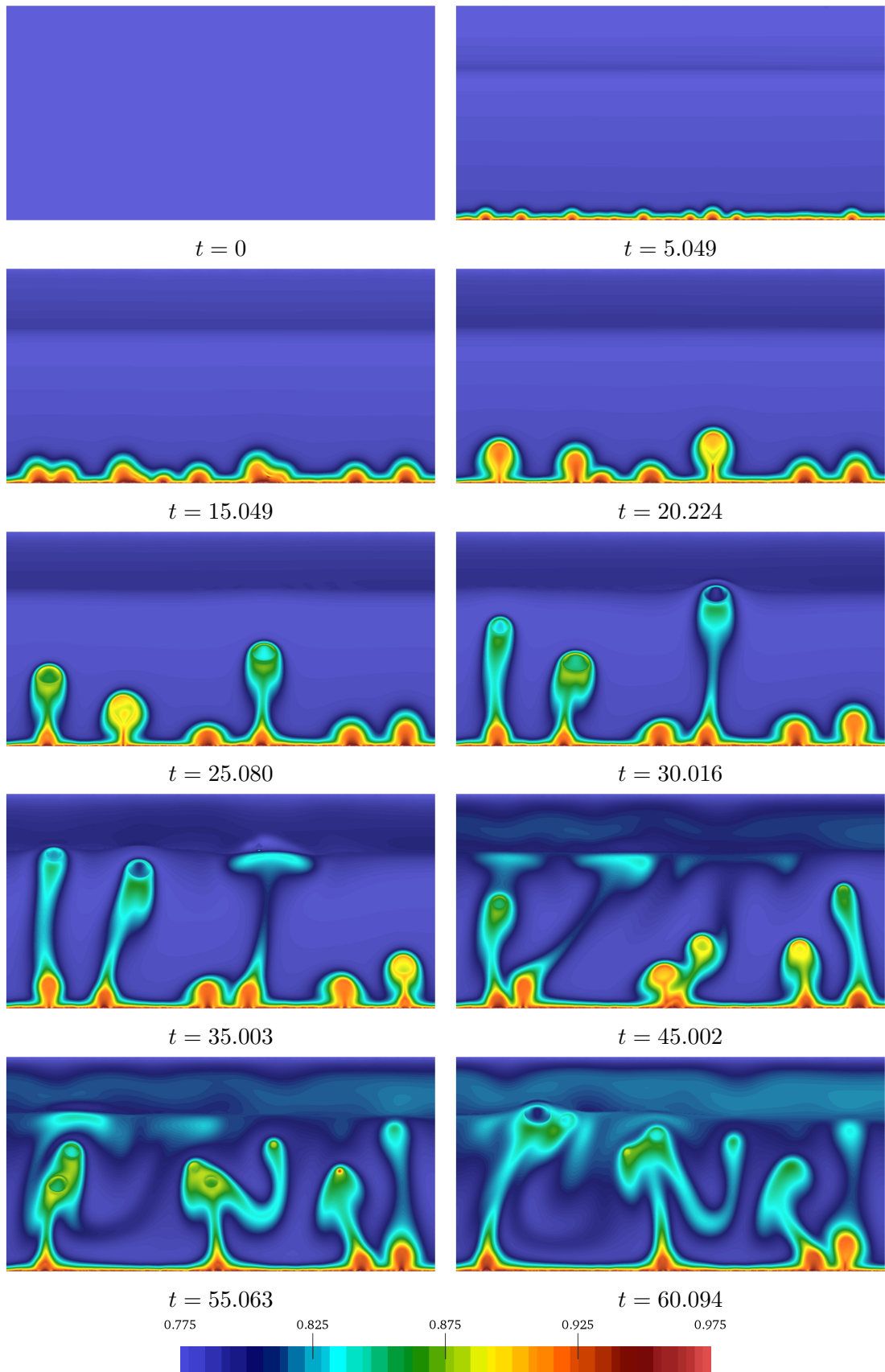


Figure 2.25: Nucleate boiling: Temperature field evolution, with 800×400 linear elements.

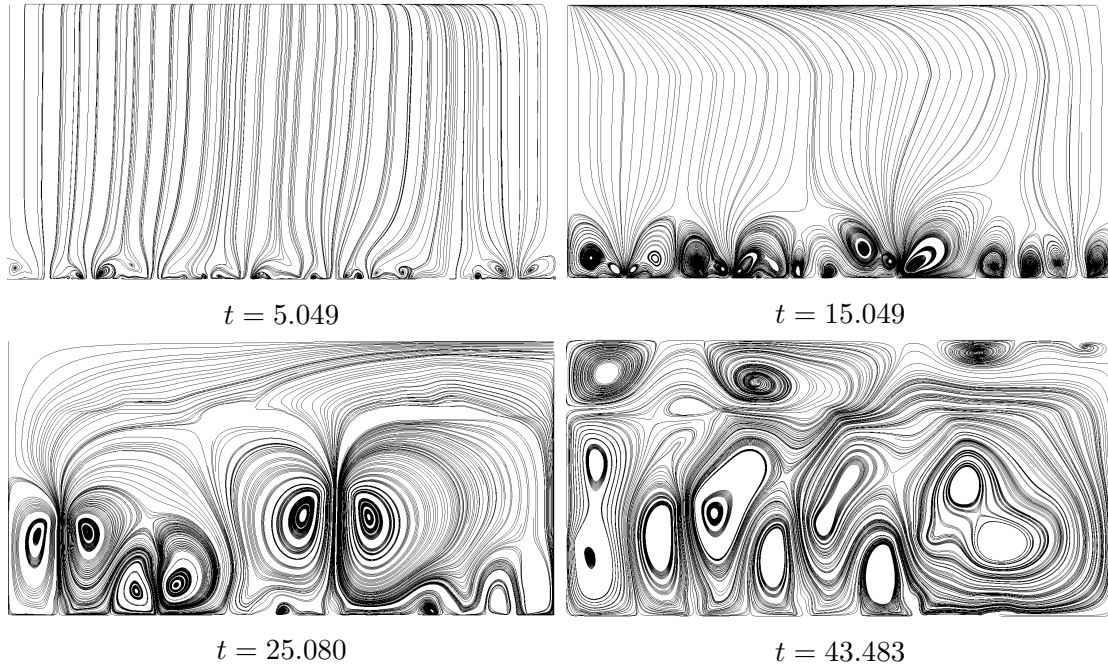


Figure 2.26: Nucleate boiling: Velocity field streamline evolution, with 800×400 linear elements.

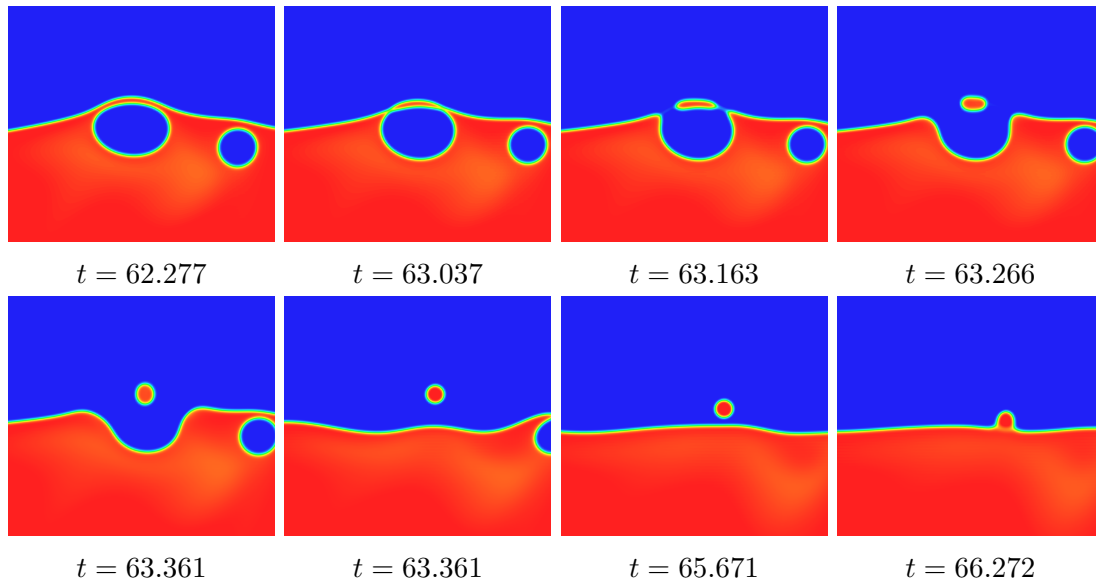


Figure 2.27: Nucleate boiling: Close-up of collapsing bubble at water level.

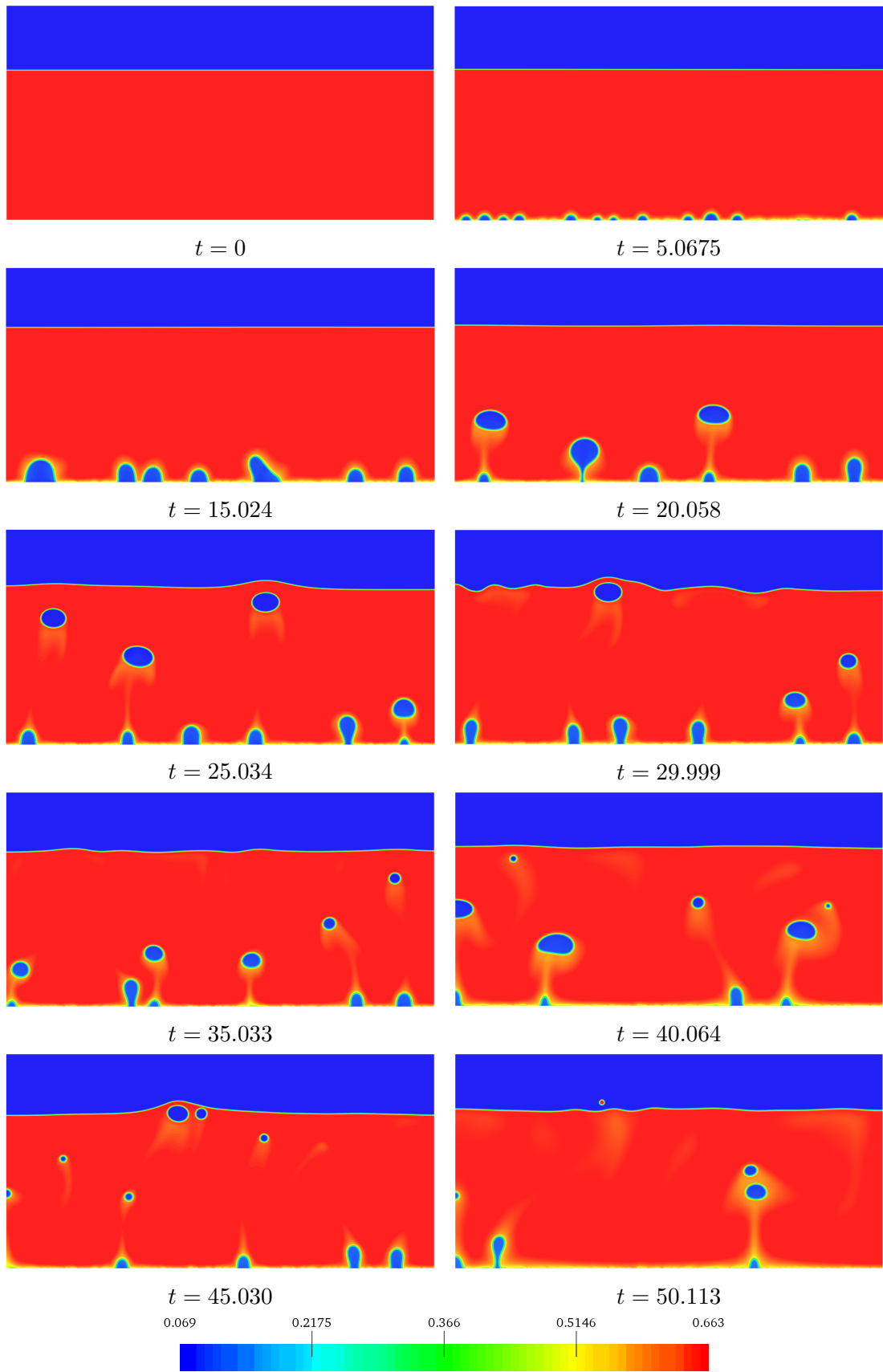


Figure 2.28: Nucleate boiling: Density field evolution with lower viscosities, using 800×400 linear elements..

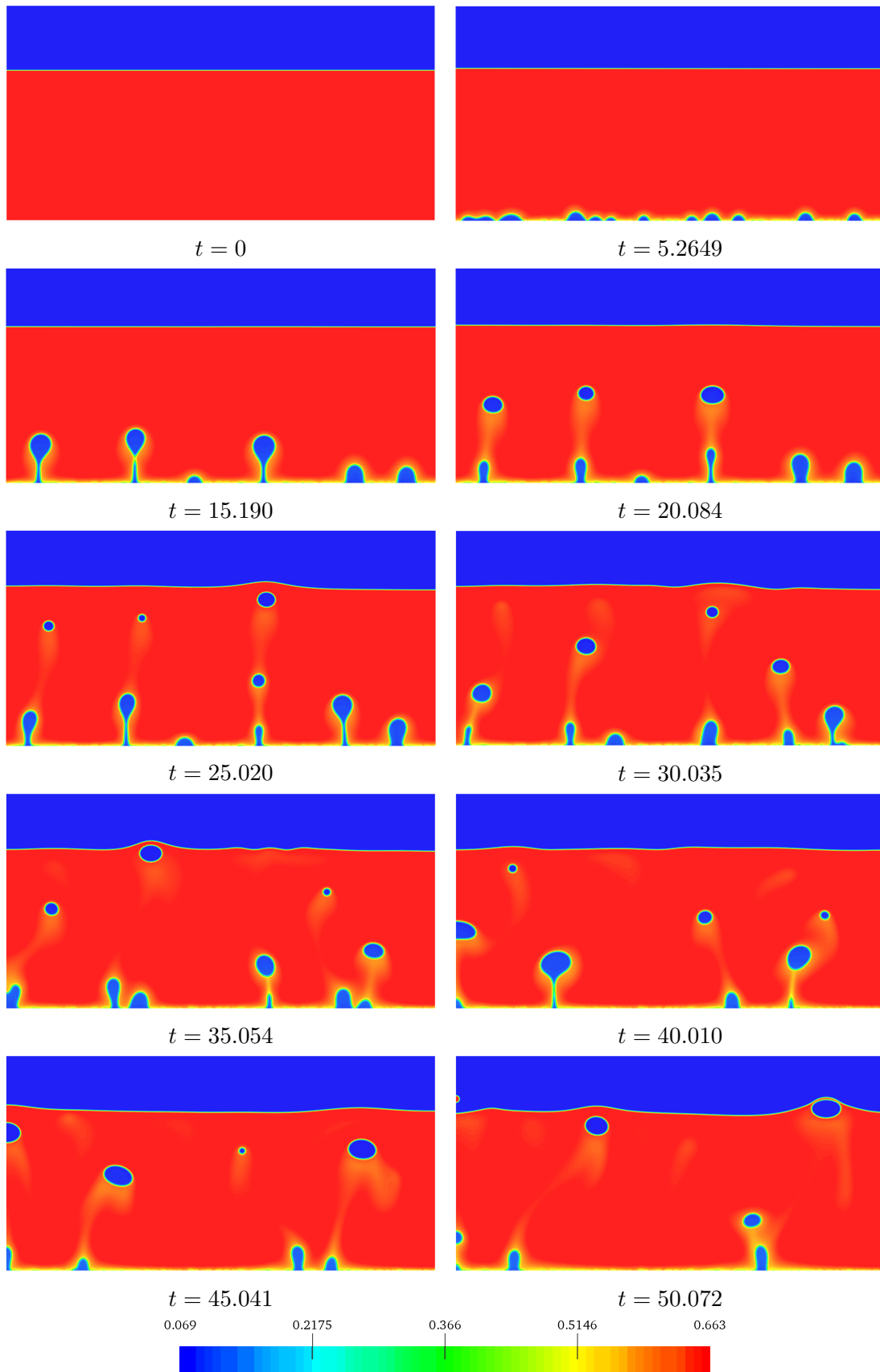


Figure 2.29: Nucleate boiling: Density field evolution with higher thermal conductivity, using 800×400 linear elements.

2.5.3 Temperature driven rising bubble

In this example a bubble is placed at a point $\mathbf{C} = [0.375, 0.375]$ in a rectangular computational domain $\Omega = [0, 0.75] \times [0, 1]$ with different temperatures prescribed on the upper and lower boundaries. The initial conditions are set as:

$$\rho_0(\mathbf{x}) = 0.3545 + 0.2479 \tanh \left(\frac{\sqrt{\text{We}} (|\mathbf{x} - \mathbf{C}| - R)}{2} \right), \quad \mathbf{x} \in \Omega, \quad (2.79a)$$

$$\mathbf{u}_0(\mathbf{x}) = \mathbf{0}, \quad \mathbf{x} \in \Omega, \quad (2.79b)$$

$$\theta_0(\mathbf{x}) = 0.85, \quad \mathbf{x} \in \Omega \setminus \Gamma_u, \quad (2.79c)$$

$$\theta_0(\mathbf{x}) = \theta_h, \quad \mathbf{x} \in \Gamma_u, \quad (2.79d)$$

$$\Upsilon_0(\mathbf{x}) = 0, \quad \mathbf{x} \in \Omega, \quad (2.79e)$$

and the boundary conditions are taken as:

$$\theta = \theta_h, \quad \text{on } \Gamma_u, \quad (2.80a)$$

$$\nabla \rho \cdot \mathbf{n} = 0, \quad \text{on } \Gamma, \quad (2.80b)$$

$$\mathbf{q} \cdot \mathbf{n} = 0, \quad \text{on } \Gamma, \quad (2.80c)$$

where Γ_u and Γ_l again represent subsets of Γ corresponding to the upper and lower boundaries respectively. The dimensionless parameters are set as: $\text{Re} = 2/h$, $\text{We} = 1/h^2$, $k = 10^{-2}$. Two cases are considered for the upper boundary temperature: $\theta_h = 0.87$ and $\theta_h = 0.9$. Slip velocity boundary conditions are applied on all surfaces. The mesh consists of 96×128 linear quadrilateral elements, and adaptive time stepping is used with an initial time step size of $\Delta t = 0.0001$.

Figures 2.30 and 2.31 show the time evolution of the density, temperature and velocity fields for $\theta_h = 0.87$ and $\theta_h = 0.9$ respectively. It can be seen that increasing θ_h results in the bubble rising an order of magnitude faster. Furthermore, the drop visibly shrinks more when θ_h is increased, which is attributed to evaporation (see Section 2.5.1).

2.6 Concluding remarks

A low order Navier-Stokes-Korteweg model has successfully been implemented for the simulation of isothermal and non-isothermal multiphase flows, with particular interest in phase transition. The model is formulated non-conservatively with the introduction of an additional auxiliary equation to reduce the system order, allowing linear finite elements to be used. The model has been demonstrated with several complex problems, including the simulation of nucleate boiling, which to the authors knowledge and at the time of this writing, has not been demonstrating using low order standard finite elements.

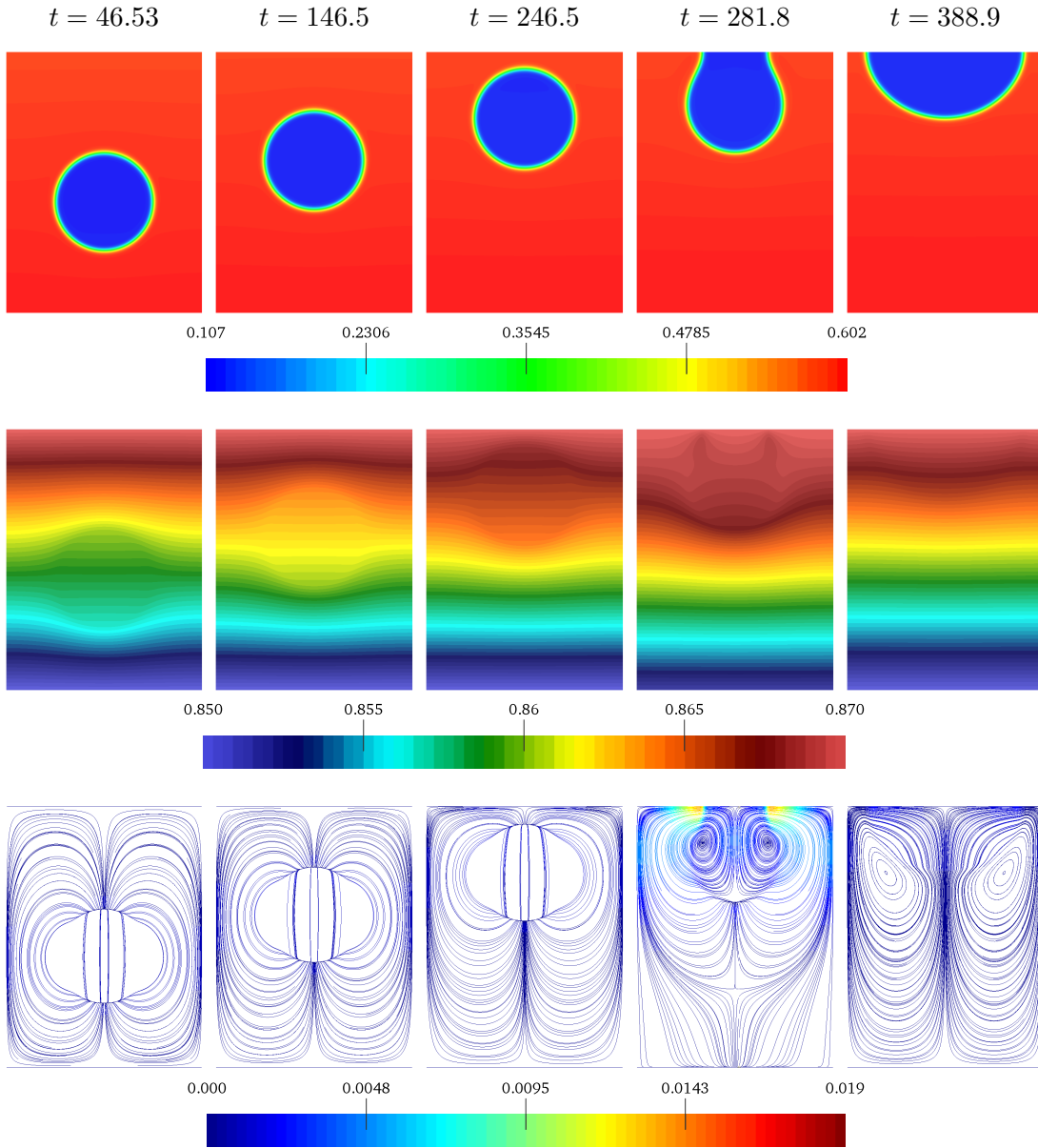


Figure 2.30: Temperature driven rising bubble: Evolution of density (top), temperature (middle) and velocity streamlines (bottom) for $\theta_h = 0.87$, with 192×256 linear elements.

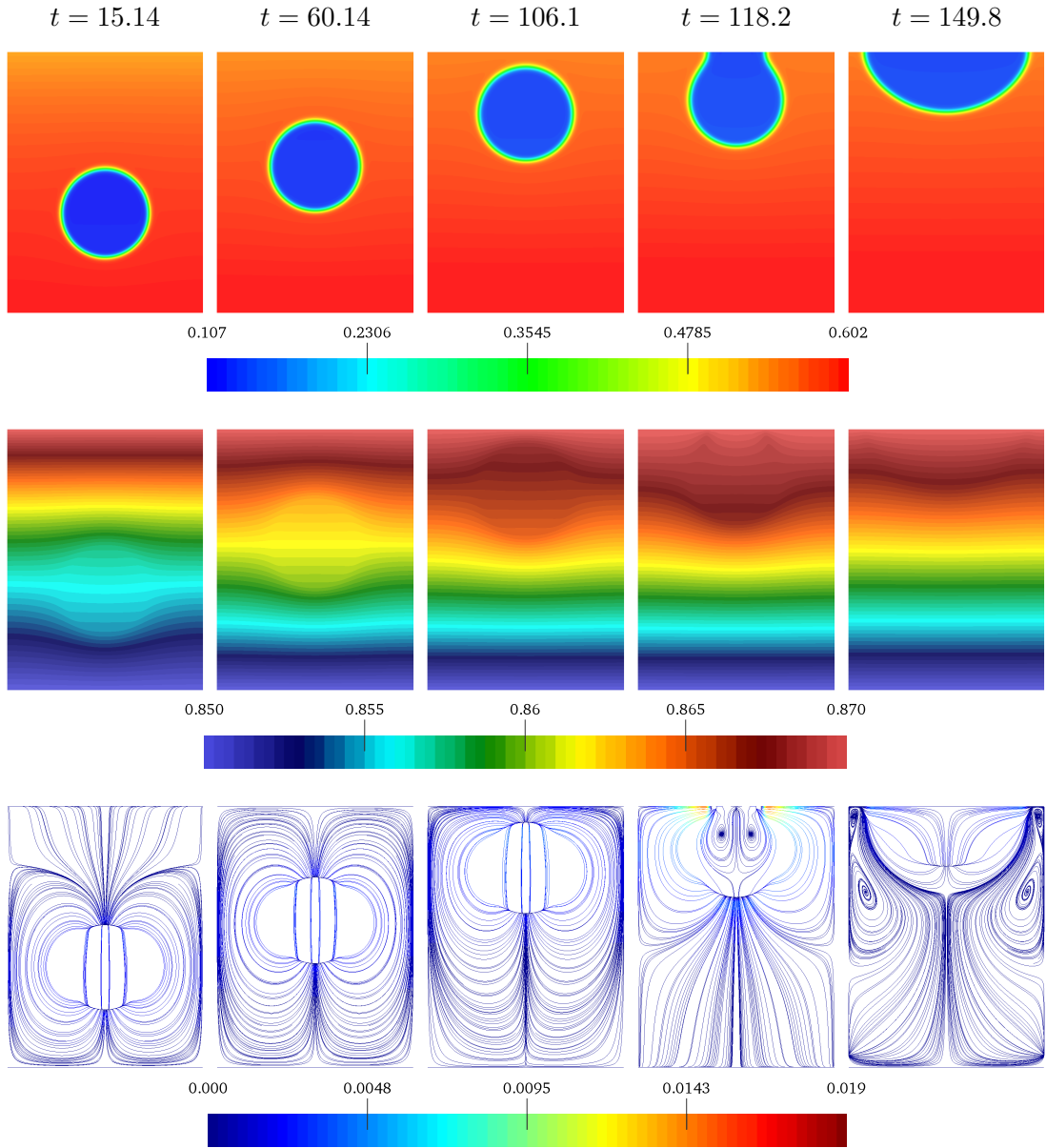


Figure 2.31: Temperature driven rising bubble: Evolution of density (top), temperature (middle) and velocity streamlines (bottom) for $\theta_h = 0.9$, with 192×256 linear elements.

Chapter 3

Binary Fluid Systems: The Cahn-Hilliard Equation

Binary fluid models introduce an auxiliary field variable, typically called the *phase-field variable* or *order parameter*, to smoothly transition quantities across the interface between two distinct values in the bulk phases. The dynamics of the phase-field variable are typically governed by the Cahn-Hilliard equation [25], or its non-conserving counterpart the Allen-Cahn equation [33]. The Cahn-Hilliard equation has been studied mathematically in [27, 89, 28]. Various numerical strategies for solving the Cahn-Hilliard and Allen-Cahn equations are explored in for instance [30, 31, 90, 91]. In the present work only the Cahn-Hilliard equation is considered.

The Cahn-Hilliard equation is used extensively in multiphase fluid flows, and has been successfully coupled with hydrodynamics as early as the 1970's, with the so-called Model H [37]. Models which couple the Navier-Stokes equations with the Cahn-Hilliard equation are referred to as Navier-Stokes-Cahn-Hilliard models, and are studied in depth in [34, 28, 15, 92]. Jacqmin suggests key ideas for deriving hydrodynamic diffuse-interface models [26]. Examples of Cahn-Hilliard based physical applications include spinodal decomposition of miscible polymer blends [93], microstructure morphological evolution with inhomogeneous elasticity [94], photovoltaics, tumour growth simulation [95], and topology optimisation [96] to name a few.

It is well known that the Cahn-Hilliard equation is capable of more than just separating/localising phases of a mixture and capturing the interface. In fact the equation inherently modifies the physical behaviour of the mixture. For instance consider the benchmark problem of spinodal decomposition, where a randomly perturbed phase-field variable is set in a square domain, see [30, 97, 31]. Here the problem is initially characterised by spinodal decomposition (rapid unmixing of phases), and later by grain coarsening. The latter stage is a clear indication of additional physical effects and is typically described as *Ostwald ripening*. This phenomenon is also observable when considering problems where a larger bubble absorbs or assimilates with a smaller one. To further highlight the physical manipulation resulting from the Cahn-Hilliard equation, consider now a mixture of two phases where the one phase is clearly more abundant than the other. For

instance a small spherical bubble situated in a large domain. The inherent nature of the Cahn-Hilliard equation dictates that the minority phase, the bubble in this case, will reduce in physical volume while it is absorbed by the majority phase. Moreover if the bubble is small enough, it will eventually vanish entirely. This phenomenon is examined in detail in Jacqmin in [26] and Yue et al. [63]. While the phase-field variable is globally conserved, there is a clear loss of volume or *shrinkage* observed in the minority phase, accompanied by a shift of the phase-field variable values in the bulk phases. In principle since the phase-field variable is constant in the bulk phases, each individual phase should also be conserved if the interface is infinitely thin. However, when considering an interface of finite size, the observed shrinkage of the minority phase occurs simultaneously with a shift of the phase-field variable from the initial values in the bulk phases. Here there is a trade-off occurring whereby the bulk free energy is increased at the expense of the surface free energy in an effort to reach the lowest energy state, and hence as a consequence the volumes of the individual phases are not conserved. In [63], the authors consider a simple problem of a static two-dimensional axisymmetric bubble in a square computational domain, and discuss methods of control shrinkage and phase-field variable shifting. They demonstrate that the amount of shrinkage and shifting is proportional to the Cahn number (ratio of interface thickness to initial bubble radius). It is further deduced that if the radius of the bubble is smaller than a *critical* radius, the bubble will eventually disappear completely. It is important to note that it is the volume fraction, and not the actual radius which determines whether the bubble will disappear. Hence for a larger computational domain, the critical radius will be larger than for a smaller computational domain. It is concluded in [63], that by setting the mobility function and interface thickness appropriately, bubble shrinkage can be significantly slowed/delayed.

The Cahn-Hilliard equation constitutes a nonlinear fourth order PDE which is usually solved with various numerical approaches ranging from finite difference, spectral formulations and finite element methods. In [31, 32], the authors use IGA with quadratic NURBS to resolve a second order differential equation leftover after integrating by parts twice. Discontinuous Galerkin methods are successfully demonstrated in [30, 97]. Here the chemical potential is introduced as an additional variable in order to reduce the problem to two second order PDEs. A linear scheme which is unconditionally energy-stable is proposed by Guillén-González and Tierra [91].

The remainder of this chapter is structured as follows: In section 3.1, the thermodynamic concepts behind the Cahn-Hilliard equation, including its derivation are presented. Section 3.3 presents the spatial and temporal discretisation of the Cahn-Hilliard equation. Section 3.4 considers a variety of numerical benchmark problems, highlighting the underlying physical processes which occur. In section 3.5, an investigation is carried out into grain coarsening and how it can be reduced. Section 3.6 studies the effect of drop shrinkage and suggests techniques to control it. Section 3.7 highlights the achievements of the chapter.

3.1 Model derivation and thermodynamics

Phase-field models are characterised by the introduction of an auxiliary function φ , a phase-field variable which localises the individual phases. φ is represented by distinct values outside the interface region (i.e. the bulk region), for example,

$$\varphi(x, t) = \begin{cases} 1, & \text{phase } a \\ -1, & \text{phase } b, \end{cases} \quad (3.1)$$

and varies with a smooth function between these bulk values within the interface region, as illustrated in Figure 3.1. From conservation of the order parameter, we can deduce that

$$\frac{\partial \varphi}{\partial t} = -\nabla \cdot \mathbf{J}, \quad (3.2)$$

where \mathbf{J} refers to a flux of the order parameter through the boundary. Similarly with advection, assuming a divergence free velocity field \mathbf{a} , the conservation equation becomes

$$\frac{\partial \varphi}{\partial t} + \mathbf{a} \cdot \nabla \varphi = -\nabla \cdot \mathbf{J}. \quad (3.3)$$

From Fick's law, the constitutive choice for \mathbf{J} (see [98, 32]) is

$$\mathbf{J} = -M(\varphi) \nabla \eta \quad \text{where} \quad M(\varphi) \geq 0. \quad (3.4)$$

Here η is again the chemical potential, which is evaluated as the variational derivative of a given free energy. Moreover $M(\varphi)$ is the mobility function, which is described in Section 3.2.3.

The mixing energy is typically described by the Ginzburg-Landau free energy functional

$$\mathcal{F}(\varphi) = \int_{\Omega} (\Psi_b + \Psi_s) \, d\Omega = \int_{\Omega} \left(F(\varphi) + \frac{\epsilon^2}{2} |\nabla \varphi|^2 \right) \, d\Omega \quad (3.5)$$

where Ψ_b and Ψ_s are respectfully the bulk (or local) and surface free energy components. Here the bulk free energy is responsible for the *hydrophobic* tendencies,

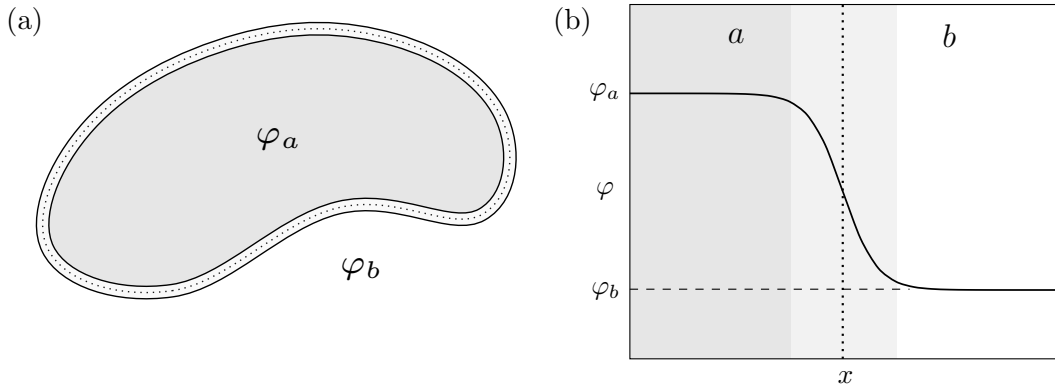


Figure 3.1: Phase-field variable spatial evolution. (a) Continuum depiction of two-phase system, (b) distribution of φ over the interface region.

or de-mixing, of the mixture. On the contrary the surface free energy is responsible for the *hydrophilic* tendencies of the mixture. These respective free energy components are balanced through the functional (3.5). ϵ is a measure of length related to the interface thickness, and $F(\varphi)$ is a double-well potential, which for order parameter definitions (3.1) is taken as

$$F(\varphi) = W (1 - \varphi^2)^2, \quad (3.6)$$

where W is the height of the well. It should be pointed out that this is a polynomial approximation of the bulk free energy term used by Cahn and Hilliard [24, 25], which is acceptable for cases where the temperature θ is close to the critical temperature θ_c . The double well function is shown in Figure 3.2.

To get the interface profile at equilibrium the energy functional is minimised by taking the variational derivative and equating it to zero. This gives the chemical potential

$$\eta = \frac{\delta \mathcal{F}}{\delta \varphi} = f(\varphi) - \epsilon^2 \Delta \varphi = 0 \quad (3.7)$$

where

$$f(\varphi) = \frac{\partial F(\varphi)}{\partial \varphi} = 4W (\varphi^3 - \varphi) \quad (3.8)$$

The function $f(\varphi)$ represents the chemical potential of a uniform solution [24], typically approximated as in Equation (3.8) for near critical mixture temperatures. For all other temperature cases (as long as $\theta < \theta_c$), a thermodynamically consistent logarithmic expression is often considered, see for instance [31].

An in depth mathematical analysis and derivation of the Cahn-Hilliard equation can be found in [24, 27, 89, 31].

3.2 The Cahn-Hilliard equation

Equation (3.2) can be described by the following boundary value problem:

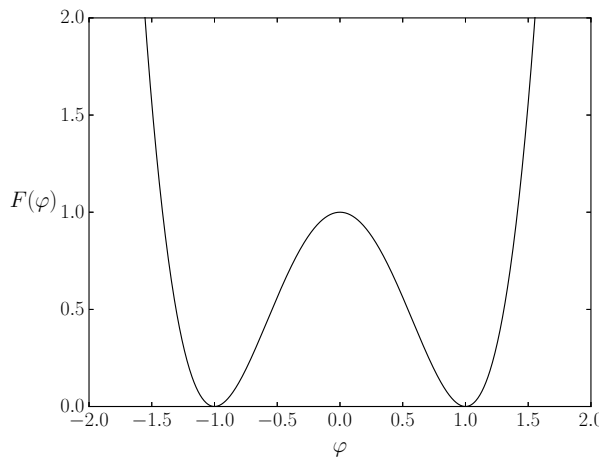


Figure 3.2: Double-well potential: $F(\varphi) = (1 - \varphi^2)^2$

Strong form: Consider a sufficiently smooth domain $\Omega \subset \mathbb{R}^d$ ($d \leq 3$) with boundary Γ which is separable into Dirichlet and Neumann subsets, Γ_g and Γ_q . The transport of φ is governed by,

$$\frac{\partial \varphi}{\partial t} + \mathbf{a} \cdot \nabla \varphi - \nabla \cdot [M(\varphi) \nabla (f(\varphi) - \epsilon^2 \Delta \varphi)] = 0 \quad \text{in } \Omega \times \mathcal{I} \quad (3.9a)$$

$$M(\varphi) \nabla (f(\varphi) - \epsilon^2 \Delta \varphi) \cdot \mathbf{n} = q \quad \text{on } \Gamma_q \times \mathcal{I} \quad (3.9b)$$

$$M(\varphi) \epsilon^2 \nabla \varphi \cdot \mathbf{n} = 0 \quad \text{on } \Gamma_q \times \mathcal{I}, \quad (3.9c)$$

where $\mathcal{I} = (0, T)$ is the time interval of interest. It is clear that Equation (3.9a) has a fourth order spatial derivative of the phase-field variable. This can be accounted for in a number of ways. Logically one could perform integration by parts twice and use C_1 continuous b-splines for the remaining second order derivative, see for instance [31]. Alternately, one could reduce the order of the problem by introducing the chemical potential (Equation 3.7) as an auxiliary variable, as is done in [90]. Instead of the chemical potential, $\lambda = \epsilon^2 \Delta \varphi$ could also be chosen as an auxiliary equation, since it is $\Delta \varphi$ which possess the higher order spatial derivative. This approach is considered by Wells et al. [30]. The two choices of auxiliary variables are compared for a simple one dimensional analysis with the initial condition shown in 3.3a. After one time step, it is clear from Figure 3.3b that using η as the auxiliary variable produces lesser spikes and would thus require less elements to accurately capture the behaviour. In this work the chemical potential will be used exclusively as the auxiliary variable for the Cahn-Hilliard equation as well as the Navier-Stokes-Cahn-Hilliard Equations to follow (Chapter 4). The strong form with auxiliary variable, considering the same domain and boundaries from Equations (3.9), involves finding φ and η such that:

$$\frac{\partial \varphi}{\partial t} + \mathbf{a} \cdot \nabla \varphi - \nabla \cdot (M(\varphi) \nabla \eta) = 0 \quad \text{in } \Omega \times \mathcal{I} \quad (3.10a)$$

$$\eta - f(\varphi) + \epsilon^2 \Delta \varphi = 0 \quad \text{in } \Omega \times \mathcal{I} \quad (3.10b)$$

$$M(\varphi) \nabla \eta \cdot \mathbf{n} = q \quad \text{on } \Gamma_q \times \mathcal{I} \quad (3.10c)$$

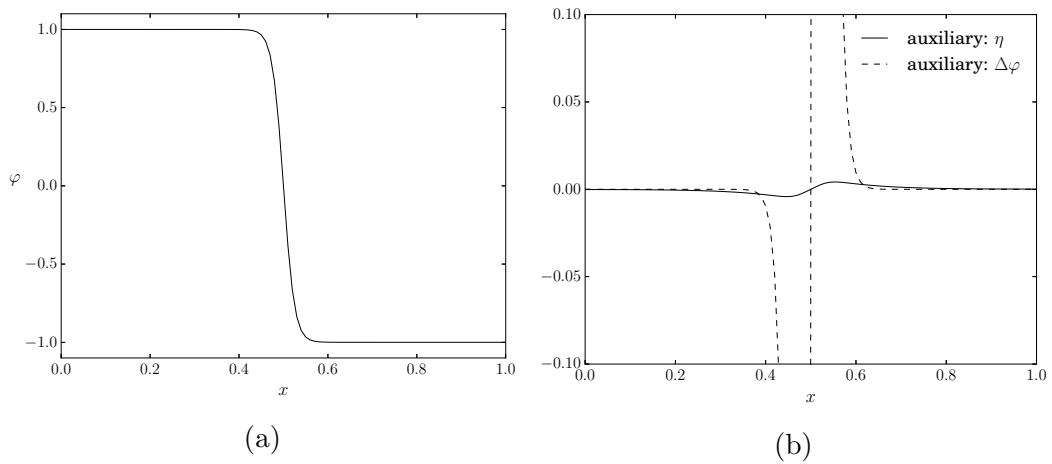


Figure 3.3: Auxiliary variable comparison: (a) initial φ distribution, (b) auxiliary variable solution comparison.

$$\nabla\varphi \cdot \mathbf{n} = 0 \quad \text{on } \Gamma_q \times \mathcal{I}. \quad (3.10d)$$

For contact angle boundary conditions, the relation

$$\frac{\nabla\varphi}{|\nabla\varphi|} \cdot \mathbf{n} = -\cos(\alpha), \quad (3.11)$$

is considered (see Figure 3.4), which would replace Equation (3.10d) with

$$\nabla\varphi \cdot \mathbf{n} + |\nabla\varphi| \cos(\alpha) = 0 \quad \text{on } \Gamma_q \times \mathcal{I}. \quad (3.12)$$

where α is again the three-phase contact angle at the boundary.

3.2.1 Exact solution of the one-dimensional Cahn-Hilliard equation

Considering a one-dimensional case where x is the spatial coordinate, an analytical expression for $\varphi(x)$ can be obtained from the chemical potential equation (3.7),

$$\frac{d^2\varphi}{dx^2} = A(\varphi^3 - \varphi), \quad (3.13)$$

where $A = \frac{4W}{\epsilon^2}$. Multiplying each side by $\frac{d\varphi}{dx}$ and integrating gives,

$$\frac{1}{2} \left(\frac{d\varphi}{dx} \right)^2 = A \left(\frac{\varphi^4}{4} - \frac{\varphi^2}{2} \right) + C, \quad (3.14)$$

where C is a constant. Considering that the limits of the gradients far from the interface are zero either side of the interface, i.e. $\lim_{x \rightarrow \infty} \frac{d\varphi}{dx} = 0$,

$$C = -A \left(\frac{1}{4} - \frac{1}{2} \right) = \frac{A}{4} \quad (3.15)$$

Substituting C back into Equation (3.14), taking the square root and integrating yields

$$-\sqrt{\frac{2}{A}} \tanh^{-1}(\varphi) = x + B, \quad (3.16)$$

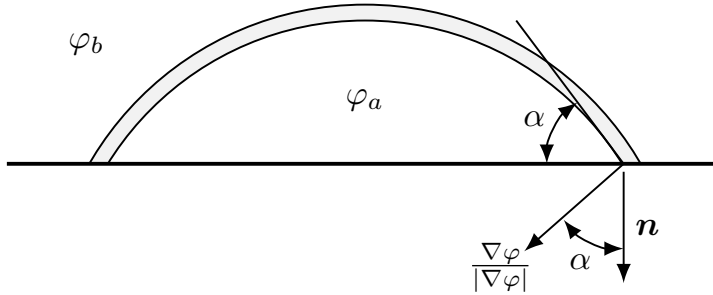


Figure 3.4: Contact angle definition.

where B is a constant. Considering again $A = \frac{4W}{\epsilon^2}$ and solving for φ yields the expression

$$\varphi(x) = -\tanh\left(\frac{\sqrt{2W}}{\epsilon}(x+B)\right). \quad (3.17)$$

3.2.2 Relating well height and interface thickness

In order to relate the well height W with the interface thickness, consider again Equation (3.17). The gradient at the interface can be written as

$$\begin{aligned} \varphi'_0 &= \frac{d\varphi(x)}{dx}\bigg|_{x=0} \\ \varphi'_0 &= \frac{\sqrt{2W}}{\epsilon} \operatorname{sech}^2\left(\frac{\sqrt{2W}}{\epsilon}(0)\right) \\ \varphi'_0 &= \frac{\sqrt{2W}}{\epsilon} \end{aligned} \quad (3.18)$$

3.2.3 Choosing the mobility function

Typically a degenerate mobility is a function active in the interface region and inactive elsewhere. In this work three options are considered for mobility, i.e.

$$M_0 = D, \quad (3.19a)$$

$$M_2(\varphi) = \begin{cases} D(1 - \varphi^2), & \text{if } |\varphi| \leq 1, \\ 0, & \text{elsewhere,} \end{cases} \quad (3.19b)$$

$$M_3(\varphi) = \begin{cases} D(-2\varphi^3 - 3\varphi^2 + 1), & \text{if } \varphi \geq -1, \\ D(2\varphi^3 - 3\varphi^2 + 1), & \text{if } \varphi \leq 1, \\ 0, & \text{elsewhere,} \end{cases} \quad (3.19c)$$

where D is a constant. The latter two mobility functions are shown in Figure 3.5 for $D = 1$. Notably, $M_3(\varphi)$, transitions smoother in the derivative. On coarse meshes, the choice of mobility can drastically change the behaviour of the model. Choosing a large constant mobility can result in the acceleration of the *Ostwald ripening* or *coarsening* effect. In essence this means the total interfacial area will reduce with time in an effort to reach the lowest energy state and hence thermodynamic equilibrium. For this reason D must be chosen small enough to ensure that the associated timescale is far larger than the time domain of interest. The reader is referred to [99] for a detailed explanation of Ostwald ripening.

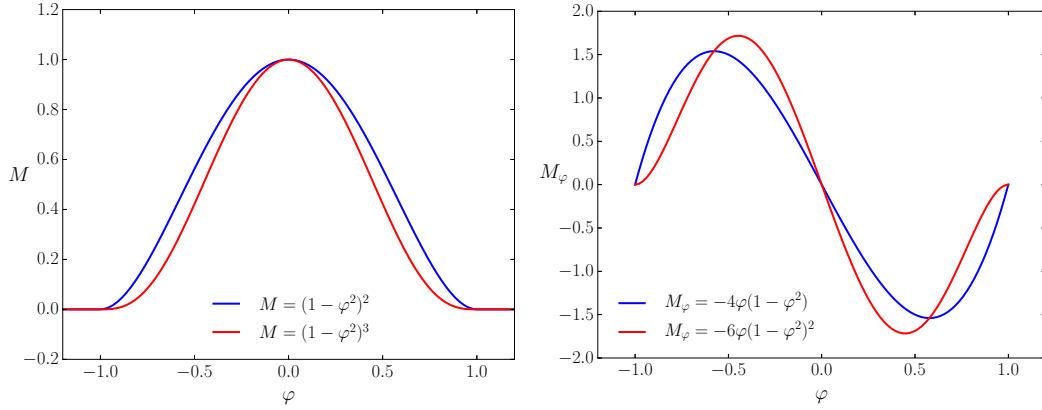


Figure 3.5: Degenerate mobility functions, $M_{2,3}$ (left) and the respective first derivatives (right), with $D = 1$ in both cases.

3.3 Numerical formulation

3.3.1 Spatial semi-discrete weak forms

The spatial discretisation of Equation (3.9a) is based on the following interpolations of phase-field variable and respective weighting function

$$\varphi^h(\mathbf{x}) = \sum_{A \in \mathcal{N}} N_A(\mathbf{x}) \varphi_A, \quad s^h(\mathbf{x}) = \sum_{A \in \mathcal{N}} N_A(\mathbf{x}) s_A, \quad (3.20)$$

where N_A and \mathcal{N} denote the basis functions and set of nodes, respectively.

Introducing \mathcal{X}^h and \mathcal{Y}^h as the trial solution and weighting function finite element spaces, the discrete weak form of Equation (3.9a) is as follows: Find $\varphi^h \in \mathcal{X}^h$, such that for all $s^h \in \mathcal{Y}^h$,

$$\begin{aligned} \int_{\Omega} s^h \left(\frac{\partial \varphi^h}{\partial t} + \mathbf{u}^h \cdot \nabla \varphi^h \right) + \nabla s^h \cdot \left(M(\varphi^h) \frac{\partial f(\varphi^h)}{\partial \varphi^h} + \epsilon^2 \frac{\partial M(\varphi^h)}{\partial \varphi^h} \Delta \varphi^h \right) \nabla \varphi^h \\ + \Delta s^h \epsilon^2 M(\varphi^h) \Delta \varphi^h \, d\Omega = 0. \end{aligned} \quad (3.21)$$

Note that the finite element spaces are Sobolev spaces with square integrable first and second derivatives, i.e. $H^2(\Omega)$ conforming.

The spatially discrete weak form of Equations (3.10a)-(3.10b) is as follows: Find $(\varphi^h, \eta^h) \in \mathcal{X}^h$, such that for all $(s^h, v^h) \in \mathcal{Y}^h$,

$$\int_{\Omega} v^h \left(\frac{\partial \varphi^h}{\partial t} + \mathbf{u}^h \cdot \nabla \varphi^h \right) + \nabla v^h \cdot (M(\varphi^h) \nabla \eta^h) \, d\Omega = 0 \quad (3.22a)$$

$$\int_{\Omega} s^h (\eta^h - f(\varphi^h)) - \nabla s^h \cdot \epsilon^2 \nabla \varphi^h \, d\Omega = 0 \quad (3.22b)$$

Here \mathcal{X}^h and \mathcal{Y}^h denote the appropriate finite element spaces of piecewise continuous linear basis functions.

3.3.2 Temporal discretisation and solution strategy

The generalised- α method is employed for the temporal discretisation. The same procedure is followed as presented in Section 2.3.2. Also an adaptive time-stepping algorithm is considered which is described in Section 2.3.4.

In terms of the solver, the direct solver, PARDISO, is used for smaller scale problems, while the iterative parallel solver PETSC [87] with a block Jacobi preconditioner is employed for larger scale problems.

3.4 Numerical examples

The two-equation form of the Cahn-Hilliard model presented in Equations (3.22a)-(3.22b) is used primarily in the simulations to follow. The one-equation form in Equation (3.21) which requires C_1 continuous b-splines is merely used comparatively. The problems are set up with the following commonalities:

- *Time integration:* In all examples to follow, generalised α time integration is used with $\rho_\infty = 0.5$.
- *Choice of ϵ :* All problems consider ϵ such that it satisfies the condition $h \leq \sqrt{\epsilon^2/2.5}$. This is deemed by Liu *et al.* [32] to be appropriate in order to avoid unphysical behaviour.

3.4.1 Evolution to static of two bubbles

This example involves two bubbles: B_1 with radius $R_1 = 0.15$, and B_2 with radius $R = 0.175$. The bubbles are situated far enough apart such that they do not coalesce, and the phase-field variable inside them is set as $\varphi = 1$. The bubbles are situated in a square region $\Omega = [0, 1] \times [0, 1]$, wherein $\varphi = -1$. The initial condition is set as:

$$\varphi_0(\mathbf{x}) = 1 + \sum_{i=1}^2 \tanh \left(\frac{\sqrt{2W} (R_i - |\mathbf{x} - \mathbf{C}_i|)}{\epsilon} \right), \quad \mathbf{x} \in \Omega, \quad (3.23a)$$

$$\eta_0(\mathbf{x}) = 0, \quad \mathbf{x} \in \Omega. \quad (3.23b)$$

Periodic boundary conditions are considered in all directions. The parameters are set as follows: $W = 2$, and $M(\varphi) = M_0$ with $D = 0.01$. Two meshes consisting of uniform linear quadrilateral elements are considered: One with a characteristic element size $h = 1/100$ (i.e. 100×100 elements), and one with $h = 1/200$. The interface thickness is set according to the characteristic element size as $\epsilon = 5h$. A fixed time step size of $\Delta t = 0.01$ is used.

The evolution of the phase-field variable with time is shown using 100×100 linear elements and the formulation in (3.10a)-(3.10b) in Figure 3.6. The time evolution of the radius is shown in Figure 3.7 for both $h = 1/100$ and $h = 1/200$. Notably as expected the increased mesh density and hence reduced interface thickness results in the smaller bubble vanishing later.

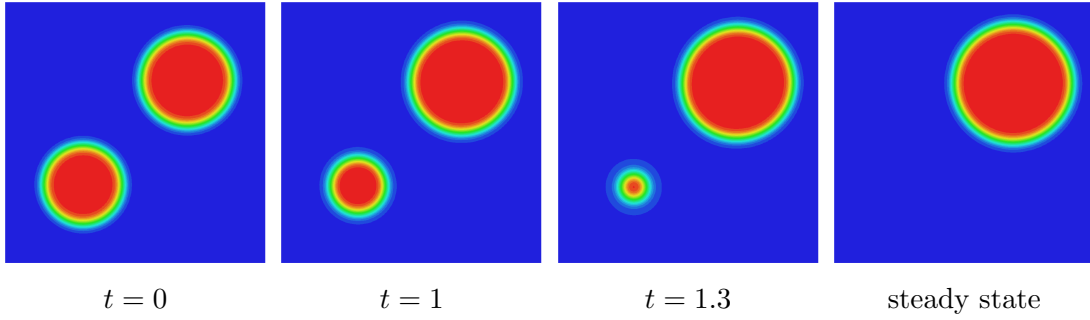


Figure 3.6: Evolution to static of two vapour bubbles: φ evolution with 100×100 linear elements.

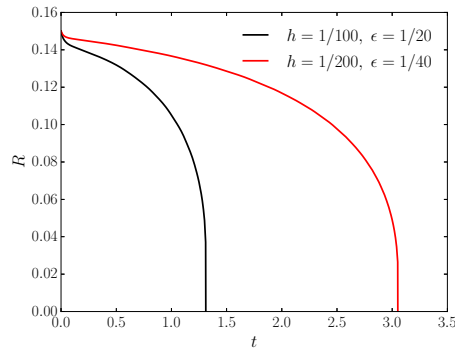


Figure 3.7: Evolution to static of two bubbles: Small bubble radius evolution.

The problem is considered with the formulation shown in Equation (3.21), where a grid consisting of a 100×100 C_1 continuous quadratic b-splines is considered. Figure 3.8a shows the comparison of the free energy observed for both formulations, and Figure 3.8b shows the free energy components for the two-equation Cahn-Hilliard model. The point at which the smaller bubble vanishes is clearly marked by a dip in the free energy. Moreover, the two-equation and one-equation formulations match well. The volume evolution for each phase is shown in Figure 3.9. A comparison is shown for the two linear element meshes considered, where the time t^* is scaled for $h = 1/200$ such that it is comparable to $h = 1/100$. Although the total volume is conserved, there is a slight variation in volume of the individual phases. The variation decreases proportionally with h . A detailed study into these effects will be covered in Section 3.6.

3.4.2 Coalescence of two bubbles

Two bubbles of equal size ($R_1 = R_2 = 0.175$) are situated in close proximity of one another, such that they are able to coalesce. The position of the bubbles are $\mathbf{C}_1 = [0.345, 0.345]$ and $\mathbf{C}_2 = [0.655, 0.655]$. The parameters are set as identical to problem 3.4.1. The initial condition is as presented in Equation (3.23).

Figure 3.10 shows the time evolution of the phase-field variable. Noteworthy it is clearly demonstrated that the model has the ability to represent fast topological changes of φ . The total energy and energy components are shown in Figure 3.11.

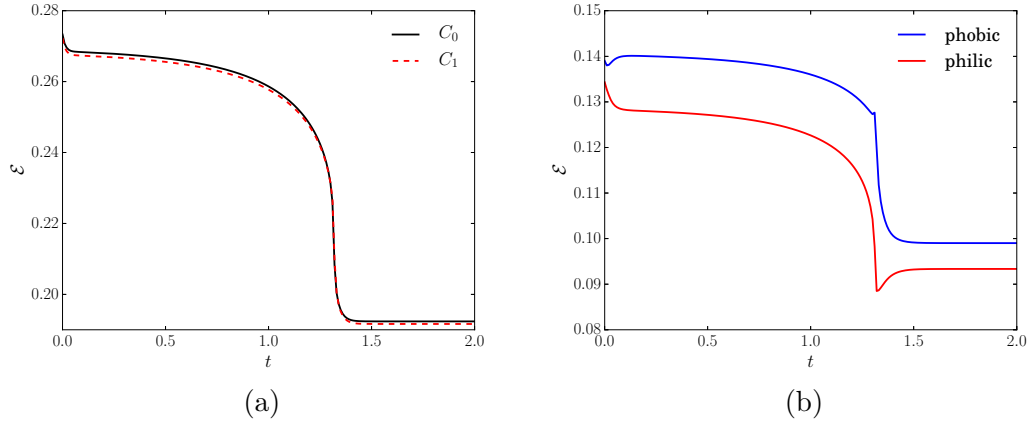


Figure 3.8: Evolution to static of two vapour bubbles: (a) Total free energy with C_0 and C_1 element formulations, (b) free energy components using C_0 element formulation.

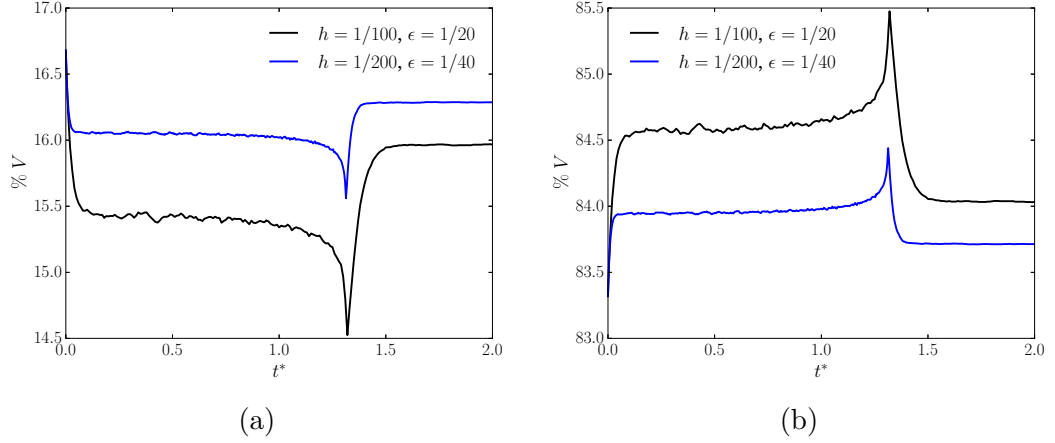


Figure 3.9: CH 2D evolution to static: Evolution of percentage of volume for (a) $\varphi = 1$, and (b) $\varphi = -1$.

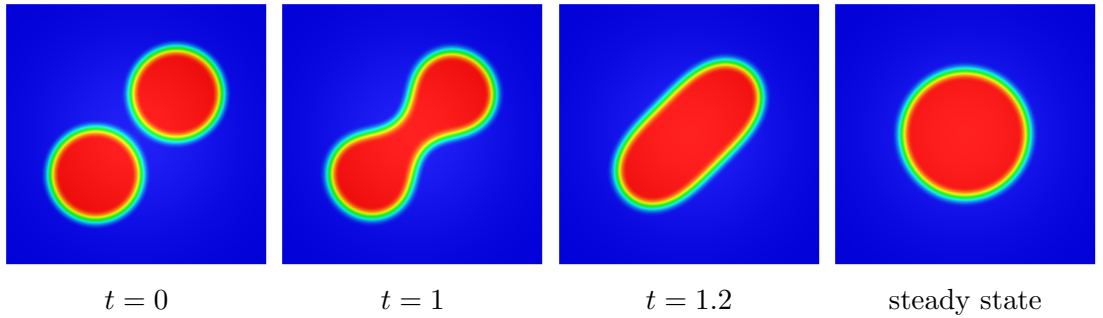


Figure 3.10: Coalescence of two vapour bubbles: φ evolution, with 100×100 linear elements.

The notable change in free energy just before $t = 1$ is associated with the merging with the two bubbles.

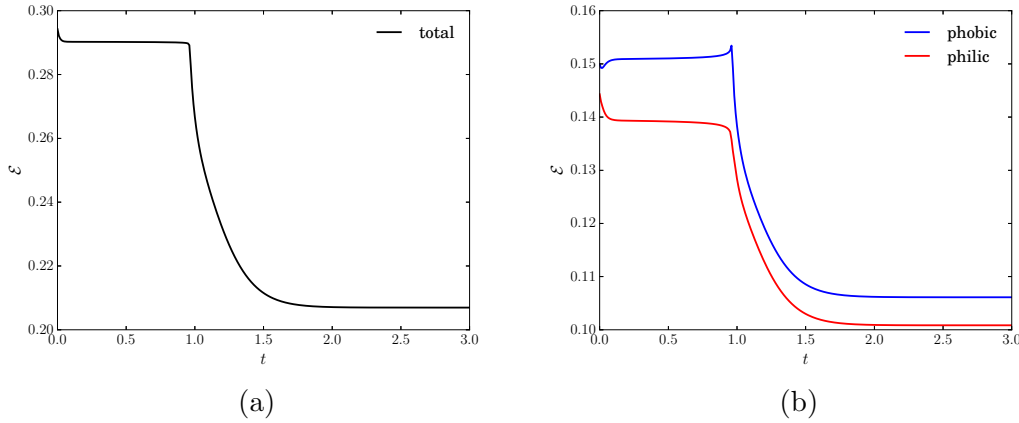


Figure 3.11: Coalescence of two vapour bubbles: Evolution of (a) total free energy, and (b) free energy components.

3.4.3 Spinodal decomposition of a randomly perturbed initial condition

The problem consists of setting a random initial condition in a domain $\Omega = [-0.5, -0.5] \times [0.5, 0.5]$ similarly to what is shown in [30, 97, 31]. The initial condition is set as:

$$\varphi_0(\mathbf{x}) = \bar{\varphi} + \delta\varphi, \quad \mathbf{x} \in \Omega, \quad (3.24)$$

$$\eta_0(\mathbf{x}) = 0, \quad \mathbf{x} \in \Omega, \quad (3.25)$$

where the random perturbation $\delta\varphi \in \{-0.1, 0.1\}$. Two cases are examined for the mean phase-field variable: case 1 involves setting $\bar{\varphi} = 0.26$, and case 2, $\bar{\varphi} = 0$. The other parameters are set to: $M(\varphi) = M_2(\varphi)$ with $D = 1$, $\epsilon = 1$ and $W = 750$. A uniform mesh with 128×128 linear quadrilateral elements is used. A fixed time step size is taken as $\Delta t = 10^{-7}$.

The time evolution of φ is shown for cases 1 and 2 in Figures 3.12 and 3.13, respectively. Observing both figures it is noticed that in the time range between approximately $t = 0$ to $t = 8.4364 \cdot 10^{-6}$, the developments are driven by spinodal decomposition, which is characterised by the rapid separation of phases. This is largely attributed to the minimisation of the hydrophobic bulk free energy component. After $t = 8.4364 \cdot 10^{-6}$, the developments occur more slowly and are characterised by coarsening (or Ostwald ripening), which is primarily attributed to the hydrophilic surface free energy component.

Three-dimensional analysis: Extending to three dimensions with the domain, $\Omega = [-0.5, 0.5] \times [-0.5, 0.5] \times [-0.5, 0.5]$, and keeping the parameters the same as before, the evolution of φ is shown for cases 1 and 2 in Figures 3.14 and 3.15 respectively.

3.4.4 Vortex induced flow

This example involves a circular bubble of radius $R = 0.18$ wherein $\varphi = -1$, under the effect of an advective field. The bubble is situated at a point $\mathbf{C} = [0.52, 0.25]$

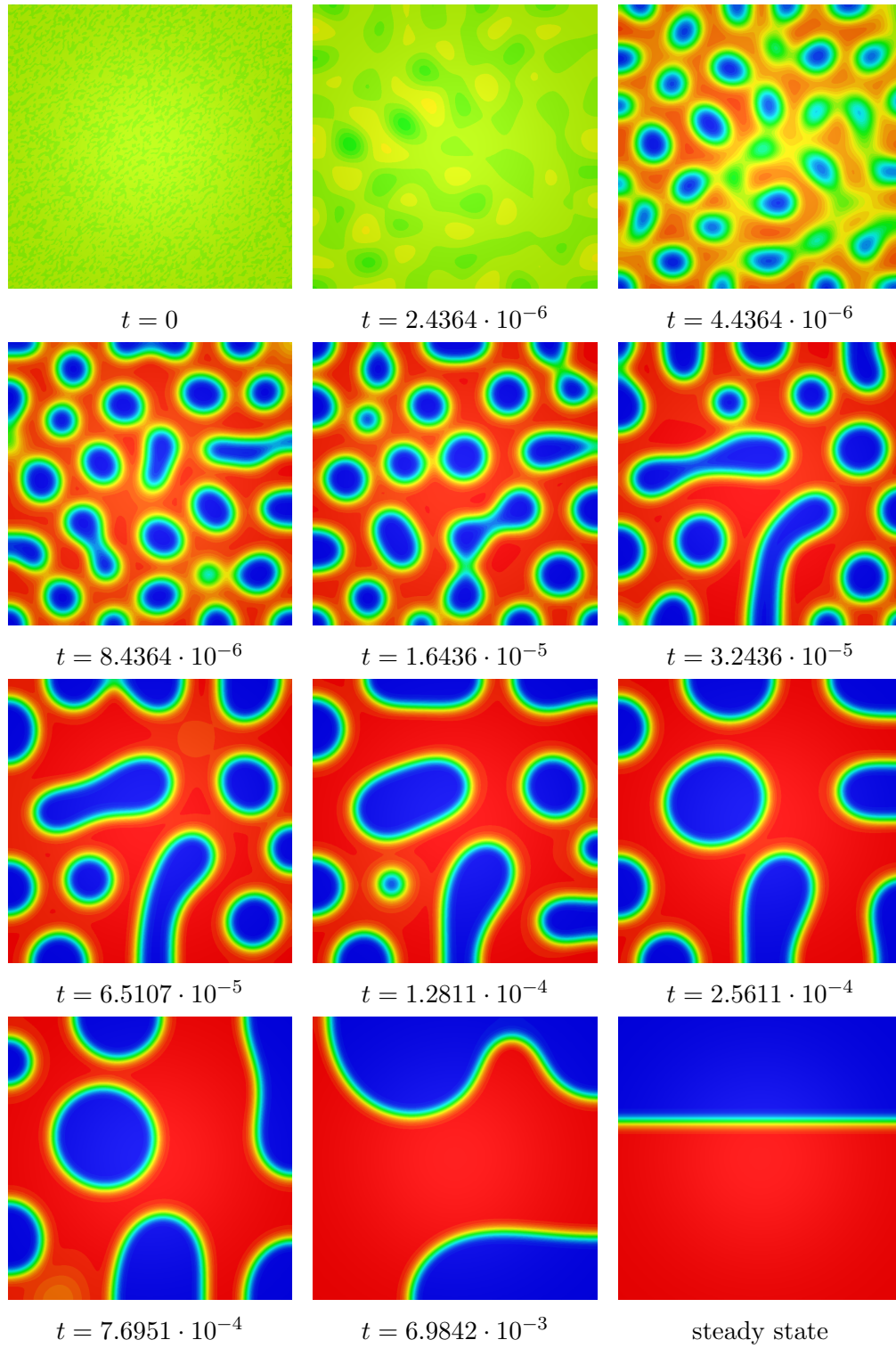


Figure 3.12: Two-dimensional spinodal decomposition of a randomly perturbed initial condition: Case 1 φ evolution with 128×128 linear elements.

in a square domain, $\Omega = [0, 1] \times [0, 1]$, wherein $\varphi = 1$. The initial condition is:

$$\varphi_0(\mathbf{x}) = \tanh \left(\frac{\sqrt{2W} (|\mathbf{x} - \mathbf{C}| - R)}{\epsilon} \right), \quad \mathbf{x} \in \Omega, \quad (3.26a)$$

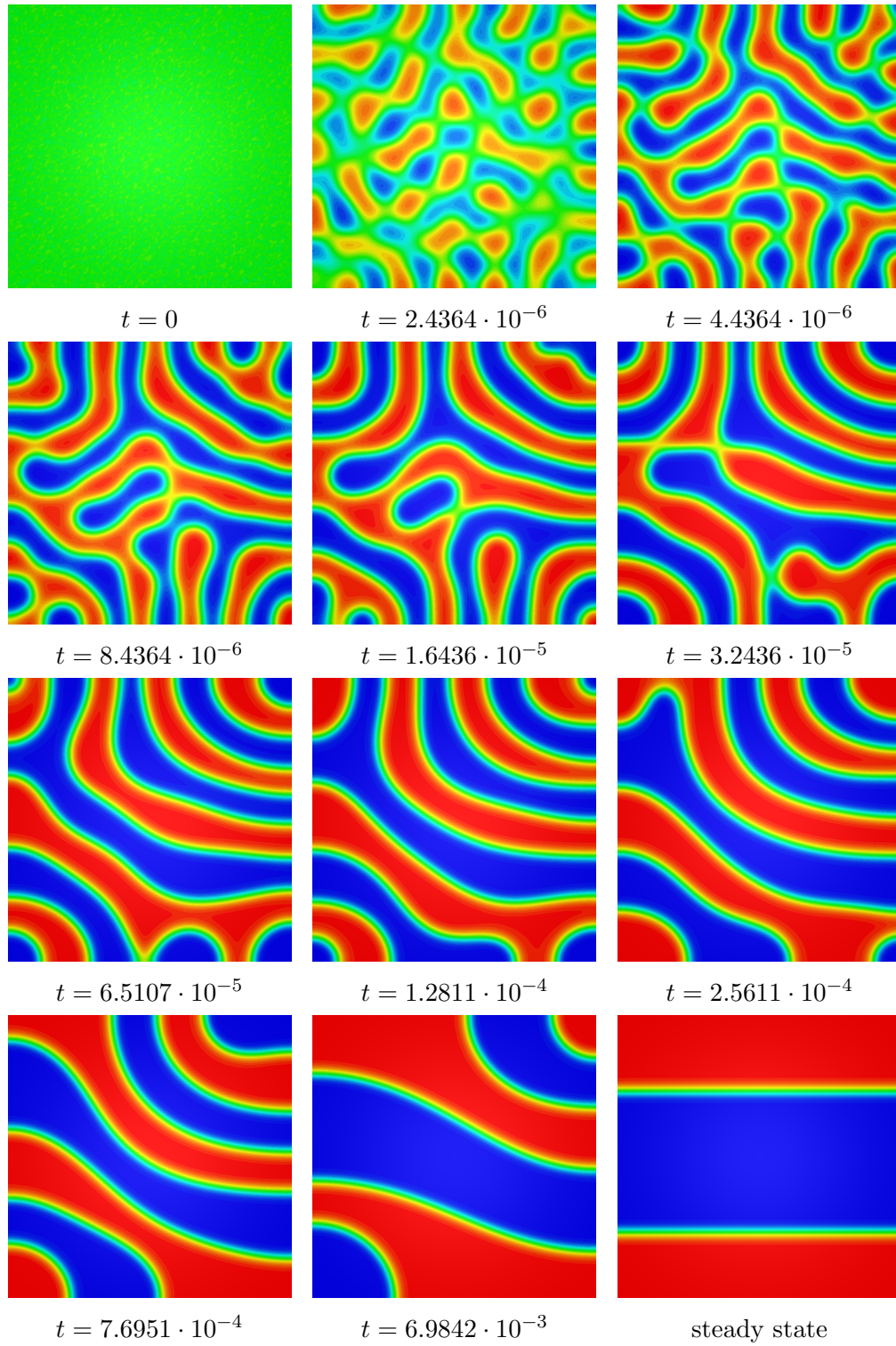


Figure 3.13: Two-dimensional spinodal decomposition of a randomly perturbed initial condition: Case 2 φ evolution with $32 \times 32 \times 32$ linear elements.

$$\eta_0(\mathbf{x}) = 0, \quad \mathbf{x} \in \Omega. \quad (3.26b)$$

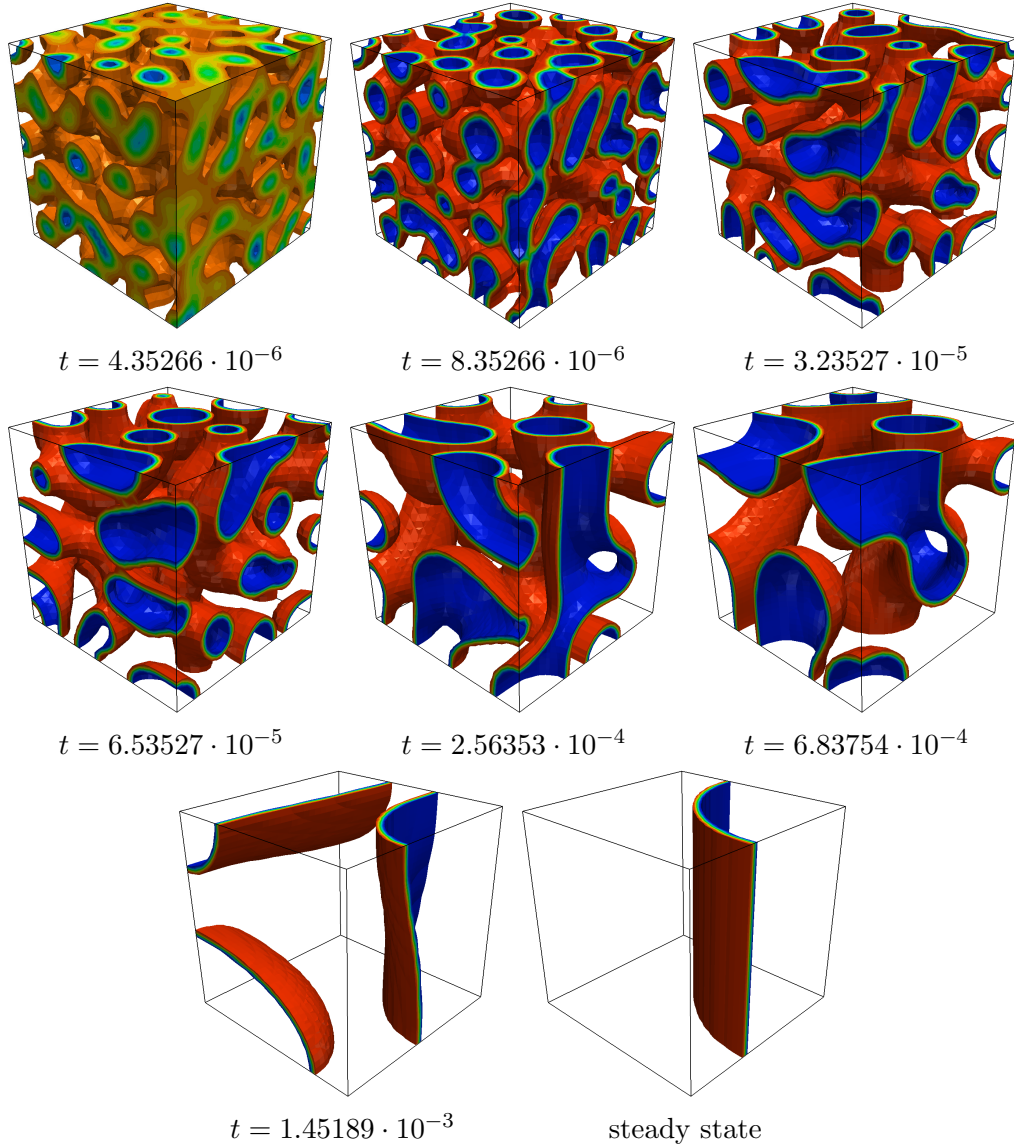


Figure 3.14: Three-dimensional spinodal decomposition of a randomly perturbed initial condition: φ evolution with $32 \times 32 \times 32$ linear elements.

The advective velocity is set as

$$\mathbf{a} = \begin{cases} -\sin(x\pi) \cos(y\pi), \\ \cos(x\pi) \sin(y\pi). \end{cases} \quad (3.27)$$

The boundary conditions are set as rotationally periodic. The other parameters are set to: $W = 1/4$, $\epsilon = 0.01$, $M(\varphi) = M_2(\varphi)$. Two cases are considered for the mobility coefficient; case 1: $D = 10^{-2}$ and case 2: $D = 10^{-4}$. The mesh is made up of 128×128 linear quadrilateral elements, and a fixed time step size of $\Delta t = 0.01$ is used.

Figures 3.16 and 3.17 show the time evolution of the phase-field variable for cases 1 and 2 respectively. The effect of decreasing the coefficient of mobility D is evident in that less coarsening/rounding is observed. This is apparent in the

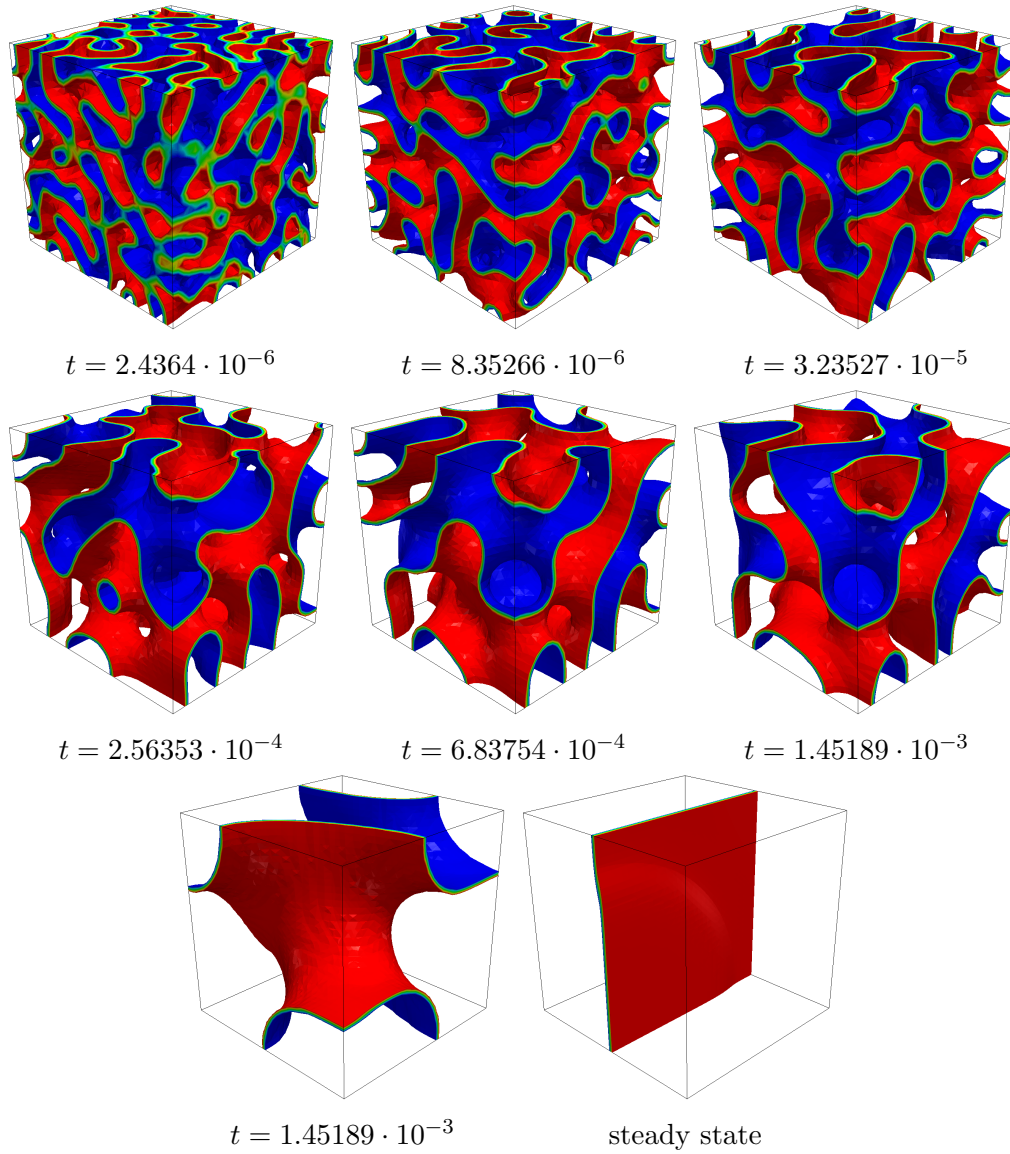


Figure 3.15: Three-dimensional spinodal decomposition of a randomly perturbed initial condition: φ evolution with $32 \times 32 \times 32$ linear elements.

increased acuteness of the tail observed with smaller mobility, and ultimately leads to lack of drop break-off. Also worth pointing out is that there is less variation from the initial configuration with the smaller mobility coefficient.

Three-dimensional analysis: The problem is extended to three-dimensions, with a domain size $\Omega = [0, 1] \times [0, 1] \times [0, 0.75]$. The parameters are kept the same, but the mesh now contains $68 \times 68 \times 51$ linear hexahedron elements. The evolution of the phase-field variable is shown in Figure 3.18.

3.5 Investigation into coarsening

Recalling the spinodal decomposition problem demonstrated in Figure 3.12, it is clear that after the initial decomposition the arbitrary bubble shapes begin

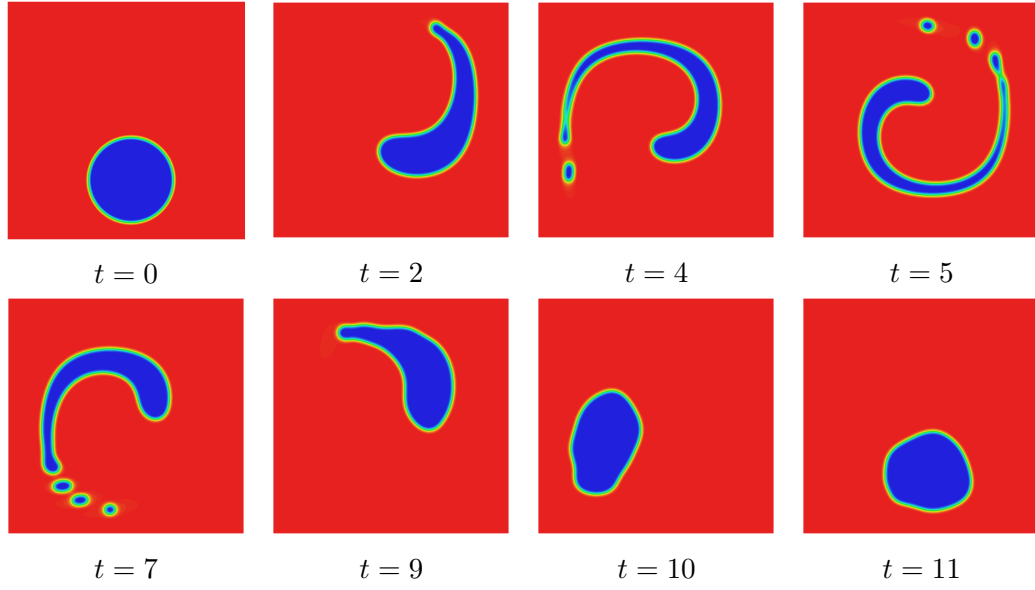


Figure 3.16: Two-dimensional circular bubble in vortex flow: φ evolution with $D = 10^{-2}$, using 128×128 linear elements.

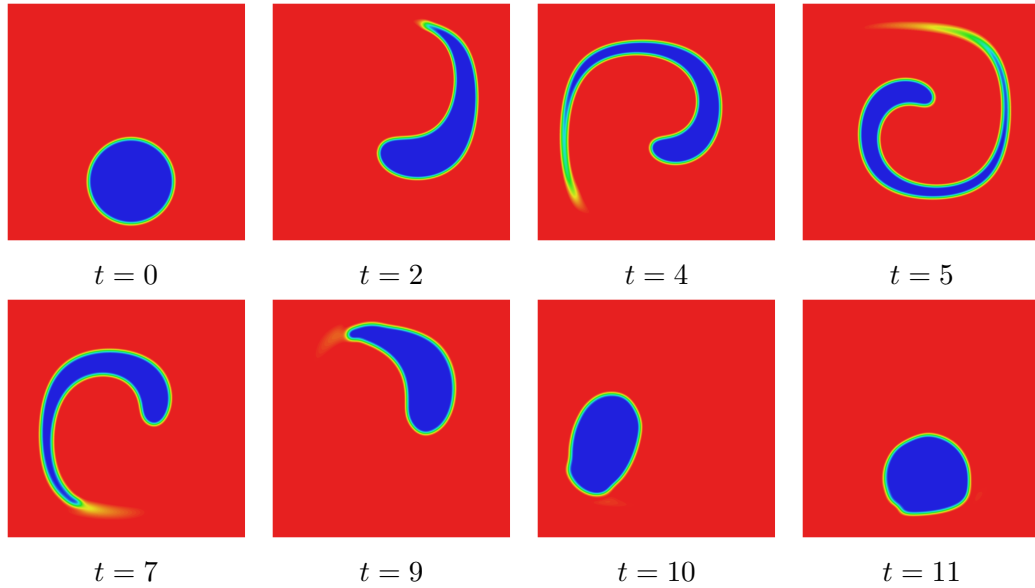


Figure 3.17: Two-dimensional circular bubble in vortex flow: φ evolution with $D = 10^{-4}$, using 128×128 linear elements.

to evolve into circular shapes, which continue coalescing and coarsening. This is an example of grain coarsening. This section focusses on understanding this phenomenon and developing strategies to control it.

3.5.1 Time scaling and setting the mobility

Up until now the relationships which the problem parameters have with each other have not been fully appreciated. This is investigated by conducting a simple

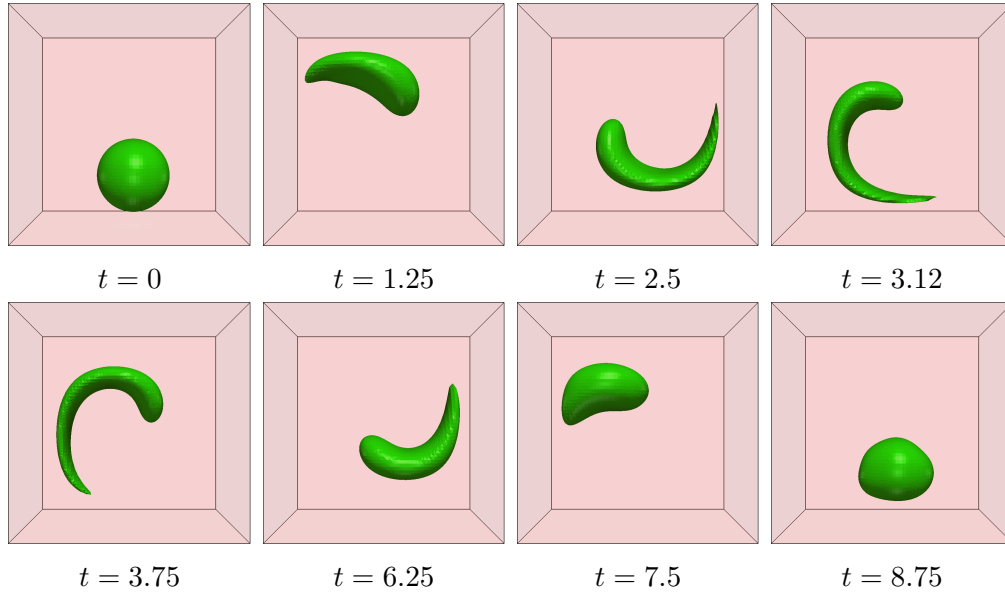


Figure 3.18: Three-dimensional spherical bubble in vortex flow: φ evolution with $D = 10^{-5}$, using $68 \times 68 \times 51$ linear elements.

experiment. An elliptic bubble with length a along the x -axis, and b along the y -axis is placed in a square domain $\Omega = [-50, 50] \times [-50, 50]$. The setup of the experiment is shown in Figure 3.19. A mesh consisting of 100×100 linear quadrilateral elements is used, and the time step size is set as the fixed value $\Delta t = 0.1$.

Results are generated from varying the parameters of the problem, where T is the recorded time for the ellipse to reach $\frac{3}{4}a$. The mobility is set as $M = 10$ for all simulations. The effective radius R , which refers to the equivalent circular radius for the same elliptic area, is considered as a measure in this example.

It is deduced from this numerical experiment that the following relationships exist:

$$T \propto \frac{1}{\epsilon^n}, \quad T \propto R^m, \quad T \propto \frac{1}{M}, \quad (3.28)$$

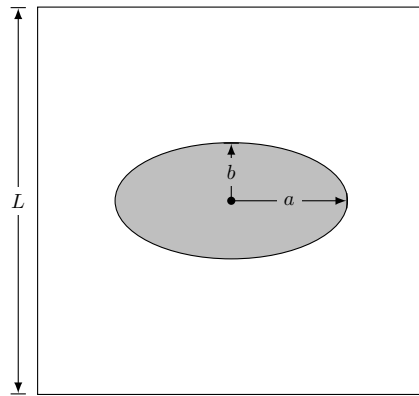


Figure 3.19: Elliptic bubble in a square domain.

and since the unit of measurement of the mobility coefficient M is $length^2/time$, it can be deduced that $m = n + 2$. With some rudimentary curve fitting and Equation (3.28), the relationship is found to be

$$T = \frac{R^4}{40M\epsilon^2}. \quad (3.29)$$

This relationship proves useful when setting up problems. The choice of mobility function for instance can now be selected based on the time scale of the problem at hand. This way the coarsening effect can be delayed beyond the physical time of interest. In the following subsection, a modification to the Cahn-Hilliard is proposed to attempt to reduce this inherent coarsening effect altogether.

3.5.2 Reduction of coarsening through modification

Cahn-Hilliard model with curvature term

Unfortunately there is limited literature which looks at the removal/control of grain coarsening. A form of the Cahn-Hilliard equation found in [100, 101] is presented with an additional term to reduce the surface energy contribution, written

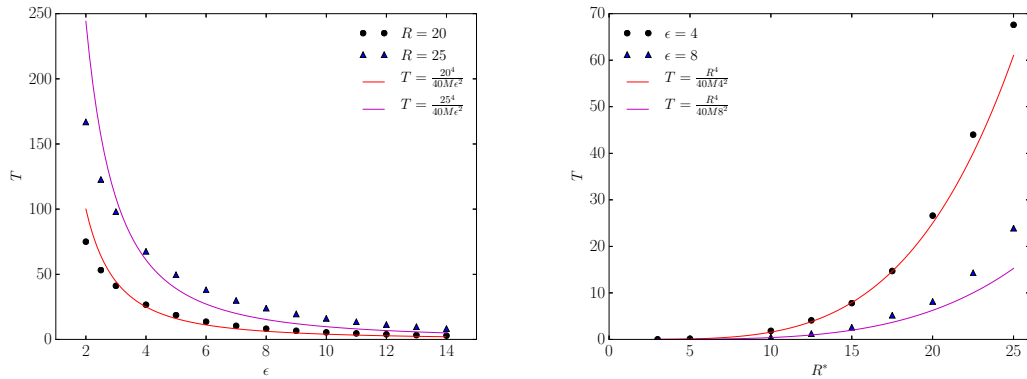


Figure 3.20: Time scaling analysis: T vs. ϵ (left), and T vs. R (right).

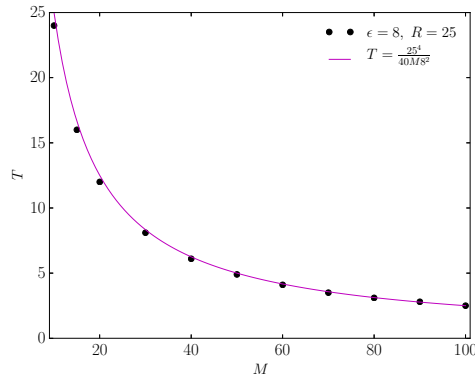


Figure 3.21: Time scaling analysis: T vs. M .

as

$$\frac{\partial \varphi}{\partial t} = \nabla \cdot [M(\varphi) \nabla (f(\varphi) - \epsilon^2 \Delta \varphi - \epsilon^2 c |\nabla \varphi|)], \quad (3.30)$$

where the curvature c is

$$c = -\nabla \cdot \mathbf{n} = -\nabla \cdot \frac{\nabla \varphi}{|\nabla \varphi|}. \quad (3.31)$$

The difficulties associated to this terms implementation is apparent when substituting Equation (3.31) into Equation (3.30), since higher order derivatives are introduced. It appears that more difficulties are introduced making this approach less feasible. An alternative approach which maintains the system order will now be proposed.

Proposed method

As pointed out previously, the coarsening or Ostwald ripening phenomenon can be attributed to the surface free energy density of the Ginzburg-Landau energy functional. As a consequence, the term $\epsilon^2 \Delta \varphi$ is directly responsible for these physical effects. The balance between the bulk and surface free energy components is however very important, as it is instrumental in retaining the interface thickness to the specified width. The bulk free energy contribution on its own would result in absolute hydrophobia, causing a sharp separation of phases. In the following proposed approach, the hydrophobic and hydrophilic contributions are kept in balance, while reducing the coarsening effect. This is achieved by projecting the surface contribution in the normal direction to the interface, thereby removing any tangential contributions.

The proposed approach is as follows:

$$\frac{\partial \varphi}{\partial t} + \mathbf{a} \cdot \nabla \varphi - \nabla \cdot (M(\varphi) \mathcal{P} \nabla \eta) = 0 \quad (3.32)$$

$$\eta - f(\varphi) + \epsilon^2 \Delta \varphi = 0 \quad (3.33)$$

where the *projection* tensor \mathcal{P} is

$$\mathcal{P} = \frac{\nabla \varphi}{|\nabla \varphi|} \otimes \frac{\nabla \varphi}{|\nabla \varphi|} = \frac{\nabla \varphi \otimes \nabla \varphi}{\nabla \varphi \cdot \nabla \varphi} \quad (3.34)$$

This approach will be referred to as the Cahn-Hilliard equation with projection (CHP). We suggest a further modification to this model, whereby a linear combination of the CH and CHP models is considered. This would result in Equation (3.32) being changed to

$$\frac{\partial \varphi}{\partial t} + \mathbf{a} \cdot \nabla \varphi - \nabla \cdot \left(M(\varphi) (A(|\nabla \varphi|) \mathcal{P} + \bar{A}(|\nabla \varphi|) \mathbf{I}) \nabla \eta \right) \quad (3.35)$$

Here $A(|\nabla \varphi|)$, shown in Figure 3.22, is taken as a cubic function expressed as

$$A(|\nabla \varphi|) = \begin{cases} 0, & \text{if } |\nabla \varphi| < \delta_1 \\ 1, & \text{if } |\nabla \varphi| > \delta_2 \\ \frac{2|\nabla \varphi|^3 - 3(\delta_1 + \delta_2)|\nabla \varphi|^2 + 6\delta_1\delta_2|\nabla \varphi| + \delta_1^3 - 3\delta_1^2\delta_2}{(\delta_1 - \delta_2)^3}, & \text{elsewhere} \end{cases} \quad (3.36)$$

where $\delta_i = \beta_i \max|\nabla\varphi|$, with β_1 , and β_2 specified as percentages applied to the maximum gradient. The maximum gradient $\max|\nabla\varphi|$ occurs at the interface. In the examples to follow, this is taken as $\max|\nabla\varphi| = \frac{1}{\sqrt{2}\epsilon}$.

Furthermore, the compliment $\bar{A}(|\nabla\varphi|) = 1 - A(|\nabla\varphi|)$.

For the sake of brevity both the CH equation (3.10a) and the CHP equation (3.35) could be written in the form

$$\frac{\partial\varphi}{\partial t} + \mathbf{a} \cdot \nabla\varphi - \nabla \cdot (M(\varphi)\mathcal{H}\nabla\eta) = 0 \quad (3.37)$$

where

$$\mathcal{H} = \begin{cases} \mathbf{I}, & \text{CH model} \\ A(|\nabla\varphi|)\mathcal{P} + \bar{A}(|\nabla\varphi|)\mathbf{I}, & \text{CHP model} \end{cases} \quad (3.38)$$

CH and CHP problem

Strong form: The Cahn-Hilliard model (3.10a)-(3.10d) is modified as follows,

$$\frac{\partial\varphi}{\partial t} + \mathbf{a} \cdot \nabla\varphi - \nabla \cdot (M(\varphi)\mathcal{H}\nabla\eta) = 0 \quad \text{in } \Omega \times \mathcal{I} \quad (3.39a)$$

$$\eta - f(\varphi) + \epsilon^2 \Delta\varphi = 0 \quad \text{in } \Omega \times \mathcal{I} \quad (3.39b)$$

$$(M(\varphi)\mathcal{H}\nabla\eta) \cdot \mathbf{n} = q \quad \text{on } \Gamma_q \times \mathcal{I} \quad (3.39c)$$

$$\nabla\varphi \cdot \mathbf{n} = 0 \quad \text{on } \Gamma_q \times \mathcal{I}. \quad (3.39d)$$

3.5.3 Numerical examples

Here we present several examples demonstrating the effect of the CHP equation in comparison to the classical CH equation. The problems are set up with the following commonalities:

- *Time integration:* The generalised- α time integration is used, with $\rho_\infty = 0.0$, unless otherwise stated.

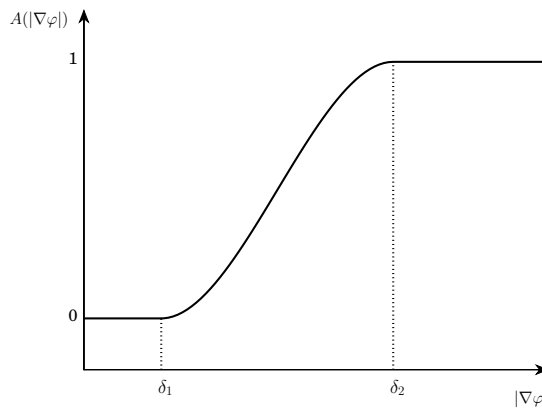


Figure 3.22: Cubic selection function $A(|\nabla\varphi|)$

- *Choice of ϵ :* The interface thickness is taken as $\epsilon = 2h$, unless otherwise stated.
- *Choice of δ_1 and δ_2 :* The CHP method is considered with $\delta_1 = 10^{-4} \max|\nabla\varphi|$, and $\delta_2 = 10^{-2} \max|\nabla\varphi|$, unless otherwise stated.

Stationary square

In this example a unit square domain $\Omega_d = [-50, 50] \times [-50, 50]$ contains a phase with $\varphi = 1$, with the exception of a square region $\Omega_s = [-20, 20] \times [-20, 20]$ wherein $\varphi = -1$. Ω_s has rounded corners with a radius $r = 2$.

The comparison between the CH and CHP equations is made for both constant and degenerate mobilities. Two cases are considered: Case 1 considers a constant mobility function $M_0(\varphi)$ and case 2 considers a cubic degenerate mobility $M_3(\varphi)$. In both cases $D = 100$. The mesh used consists of 128×128 linear quadrilateral elements.

Case 1: A comparison of the φ evolution between the CH and CHP models is shown in Figure 3.23. A comparison of the interface position between the CH and CHP models is shown in Figure 3.24. It is observable from both Figures 3.23 and 3.24 that the CHP model slightly delays the coarsening effect when compared to the CH model. A comparison of the total energy as well as the specific free energy components is shown in Figure 3.25. The total free energy lines flatten out once the square has completely coarsened into a circle. This flattening occurs at around $t = 7$ for the CH model, and around $t = 15$ for the CHP model. The effect of varying δ_2 is demonstrated in Figure 3.26. Observably there is a very slight improvement from using $\delta_2 = 10^{-2} \max|\nabla\varphi|$ and $\delta_2 = 10^{-3} \max|\nabla\varphi|$. Using $\delta_2 = 10^{-3} \max|\nabla\varphi|$ introduces more numerical complexity resulting in slower convergence, and thus the choice of $\delta_2 = 10^{-2}$ is justified.

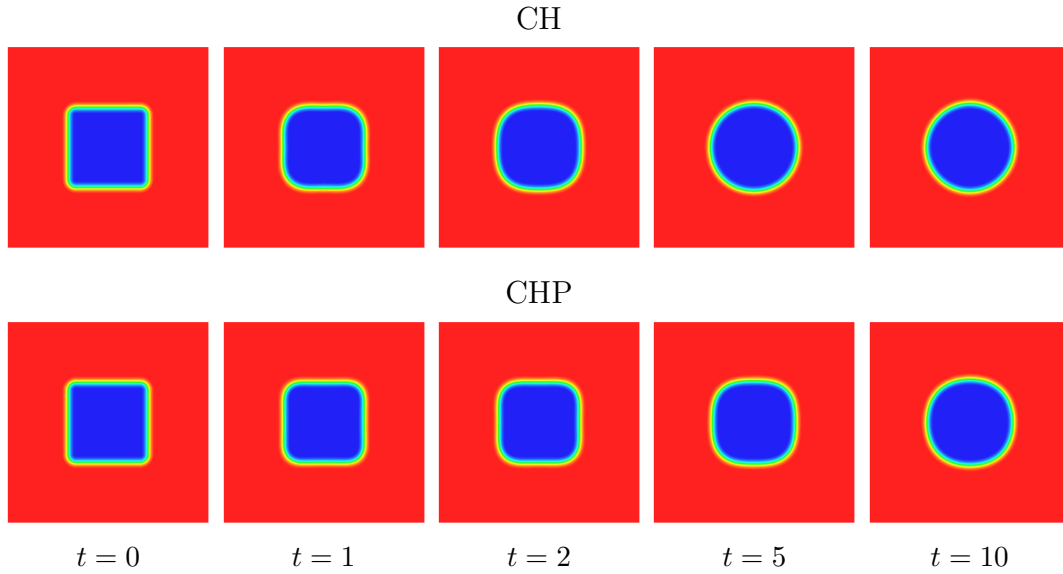


Figure 3.23: Stationary square case 1: Comparison of φ evolution for the CH and CHP models.

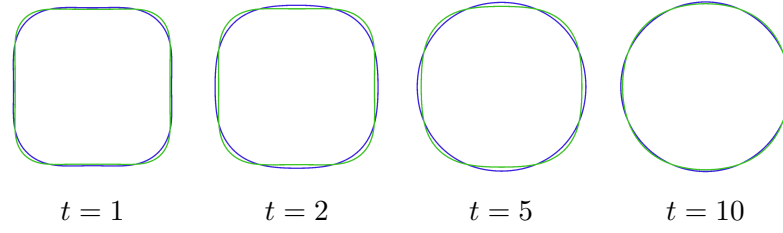


Figure 3.24: Stationary square case 1: Comparison of interface position obtained with the CH (blue) and CHP (green) models.

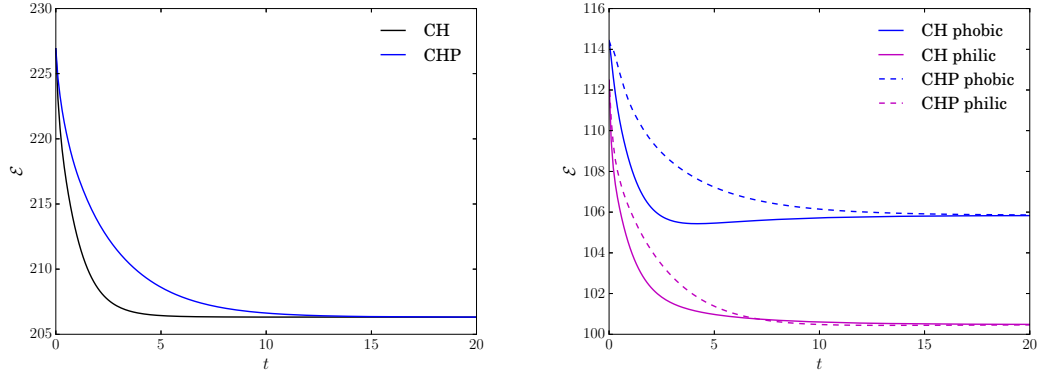


Figure 3.25: Stationary square case 1: Comparison of total free energy (left) and bulk and surface energy components (right) for the CH and CHP models.

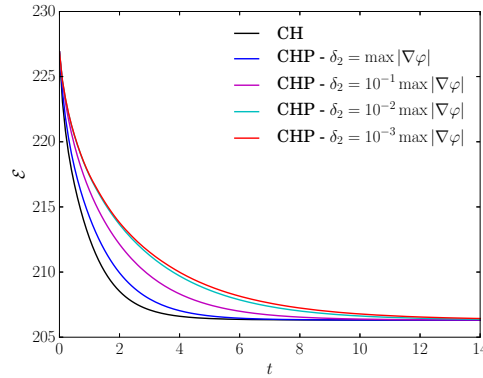


Figure 3.26: Stationary square case 1: Comparison of total energy from the CH model and CHP model with different choices of δ_2 .

Case 2: A comparison between the φ evolution between the CH and CHP models is shown in Figure 3.27. A comparison between the interface position of the CH and CHP models is shown in Figure 3.28. Clearly there is a more significant reduction in coarsening when compared to case 1. By the time that the square has become completely round with the CH model, barely any rounding is observed with the CHP model. This is reflected in the total energy evolution shown in Figure 3.29.

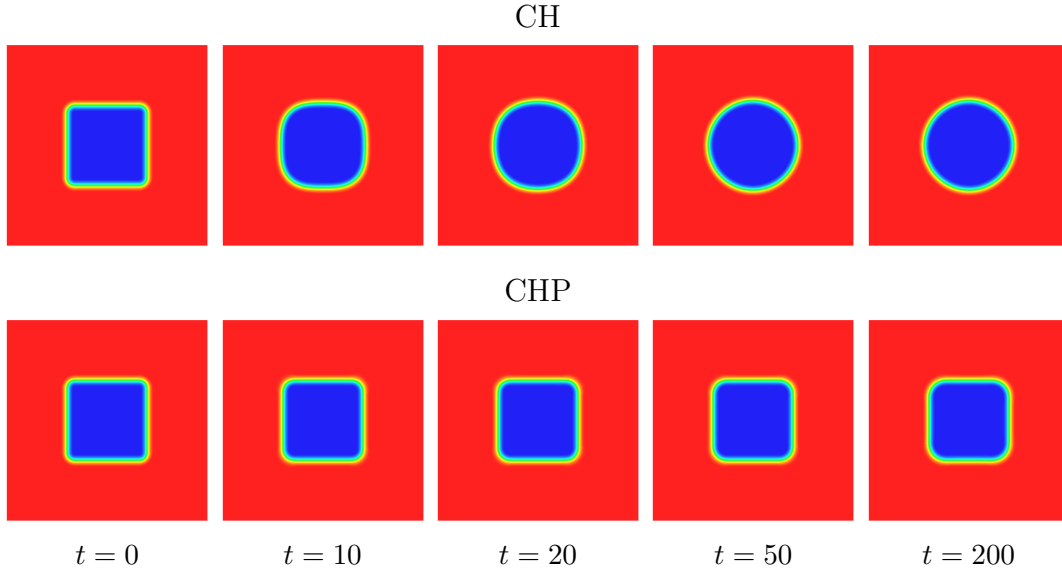


Figure 3.27: Stationary square case 1: Comparison of φ evolution for the CH and CHP models.

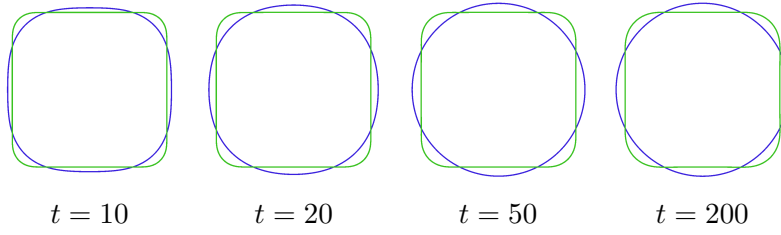


Figure 3.28: Stationary square case 2: Comparison of interface position obtained with the CH (blue) and CHP (green) models.

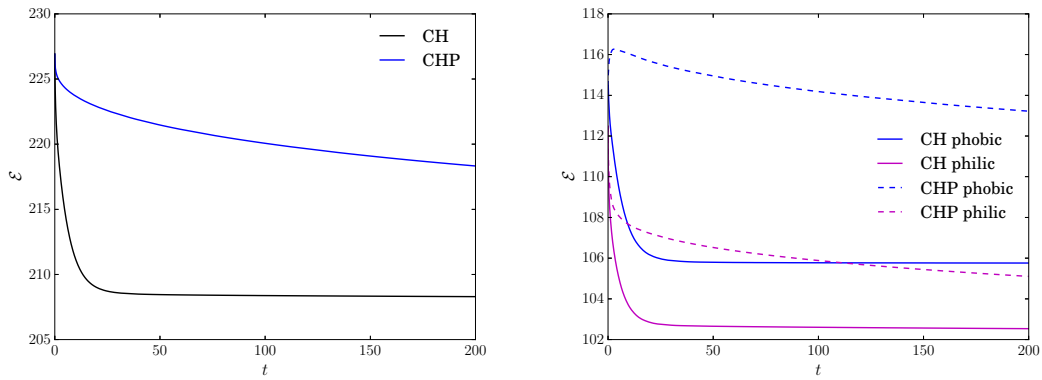


Figure 3.29: Stationary square case 2: Comparison of total free energy (left) and bulk and surface energy components (right) for the CH and CHP models.

Rotating square

Here an advective velocity field $\mathbf{a} = [y, -x]$, where x, y are spatial coordinates, is introduced for the problem considered in Section 3.5.3. The same parameters

are applied as in Section 3.5.3, with the exception of the time step size which is chosen as a fraction of a full revolution period ($t = 2\pi/500$).

A comparison of the evolution of φ for the CH and CHP models with degenerate mobility is shown in Figure 3.30. The CH model experiences significantly more coarsening than the CHP model. After a complete rotation the square has barely changed when considering the CHP model. The total free energy as well as the bulk and surface free energy components are shown in Figure 3.31. Similarly to the stationary square problem, it is clear that the free energy corresponding the CH model reaches its lowest state considerably sooner than the CHP model.

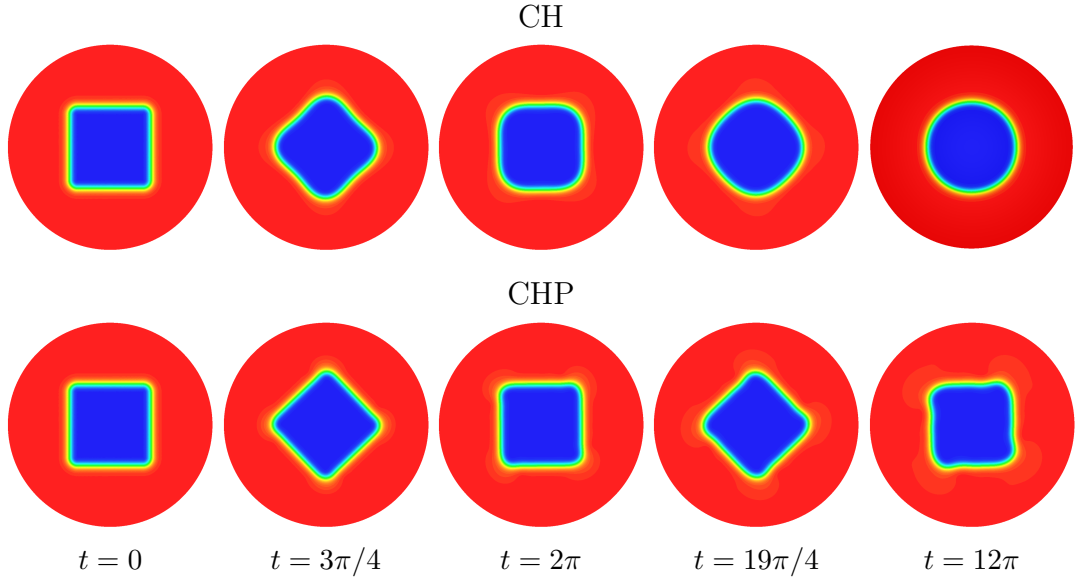


Figure 3.30: Rotating square: Comparison of φ obtained with the CH and CHP models.

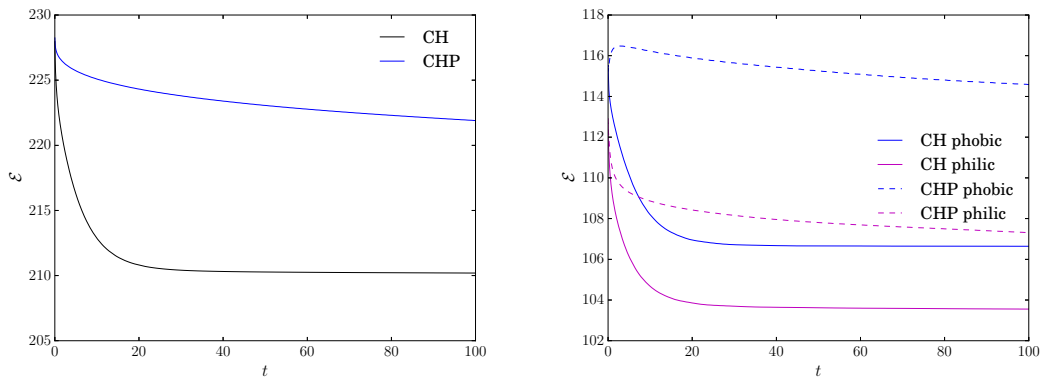


Figure 3.31: Rotating square: Comparison of total free energy (left) and bulk and surface energy components (right) for the CH and CHP models.

3.6 Investigation into shrinkage

It is remarked in [63], that if the time scale of interest for a particular two-phase mixture, for instance a bubble of phase a situated in a square domain of phase b , is considerably shorter than the shrinkage time, there would be minimal loss of mass even if the initial radius is smaller than the critical radius. In this section strategies for reducing this shrinkage effect are explored.

3.6.1 Evaluation of non-critical shrinkage

Consider once more the problem of a two or three-dimensional bubble situated in a square or cubic domain, as shown in Figure 3.32 with the appropriate volume fractions α . Yue et al. [63] analytically evaluate the amount which the phase-field variable shifts, assuming this shift is equal in the two bulk regions, as

$$\delta\varphi = \begin{cases} \frac{\sqrt{2}}{6} \frac{\epsilon}{R_0}, & (2D), \\ \frac{\sqrt{2}}{3} \frac{\epsilon}{R_0}, & (3D), \end{cases} \quad (3.40)$$

where R_0 is the initial bubble radius. For simplicity, the Cahn number is introduced as $Cn = \epsilon/R_0$. Furthermore the change in radius associated with shrinkage

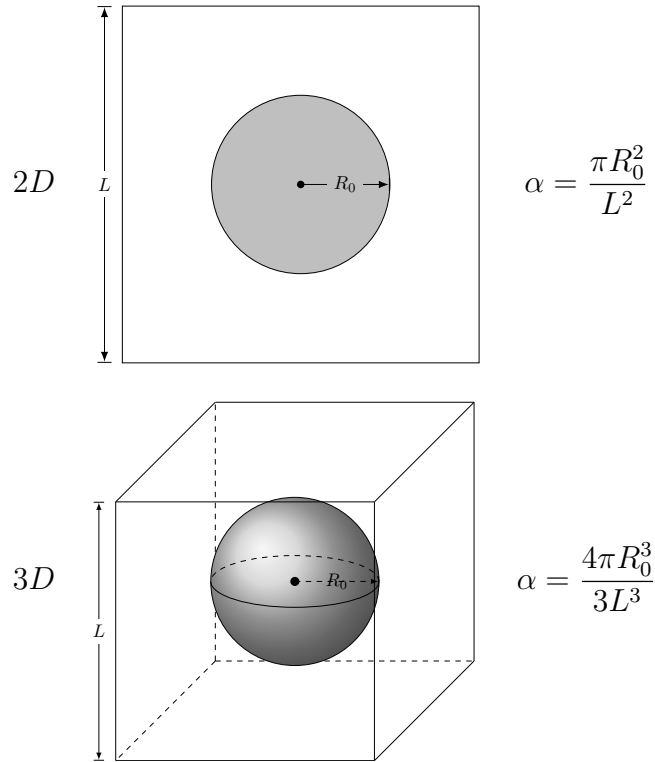


Figure 3.32: Investigation into shrinkage: 2D and 3D geometries.

is evaluated as

$$\delta R = \begin{cases} -\frac{\sqrt{2}}{24} \frac{\epsilon}{\alpha}, & (2D), \\ -\frac{\sqrt{2}}{18} \frac{\epsilon}{\alpha}, & (3D). \end{cases} \quad (3.41)$$

A simulation is set up following [63], where the problem parameters are set as: $L = 4$, $R_0 = 1$, $M(\varphi) = M_0$ with $D = 1$. A range of ϵ are tested between the values of 0.01 and 0.2. In order to represent the interface with sufficient accuracy, $h = \epsilon/2$ is used as the element size for a uniform quadrilateral mesh. Figure 3.33 shows the comparison of the analytical expressions (3.40)-(3.41) with two-dimensional finite element simulations. The observations made in [63] are clearly confirmed with the present finite element formulation. That is when the volume occupied by the bubble is less than that of the square domain, an expected shift of the phase-field variable occurs in the bulk regions, which is accompanied by a volume reduction of the bubble.

3.6.2 Evaluation of critical volume fraction

Setting a mixture of two phases requires that there is a minimum volume fraction, which if reduced further will result in a single phase problem as a result of the minority phase vanishing completely. To avoid this it is important to obtain the critical volume fraction α for any interface thickness ϵ .

Consider a one-dimensional domain of length L , where we refer to the volume of one phase as l_α , giving a volume fraction of $\alpha = l_\alpha/L$. The free energy of this problem is defined as

$$\Psi = F(\varphi) + \frac{\epsilon^2}{2} |\nabla \varphi|^2$$

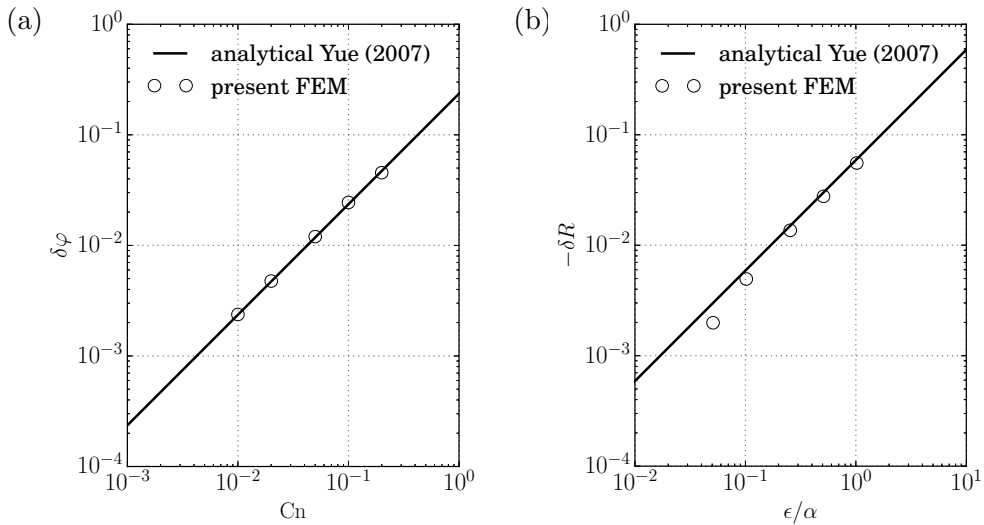


Figure 3.33: Investigation into shrinkage: Comparison of (a) phase shift, and (b) dimensionless radius shrinkage, with analytical expressions from [63].

$$= W (1 - \varphi^2)^2 + \frac{\epsilon^2}{2} \left(\frac{d\varphi}{dx} \right)^2. \quad (3.42)$$

Now defining the equation for φ as in Equation (3.17),

$$\varphi = \tanh \left(\frac{\sqrt{2W}}{\epsilon} (l_\alpha - x) \right), \quad (3.43)$$

with its derivative as

$$\frac{d\varphi}{dx} = \frac{\sqrt{2W}}{\epsilon} \left(\tanh^2 \left(\frac{\sqrt{2W}}{\epsilon} (l_\alpha - x) \right) - 1 \right) \quad (3.44)$$

$$= \frac{\sqrt{2W}}{\epsilon} (\varphi^2 - 1). \quad (3.45)$$

Substituting Equations (3.43) and (3.45) into (3.42) gives

$$\Psi = 2W \operatorname{sech}^4 \left(\frac{\sqrt{2W}}{\epsilon} (x - l_\alpha) \right). \quad (3.46)$$

Now the energy Ψ is evaluated by integrating over the length,

$$\begin{aligned} \Psi &= \frac{1}{L} \int_0^L 2W \operatorname{sech}^4 \left(\frac{\sqrt{2W}}{\epsilon} (x - l_\alpha) \right) dx \\ &= \frac{\sqrt{2W}\epsilon}{3L} \tanh \left(\frac{\sqrt{2W}}{\epsilon} (x - l_\alpha) \right) \left(\operatorname{sech}^2 \left(\frac{\sqrt{2W}}{\epsilon} (x - l_\alpha) \right) + 2 \right) \Big|_0^L. \end{aligned} \quad (3.47)$$

To evaluate the critical fraction we first should consider the free energy obtained from setting an equivalent average mixture phase φ^* . To evaluate φ^* we integrate φ over the domain, such that

$$\begin{aligned} \varphi^* &= \frac{1}{L} \int_0^L \tanh \left(\frac{\sqrt{2W}}{\epsilon} (l_\alpha - x) \right) dx \\ &= -\frac{\epsilon}{\sqrt{2W}L} \log \left(\frac{\cosh \left(\frac{\sqrt{2W}}{\epsilon} (l_\alpha - L) \right)}{\cosh \left(\frac{\sqrt{2W}}{\epsilon} l_\alpha \right)} \right). \end{aligned} \quad (3.48)$$

Evaluating the energy by substituting Equation (3.48) into the free energy equation gives

$$\Psi^* = W \left[1 - \left(\frac{\epsilon}{\sqrt{2W}L} \log \left(\frac{\cosh \left(\frac{\sqrt{2W}}{\epsilon} (l_\alpha - L) \right)}{\cosh \left(\frac{\sqrt{2W}}{\epsilon} l_\alpha \right)} \right) \right)^2 \right]^2. \quad (3.49)$$

Figure 3.34(a) shows the ϕ distribution when $\alpha = 0.6$, $L = 1$, $\epsilon = 0.3$, and $W = 2$. Here we evaluate $\varphi^* = 0.2$. Figure 3.34(b) shows the variation of the energy with respect to α for the same parameters mentioned above.

Setting $\Psi = \Psi^*$ one can evaluate the critical α . The intersection point is retrieved when Equation (3.49) is equated to Equation (3.47). Figure 3.35 shows the relationship between α and ϵ/L . The 1D finite element results are also comparatively shown for the problem.

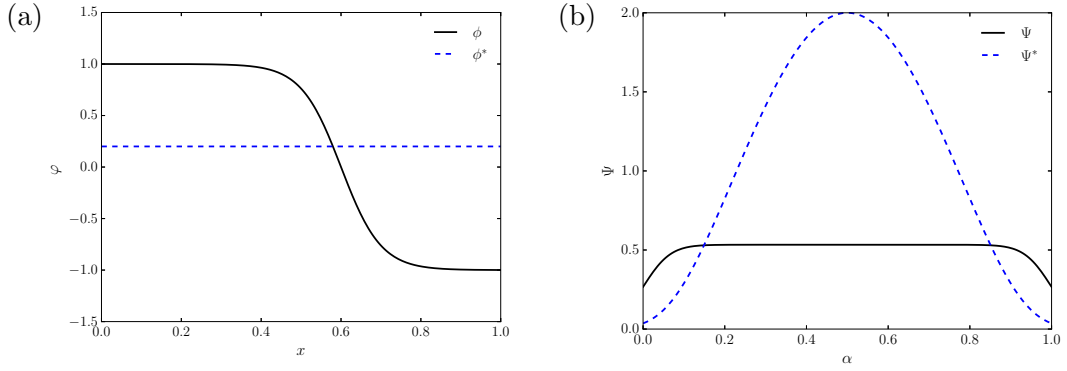


Figure 3.34: CH equation 1D: ϕ distribution (a), and energy with respect to α (b).

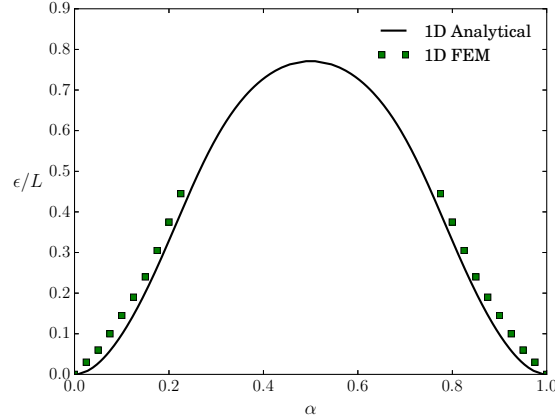


Figure 3.35: CH equation 1D: ϵ vs. critical α .

3.6.3 Suggestions for double well potentials

In typical settings, the standard double well potential term from Equation 3.6 is expected to sufficiently localise the individual phases within the confines of $\varphi = [-1, 1]$. However, as demonstrated in Section 3.6.2 as well as [63], if the critical radius is surpassed a bubble will shrink or even disappear entirely. The role of the double well potential in relation to the bubble shrinkage will now be investigated.

Consider an alternative double well potential with steeper gradients,

$$F_2(\varphi^n) = W \frac{(e^{\varphi^n} - e)^2}{(e - 1)^2}, \quad (3.50)$$

where n is the polynomial order, $n = 2, 4, 6, \dots$. For brevity we define the standard double well potential from Equation (3.50) as $F_1(\varphi)$. Figure 3.36 shows a comparison of the various double well potentials. It is evident that n controls the steepness of the double well $F_2(\varphi^n)$ at the extremes. Using $F_2(\varphi^2)$ for the problem in Section 3.6.1, a comparison can be made with $F_1(\varphi)$, as shown in Figure 3.37. It is clear from Figure 3.37 that using $F_2(\varphi^2)$ reduces the observable phase shift and radius shrinkage.

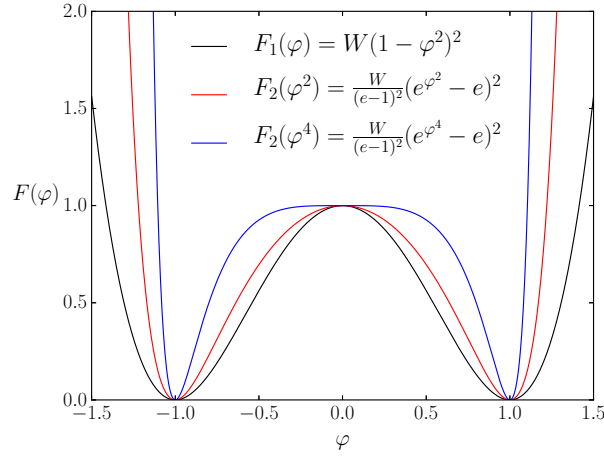


Figure 3.36: Double well potential comparison.

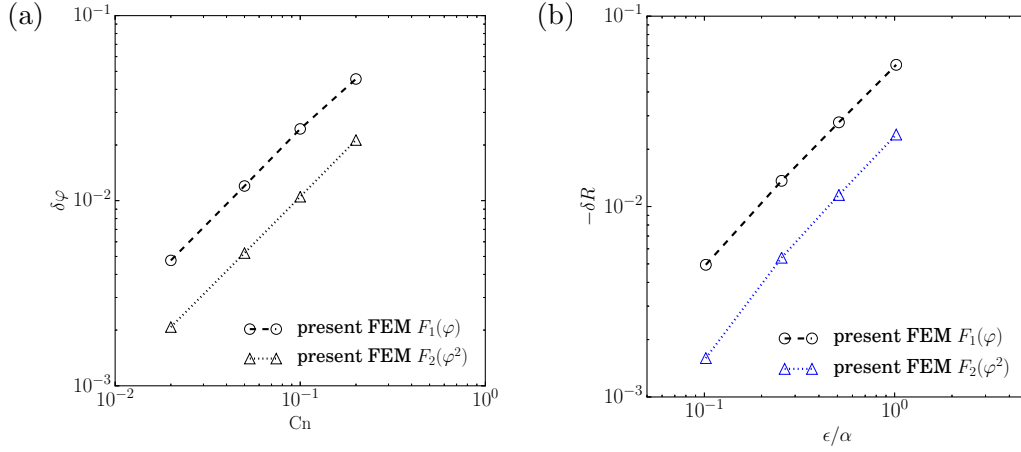


Figure 3.37: Investigation into shrinkage: Comparison of (a) phase shift, and (b) dimensionless radius shrinkage, with analytical expressions from [63].

Below the critical volume fraction: Consider now a bubble with a radius smaller than the critical radius. The initial radius is taken as $R_0 = 0.1$ and a two-dimensional square domain is used with $L = 1$. The mesh used consists of 200×200 linear quadrilateral elements, such that the characteristic element size is $h = 1/200$. The other parameters are as before. Adaptive time stepping is used with an initial time step size of $\Delta t = 0.0001$, and the problems are run until a steady state solution is achieved.

Figure 3.38 shows the initial condition and steady state solutions of φ obtained from considering the different double well types presented thus far. From Figure 3.38b it can be seen that when using the standard double well potential $F_1(\varphi)$, the bubble completely vanishes. Using $F_2(\varphi^n)$, the bubble does not disappear as seen in Figure 3.38c using $n = 2$ and Figure 3.38d using $n = 4$. It is also evident that although the bubble remains, there is a slight reduction in radius when using $n = 2$, and no noticeable change when using $n = 4$. The evolution of the circle radius for each well type is shown in Figure 3.39. While the bubble completely disappears using $F_1(\varphi)$, the radius reduces by less than 1% using $F_2(\varphi^2)$ and less

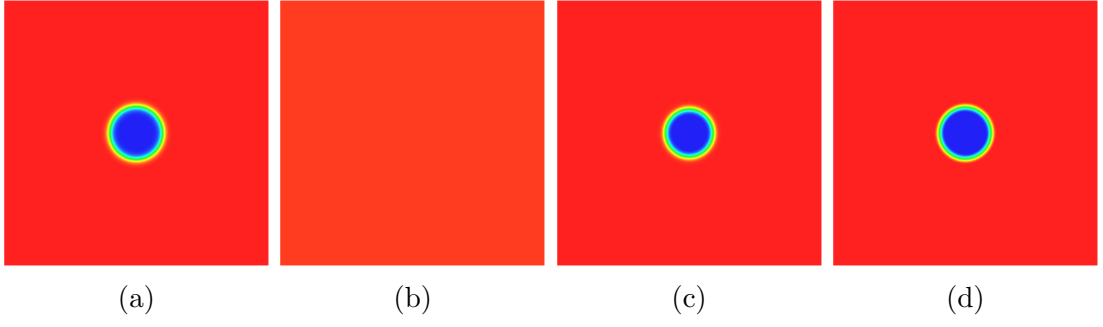


Figure 3.38: Double well potential comparison: (a) Initial condition, and steady state φ solution using double well potential (b) $F_1(\varphi)$, (c) $F_2(\varphi^2)$, and (d) $F_2(\varphi^4)$.

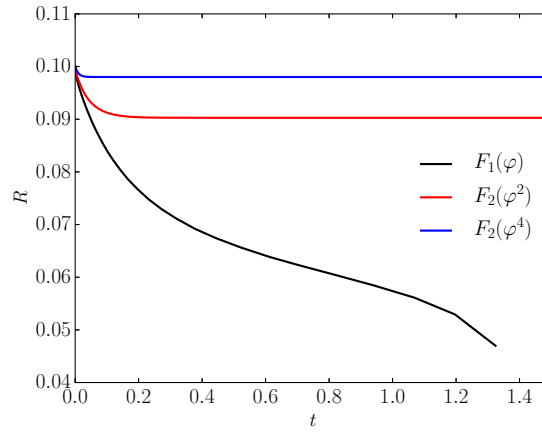


Figure 3.39: Double well potential comparison: Evolution of circle radius.

than 0.2% using $F_2(\varphi^4)$. The bubble shrinks in all cases since the minimisation of the double well potential yields a final bubble shape which enjoys a lower energy. This energy state is higher when using the $F_2(\varphi^n)$ functions, and consequently less shrinkage occurs. Figure 3.40 shows the time step size versus the time iteration. Since different physical events occur in all three cases, the plots are not exactly

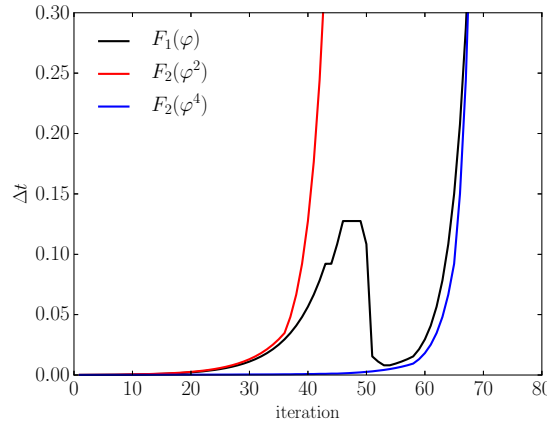


Figure 3.40: Double well potential comparison: Evolution of time step size Δt .

comparable. Clearly when the bubble vanishes using $F_1(\varphi)$, the time step size reduces drastically as a result of the notable physical event taking place. With $F_2(\varphi^2)$ this physical event does not happen and thus the problem converges to steady state sooner. With the added nonlinearity of $F_2(\varphi^4)$, even though the bubble undergoes minimal physical change, the convergence is slightly poorer, meaning that roughly the same amount of time iterations are required as for $F_1(\varphi)$.

It can be concluded that using $F_2(\varphi^n)$ and increasing the order n is a feasible solution for reducing/removing the shrinkage for a simple problem such as the one presented. However, it is expected that implementing this strategy for more complex problems may affect the convergence due to the increased nonlinearity.

3.6.4 Initial conditions to account for sub-critical volume fractions

Considering the 2D geometry in Figure 3.32, the total energy can be expressed as a combination of the individual energies of the bulk regions and the interface region, as follows:

$$\Psi = \Psi_a + \Psi_b + \Psi_i, \quad (3.51)$$

where a and b refer to the bulk regions outside and inside a bubble perimeter respectively, and i refers to the interface region. From Equation (3.51) we can obtain the initial values of φ_a and φ_b required to minimise the energy. This can be rewritten to account for the absolute areas occupied by each region,

$$\begin{aligned} \Psi = & \left(L^2 - \pi \left(R + \frac{\epsilon}{2} \right)^2 \right) F(\varphi_a) + \pi \left(R - \frac{\epsilon}{2} \right)^2 F(\varphi_b) \\ & + 2\pi R \int_{-\epsilon/2}^{\epsilon/2} F(\varphi) + \frac{\epsilon^2}{2} |\nabla \varphi|^2 dx. \end{aligned} \quad (3.52)$$

In order to integrate the energy over the interface region, we need to select a profile for φ . For simplicity, consider the linear profile

$$\varphi = \frac{\varphi_b - \varphi_a}{\epsilon} x + \frac{\varphi_a + \varphi_b}{2} \quad (3.53)$$

The associated energy is then

$$\begin{aligned} & \int_{-\epsilon/2}^{\epsilon/2} F(\varphi) + \frac{\epsilon^2}{2} |\nabla \varphi|^2 dx \\ &= \int_{-\epsilon/2}^{\epsilon/2} W \left(1 - \left(\frac{\varphi_b - \varphi_a}{\epsilon} x + \frac{\varphi_a + \varphi_b}{2} \right)^2 \right)^2 + \frac{1}{2} (\varphi_b - \varphi_a)^2 dx \\ &= \frac{W\epsilon}{15} \left(3\varphi_a^4 + 3\varphi_a^3\varphi_b + 3\varphi_a^2\varphi_b^2 - 10\varphi_a^2 + 3\varphi_a\varphi_b^3 - 10\varphi_a\varphi_b + 3\varphi_b^4 \right. \\ & \quad \left. - 10\varphi_b^2 + 15 \right) + \frac{\epsilon}{2} (\varphi_a - \varphi_b)^2. \end{aligned} \quad (3.54)$$

Substituting (3.54) into (3.52) gives

$$\begin{aligned} \Psi = & W \left(L^2 - \pi \left(R + \frac{\epsilon}{2} \right)^2 \right) (1 - \varphi_a^2)^2 + W \pi \left(R - \frac{\epsilon}{2} \right)^2 (1 - \varphi_b^2)^2 \\ & + \frac{2\pi RW\epsilon}{15} \left(3\varphi_a^4 + 3\varphi_a^3\varphi_b + 3\varphi_a^2\varphi_b^2 - 10\varphi_a^2 + 3\varphi_a\varphi_b^3 - 10\varphi_a\varphi_b + 3\varphi_b^4 \right. \\ & \left. - 10\varphi_b^2 + 15 \right) + \pi R\epsilon(\varphi_a - \varphi_b)^2. \end{aligned} \quad (3.55)$$

Minimising (3.55), we get the following system

$$\begin{aligned} \frac{\partial \Psi}{\partial \varphi_a} = & 4W \left(L^2 - \pi \left(R + \frac{\epsilon}{2} \right)^2 \right) (\varphi_a^3 - \varphi_a) \\ & + \frac{2\pi RW\epsilon}{15} (12\varphi_a^3 + 9\varphi_a^2\varphi_b + 6\varphi_a\varphi_b^2 - 20\varphi_a + 3\varphi_b^3 - 10\varphi_b) \\ & + 2\pi R\epsilon(\varphi_a - \varphi_b) = 0, \end{aligned} \quad (3.56)$$

$$\begin{aligned} \frac{\partial \Psi}{\partial \varphi_b} = & 4W \pi \left(R - \frac{\epsilon}{2} \right)^2 (\varphi_b^3 - \varphi_b) \\ & + \frac{2\pi RW\epsilon}{15} (3\varphi_a^3 + 6\varphi_a^2\varphi_b + 9\varphi_a\varphi_b^2 - 10\varphi_a + 12\varphi_b^3 - 20\varphi_b) \\ & + 2\pi R\epsilon(\varphi_a - \varphi_b) = 0, \end{aligned} \quad (3.57)$$

Once φ_a and φ_b are obtained using the Newton-Raphson method, the initial condition can be set as follows

$$\varphi(x) = \varphi_{avg} + \varphi_{dif} \tanh \left(\frac{\sqrt{2W}}{\epsilon} (x + B) \right), \quad (3.58)$$

where,

$$\varphi_{avg} = \frac{\varphi_a + \varphi_b}{2}, \quad \varphi_{dif} = \frac{\varphi_b - \varphi_a}{2}. \quad (3.59)$$

Note that the linear profile chosen in Equation (3.53) is merely for brevity, since a lower number of terms result from the integration. In practice a hyperbolic tangent profile as presented in Equation (3.58) will replace the linear profile in that step.

To demonstrate the effectiveness of this strategy, consider a small drop of radius $R = 0.125$ placed in a square domain $[0, 1] \times [0, 1]$. The profile of the drop is set with the hyperbolic tangent function (3.58) with $B = 0$. Considering the element size $h = 1/64$, the interface thickness is set as $\epsilon = 5h$, such that the bubble is expected to vanish. Also $W = 2$ in this example. It is evaluated from solving Equation (3.57) that the initial φ in the bulk phases should be set as $\varphi_a = -0.946$ outside the bubble and $\varphi_b = 0.998$ inside the bubble, in order for the bubble to remain. Figure 3.41 shows a comparison of the radius evolution with time between setting the initial condition (3.58) using $[\varphi_a, \varphi_b] = [-0.946, 0.998]$ and $[\varphi_a, \varphi_b] = [-1, 1]$. Notably there is minimal reduction in radius observed from using the adjusted bulk phase-field variable values, whereas with $[\varphi_a, \varphi_b] = [-1, 1]$, the bubble completely vanishes as expected.

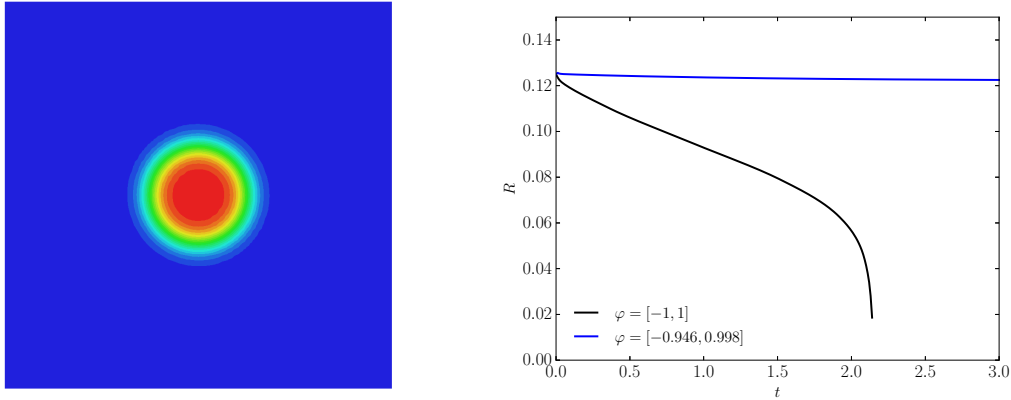


Figure 3.41: CH setting initial φ : Initial condition (left), and evolution of radius for various initial bulk φ values.

3.7 Concluding remarks

As an initial objective the author aims to identify a phase dynamics equation which does not possess any physical interference, i.e. one which just separates the individual phases. It is expected that if the phase dynamics equation is coupled with the Navier-Stokes equations for instance, the physics such as those associated with surface tension, should be governed primarily by the latter set of equations. The Cahn-Hilliard equation is formulated with finite elements using an auxiliary equation to reduce the fourth order PDE to two second order PDEs. A number of numerical benchmark problems are demonstrated where the inherent phenomena associated with the Cahn-Hilliard equation, namely the effects of grain coarsening and shrinkage, are clearly observed which confirms observations made in a previous study [63].

A modification to the formulation is proposed for reducing the coarsening effect in Section 3.5. The modified Cahn-Hilliard equation is compared with its unaltered counterpart through a series of examples involving a square bubble, which is either stationary or in an advective field. It is observed in the stationary case that the modified equation significantly reduces the coarsening of the bubble when using a degenerate mobility function, whereas only slightly when considering a constant mobility. Similar observations are made when applying a rotational advective field. Notably the modification does not come at the expense of computational efficiency, since the number of iterations and physical times remain roughly the same.

Next the attention of the author is turned to controlling drop shrinkage in Section 3.6. The effect of using different double well potentials to localise the phases is demonstrated. It is found that there is a compromise between reducing amount of physical shrinkage and increasing the computational effort. A methodology is proposed in which the the expected initial phase-field variable values in the bulk regions are calculated and set based on the problem geometry such that drop shrinkage is minimised. It is shown with a demonstration of a stationary circular drop in a square domain, that when setting the initial conditions based on these

calculated values, a significant decrease in drop shrinkage is observed.

Chapter 4

Binary Fluid Systems: The Navier-Stokes-Cahn-Hilliard Equations

The popularity and convenience of the Cahn-Hilliard equation lies with the fact that it can easily be coupled with physics models, and hydrodynamics is no exception. Combining the Navier-Stokes equations with the Cahn-Hilliard equation results in the Navier-Stokes-Cahn-Hilliard model, which has become a common choice for the simulation of immiscible two-component fluid flows. Typically for realistic flow simulations the thickness of the interface separating the fluid components is often too small to be considered numerically. The model is however provably shown to converge to sharp interface models, see Magaletti et al. [102].

Numerous numerical strategies have been developed to solve the Navier-Stokes-Cahn-Hilliard equations. The use of a spectral-element type discretisation has been shown effective in [103, 104, 92]. A finite difference discretisation is effectively implemented by Kim et al. [105]. Approaches based on the finite element method, including those with adaptive re-meshing, are also frequently employed in [106, 107, 108, 109, 110]. Guo et al. [111] present an adaptive mesh strategy, using an energy preserving C_0 finite element method to solve problems of high topological complexity. A discontinuous Galerkin finite element approach is used by Giesselmann and Pryer [112] to model the quasi-incompressible Navier-Stokes-Cahn-Hilliard equations. One of the more recent approaches is based on using IGA, which is successfully demonstrated in [98, 113, 114]. There have also been recent advancements in fractional step type schemes for the mentioned incompressible phase field models. Shen et al. [36] present a three stage decoupling where the computations of the Allen-Cahn equation, i.e. the phase-field variable and chemical potential, are decoupled from the Navier-Stokes equations, in which the pressure and velocity fields are also decoupled. Similar strategies for the Navier-Stokes-Cahn-Hilliard equations are proposed in [115, 116, 117], and [118], where the latter only decouples the Cahn-Hilliard equation from the Navier-Stokes equations. Yang et al. [119] and more recently Chiu [120] successfully implemented a Navier-Stokes-Allen-Cahn type model to simulate surface tension dominated drop dynamics problems.

4.1 The Navier-Stokes-Cahn-Hilliard equations

Coupling the Cahn-Hilliard model (3.10) with the incompressible Navier-Stokes equations, yields the Navier-Stokes-Cahn-Hilliard equations used for modelling two-phase immiscible multiphase flows. The strong form of these equations are written as follows.

Strong form: Consider again the domain $\Omega \subset \mathbb{R}^d$ ($d \leq 3$) bounded by Γ , with Neumann and Dirichlet subsets, Γ_g and Γ_q , and containing a mixture of two immiscible incompressible fluids with different densities ρ_a and ρ_b for the time interval $\mathcal{I} = (0, T)$. In this work, the Navier-Stokes-Cahn-Hilliard boundary value problem consists of finding the velocity \mathbf{u} , pressure p , phase-field variable φ and chemical potential η , such that

$$\begin{aligned} \rho(\varphi) \left(\frac{\partial \mathbf{u}}{\partial t} + (\mathbf{u} \cdot \nabla) \mathbf{u} - \mathbf{b} \right) + (\mathbf{J}(\varphi, \eta) \cdot \nabla) \mathbf{u} & \quad \text{in } \Omega \times \mathcal{I} \\ + \nabla p - \nabla \cdot (2\mu(\varphi) \nabla^s \mathbf{u}) - \kappa \eta \nabla \varphi = \mathbf{0} & \end{aligned} \quad (4.1a)$$

$$\nabla \cdot \mathbf{u} = 0 \quad \text{in } \Omega \times \mathcal{I} \quad (4.1b)$$

$$\frac{\partial \varphi}{\partial t} + \mathbf{u} \cdot \nabla \varphi - \nabla \cdot (M(\varphi) \nabla \eta) = 0 \quad \text{in } \Omega \times \mathcal{I} \quad (4.1c)$$

$$\eta - f(\varphi) + \epsilon^2 \Delta \varphi = 0 \quad \text{in } \Omega \times \mathcal{I} \quad (4.1d)$$

$$M(\varphi) \nabla \eta \cdot \mathbf{n} = 0 \quad \text{on } \Gamma_q \times \mathcal{I} \quad (4.1e)$$

$$\nabla \varphi \cdot \mathbf{n} + \|\nabla \varphi\| \cos(\alpha) = 0 \quad \text{on } \Gamma_q \times \mathcal{I}, \quad (4.1f)$$

where \mathbf{b} is the body force, and $M(\varphi)$ is again the mobility function as described in Section 3.2.3.

The model presented in Equations (4.1) is based on the Abels et al. model [14] and is thermodynamically consistent. It allows for variable densities, and agrees with sharp interface models for $\epsilon \rightarrow 0$.

Cahn and Hilliard [25] describe surface tension as the excess free energy per unit surface area. It follows that in the case of a plane phase-field interface at equilibrium, the surface tension coefficient, γ , is related to the phase-field variable φ by

$$\gamma = \kappa \int_{-\infty}^{\infty} \left(\frac{d\varphi}{dx} \right) dx. \quad (4.2)$$

In order to achieve consistency of the surface tension term in Equation (4.1a) with the Young-Laplace sharp interface surface tension model, the factor κ must be chosen as

$$\kappa = \frac{3}{4\sqrt{2W}} \frac{\gamma}{\epsilon}, \quad (4.3)$$

Equation (4.2) is successfully implemented in numerous studies [26, 121, 39, 114]. A Navier-Stokes-Cahn-Hilliard model using Equation (4.3) is shown to approach the sharp-interface model as $\epsilon \rightarrow 0$ in [122].

In the present work, the surface tension stress term $\eta \nabla \varphi$ (see also Boyer [15]) is used in Equation (4.1a), instead of $\gamma \epsilon \nabla \cdot (\nabla \varphi \otimes \nabla \varphi)$ (see Abels et al. [14]). The former term is easily derived from the latter, and the resulting pressure term in Equation (4.1a) is now a modified pressure term $\nabla \hat{p}$, where $\hat{p} = (p + \Psi)$. This modified pressure is similar to the original pressure, in fact, it is identical in the bulk regions where Ψ vanishes. Advantageously the modified pressure varies generally more smoothly across interface regions than the original pressure.

In Equation (4.1a), the relative diffusive flux is expressed as

$$\mathbf{J} = -\rho_{dif} M(\varphi) \nabla \eta. \quad (4.4)$$

The density and viscosity are described by the linear approximations

$$\begin{aligned} \rho(\varphi) &= \rho_{dif} \varphi + \rho_{avg}, \\ \mu(\varphi) &= \mu_{dif} \varphi + \mu_{avg}, \end{aligned} \quad (4.5)$$

where,

$$\rho_{dif} = \frac{\rho_a - \rho_b}{2}, \quad \rho_{avg} = \frac{\rho_a + \rho_b}{2}, \quad (4.6)$$

$$\mu_{dif} = \frac{\mu_a - \mu_b}{2}, \quad \mu_{avg} = \frac{\mu_a + \mu_b}{2}. \quad (4.7)$$

If necessary, a cut-off function $\bar{\varphi}$ can be incorporated in Equation (4.5), where

$$\bar{\varphi} = \begin{cases} \varphi & \text{if } |\varphi| \leq 1, \\ \text{sign}(\varphi) & \text{if } |\varphi| > 1. \end{cases} \quad (4.8)$$

This would ensure that ρ and μ remain within the physical bounds of the specified bulk phases, and has been effectively used in [123].

Remark 1. In the model given by Equations (4.1) the physical quantities and the Young-Laplace surface tension term occur only in the momentum equation. The CH equation (3.10) merely governs the transport of the order parameter φ . Traditional representations of the Navier-Stokes-Cahn-Hilliard equations such as those used in [28, 39, 14] can easily be recovered by introducing appropriate scalar factors in Equations (4.1c) or (4.1d).

4.2 Numerical formulation

4.2.1 Mixed Taylor-Hood formulation

In order to satisfy the LBB stability condition, a Taylor-Hood element is chosen for the spatial discretisation (see Figure 4.1). Thus, the velocity, phase-field variable and chemical potential interpolations are piecewise quadratic, while the pressure interpolation is piecewise linear.

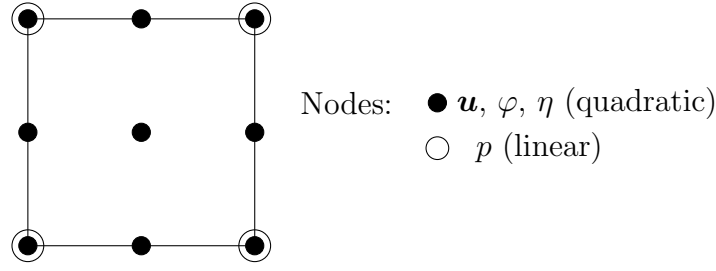


Figure 4.1: Two-dimensional Taylor-Hood interpolations.

The discrete weak form of the Navier-Stokes-Cahn-Hilliard problem (4.1) reads: Find $(\mathbf{u}^h, p^h, \varphi^h, \eta^h) \in (\mathcal{S}^h, \mathcal{P}^h, \mathcal{X}^h, \mathcal{Z}^h)$, such that, for all $(\mathbf{w}^h, q^h, s^h, v^h) \in (\mathcal{V}^h, \mathcal{P}^h, \mathcal{Y}^h, \mathcal{W}^h)$,

$$\int_{\Omega} \mathbf{w}^h \cdot \left(\rho(\varphi^h) \left(\frac{\partial \mathbf{u}^h}{\partial t} + \mathbf{u}^h \cdot \nabla \mathbf{u}^h - \mathbf{b} \right) - \mathbf{J}(\varphi^h, \eta^h) \cdot \nabla \mathbf{u}^h - \kappa \eta^h \nabla \varphi^h \right) - (\nabla \cdot \mathbf{w}^h) p^h + \nabla \mathbf{w}^h : (2\mu(\varphi^h) \nabla^s \mathbf{u}^h) \, d\Omega = 0 \quad (4.9a)$$

$$\int_{\Omega} \nabla q^h \cdot \mathbf{u}^h \, d\Omega = 0 \quad (4.9b)$$

$$\int_{\Omega} v^h \left(\frac{\partial \varphi^h}{\partial t} + \mathbf{u}^h \cdot \nabla \varphi^h \right) + \nabla v^h \cdot (M(\varphi^h) \nabla \eta^h) \, d\Omega = 0 \quad (4.9c)$$

$$\int_{\Omega} s^h (\eta^h - f(\varphi^h)) - \nabla s^h \cdot \epsilon^2 \nabla \varphi^h \, d\Omega - \int_{\Gamma} s^h \epsilon^2 |\nabla \varphi^h| \cos(\alpha) \, d\Gamma = 0, \quad (4.9d)$$

where $\mathcal{S}^h, \mathcal{P}^h, \mathcal{X}^h, \mathcal{Z}^h, \mathcal{V}^h, \mathcal{Y}^h$ and \mathcal{W}^h are the appropriate finite element spaces of piecewise continuous quadratic and linear basis functions.

4.2.2 Stabilised formulation

The standard SUPG/PSPG stabilisation strategy (see, for instance [124, 125, 80, 126, 127]) is applied to the Navier-Stokes-Cahn-Hilliard momentum equation. This allows for the use of piecewise linear equal order interpolations for u, p, φ and η .

The SUPG/PSPG stabilised discrete weak form reads: Find $(\mathbf{u}^h, p^h, \varphi^h, \eta^h) \in (\mathcal{S}^h, \mathcal{P}^h, \mathcal{X}^h, \mathcal{Z}^h)$, such that, for all $(\mathbf{w}^h, q^h, s^h, v^h) \in (\mathcal{V}^h, \mathcal{P}^h, \mathcal{Y}^h, \mathcal{W}^h)$,

$$\begin{aligned} & \int_{\Omega} \mathbf{w}^h \cdot \left(\rho(\varphi^h) \left(\frac{\partial \mathbf{u}^h}{\partial t} + \mathbf{u}^h \cdot \nabla \mathbf{u}^h - \mathbf{b} \right) - \mathbf{J}(\varphi^h, \eta^h) \cdot \nabla \mathbf{u}^h - \kappa \eta^h \nabla \varphi^h \right) \\ & \quad - (\nabla \cdot \mathbf{w}^h) p^h + \nabla \mathbf{w}^h : (2\mu(\varphi^h) \nabla^s \mathbf{u}^h) \, d\Omega \\ & + \sum_{e=1}^{n_{el}} \int_{\Omega_e} \left[\tau_u \rho(\varphi^h) (\mathbf{u}^h \cdot \nabla \mathbf{w}^h) + \tau_p \nabla q^h \right] \cdot \left[\rho(\varphi^h) \left(\frac{\partial \mathbf{u}^h}{\partial t} + \mathbf{u}^h \cdot \nabla \mathbf{u}^h - \mathbf{b} \right) \right. \\ & \quad \left. - \mathbf{J}(\varphi^h, \eta^h) \cdot \nabla \mathbf{u}^h - \kappa \eta^h \nabla \varphi^h + \nabla p^h \right] \, d\Omega = 0 \end{aligned} \quad (4.10a)$$

$$\int_{\Omega} \nabla q^h \cdot \mathbf{u}^h \, d\Omega = 0 \quad (4.10b)$$

$$\int_{\Omega} v^h \left(\frac{\partial \varphi^h}{\partial t} + \mathbf{u}^h \cdot \nabla \varphi^h \right) + \nabla v^h \cdot (M(\varphi^h) \nabla \eta^h) \, d\Omega = 0 \quad (4.10c)$$

$$\int_{\Omega} s^h (\eta^h - f) - \nabla s^h \cdot \epsilon^2 \nabla \varphi^h \, d\Omega - \int_{\Gamma} s^h \epsilon^2 |\nabla \varphi^h| \cos(\alpha) \, d\Gamma = 0. \quad (4.10d)$$

where \mathcal{S}^h , \mathcal{P}^h , \mathcal{X}^h , \mathcal{Z}^h , \mathcal{V}^h , \mathcal{Y}^h and \mathcal{W}^h are the appropriate finite element spaces of piecewise continuous linear basis functions.

Following [81], the stabilisation parameters, $\tau_{\mathbf{u}}$ and τ_p are defined as

$$\tau_{\mathbf{u}} = \left(\frac{1}{\tau_p^2} + \left(\frac{2\rho|\mathbf{u}_e|}{h_e} \right)^2 \right)^{-\frac{1}{2}}, \quad \tau_p = \frac{h_e^2}{4\mu}, \quad (4.11)$$

where h_e is the characteristic size of the element, evaluated as $h_e = V_e^{1/d}$, with d representing the number of spatial dimensions and V_e , the element volume or area. The vector \mathbf{u}^e is the velocity in the element centroid.

4.2.3 Temporal discretisation and solution strategy

The generalised- α scheme is considered for the time integration. The scheme is as shown in Section 2.3.2. Adaptive time stepping (see Section 2.3.4) is also implemented in several numerical examples presented in the sections to follow.

The problems described by Equations (4.9) and (4.10) are highly nonlinear and thus a Newton-Raphson procedure is employed based on the consistent linearisation of all nonlinear terms. For smaller scale problems, a direct linear solver (PARDISO [84, 85, 86]) is used, whereas for larger scale problems, an iterative parallel solver (PETSC [87]) with a block Jacobi pre-conditioner is employed.

4.3 Numerical Examples

In the following examples the proposed methodology is applied to a number of two and three-dimensional problems. Subsections 4.3.1-4.3.9 present surface tension dominated problems, while the simulations described in Subsections 4.3.10-4.3.12 do not feature any surface tension effects. Finally, Subsection 4.3.13 presents an industrial case study.

The properties of water and air used in the following examples are:

$$\begin{aligned} \text{water: } \rho &= 0.998 \quad \text{g/cm}^3, \\ \mu &= 0.0101 \quad \text{g/(cm s)}, \\ \text{air: } \rho &= 0.0012 \quad \text{g/cm}^3, \\ \mu &= 0.000182 \quad \text{g/(cm s)}, \\ \text{water/air: } \gamma &= 73.0 \quad \text{g/s}^2, \\ \text{gravity: } g &= 980.0 \quad \text{cm/s}^2. \end{aligned}$$

Unless otherwise stated, the computations are based on the stabilised formulation given by Equations (4.10) and the Cahn-Hilliard parameters are set as follows:

$$\text{mobility function: } M_0 = 10^{-3} \text{ cm}^2/\text{s},$$

$$\begin{aligned} \text{well height: } W &= 0.25, \\ \text{interface thickness: } \epsilon &= 2h, \end{aligned}$$

where h corresponds to the characteristic size of the element used, which is taken as the largest element size of the respective mesh.

The relative diffusive flux term $(\mathbf{J} \cdot \nabla) \mathbf{u}$ is neglected in the following examples as its effect is observably negligible.

4.3.1 Static bubble

A bubble of radius R is placed at coordinate $\mathbf{C} = [0.5, 0.5]$ in the centre of a square domain, $\Omega = [0, 1] \times [0, 1]$. The densities and viscosities, as well as the surface tension coefficient, are set to 1. The initial condition for φ is taken as,

$$\varphi_0(\mathbf{x}) = \tanh\left(\frac{R - |\mathbf{x} - \mathbf{C}|}{\sqrt{2}\epsilon}\right), \quad \mathbf{x} \in \Omega. \quad (4.12a)$$

No-slip velocity boundary conditions are set on all boundaries. The pressure difference between the centre of the bubble and a point outside the bubble at coordinate $[1.0, 0.5]$, are compared to the Young-Laplace equation,

$$\Delta p = \frac{\gamma}{R}. \quad (4.13)$$

Two meshes are considered: a mesh with 256×256 mixed Taylor-Hood elements, and a mesh with 512×512 stabilised linear quadrilateral elements. For both meshes, the interface thickness is set as $\epsilon = 1/128$. All simulations are run until $T = 10$. Figure 4.2 shows the excellent agreement between the analytical expression and the numerical experiment, for a range of values of R .

4.3.2 Small amplitude oscillations of a two-dimensional drop

This example is inspired by the oscillation experienced by liquid drops in the presence of an acoustic field for instance (see Figure 4.3 [128]).

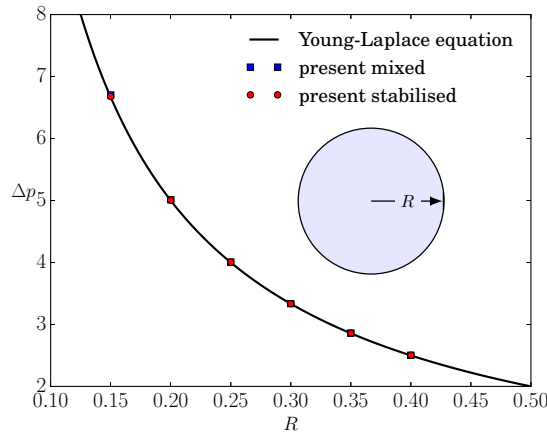


Figure 4.2: Static bubble: Comparison between numerical and analytical (Young-Laplace) pressure drop.

Figure 4.3: Shape oscillation experiment for 2nd, 3rd and 4th harmonics [128].

A small two-dimensional drop of water with radius $R = 0.0125$ cm is placed in the centre of a square domain $\Omega = [-0.025, 0.025] \times [-0.025, 0.025]$ cm² which is filled with air. The radial position of the drop is described by the equation,

$$r_n(\theta) = R + A \cos(n\theta), \quad (4.14)$$

where A is set to $0.02R$ for all simulations, and n is the mode order (see [129, 5, 9, 130]). The initial condition for φ is set as:

$$\varphi_0(\mathbf{x}) = \tanh\left(\frac{r_n - |\mathbf{x}|}{\sqrt{2}\epsilon}\right), \quad \mathbf{x} \in \Omega. \quad (4.15a)$$

The boundary conditions are set as no-slip for the velocity. The effects of gravity are neglected, and the mobility is set as $M_3(\varphi)$, with $D = 10^{-2}$. The mesh considered has 512×512 linear quadrilateral elements, and a fixed time step size of $\Delta t = 1 \times 10^{-6}$ s is used.

Figure 4.4 shows the evolution of the oscillation amplitude for modes $n = 2, 3, 4$. The observed period matches very well with the analytical period,

$$\tau = \frac{2\pi}{\omega_n}, \quad (4.16)$$

where following [9],

$$\omega_n^2 = (n^3 - n) \frac{\gamma}{\rho R^3}, \quad (4.17)$$

A comparison of the numerical and analytical periods is given in Table 4.1.

Table 4.1: Small amplitude oscillations of a two-dimensional drop: Numerical and analytical periods.

n	τ [numerical]	τ [analytical (4.16)]
2	$4.190 \cdot 10^{-4}$	$4.192 \cdot 10^{-4}$
3	$2.110 \cdot 10^{-4}$	$2.096 \cdot 10^{-4}$
4	$1.350 \cdot 10^{-4}$	$1.326 \cdot 10^{-4}$

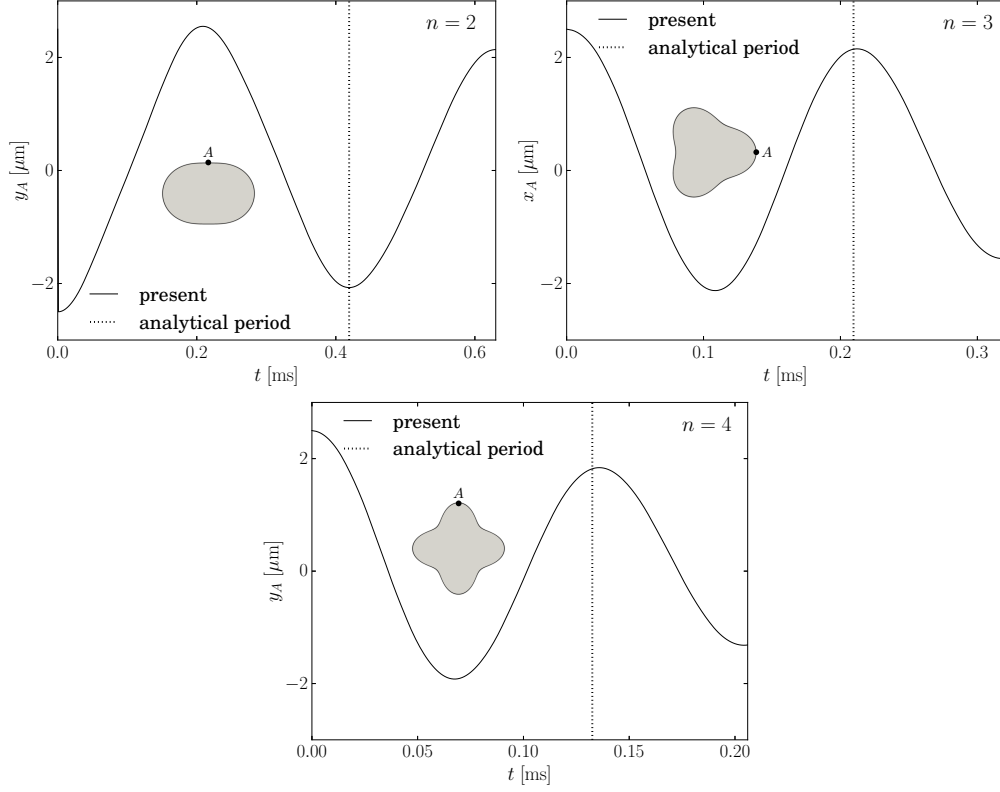


Figure 4.4: Small amplitude oscillations of a two-dimensional drop: Amplitude evolution for $n = 2, 3, 4$, with 512×512 linear elements.

4.3.3 Large amplitude oscillation of a two-dimensional drop

A two-dimensional drop is set up similarly to Subsection 4.3.2, with a larger initial amplitude $A = 0.2R$.

Figure 4.5 shows the evolution of the amplitude for the cases $n = 2, 3, 4$. It is clear that the periods observed in the present study slightly lag behind the analytical period. This is due to the larger amplitudes (compared to Subsection 4.3.2), which exceed the linear range and cause strongly nonlinear behaviour. Figure 4.6 shows the interface in terms of the isolines of φ at $\varphi = 0$. Figure 4.7 shows the velocity streamlines at different time instances. Notably the axes of symmetry for all three modes are clearly defined. Figure 4.8 shows the pressure distributions at different times within a single period of oscillation. Clearly the pressure variation in the air is minimal, and higher pressure concentrations are present in regions with more curvature, as expected from the Young-Laplace equation. The accurate conservation of the volumes of water and air are demonstrated in Figure 4.9 for $n = 4$, where the relative volume error is defined as $\epsilon(t_n) = (V_n - V_0)/V_0$. It is observed that for both air and water, the relative error does not exceed 0.015%.

4.3.4 Capillary rise

The capillary rise of fluid between two parallel plates is simulated. Figure 4.10 illustrates typical initial and final configurations of this problem. The column

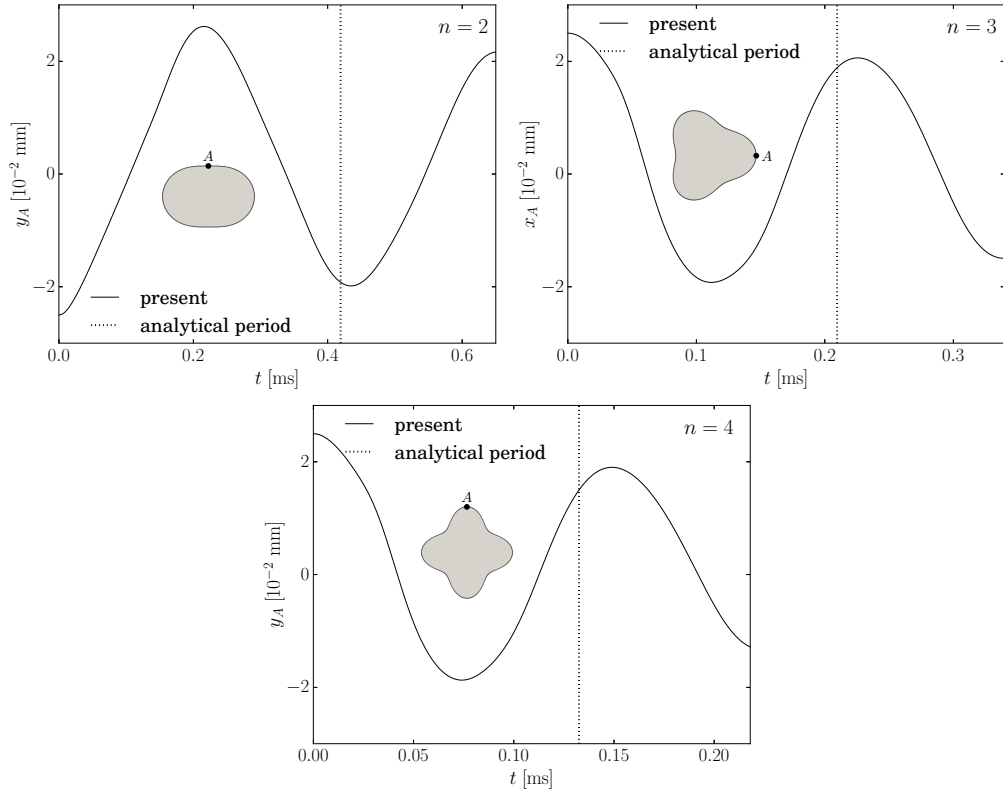


Figure 4.5: Large amplitude oscillation of a two-dimensional drop: Amplitude evolution for $n = 2, 3, 4$, with 512×512 linear elements.

height can accurately be approximated using Jurin's law [131]:

$$\Delta h = \frac{\gamma \cos \alpha}{\rho g R} \quad (2D), \quad (4.18)$$

$$\Delta h = \frac{2\gamma \cos \alpha}{\rho g R} \quad (\text{axisymmetric}), \quad (4.19)$$

where R is the pipe radius and α is the contact angle. The two-dimensional problem is described as follows: Two parallel plates at a distance $R = 1$ mm, are placed in the centre of a container filled with air, $\Omega = [0, 10] \times [0, 8]$ mm². The initial water level in the container is set to 4 mm, such that the initial condition for φ can be written as,

$$\varphi_0(x, y) = \tanh \left(\frac{4 \text{ mm} - y}{\sqrt{2}\epsilon} \right), \quad (x, y) \in \Omega. \quad (4.20a)$$

Slip velocity boundary conditions are applied on the vertical and upper boundaries, as well as on the tube walls, while a no-slip condition is considered for the lower boundary. The contact angle α is applied on the inner tube walls. The external air pressure is set to zero. A symmetry condition is applied on the left vertical wall. Two uniform meshes with linear quadrilateral elements are considered: a coarse mesh with 64×24 elements, and a fine mesh with 256×96 elements. Adaptive time stepping is used, with the initial time step size being $\Delta t = 0.001$.

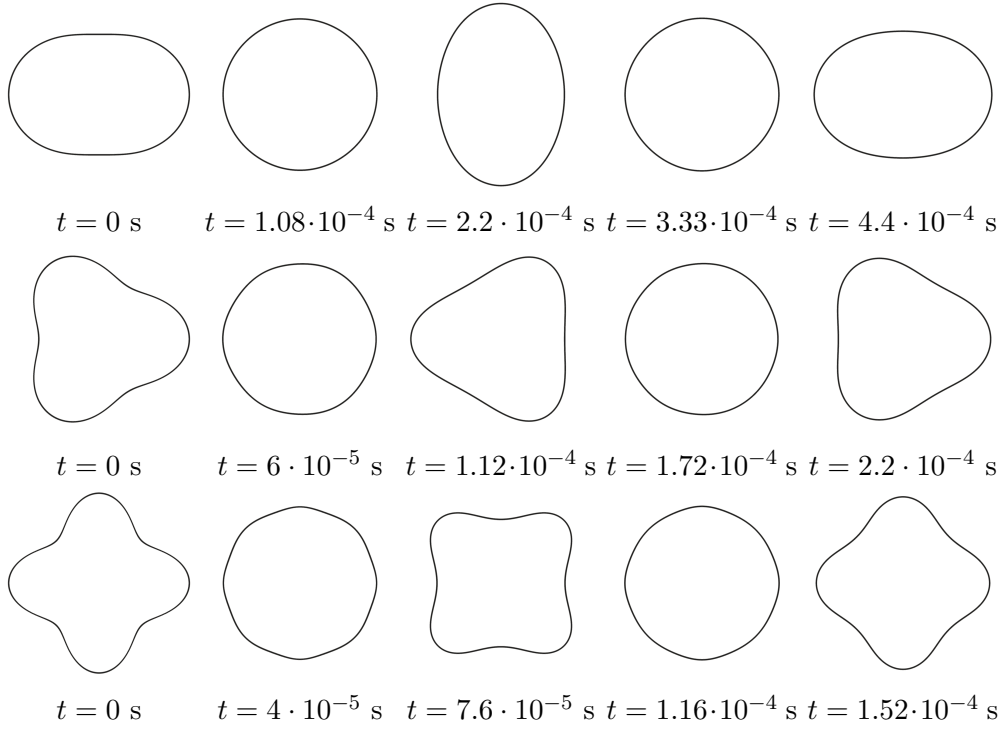


Figure 4.6: Large amplitude oscillation of a two-dimensional drop: Interface isolines for $n = 2, 3, 4$.

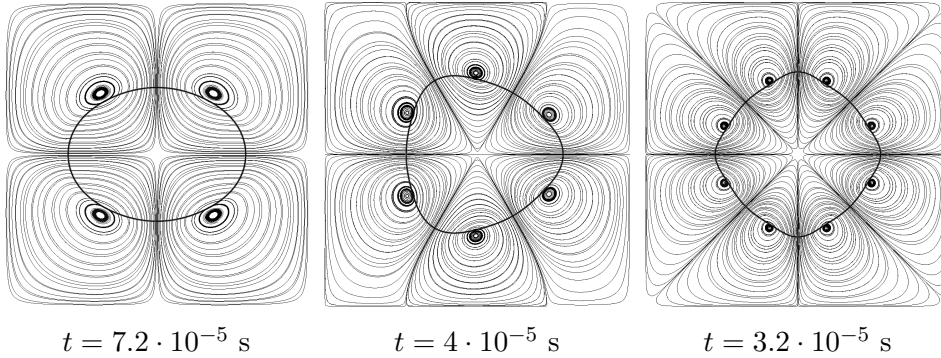


Figure 4.7: Large amplitude oscillations of a two-dimensional drop: Velocity streamlines at different time instances for $n = 2, 3, 4$

The simulations are allowed to develop until a steady state solution is reached. The recorded fluid levels Δh are shown with respect to various hydrophilic and hydrophobic contact angles in Figure 4.11. The numerical fluid levels are obtained as

$$\Delta h = \frac{1}{3} [\Delta h(0) + \Delta h(R/2) + \Delta h(R)]. \quad (4.21)$$

The fluid level heights are tabulated in Table 4.2. The equilibrium configurations are shown in Figure 4.12.

Three-dimensional analysis: The capillary rise in a circular pipe of radius R is also considered. Following Equation (4.19) it is expected that twice the fluid level

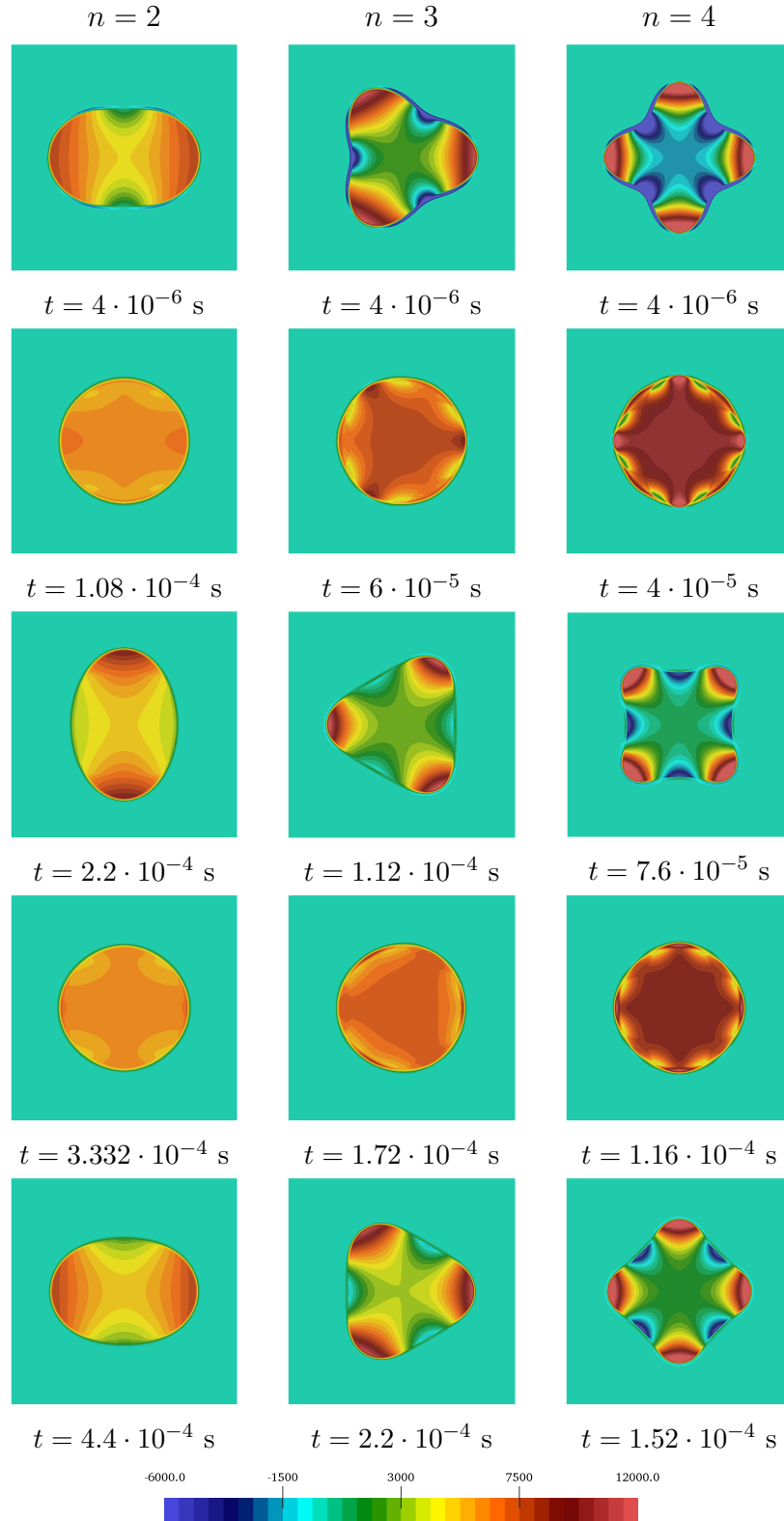


Figure 4.8: Large amplitude oscillation of a two-dimensional drop: Pressure contour plots.

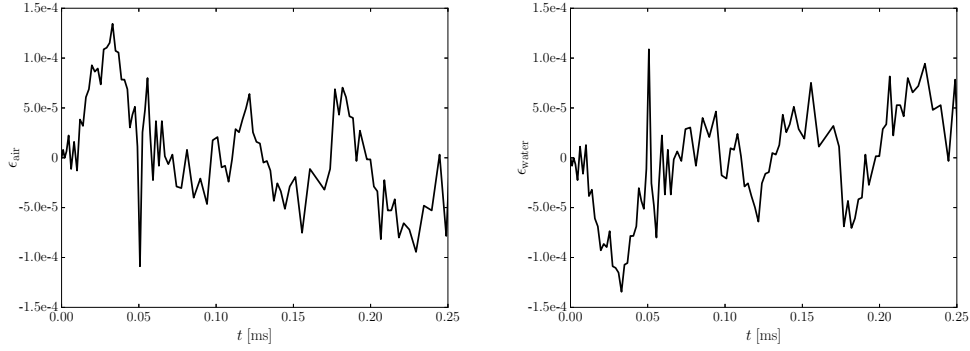


Figure 4.9: Large amplitude oscillation of a two-dimensional drop: Relative volume changes for air and water for $n = 4$.

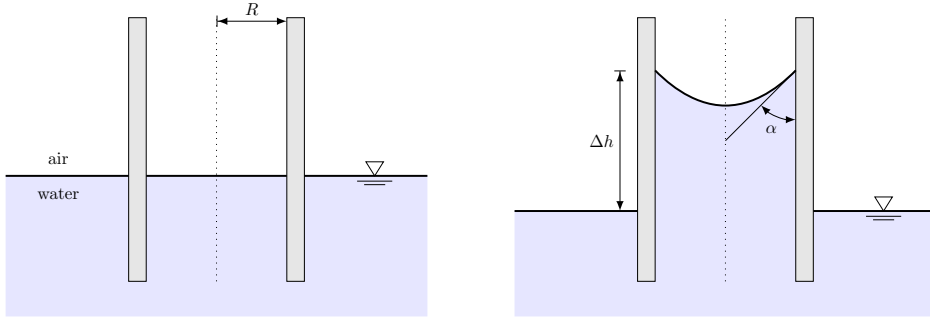


Figure 4.10: Capillary rise: Initial (left) and final (right) configurations.

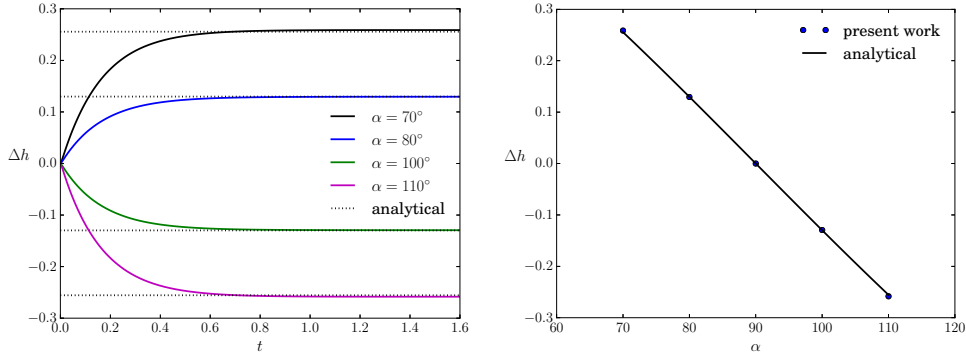


Figure 4.11: Capillary rise between two parallel plates: Fluid level evolution with respect to time (left) and contact angle (right) compared to Jurin's law, with 256×96 linear elements.

height is reached. The mesh consisting of 1,559,048 linear hexahedron elements is shown in Figure 4.13, where only the bottom half is shown. The steady state solutions to φ are shown in Figure 4.14 and Table 4.3 shows corresponding fluid levels for the present numerical solution and the analytical solution. Clearly, excellent correspondence between numerical and analytical results is observed in all comparisons.

Table 4.2: Capillary rise between two parallel plates: Fluid level heights.

α	Δh [coarse]	Δh [fine]	Δh [Jurin's law (4.18)]
70°	0.2587	0.2567	0.2553
80°	0.1295	0.1292	0.1296
100°	-0.1294	-0.1292	-0.1296
110°	-0.2583	-0.2567	-0.2553

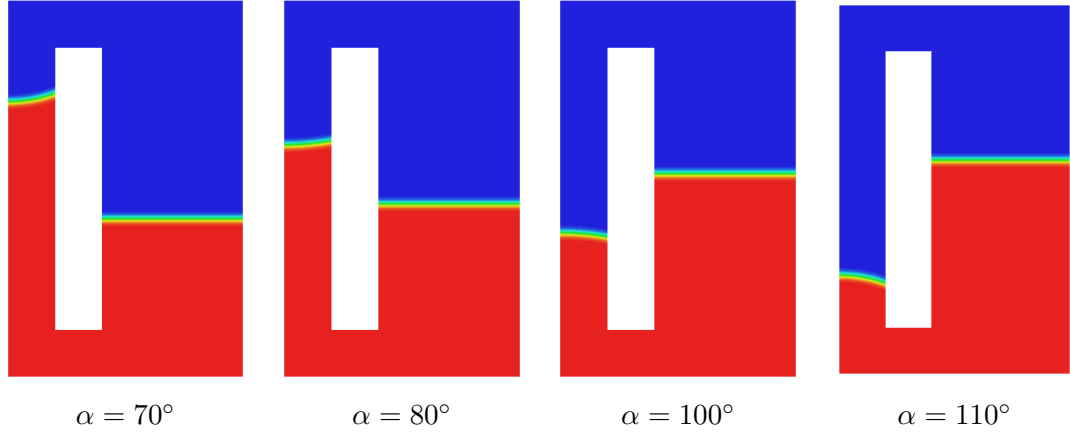
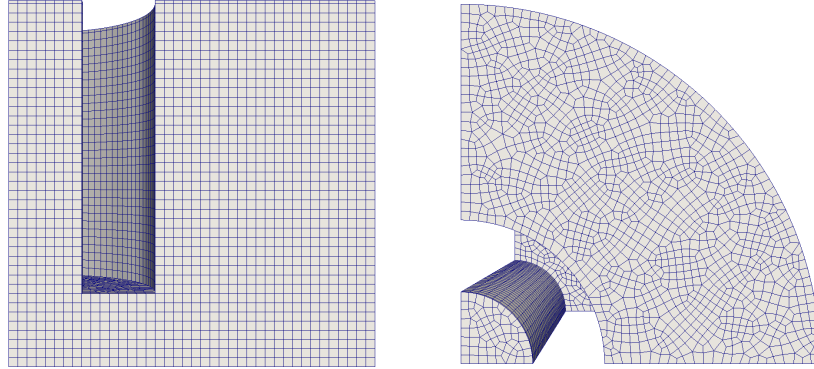
Figure 4.12: Capillary rise between two parallel plates: One half of the equilibrium configurations of φ for various contact angles, with 256×96 linear elements.

Figure 4.13: Capillary rise in a circular pipe: Slice through horizontal axis of finite element mesh with 1,559,048 linear elements.

Table 4.3: Capillary rise in a circular pipe: Fluid level heights.

α	Δh	Δh [Jurin's law (4.19)]
80°	0.2574	0.2595
100°	-0.2557	-0.2595

4.3.5 Sessile drop

A small water bubble in the presence of gravity is placed on a solid surface at the bottom of a rectangular domain filled with air, as shown in Figure 4.15. The

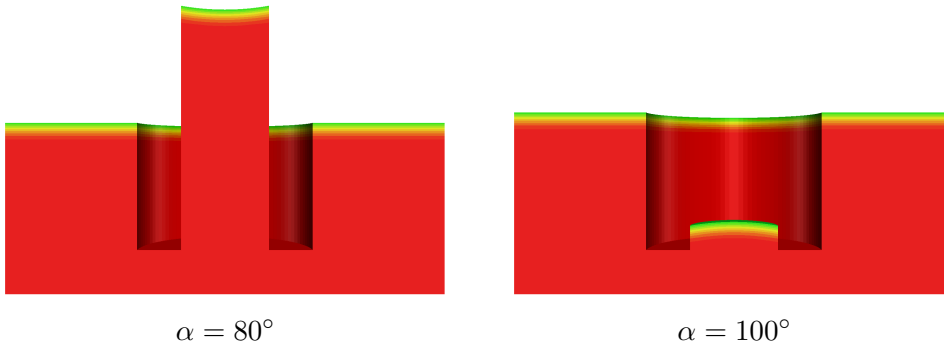


Figure 4.14: Capillary rise in a circular pipe: Equilibrium configurations of φ , the part of the domain filled with air is not shown.

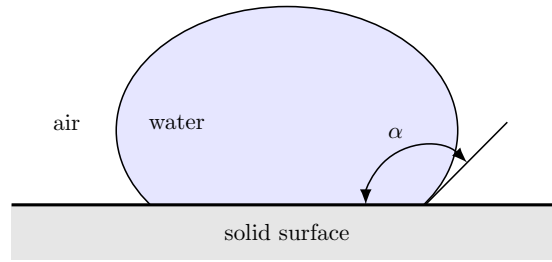


Figure 4.15: Sessile drops: Geometry.

rectangular domain is of dimensions $\Omega = [0, 1.5] \times [0, 0.5]$ cm², and the drop of radius is $R = 0.25$ cm is situated at the position $\mathbf{C} = [0.75, 0]$. The initial condition for φ is set as:

$$\varphi_0(\mathbf{x}) = \tanh\left(\frac{R - |\mathbf{x} - \mathbf{C}|}{\sqrt{2}\epsilon}\right), \quad \mathbf{x} \in \Omega. \quad (4.22a)$$

Slip boundary conditions are applied at the lower boundary. In order to reduce dynamic effects and accelerate the computation of the equilibrium configuration, the viscosities are multiplied by a factor of 100. A uniform mesh with 192×64 linear quadrilateral elements is used. Adaptive time stepping is used, with an initial time step size of $\Delta t = 0.001$.

The final configurations of the two-dimensional drops subject to various contact angles are shown in Figure 4.16. In Figure 4.17, the results are compared to the exact equilibrium configuration obtained by numerically solving a set of ordinary differential equations [132].

Three-dimensional analysis: The problem is extended to three dimensions, with $\Omega = [0, 1.5] \times [0, 0.5] \times [0, 1.5]$. The mesh is constructed uniformly with $96 \times 32 \times 96$ linear hexahedron elements. Figures 4.18 and 4.19 show the results obtained for the three-dimensional case. A very good match is observable for both two and three-dimensional cases.

4.3.6 Pendant drop

In this example a small water drop is suspended on the upper surface of a square domain $\Omega = [0, 0.6] \times [0, 0.6]$ cm² filled with air. The problem setup is identical

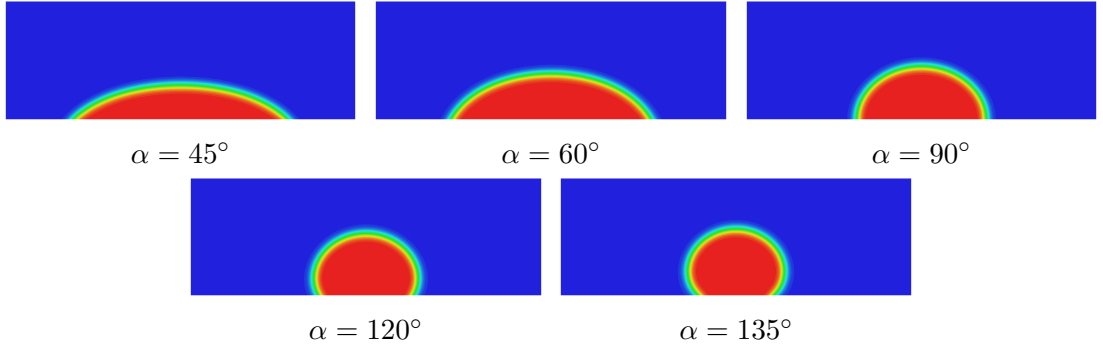


Figure 4.16: Sessile drop in two dimensions: Equilibrium configuration of φ using 192×64 linear elements.

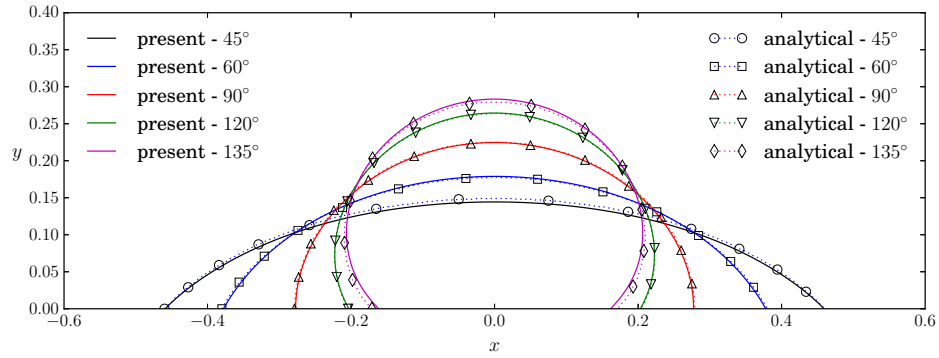


Figure 4.17: Sessile drop in two dimensions: Comparison of numerical results with the analytical solution given by Pozrikidis [132], using 96×64 linear elements.

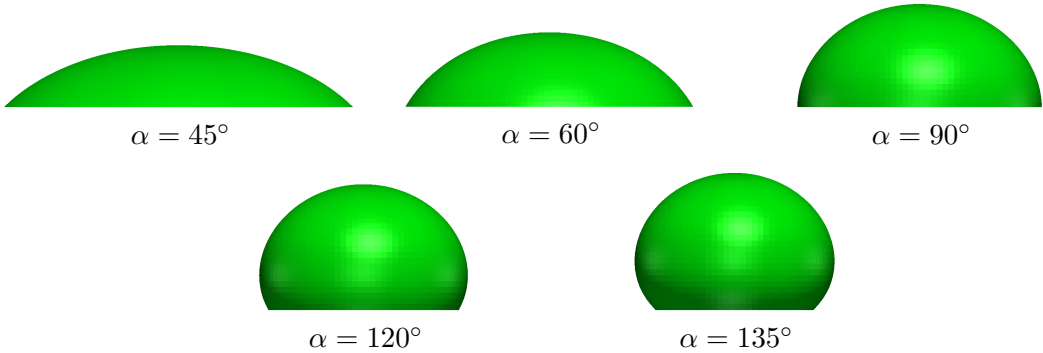


Figure 4.18: Sessile drop: Steady state φ solution for a small three-dimensional sessile drops with various contact angles, using $96 \times 32 \times 96$ linear elements.

to Subsection 4.3.5, with the exception of the position of the drop, which is now $\mathbf{C} = [0.3, 0.6]$. The final configurations of the two-dimensional drops subject to various contact angles are shown in Figure 4.20. A comparison of various contact angles to the solution presented in [132] is shown in Figure 4.21. Clearly there is a very good match between the analytical and numerical solutions.

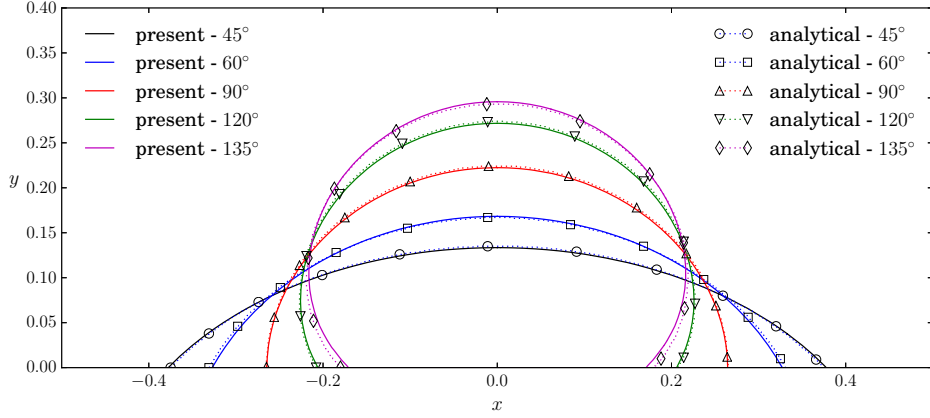


Figure 4.19: Sessile drop: Comparison of a small three-dimensional sessile drops with various contact angles to the analytical solution given by Pozrikidis [132], using $96 \times 32 \times 96$ linear elements.

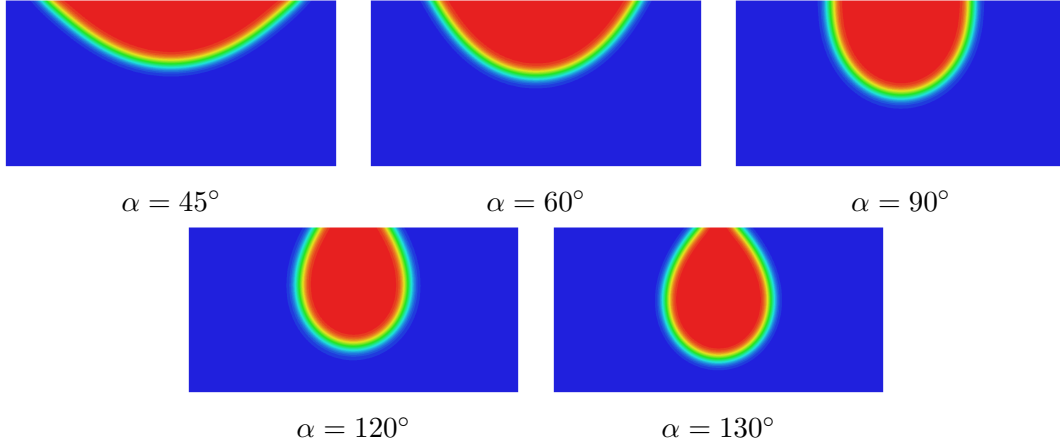


Figure 4.20: Pendant drop: Steady state φ solution for small two-dimensional pendant drops with various contact angles, using 128×64 linear elements.

4.3.7 Rising bubble

In this example a bubble of radius $R = 0.25$ consisting of a light fluid is placed at position $\mathbf{C} = [0.5, 0.5]$ of a rectangular domain $\Omega = [0, 1] \times [0, 2]$ which is filled with a heavier fluid. The parameters are set as given in [114], with the heavier fluid properties $\rho = 1000$, $\mu = 10$, and the lighter bubble properties $\rho = 1$, $\mu = 1$. The surface tension parameter and the acceleration vector are set, respectively, to $\gamma = 1.96$ and $b = [0, -0.98]^T$. The initial condition for φ is set as,

$$\varphi_0(\mathbf{x}) = \tanh\left(\frac{R - |\mathbf{x} - \mathbf{C}|}{\sqrt{2}\epsilon}\right), \quad \mathbf{x} \in \Omega. \quad (4.23)$$

The boundaries are set up such that the fluids are allowed to slip along the left and right boundaries, but not along the top and bottom boundaries. The mesh consists of 128×256 linear elements, and a fixed time step size of $\Delta t = 0.01$ is used.

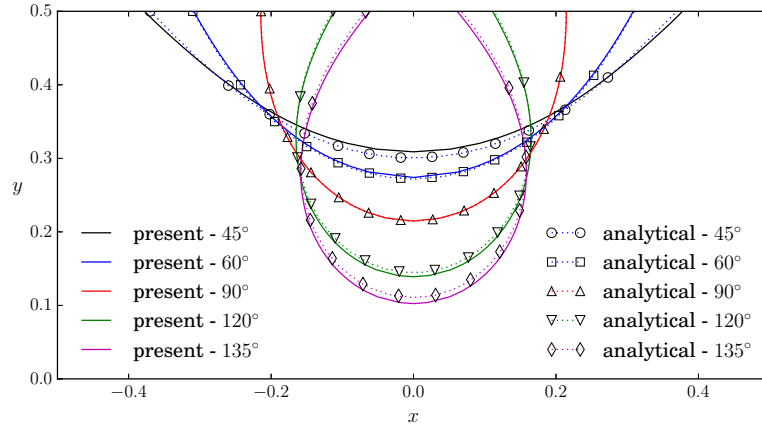


Figure 4.21: Pendant drop: Comparison of small two-dimensional pendant drops with different contact angles to the analytical solution given by Pozrikidis [132], using 128×64 linear elements.

It is expected that due to the large density difference, there would be an overpowering body force contribution acting on either side of the interface in comparison to the rather negligible surface tension forces. Thus the bubble would experience large deformations characterised by long and narrow filaments at the edges. This behaviour is observable in Figure 4.22, where the solution to φ is shown at different time instances. The observations match well with those made in [114].

4.3.8 Faucet leak in two dimensions

In this example we consider a *leaky faucet* problem, which consists of water dripping from a faucet into a pool of water at the bottom of a rectangular box filled with air, as shown in Figure 4.23. The dimensions of the box are $[0, 2] \times [0, 4.5]$ cm², the height of the pool is $H = 0.4$ cm, and the radius of the faucet is $R = 0.26$ cm.

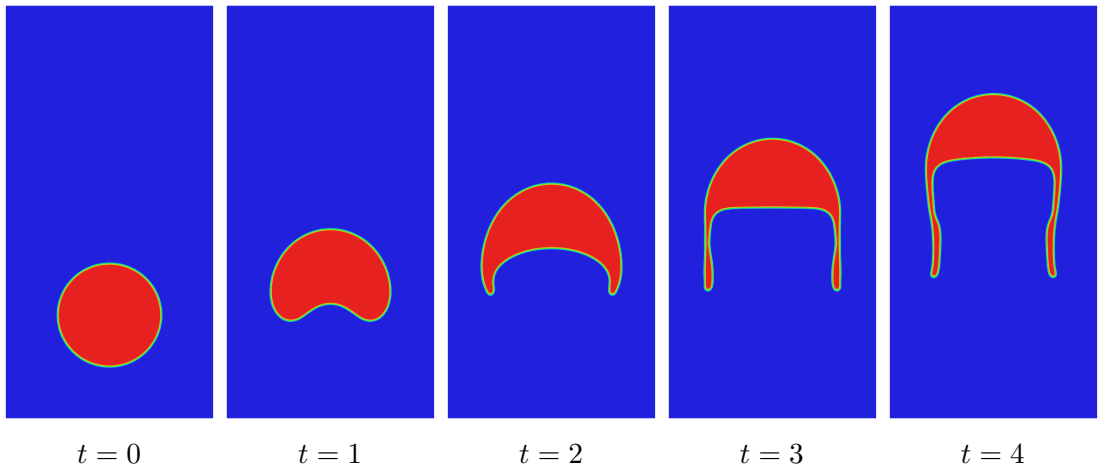


Figure 4.22: Rising bubble: φ evolution using 128×256 linear elements.

The simulations are run with filling velocities \mathbf{u}_{fill} set as 0.33546, 10 and 20 cm s⁻¹, which are set uniformly at the inlet. The initial condition for φ is set as,

$$\varphi_0(x, y) = \begin{cases} \tanh\left(\frac{0.4 \text{ cm} - y}{\sqrt{2}\epsilon}\right), & \text{for } y < 1 \text{ cm}, \\ \tanh\left(\frac{y - 4.13 \text{ cm}}{\sqrt{2}\epsilon}\right), & \text{for } x < 0.36 \text{ cm}, \end{cases} \quad (4.24)$$

where $(x, y) \in \Omega$. At the beginning of the simulation the faucet is completely closed, after which the inlet velocity is ramped smoothly up to the filling velocity with the function $\frac{1}{2}(1 - \cos(\pi \min(t/T, 1)))$, where $T = 0.01$ s. A uniform mesh comprising of 35,712 linear elements is considered in all simulations. Adaptive time stepping is used, with an initial time step size of $\Delta t = 0.0001$. The mobility is set as M_0 with $D = 0.5$ cm s⁻². Slip boundary conditions are applied on all surfaces.

The evolution of φ is shown in Figure 4.25, illustrating the ability of the described formulation to deal with highly complex physical problems resulting in significant topology changes. It is noted that small filling velocities lead to the development of non-physical flows in the air domain that originate from the tip of the drop. This phenomenon is likely to be triggered by the combination of the massively different values of density and viscosity of water and air with an imbalance of the selected mobility, interface thickness, mesh density and relatively large time domain of interest.

4.3.9 Faucet leak in three dimensions

A three-dimensional faucet leak is now considered with a similar setup to Subsection 4.3.8. In this analysis the drop break-off is particularly of interest, thus the domain size is reduced to $[0, 2 \text{ cm}] \times [0, 3 \text{ cm}]$, and the pool at the bottom has

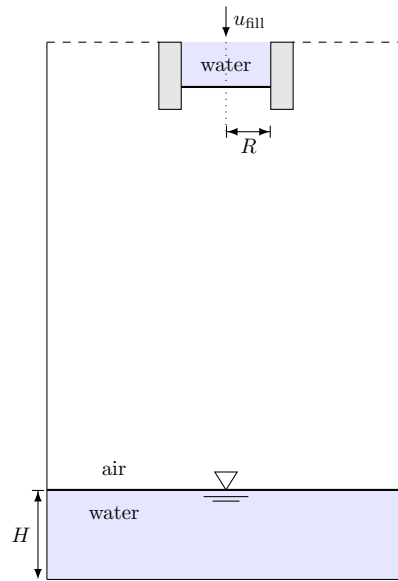


Figure 4.23: Filling drop in two dimensions: Geometry.

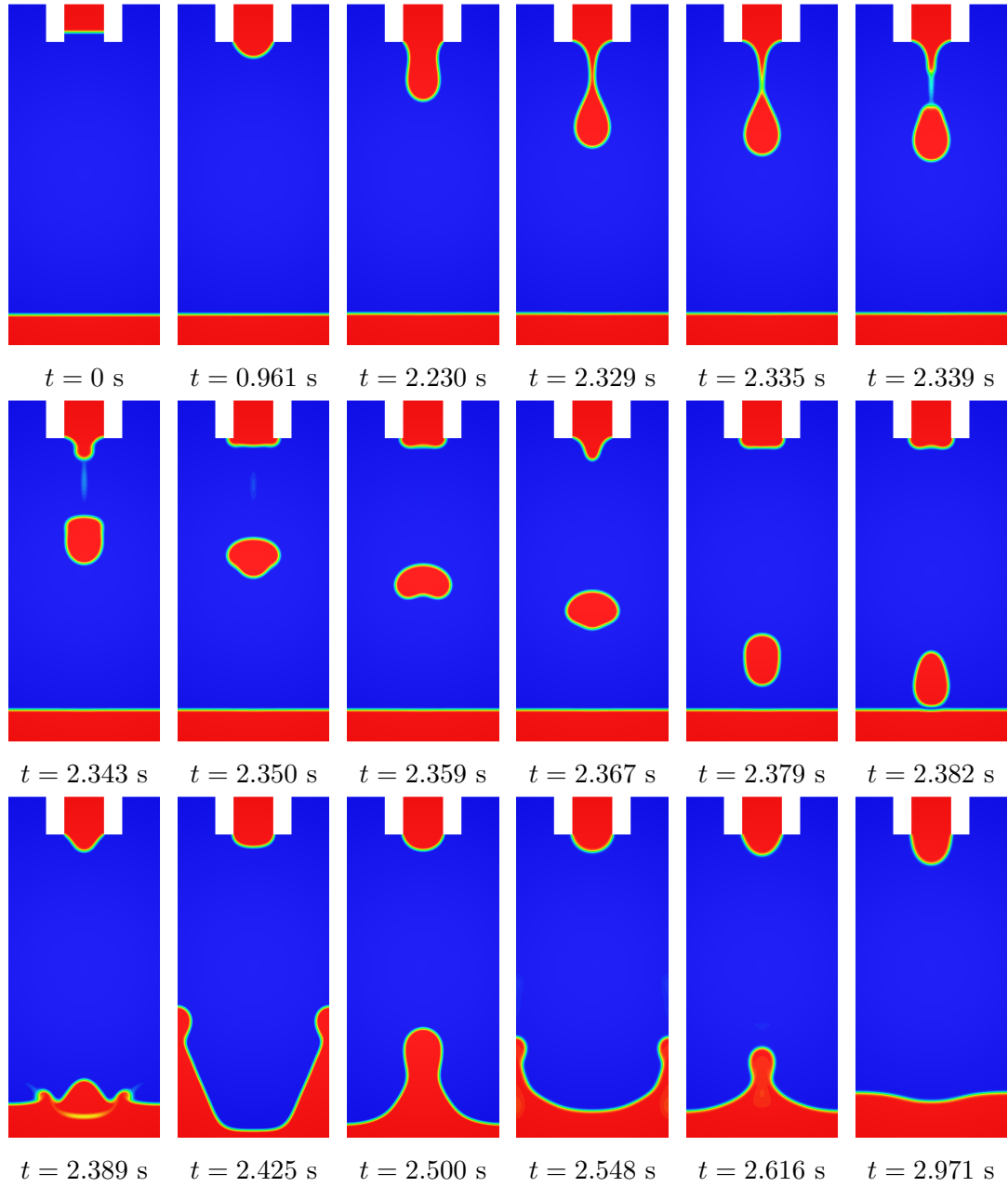


Figure 4.24: Faucet leak in two dimensions: Evolution of φ with $\mathbf{u}_{\text{fill}} = 0.33546 \text{ cm s}^{-1}$, using 35,712 linear elements.

been removed. A 15° wedge is considered due to the symmetry of the problem, as shown in Figure 4.27, which consists of 1,004,665 linear tetrahedron elements. Adaptive time stepping is used, with an initial time step size of $\Delta t = 0.0001$. The same filling velocities used in Subsection 4.3.8 are considered.

The evolution of φ is shown in Figure 4.29. A visual comparison of the drop configuration at different time instances is made with Dettmer and Perić [5] in Figure 4.32. It is clear for all three velocity cases that there is a close match with [5] at all stages in the drop formation. The vertical velocity component during break-off is visible in Figure 4.34. In Figure 4.35, the tip position evolution

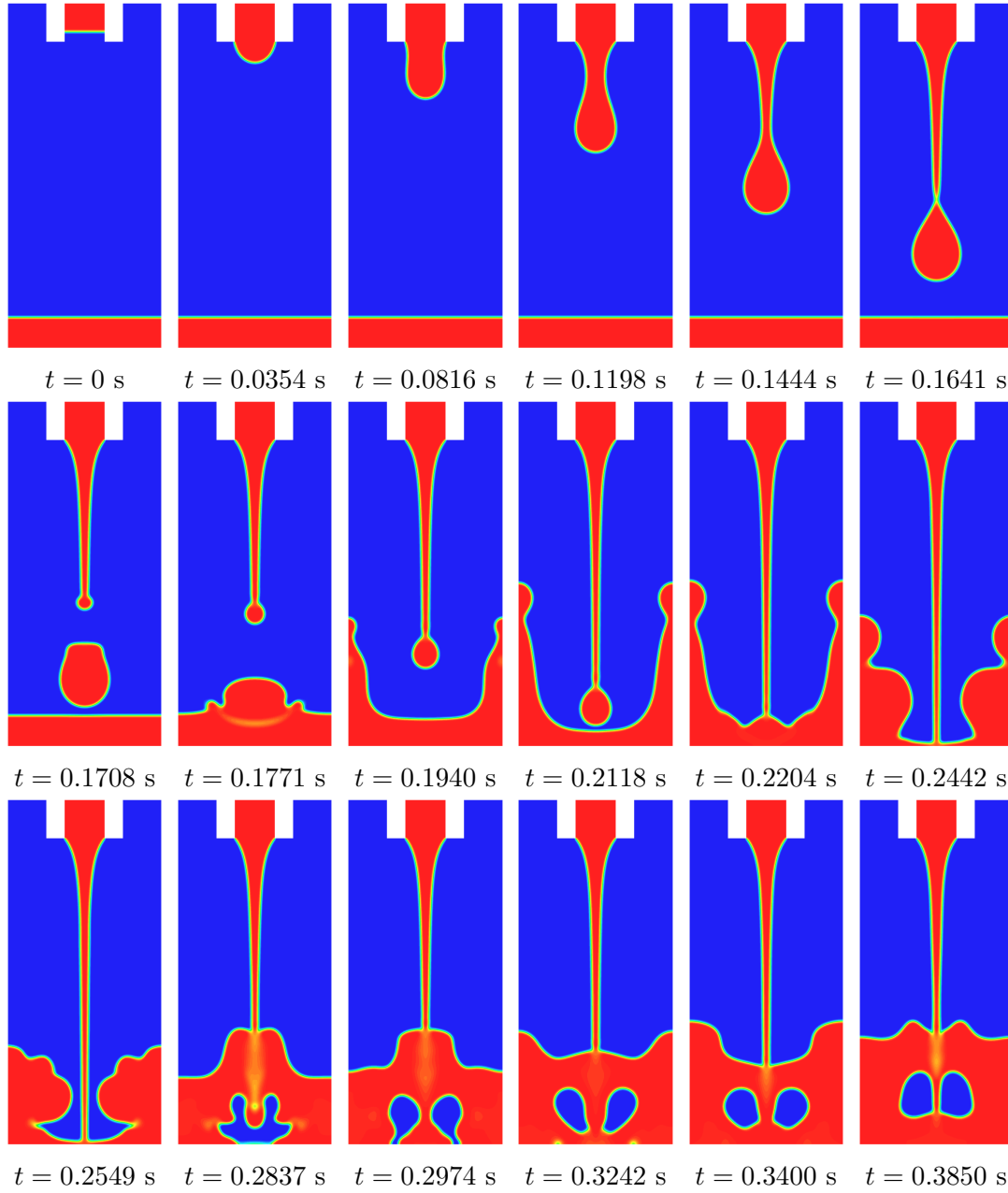


Figure 4.25: Faucet leak in two dimensions: Evolution of φ with $\mathbf{u}_{\text{fill}} = 10 \text{ cm s}^{-1}$, using 35,712 linear elements.

compared with [5] is shown along with the water the volume evolution. Unlike in the present study, the initial configuration in [5] is set as an equilibrium pendant drop, thus these results are shifted in time to the appropriate position. It is observable that the tip position evolution matches well with [5].

4.3.10 Broken dam

A fluid column ($\rho = 1$, $\mu = 0.01$) of width $b = 3.5$ and height $h = 7$ is placed in a rectangular domain ($\rho = 0.001$, $\mu = 0.0001$) of dimensions $[0, 15] \times [0, 10]$. The

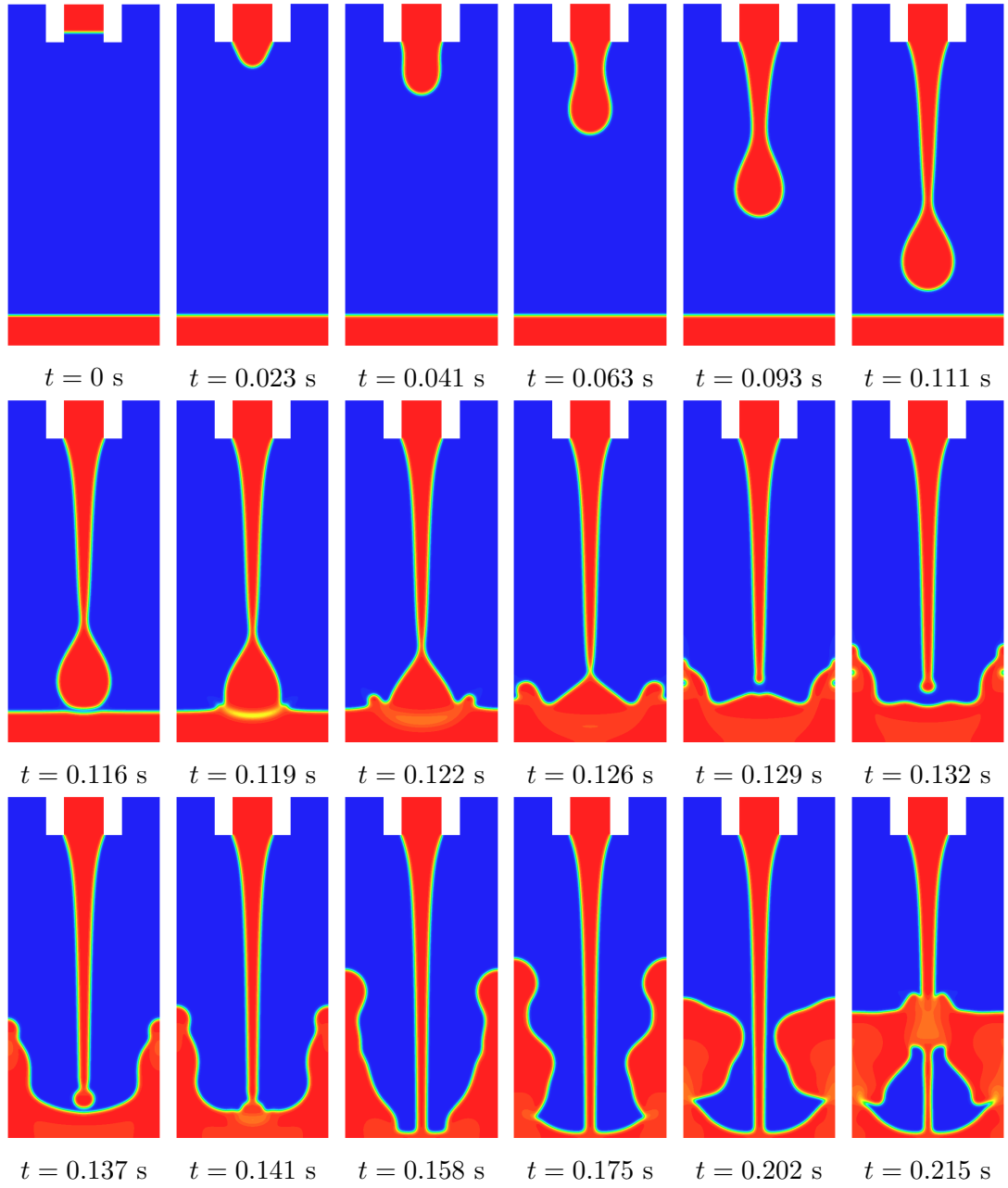


Figure 4.26: Faucet leak in two dimensions: Evolution of φ with $\mathbf{u}_{\text{fill}} = 20 \text{ cm s}^{-1}$, using 35,712 linear elements.

initial condition for φ is set as:

$$\varphi_0(x, y) = \begin{cases} \tanh\left(\frac{h-y}{\sqrt{2}\epsilon}\right), & \text{for } x \leq b-r, y \geq h-r, \\ \tanh\left(\frac{b-x}{\sqrt{2}\epsilon}\right), & \text{for } x \geq b-r, y \leq h-r, \\ \tanh\left(\frac{r-d(x, y)}{\sqrt{2}\epsilon}\right), & \text{for } x > b-r, y > h-r, \end{cases} \quad (4.25)$$

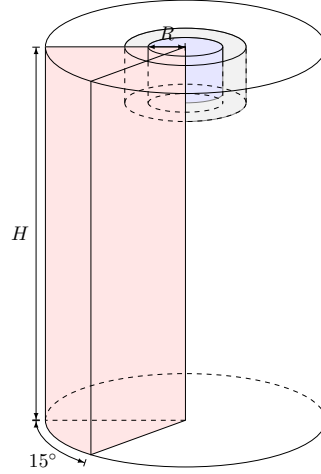


Figure 4.27: Faucet leak in three dimensions: Geometry with 15° wedge.

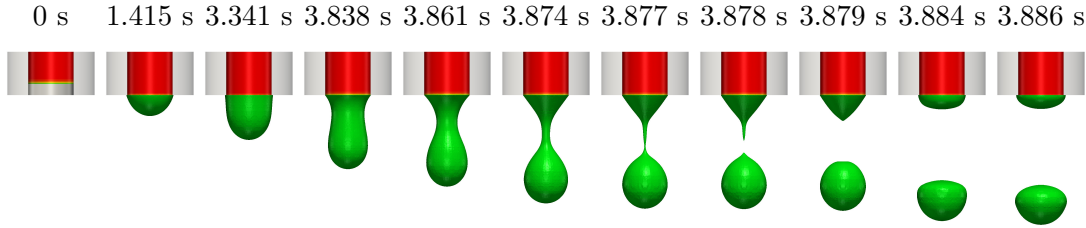


Figure 4.28: Faucet leak in three dimensions: Evolution of φ for $u_{\text{fill}} = 0.33546 \text{ cm s}^{-1}$, with 1,004,665 linear elements.

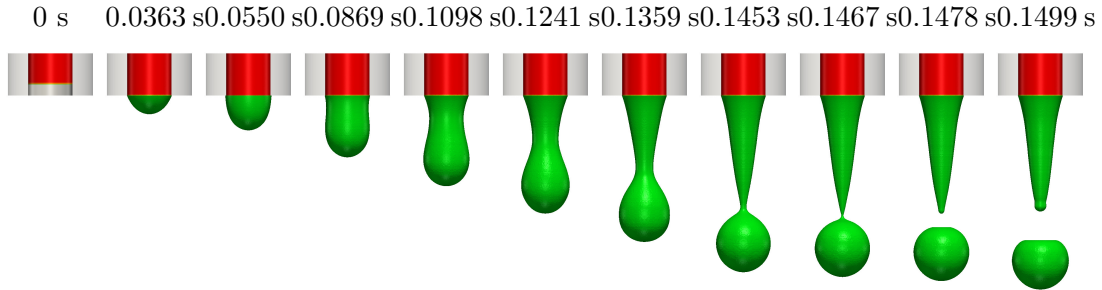


Figure 4.29: Faucet leak in three dimensions: Evolution of φ for $u_{\text{fill}} = 10 \text{ cm s}^{-1}$, with 1,004,665 linear elements.

where $r = 0.5$ is the column corner radius, $d(x, y)$ is the Euclidean distance from the point $[b - r, h - r]$, and $(x, y) \in \Omega$. The gravitational acceleration is set by using $\mathbf{b} = [0, -1]^T$, and the surface tension coefficient is set to zero, *i.e.* $\gamma = 0$. The fluid is allowed to slip on the horizontal and vertical surfaces, and is allowed to adopt any contact angle by replacing the boundary terms in Equations (4.9d) and (4.10d), such that the terms become

$$\int_{\Omega} s^h (\eta^h - f) - \nabla s^h \cdot \epsilon^2 \nabla \varphi^h \, d\Omega - \int_{\Gamma} s^h \epsilon^2 \nabla \varphi^h \cdot \mathbf{n} \, d\Gamma = 0. \quad (4.26)$$

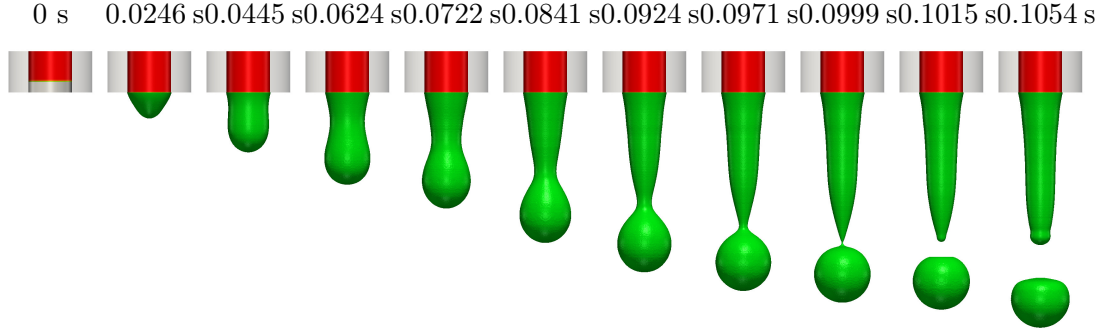


Figure 4.30: Faucet leak in three dimensions: Evolution of φ for $u_{\text{fill}} = 20 \text{ cm s}^{-1}$, with 1,004,665 linear elements.

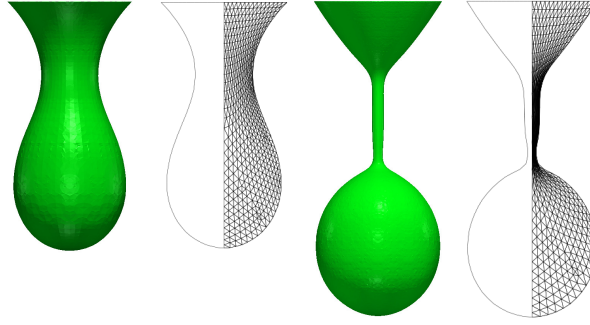


Figure 4.31: Faucet leak in three dimensions: Comparison of interface isolines with [5] for $u_{\text{fill}} = 0.33546 \text{ cm s}^{-1}$.

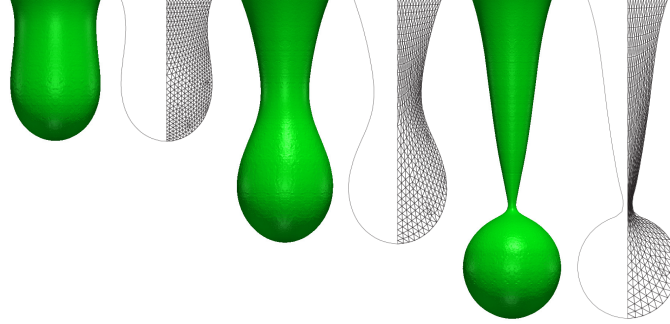


Figure 4.32: Faucet leak in three dimensions: Comparison of interface isolines with [5] for $u_{\text{fill}} = 10 \text{ cm s}^{-1}$.

The mesh consists of 192×128 uniform linear quadrilateral elements, and the time step size is set fixed as $\Delta t = 0.01$.

The geometry of the problem and the tip displacement evolution are shown in Figure 4.37. The tip displacement evolutions agrees well with experimental results taken from [7]. The evolution of φ is shown at several time instances in Figure 4.38.

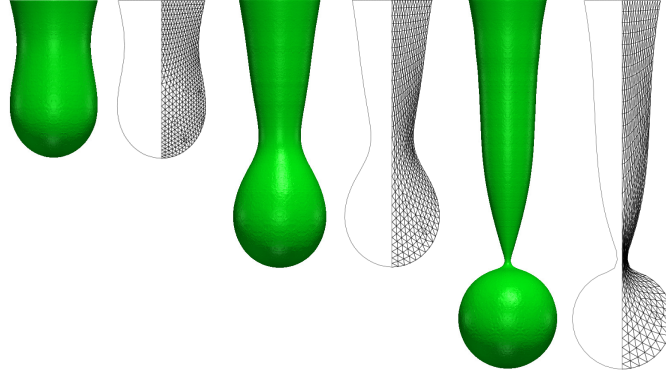


Figure 4.33: Faucet leak in three dimensions: Comparison of interface isolines with [5] for $u_{\text{fill}} = 20 \text{ cm s}^{-1}$.

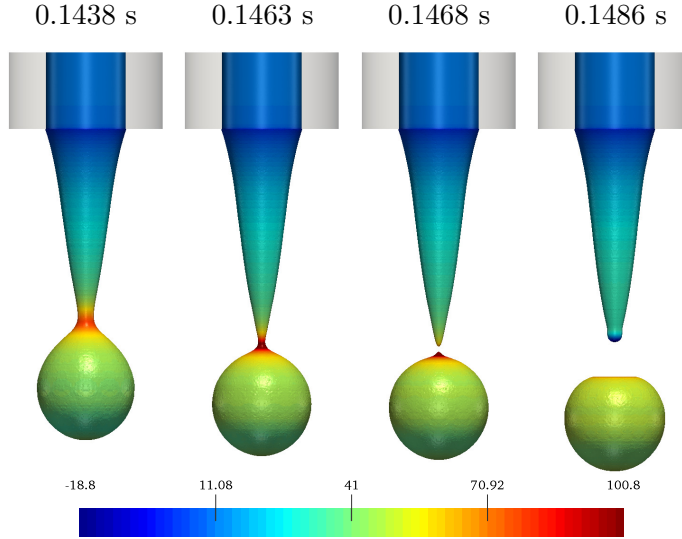


Figure 4.34: Faucet leak in three dimensions: Evolution of vertical velocity for $u_{\text{fill}} = 10 \text{ cm s}^{-1}$, using 1,004,665 linear elements.

4.3.11 Sloshing tank

Following [5], a sloshing tank of size $\Omega = [0, 1] \times [0, 1.2]$ is set up with the following parameters $\rho_1 = 1$, $\rho_2 = 0.001$, $\mu_1 = 0.01$, $\mu_2 = 0.0001$, $\mathbf{b} = [0, -1]^T$. The surface tension effects are neglected. The initial condition for φ is set as:

$$\varphi_0(x, y) = \tanh\left(\frac{y - 1 - 0.01 \cos(\pi x)}{\sqrt{2}\epsilon}\right), \quad (x, y) \in \Omega. \quad (4.27)$$

Slip boundary conditions are applied to the vertical walls, while no-slip is considered for the lower boundary. The fluid at the edges is allowed to freely adopt any contact angle by using Equation (4.26). A uniform mesh with 48,000 linear quadrilateral elements is selected, and a fixed time step size of $\Delta t = 0.1$ is chosen.

Figure 4.39 shows that the frequency at the left and right edges agrees excellently with [5].

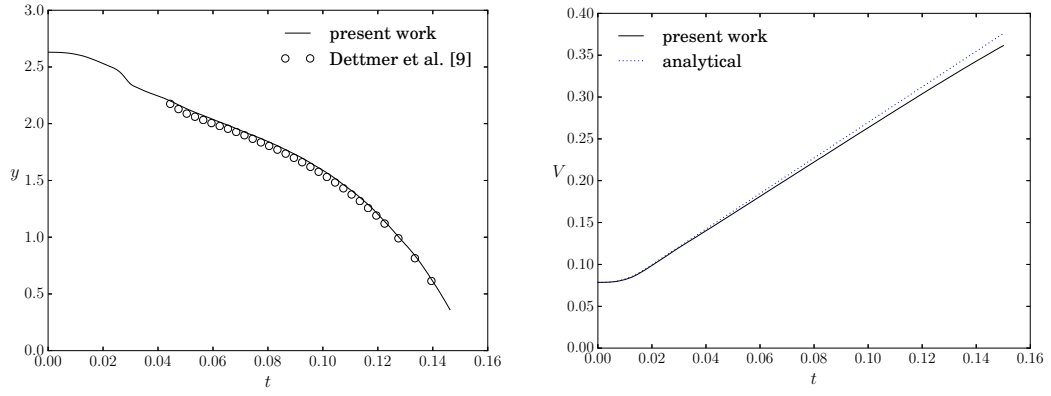


Figure 4.35: Faucet leak in three dimensions: Tip position comparison with [5] (left), and water volume evolution comparison with analytical solution (right) for $\mathbf{u}_{\text{fill}} = 10 \text{ cm s}^{-1}$.

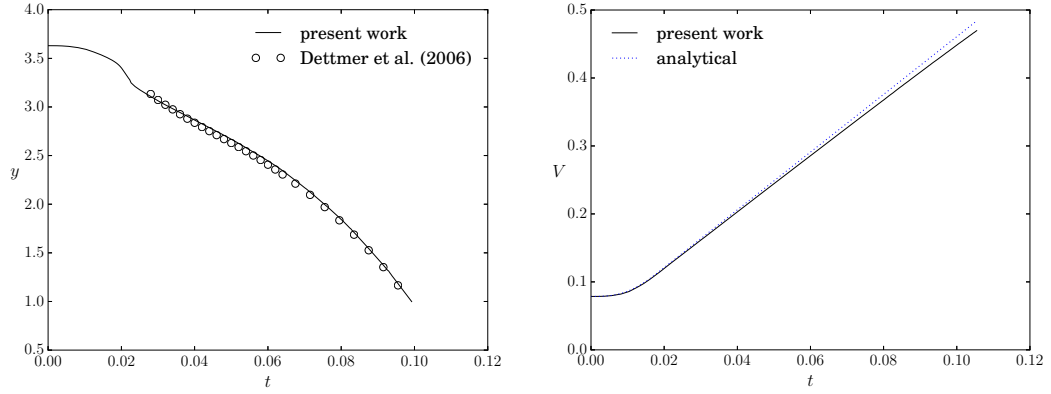


Figure 4.36: Faucet leak in three dimensions: Tip position comparison with [5] (left), and water volume evolution comparison with analytical solution (right) for $\mathbf{u}_{\text{fill}} = 20 \text{ cm s}^{-1}$.

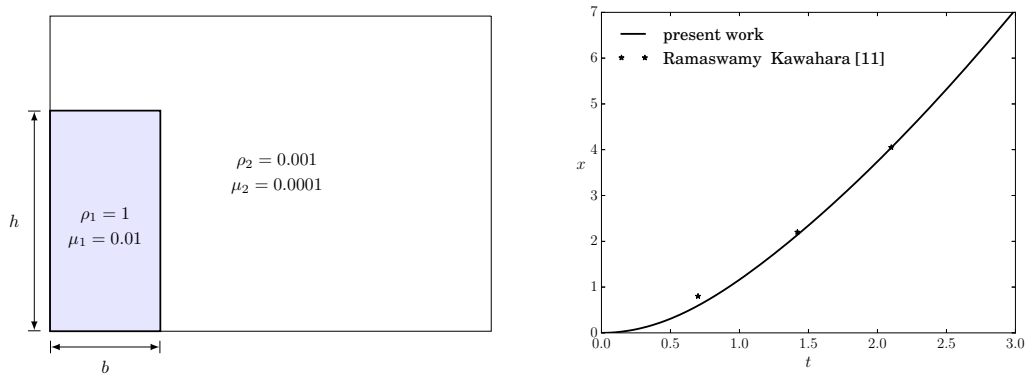


Figure 4.37: Broken dam: Geometry (left) and evolution of tip displacement (right).

4.3.12 Rayleigh-Taylor instability

The Rayleigh-Taylor instability problem described in [114] is considered. The conventional Rayleigh-Taylor problem consists of a fluid A sitting on top of a

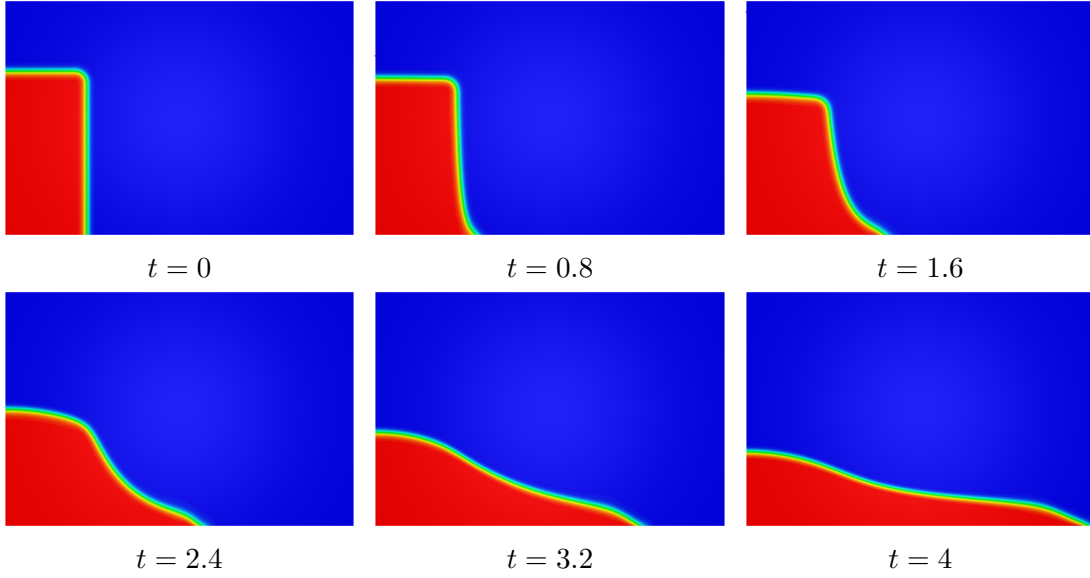


Figure 4.38: Broken dam: φ evolution using 192×128 elements.

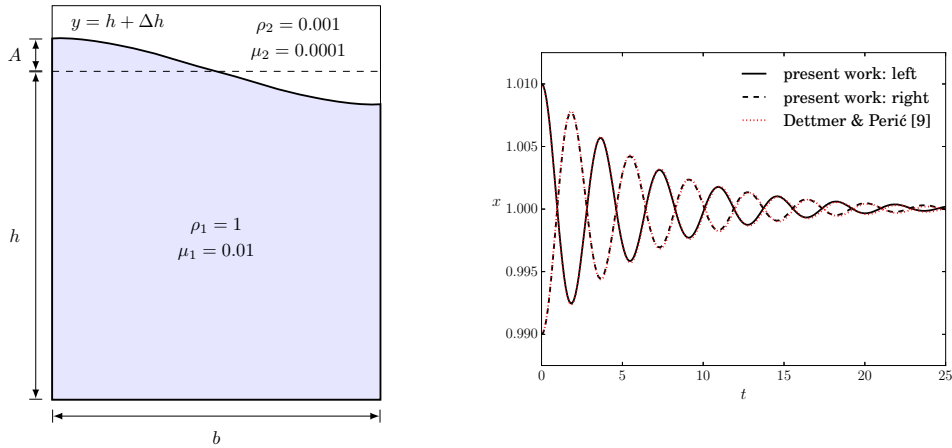


Figure 4.39: Sloshing tank: Geometry (left) and amplitude frequency (right), with 48,000 linear quadrilateral elements.

less dense fluid B . Any perturbation between the fluid layers in combination with gravitational force, will cause fluid A to drive into fluid B resulting in the well known mushroom cloud effect synonymous with Rayleigh-Taylor instability. A domain of size $[0, 1] \times [0, 4]$ is considered with the higher density fluid having $\rho_1 = 3$ and $\mu_1 = 0.0031316$, and the lower density fluid having $\rho_2 = 1$, $\mu_2 = 0.0031316$. The gravitational acceleration is taken as $g = 9.80665$. The initial condition for φ is given by

$$\varphi_0(x, y) = \tanh \left(\frac{y - 2 - 0.1 \cos(2\pi x)}{\sqrt{2}\epsilon} \right), \quad (x, y) \in \Omega. \quad (4.28)$$

The upper and lower boundaries are set to no-slip, and the left and right boundaries are set to slip conditions. In concurrence with [114], the other parameters are chosen as follows: $\gamma = 0.01$, $\epsilon = 0.005$, $\alpha = \pi/2$. The mobility function is chosen as

$M_2(\varphi)$ with $D = 4 \cdot 10^{-5}$. Two meshes are compared, a mesh with 256×1024 linear stabilised elements and a mesh with 128×512 mixed Taylor-Hood elements. For comparison we consider the results from Guermond and Quartapelle [133] where surface tension effects are ignored. It should be mentioned that in [114], the author states that the surface tension coefficient is set as small but not zero, in order to avoid the CH equation becoming a pure transport equation, since setting $\gamma = 0$ would render $\eta = 0$ in the conventional formulation. In this work, we consider $\gamma = 0.01$ with the conventional Abels et al. formulation [14], as well as $\gamma = 0$ with the formulation presented in Section 4.2. For the latter formulation the mobility coefficient is increased to $D = 10^{-3}$, since it is no longer necessary to set it so small. The evolution of φ is shown in Figure 4.40. Figure 4.41 shows the position along the vertical axis of the rising and falling interface tips for the stabilised and mixed formulations. The time scaling of the reference solution [133] required mapping according to $t = \sqrt{2/g} \hat{t}$ to account for the non-dimensionality of the variables. The results for the stabilised and mixed formulations are in agreement with the reference, and nearly indistinguishable from each other. Observing the plot corresponding to $\gamma = 0$, it appears that neglecting surface tension effects does not really alter the displacements observed, although it does confirm that γ can be set to zero without encountering numerical problems.

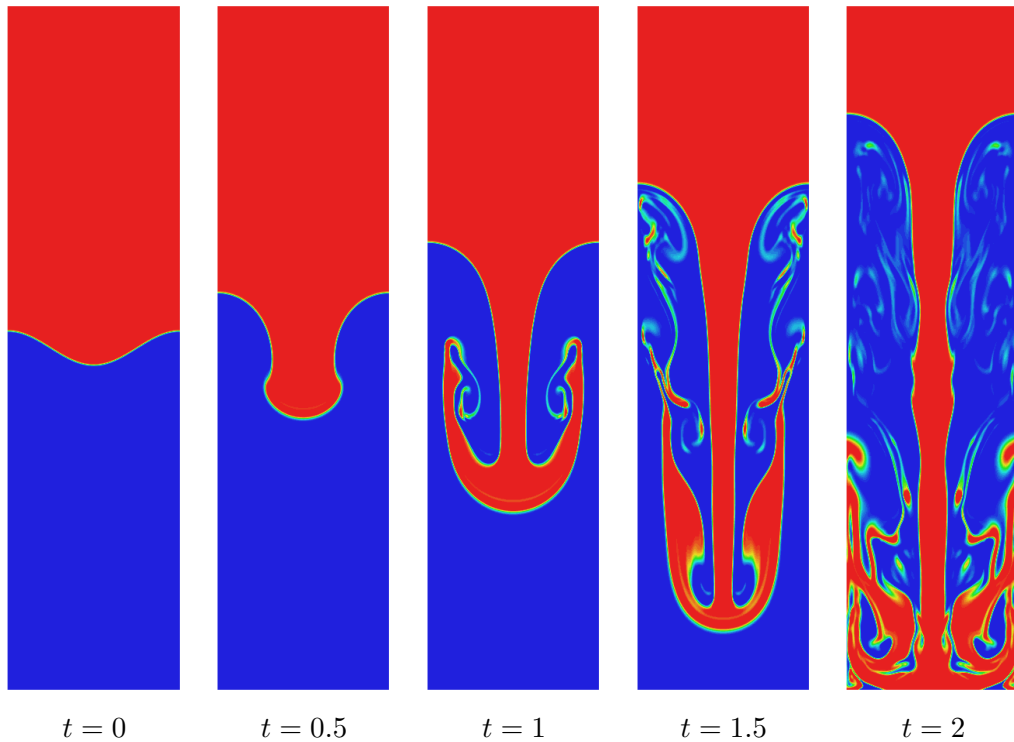


Figure 4.40: Rayleigh-Taylor instability: Evolution of phase field variable φ , with 256×1024 linear elements.

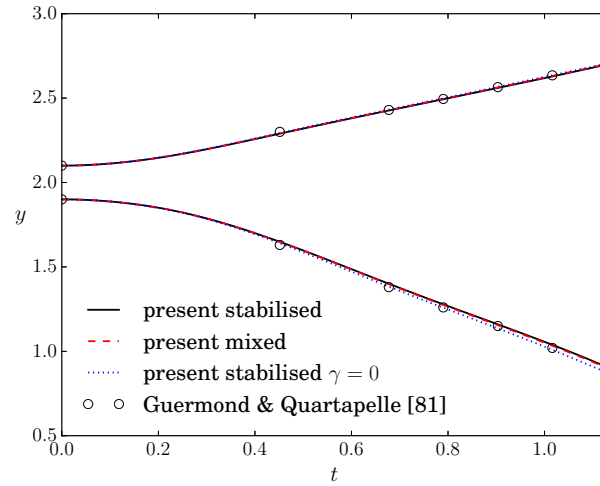


Figure 4.41: Rayleigh-Taylor instability: y position of interface at the left wall and at the centre. Comparison with [133].

4.3.13 Industrial case study: Flow splitting device

This example consists of simulating a flow splitter which distributes oil to the camshaft and cam shifting system of an internal combustion engine. Oil flows through an inlet tube from the main gallery and splits off into two outlet tubes: the variable cam timing (VCT) outlet, and the camshaft lubrication oil gallery outlet. The lubrication oil is expected to enter the inlet with a small concentration of air bubbles. It is desirable that a pressure is selected at the VCT outlet such that the highest concentration of oil flows through the VCT outlet (in terms of flow rate), while the air is restricted.

The two-dimensional geometry considered is illustrated in Figure 4.42. The diameters are taken as: $d_i = 6$ mm, $d_v = 5$ mm, $d_g = 8.1$ mm, and $d_t = 2$ mm. Initially the domain is filled with static lubricating oil, i.e. $\varphi_0 = 1$. In order to push air bubbles through the device, the boundary condition for φ at the inlet boundary $\Gamma_i \in \Gamma$ is taken as

$$\varphi(x, t) = \begin{cases} 1 - \mathcal{T}_\varphi(t) \left[1 + \cos \left(\frac{6\pi}{d_i} \max \left(|x - \frac{d_i}{2}| - \frac{d_i}{12}, 0 \right) \right) \right], & \text{for } |x - \frac{d_i}{2}| < \frac{d_i}{4}, \\ 1, & \text{otherwise,} \end{cases} \quad (4.29)$$

where the time dependent function for $t \in \mathcal{I}$, is described for one time period T as

$$\mathcal{T}_\varphi(t) = \begin{cases} \frac{1}{2} \left[1 - \cos \left(\frac{\pi}{T_r} t \right) \right], & \text{for } t < T_r, \\ 1, & \text{for } T_r \leq t < T_r + T_a, \\ \frac{1}{2} \left[1 - \cos \left(\frac{\pi}{T_r} (t - T_a) \right) \right], & \text{for } T_r + T_a \leq t < 2T_r + T_a, \\ 0, & \text{for } 2T_r + T_a \leq t < T, \end{cases} \quad (4.30)$$

where T_a , and T_r are the time periods assigned to the air and the smooth ramp. The spatial and temporal functions in Equations (4.29) and (4.30) are shown

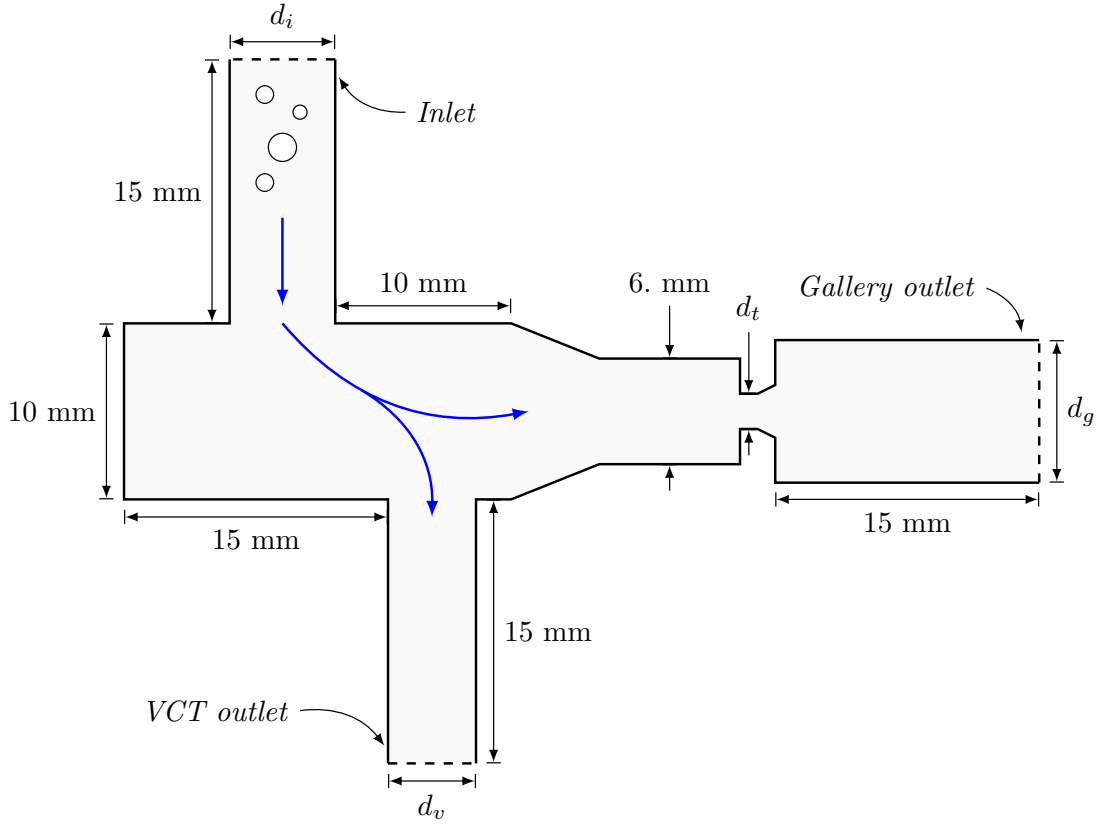
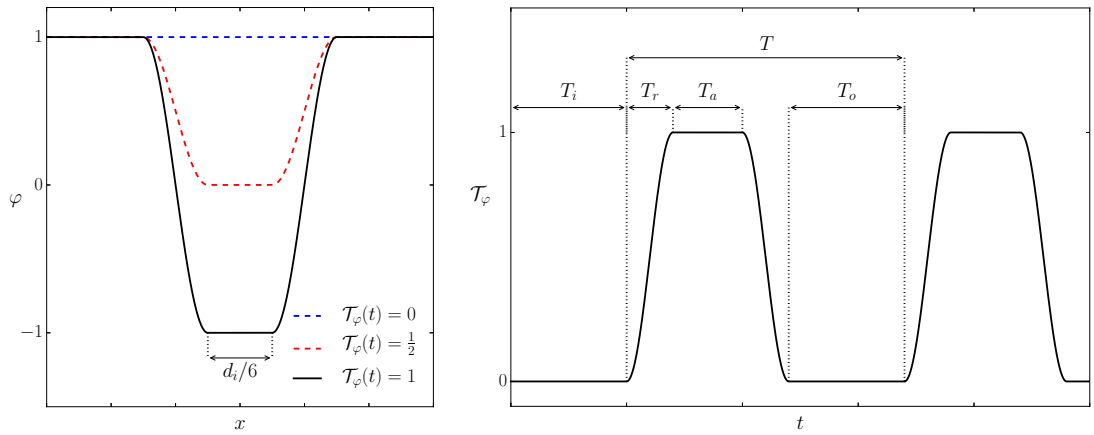


Figure 4.42: Geometry of flow splitting device.

in Figure 4.43, where the latter function is set periodically over T . T_i denotes the time period before the first bubble is activated, and T_o denotes the time period between bubble activation or simply the oil activation. For all simulations, $T_i = 0.2$ s, $T_a = 0.3T$, $T_o = 0.3T$, $T_r = 0.2T$, with $T = 0.025$ s. The velocity

Figure 4.43: Flow splitting device: Spatial (left) and temporal (right) functions for φ at inlet boundary.

boundary conditions are set as no-slip on the domain walls, while at the inlet,

$$\mathbf{u}(x, t) = \left\{ u_{\text{in}} \mathcal{T}_u(t) \left(\frac{0}{4x(x - d_i)} \right) \right\}, \quad x \in \Gamma_i, \quad (4.31a)$$

$$p = p_v, \quad \text{on } \Gamma_v. \quad (4.31b)$$

$$p = 0.5 \text{ bar}, \quad \text{on } \Gamma_g. \quad (4.31c)$$

Here Γ_v and Γ_g are subsets of Γ associated with the VCT and gallery outlets, respectively. The inlet velocity is set as $u_{\text{in}} = 150 \text{ cm/s}$ for the quadratic velocity profile, and the time ramping function is described as

$$\mathcal{T}_u(t) = \frac{1}{2} \left[1 - \cos \left(\pi \min \left(\frac{t}{T}, 1 \right) \right) \right], \quad (4.32)$$

where $T = 0.005 \text{ s}$. The pressure p_v is considered a variable to be set above and below the gallery pressure of 0.5 bar. Three cases are considered for comparison, $p_v = 0.49, 0.5, 0.51 \text{ bar}$.

The properties of the lubrication oil are chosen as: $\rho = 0.8 \text{ g/cm}^3$, $\mu = 0.05 \text{ g cm}^{-1} \text{ s}^{-1}$. The surface tension coefficient (with respect to the oil and air) is set as $\gamma = 30 \text{ g/s}^2$. The other parameters are set as: $M = 0.05 \text{ cm s}^{-2}$, and $\epsilon = 1.2h$, where h is obtained as the maximum characteristic element size in the mesh. The mesh is constructed of 197,814 linear triangular elements, and adaptive time stepping is considered with the maximum time step size set to $\Delta t = 0.002 \text{ s}$.

Figures 4.44 to 4.47 show specific time instances for phase-field variable and velocity magnitude solutions, considering the three cases of p_v . It is clear that varying the pressure at the VCT outlet between 0.49 – 0.51 bar, while retaining a pressure of 0.5 bar at the gallery outlet, changes the path of the air bubbles. With 0.49 bar at the VCT outlet, the air bubbles are primarily directed towards the VCT outlet as a result of additional flow velocity arriving from the gallery outlet. The opposite effect is observed when the VCT pressure is set to 0.51 bar with the majority of the air bubbles now being directed toward the gallery outlet as a result of the lower pressure region. The flow rates of air and oil, Q_a and Q_o , at the VCT outlet is shown in Figure 4.48, and likewise at the gallery outlet in Figure 4.49. From Figure 4.48, it is clear that the oil flow rate Q_o increases at the VCT outlet with decreasing pressure. The same relation exists with the air flow rate Q_a . Figure 4.49 shows that there is an increase in Q_o and Q_a corresponding to an increase in pressure. It is evident that with further flow development, there would be air bubbles flowing through both outlets when $p_v = p_g$. Furthermore there would be less or no air bubbles flowing through the gallery outlet for $p_v < p_g$, and less or no air bubbles flowing through the VCT outlet for $p_v > p_g$. This is confirmed from observing Figure 4.47. Notably an increase in oil flow rate corresponds with an increase in air flow rate, and thus to completely constrict air flow from an outlet, the oil flow rate would be compromised.

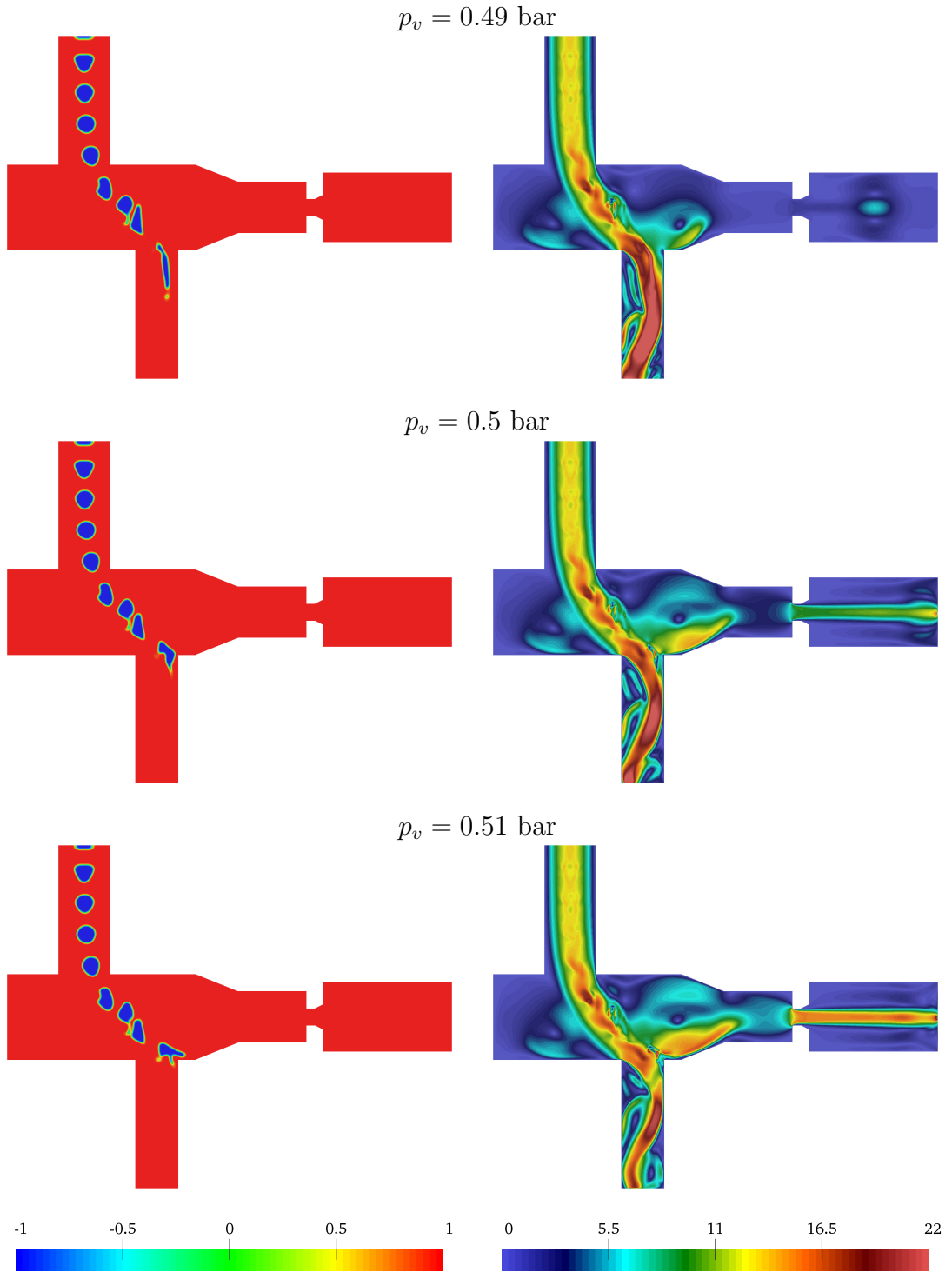


Figure 4.44: Flow splitting device: Solution to φ and $|\mathbf{u}|$ for $p_v = 0.49, 0.5, 0.51$ bar, for time instance $t \approx 0.0405$ s, with 197,814 linear elements.

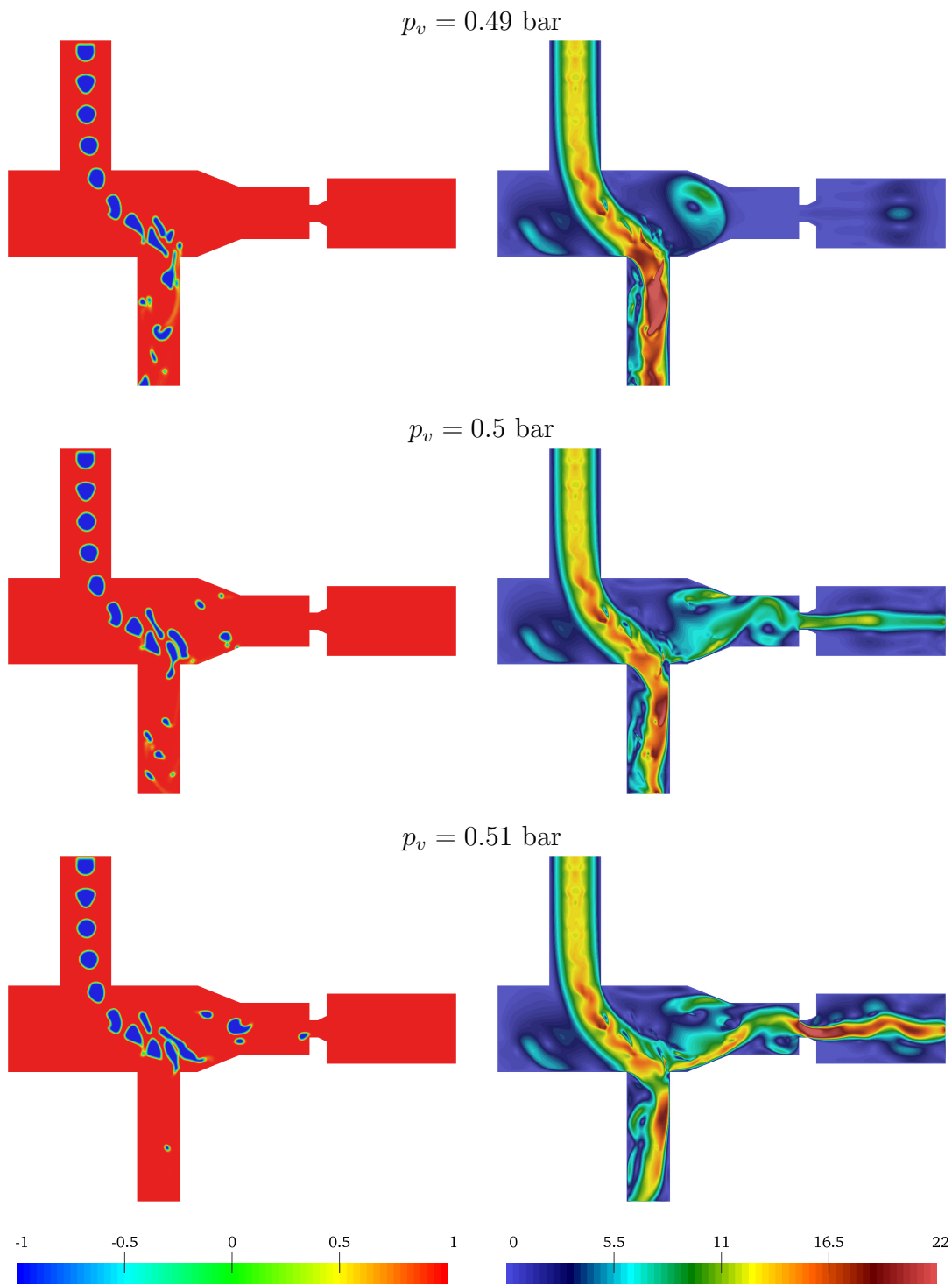


Figure 4.45: Flow splitting device: Solution to φ and $|\mathbf{u}|$ for $p_v = 0.49, 0.5, 0.51$ bar, for time instance $t \approx 0.0542$ s, with 197,814 linear elements.

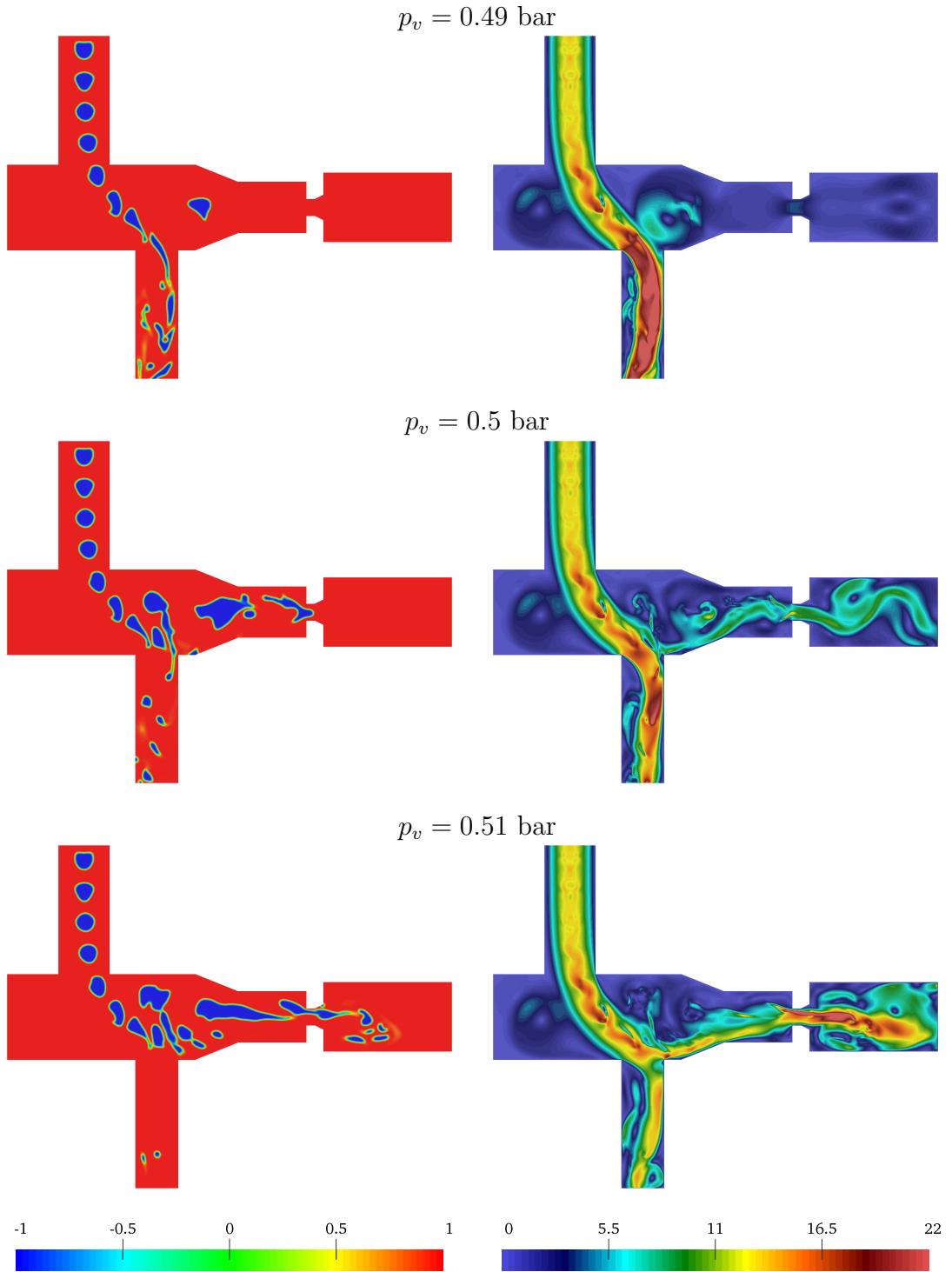


Figure 4.46: Flow splitting device: Solution to φ and $|\mathbf{u}|$ for $p_v = 0.49, 0.5, 0.51$ bar, for time instance $t \approx 0.0795$ s, with 197,814 linear elements.

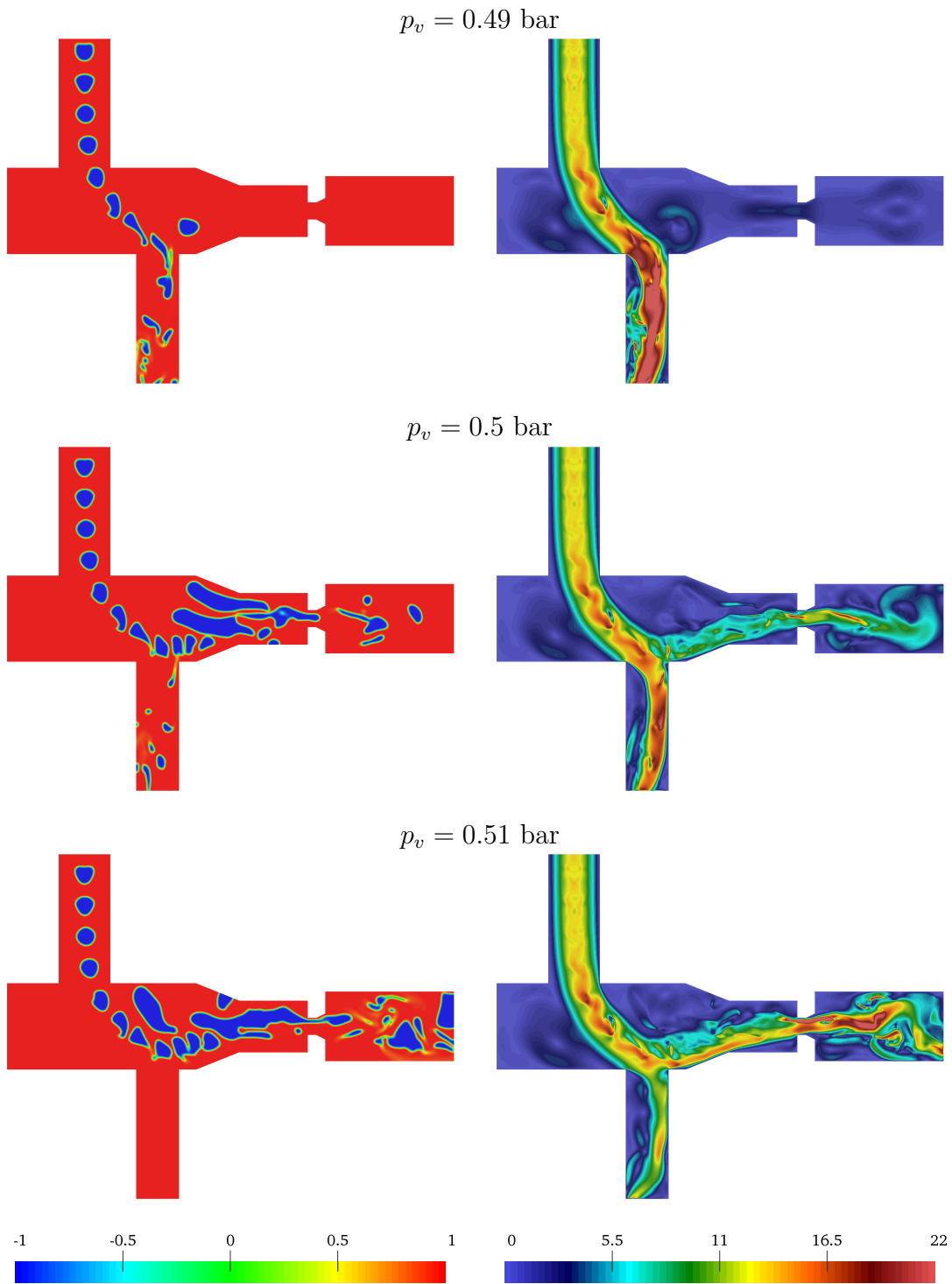


Figure 4.47: Flow splitting device: Solution to φ and $|\mathbf{u}|$ for $p_v = 0.49, 0.5, 0.51$ bar, for time instance $t \approx 0.12$ s, with 197,814 linear elements.

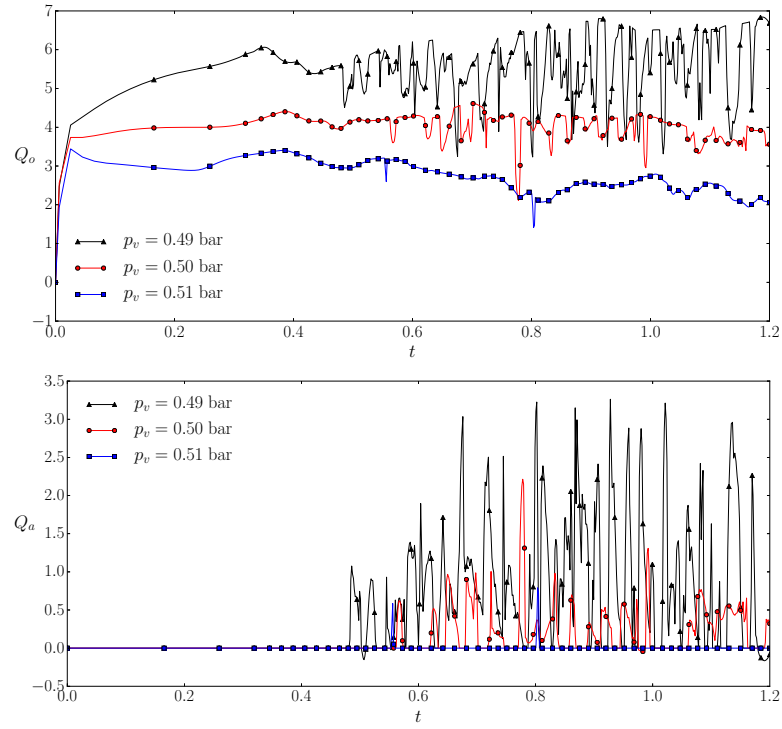


Figure 4.48: Flow splitting device: Flow rate of oil Q_o (above) and of air Q_a (below) at the VCT outlet up until $t = 1.2$ s.

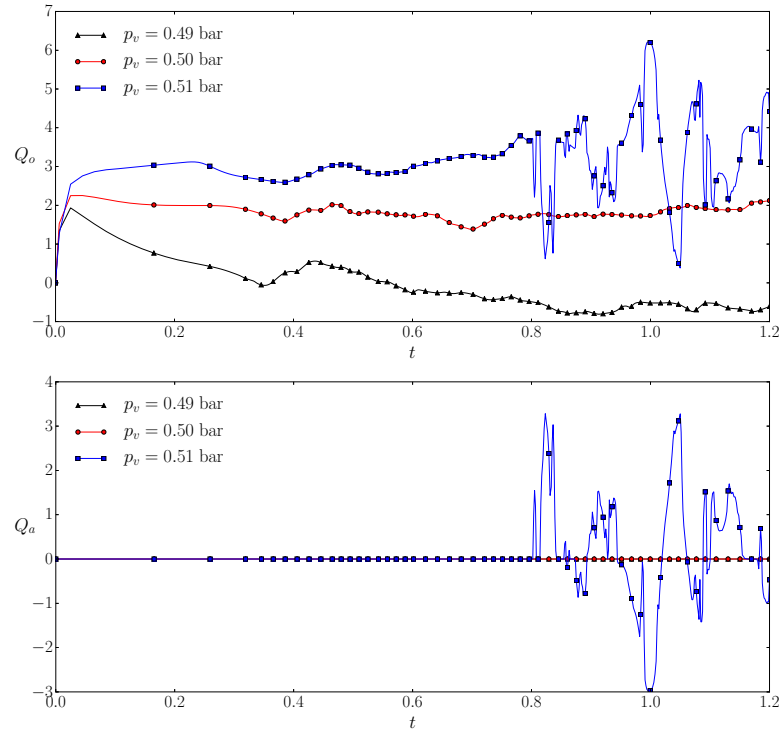


Figure 4.49: Flow splitting device: Flow rate of oil Q_o (above) and of air Q_a (below) at the gallery outlet up until $t = 1.2$ s.

4.4 Concluding remarks

In this work two novel finite element formulations are presented for modelling the Navier-Stokes-Cahn-Hilliard equations; The first uses mixed Taylor-Hood elements, while the second uses linear equal order stabilised SUPG/PSPG elements. The former formulation is primarily considered for comparative purposes. The models are formulated with two key aspects in mind:

- i. The ability to deactivate surface tension effects. This is done by removing the surface tension coefficient from the Cahn-Hilliard equation, and hence any instabilities which would result from setting it to zero. Thus, it is ensured that the Cahn-Hilliard equation exclusively deals with phase dynamics, while the Navier-Stokes equations alone control the physical phenomena.
- ii. Computational efficiency, which relates specifically to the stabilised formulation. Here the standard SUPG/PSPG stabilisation is introduced in the momentum equation, which allows for the use of efficient equal order linear elements. The employment of linear elements greatly improves the overall computational efficiency, which is crucial for the simulation of realistic three dimensional problems.

A number of benchmark/example problems are solved with the proposed methodologies. The examples in Subsections 4.3.1-4.3.9 demonstrate problems dominated by surface tension, while problems without surface tension are investigated in Subsections 4.3.10-4.3.12. In all cases the available reference solutions are reproduced accurately. Particularly noteworthy is the agreement of the results with those obtained from an arbitrary Lagrangian-Eulerian (ALE) based strategy in [5]. It is demonstrated in Subsections 4.3.3 and 4.3.9 that the volumes of the two fluid phases are conserved with good accuracy. Finally, an industry related problem is simulated in Subsection 4.3.13. The ability of the stabilised formulation to deal with highly advective multiphase flows with large topological changes is clearly demonstrated with this problem.

Chapter 5

Increasing Computational Efficiency: Segregation Strategies

In the simulation of incompressible fluid flow, one of the main challenges is posed by the coupling of the velocity and pressure fields through the incompressibility constraint. This has motivated the development of fractional step or splitting methods. These methods are based on the decoupling of the velocity-pressure system by splitting it into a sequence of “fractional” or “segregated” solution steps. Although the general idea remains the same, this splitting has been formulated in a number of ways over the years; often in the form of projection methods [134, 135], pressure or velocity correction methods [136, 137, 138], consistent splitting methods [139], viscosity splitting methods [140] or characteristic-based split (CBS) methods [141], to name just a few. Arguably the most widely used fractional step methods for incompressible fluid flow are the original projection schemes proposed independently by Chorin [134] and Temam [135, 142] in the 1960’s. In short, these projection methods are based on an orthogonal projection onto a subspace of solenoidal vector fields, see [135] for a thorough explanation. The basic idea is to acquire an intermediate velocity field (Step 1) by solving the momentum equation without the pressure gradient, i.e. considering only viscous, inertia and convection terms, and subsequently computing the pressure and divergence-free end-of-step velocity (Step 2). The appealing benefits of this approach consist in smaller system matrices, dimensionally uniform solution and right hand side vectors and, importantly, the fact that the pressure is obtained efficiently in Step 2 from solving the Poisson equation. The drawbacks of such strategies include additional complexity in the application of the boundary conditions and most of all the introduction of a so-called splitting error, which brings about a relative loss of temporal accuracy compared to a respective coupled approach. Due to their semi-explicit nature, it is crucial that temporal stability and accuracy are in the focus of all development in the area of the fractional step solution schemes.

As mentioned above, in the classical projection methods by Chorin and Temam, the intermediate velocity is computed independently of the pressure. It is well-understood that this restricts these methods to first order accuracy in time. If, in the first step, the pressure is approximated by the solution from the previous time step, then a pressure increment can be computed in the second step and

an overall second order accurate scheme can be formulated. This approach is typically known as the “incremental projection” or “pressure correction” method and was first considered in, for instance, [136, 137]. It is clear that the accuracy of the pressure extrapolation used in the first step must be increased in order to formulate a more accurate methodology. It is noted that, despite these efforts, the first order accurate schemes are still widely used. The analysis of the properties of the different schemes is not trivial and is an active area of research, see for instance [143, 144, 145, 146]. The present chapter has multiple objectives:

1. Presentation of a discrete model problem consisting of point masses and dash-pots which allows for detailed insight into the properties of projection schemes and is a useful tool for new development;
2. Discussion of high-frequency damping of projection schemes;
3. Presentation of two new families of projection schemes based on the generalised midpoint rule and the generalised- α method [79].

Prior to the further explanation of the objectives, it is pointed out that the work presented in this chapter is relevant for projection methods based on the finite volume as well as finite element formulations, even though Sections 5.2 and 5.3 are set in the context of the finite element method.

Objective 1 is motivated by the successful recent employment of the basic model problems in the area of the partitioned schemes for fluid-structure interaction. Here, the analyses of appropriate spatially discrete model problems has allowed for in-depth insight into temporal and added mass related instabilities [147, 148, 149] and is increasingly used for new method development [150, 151]. The investigation undertaken in the context of Objective 2 led to the observation that it is impossible to formulate a projection scheme for the model problem which is second order accurate and possesses high-frequency damping. This is an important finding which, to the best of our knowledge, has not been reported elsewhere and which may explain why second order accurate projection schemes have generally not replaced first order schemes. Objective 3 is the attempt to formulate a methodology which is more accurate than basic backward Euler based projection schemes, but offers some high-frequency damping.

The beneficial role of high-frequency damping in incremental numerical solution schemes for partial differential equations in time and space is well-known: The numerical analyst chooses the spatial and temporal discretisation suitable for the length and time scales which are of interest and represent the main system response. Hence, a robust methodology requires high-frequency damping to damp out the effect of the unresolved scales. In particular, high-frequency damping allows for a larger degree of independence between the spatial and temporal resolutions, i.e. a larger range of Courant numbers. In the context of the monolithic solution schemes for computational fluid dynamics, the generalised- α method, which is unconditionally stable, second order accurate and offers control over high-frequency damping, has therefore become very popular, see for instance [82, 152, 80, 153]. It was proposed in [79] and is related to its counterpart formulated earlier for solid dynamics in [78] (see also [154]). In the present work, a

projection scheme is formulated based on the generalised- α method. It is shown clearly how the proposed methodology is related to the backward differencing schemes which are commonly employed for projection schemes.

A discussion of projection schemes generally also comments on the issue of spurious pressure oscillations. This is discussed briefly in Subsection 5.2.3. Another aspect which has been addressed in a number of publications is the occurrence of undesired effects due to non-physical artificial boundary conditions along Dirichlet boundaries [155, 156]. An extensive study of the “rotational forms” which remove such effects can be found in [144]. In [157] a corresponding formulation has been used in the context of fluid-structure interaction. Since, in the examples presented in Section 5.3, no evidence of non-physical boundary layers has been detected even for large time steps, the issue is not considered in this work. The proposed formulations can, however, also be applied to projection schemes which include the rotational forms.

The remainder of this chapter is structured as follows: In Section 5.1, the model problem is presented, the new projection schemes are proposed and applied to the model problem. The responses of the schemes and the spectral radii of the amplification matrices are studied in detail. In Section 5.2, the projection methods are formulated for the incompressible Navier-Stokes equations using finite elements. Numerical examples are presented in Section 5.3, before the conclusions are drawn in Section 5.4.

Throughout this chapter, the terms “monolithic” or “coupled” refer to solution schemes based on the simultaneous computation of velocities and pressures.

5.1 Analysis of projection schemes

5.1.1 1D model problem with analytical solution

The model problem consists of a one-dimensional mass-dashpot system with three degrees of freedom as shown in Figure 5.1. The motion of the masses are subject to the physical constraint,

$$\xi_1 u_1 + \xi_2 u_2 + \xi_3 u_3 = 0, \quad (5.1)$$

where ξ_1 , ξ_2 and ξ_3 are scalar factors, and the velocities of the point masses are denoted by, respectively, u_1 , u_2 and u_3 . All point masses are equal. This choice does not imply a loss of generality, but allows for a clearer presentation

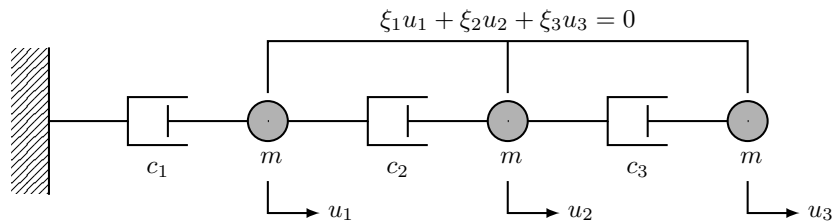


Figure 5.1: 1D model problem.

which is more aligned with the formulation for the incompressible Navier-Stokes equations in Section 3. The constraint (5.1) is imposed on the system by employing a Lagrange multiplier. A thorough description of this methodology is given in Joosten *et al.* [149].

Thus, the governing equations read

$$\dot{\mathbf{u}} + \mathbf{C}\mathbf{u} + \mathbf{b}\lambda = \mathbf{0}, \quad (5.2a)$$

$$\mathbf{b} \cdot \mathbf{u} = 0, \quad (5.2b)$$

where $\dot{\mathbf{u}} = \{\dot{u}_1, \dot{u}_2, \dot{u}_3\}^T$ and $\mathbf{u} = \{u_1, u_2, u_3\}^T$ are the accelerations and velocities of the point masses respectively and λ is the Lagrange multiplier. The matrix \mathbf{C} and the vector \mathbf{b} are

$$\mathbf{C} = \frac{1}{m} \begin{bmatrix} c_1 + c_2 & -c_2 & 0 \\ -c_2 & c_2 + c_3 & -c_3 \\ 0 & -c_3 & c_3 \end{bmatrix}, \quad \mathbf{b} = \frac{1}{m} \begin{Bmatrix} \xi_1 \\ \xi_2 \\ \xi_3 \end{Bmatrix}, \quad (5.3)$$

where the parameters c_1 , c_2 and c_3 are the respective damping coefficients for the three dashpots. It is straightforward to show that the problem (5.2) can be reduced to a system of two linear differential equations, expressed as

$$\begin{Bmatrix} \dot{u}_1 \\ \dot{u}_2 \end{Bmatrix} + \begin{bmatrix} k_{11} & k_{12} \\ k_{21} & k_{22} \end{bmatrix} \begin{Bmatrix} u_1 \\ u_2 \end{Bmatrix} = \begin{Bmatrix} 0 \\ 0 \end{Bmatrix}, \quad (5.4)$$

where k_{11} , k_{12} , k_{21} and k_{22} depend on the problem parameters. Solving this system yields u_1 and u_2 . Subsequently, u_3 is obtained by using the constraint (5.1). The Lagrange multiplier λ can be evaluated by substituting the velocities back into Equation (5.2a). The analytical solutions for \mathbf{u} and λ render lengthy terms, which are not shown here for the sake of brevity.

Remark 1: It could be argued that the model problem (5.2) is not fully representative of a viscous incompressible flow problem. However, it possesses very similar characteristics. The masses and dampers of the 1D system are concurrent with the inertial and viscous terms obtained from the Navier-Stokes equations after appropriate discretisation. Moreover, the constraint (5.1) represents well the effect of incompressibility in fluid flow problems, where also a Lagrange multiplier, namely the pressure, is used to impose the linear incompressibility constraint. Due to the absence of an advective component, the model problem is linear and therefore suitable for detailed analyses. In the discretisation of the Navier-Stokes equations the presence of the advection term results in complex eigenvalues of the system matrix. A similar effect can be achieved in the model problem by using complex damping coefficients.

In recent years similar model problems were used successfully, for instance in [147, 149, 148, 158], to study the computational strategies for fluid-structure interaction.

5.1.2 Time integration schemes

For the purpose of introducing the different time integration schemes, the following general first order differential equation is considered

$$\dot{\mathbf{u}} = \mathbf{f}(t, \mathbf{u}), \quad (5.5)$$

with \mathbf{f} being a function of time t and the solution variable \mathbf{u} .

Backward differentiation formula (BDF)

BDF schemes are implicit linear multi-step methods which allow the derivative of a function to be expressed as a linear combination of solution variables associated with previous time instants. If one considers the differential Equation (5.5) with BDF time integration, the general expression reads

$$\dot{\mathbf{u}}^{n+1} = \mathbf{f}(t^{n+1}, \mathbf{u}^{n+1}), \quad (5.6)$$

where $\Delta t = t^{n+1} - t^n$ is the time step size, N is the total number of time steps and $n \in \{0, 1, \dots, N\}$. Depending on the order s of the scheme, the time derivatives of the consequent BDFs scheme are approximated as

$$\dot{\mathbf{u}}^{n+1} = \begin{cases} \frac{1}{\Delta t} (\mathbf{u}^{n+1} - \mathbf{u}^n), & \text{for } s = 1, \\ \frac{1}{2\Delta t} (3\mathbf{u}^{n+1} - 4\mathbf{u}^n + \mathbf{u}^{n-1}), & \text{for } s = 2, \\ \frac{1}{6\Delta t} (11\mathbf{u}^{n+1} - 18\mathbf{u}^n + 9\mathbf{u}^{n-1} - 2\mathbf{u}^{n-2}), & \text{for } s = 3, \\ \dots & \end{cases} \quad (5.7)$$

It is observed that, for $s = 1$, the scheme is identical to the backward Euler method (BE). Since only the first order BDF1 and second order BDF2 methods are unconditionally stable, the orders $s > 2$ will be disregarded in this study.

Generalised midpoint rule (GM)

The generalised midpoint rule (GM) can be described as a modified Euler method, which in the case of Equation (5.5) is expressed as

$$\dot{\mathbf{u}}^{n+\gamma} = \mathbf{f}(t^{n+\gamma}, \mathbf{u}^{n+\gamma}), \quad (5.8)$$

with

$$\dot{\mathbf{u}}^{n+\gamma} = \frac{\mathbf{u}^{n+1} - \mathbf{u}^n}{\Delta t}, \quad (5.9)$$

$$\mathbf{u}^{n+\gamma} = (1 - \gamma) \mathbf{u}^n + \gamma \mathbf{u}^{n+1}, \quad (5.10)$$

$$t^{n+\gamma} = (1 - \gamma) t^n + \gamma t^{n+1}, \quad (5.11)$$

where γ is a scalar time integration parameter. It can be observed that setting $\gamma = 1/2$ recovers the second order accurate trapezoidal rule (TR), and setting

$\gamma = 0$ recovers the backward Euler method (BE/BDF1). Thus the generalised-midpoint rule represents an interpolation between the backward Euler method and the trapezoidal rule. Notably varying γ allows the high frequency damping to be controlled by the user, which is demonstrated clearly in [80, 159]. The limit ρ_∞ of the spectral radius as $\Delta t \rightarrow \infty$ is related to the parameter γ by

$$\gamma = \frac{1}{1 + \rho_\infty^h}. \quad (5.12)$$

The method is unconditionally stable for $1/2 \leq \gamma \leq 1$ which corresponds to $0 \leq \rho_\infty \leq 1$, see [80] or [78] for a thorough explanation.

Generalised- α method (AM)

The generalised- α method is an implicit and unconditionally stable single-step time integration method. The scheme is presented in Section 2.3.2, but is repeated here for consistency. Applying the generalised- α method to the first order problem in Equation (5.5) gives

$$\dot{\mathbf{u}}^{n+\alpha_m} = \mathbf{f}(t^{n+\alpha_f}, \mathbf{u}^{n+\alpha_f}), \quad (5.13)$$

where

$$\dot{\mathbf{u}}^{n+\alpha_m} = (1 - \alpha_m) \dot{\mathbf{u}}^n + \alpha_m \dot{\mathbf{u}}^{n+1}, \quad (5.14)$$

$$t^{n+\alpha_f} = (1 - \alpha_f) t^n + \alpha_f t^{n+1}, \quad (5.15)$$

$$\mathbf{u}^{n+\alpha_f} = (1 - \alpha_f) \mathbf{u}^n + \alpha_f \mathbf{u}^{n+1}, \quad (5.16)$$

$$\frac{\mathbf{u}^{n+1} - \mathbf{u}^n}{\Delta t} = (1 - \gamma) \dot{\mathbf{u}}^n + \gamma \dot{\mathbf{u}}^{n+1}. \quad (5.17)$$

The parameters α_m , α_f and γ may be expressed in terms of the spectral radius ρ_∞ for an infinitely large time step as follows

$$\alpha_m = \frac{1}{2} \frac{3 - \rho_\infty^h}{1 + \rho_\infty^h}, \quad \alpha_f = \frac{1}{1 + \rho_\infty^h}, \quad \gamma = \frac{1}{2} + \alpha_m - \alpha_f. \quad (5.18)$$

For $\rho_\infty = 0$, the time integration parameters become: $\alpha_m = 3/2$, $\alpha_f = 1$ and $\gamma = 1$, which when applied to Equation (2.59) gives

$$\dot{\mathbf{u}}^{n+3/2} = \mathbf{f}(t^{n+1}, \mathbf{u}^{n+1}). \quad (5.19)$$

With Equations (2.60) and (2.63), the following is obtained

$$\dot{\mathbf{u}}^{n+3/2} = \frac{3\dot{\mathbf{u}}^{n+1} - \dot{\mathbf{u}}^n}{2} = \frac{3\mathbf{u}^{n+1} - 4\mathbf{u}^n + \mathbf{u}^{n-1}}{2\Delta t}. \quad (5.20)$$

This is identical to the expression in Equation (5.7) for $s = 2$. It can thus be concluded that the generalised- α method with $\rho_\infty = 0$ is equivalent to the BDF2 method. This observation is also made in [160]. For $\rho_\infty = 1$, the generalised- α method coincides with the trapezoidal rule (TR). Thus, the generalised- α method represents an interpolation between the BDF2 and TR.

5.1.3 Projection schemes

In the following paragraphs, the time integration techniques of Subsection 5.1.2 are employed in the context of projection methods for the simulation of the model problem described in Subsection 5.1.1.

The adopted strategy is based on the elimination of the end-of-step velocity, an approach first considered by Guermond and Quartapelle [161, 162, 144]. Furthermore, an incremental projection (or pressure-correction) approach is followed, whereby an approximation of the pressure, or in the context of the model problem (5.2), λ , is included in the first step. This is generally referred to as a pressure-correction method. All schemes presented in the following allow for a varying time step size Δt and for adaptive time stepping.

Generalised midpoint rule projection method

Typically incremental projection methods are comprised of two steps. The first step, or *viscous* step, contains the viscous contribution of the momentum equation and a predictor for the pressure. In the context of the model problem, the first step of the GM projection method involves the computation of an intermediate velocity at time instant t^{n+1} from

$$\frac{1}{\Delta t} (\tilde{\mathbf{u}}^{n+1} - \mathbf{u}^n) + \mathbf{C}\tilde{\mathbf{u}}^{n+\gamma} + \delta \mathbf{b}\lambda^{*,n+\gamma} = \mathbf{0}, \quad (5.21)$$

with

$$\tilde{\mathbf{u}}^{n+\gamma} = \gamma \tilde{\mathbf{u}}^{n+1} + (1 - \gamma) \tilde{\mathbf{u}}^n \quad (5.22)$$

$$\lambda^{*,n+\gamma} = \gamma \lambda^{*,n+1} + (1 - \gamma) \lambda^n. \quad (5.23)$$

The role of the scalar factor δ is explored further in Section 5.1.3. It is well known that second order accuracy of the overall scheme can be achieved by using a first order predictor for the Lagrange multiplier

$$\lambda^{*,n+1} = \lambda^n. \quad (5.24)$$

The second step is based on the equations

$$\frac{1}{\Delta t} (\mathbf{u}^{n+1} - \tilde{\mathbf{u}}^{n+1}) + \mathbf{b} (\lambda^{n+\gamma} - \delta \lambda^{*,n+\gamma}) = \mathbf{0}, \quad (5.25a)$$

$$\mathbf{b} \cdot \mathbf{u}^{n+1} = 0, \quad (5.25b)$$

where

$$\lambda^{n+\gamma} = \gamma \lambda^{n+1} + (1 - \gamma) \lambda^n. \quad (5.26)$$

Crucially, it is observed that the sum of Equations (5.21) and (5.25a) recovers the momentum Equation (5.2a) whereby the inertia term is expressed in terms of the end-of-step velocity \mathbf{u}^{n+1} and the viscous term is evaluated for the intermediate velocity $\tilde{\mathbf{u}}^{n+1}$. Substituting the expressions (5.23), (5.24) and (5.26) into Equation (5.25a) renders

$$\frac{1}{\Delta t} (\mathbf{u}^{n+1} - \tilde{\mathbf{u}}^{n+1}) + \mathbf{b} (\gamma \lambda^{n+1} + (1 - \gamma - \delta) \lambda^n) = \mathbf{0}. \quad (5.27)$$

Multiplying Equation (5.27) by \mathbf{b} and recalling Equation (5.25b) results in a scalar equation from which λ^{n+1} can be obtained,

$$-\frac{1}{\Delta t} \mathbf{b} \cdot \tilde{\mathbf{u}}^{n+1} + \mathbf{b} \cdot \mathbf{b} (\gamma \lambda^{n+1} + (1 - \gamma - \delta) \lambda^n) = 0. \quad (5.28)$$

Notably, in the context of the incompressible Navier-Stokes equations, the scalar product with \mathbf{b} corresponds to the application of the divergence operator, which results in a Poisson equation for the pressure increment. The end-of-step velocity \mathbf{u}^{n+1} is explicitly computed from Equation (5.27) by substituting λ^{n+1} back into the equation, as follows

$$\mathbf{u}^{n+1} = \tilde{\mathbf{u}}^{n+1} - \Delta t \mathbf{b} (\gamma \lambda^{n+1} + (1 - \gamma - \delta) \lambda^n). \quad (5.29)$$

The second step is generally called the *projection* step since it decomposes the intermediate velocity into the pressure and divergence free end-of-step velocity, as shown in Equations (5.28) and (5.29) respectively.

End-of-step elimination: It is common practice to eliminate the end-of-step velocity from the scheme by substituting the divergence free velocity \mathbf{u}^n , obtained by considering Equation (5.29) at time instant t^n , into the first step (5.21). The explicit step (5.29) is then no longer necessary. Furthermore the intermediate velocity also converges to the exact solution as Δt is reduced. The first step of the GM projection method with end-of-step elimination, from which $\tilde{\mathbf{u}}^{n+1}$ is computed, reads

$$\frac{1}{\Delta t} (\tilde{\mathbf{u}}^{n+1} - \tilde{\mathbf{u}}^n) + \mathbf{C} \tilde{\mathbf{u}}^{n+\gamma} + \mathbf{b} ((\gamma + \delta) \lambda^n + (1 - \gamma - \delta) \lambda^{n-1}) = 0. \quad (5.30)$$

The Lagrange multiplier λ^{n+1} is then computed as before from Equation (5.28). There is no need to compute the end-of-step velocity \mathbf{u}^{n+1} , but if desired it can be evaluated from Equation (5.29).

The system of Equations (5.30) and (5.28) can be expressed in matrix form as

$$\tilde{\mathbf{U}}^{n+1} = \mathbf{A}_{\text{GM}} \tilde{\mathbf{U}}^n, \quad (5.31)$$

where $\tilde{\mathbf{U}}^n = \{\tilde{\mathbf{u}}_1^n, \tilde{\mathbf{u}}_2^n, \tilde{\mathbf{u}}_3^n, \Delta t \lambda^n\}^T$, and $\tilde{\mathbf{U}}^{n+1}$ is expressed analogously. \mathbf{A}_{GM} is the amplification matrix for the generalised-midpoint rule scheme and its coefficients depend on the problem parameters and on the time step size Δt .

Generalised- α projection method

Adopting the integration scheme presented in Subsection 5.1.2, and following the approach described in the previous section for the generalised midpoint rule, the first step of the AM projection method, from which $\tilde{\mathbf{u}}^{n+1}$ is evaluated, is expressed as

$$\left(1 - \frac{\alpha_m}{\gamma}\right) \dot{\mathbf{u}}^n + \frac{\alpha_m}{\gamma \Delta t} (\tilde{\mathbf{u}}^{n+1} - \mathbf{u}^n) + \mathbf{C} \tilde{\mathbf{u}}^{n+\alpha_f} + \delta \mathbf{b} \lambda^{*,n+\alpha_f} = 0, \quad (5.32)$$

with

$$\tilde{\mathbf{u}}^{n+\alpha_f} = \alpha_f \tilde{\mathbf{u}}^{n+1} + (1 - \alpha_f) \tilde{\mathbf{u}}^n, \quad (5.33)$$

$$\lambda^{*,n+\alpha_f} = \alpha_f \lambda^{*,n+1} + (1 - \alpha_f) \lambda^n, \quad (5.34)$$

where the parameters α_m , α_f and γ are as shown in Equation (2.64), and the predictor $\lambda^{*,n+1}$ is the same as in Equation (5.24).

The second step is obtained as

$$\frac{\alpha_m}{\gamma \Delta t} (\mathbf{u}^{n+1} - \tilde{\mathbf{u}}^{n+1}) + \mathbf{b} (\lambda^{n+\alpha_f} - \delta \lambda^{*,n+\alpha_f}) = \mathbf{0}, \quad (5.35a)$$

$$\mathbf{b} \cdot \mathbf{u}^{n+1} = 0. \quad (5.35b)$$

Similarly to the manipulation of Equation (5.25a), Equation (5.35a) can be rewritten as

$$\frac{\alpha_m}{\gamma \Delta t} (\mathbf{u}^{n+1} - \tilde{\mathbf{u}}^{n+1}) + \mathbf{b} (\alpha_f \lambda^{n+1} + (1 - \alpha_f - \delta) \lambda^n) = \mathbf{0}. \quad (5.36)$$

Multiplying Equation (5.36) by \mathbf{b} and recalling Equation (5.35b) renders

$$-\frac{\alpha_m}{\gamma \Delta t} \mathbf{b} \cdot \tilde{\mathbf{u}}^{n+1} + \mathbf{b} \cdot \mathbf{b} (\alpha_f \lambda^{n+1} + (1 - \alpha_f - \delta) \lambda^n) = 0, \quad (5.37)$$

which can be solved for λ^{n+1} . The end-of-step velocity is obtained from

$$\mathbf{u}^{n+1} = \tilde{\mathbf{u}}^{n+1} - \frac{\gamma \Delta t}{\alpha_m} \mathbf{b} (\alpha_f \lambda^{n+1} + (1 - \alpha_f - \delta) \lambda^n). \quad (5.38)$$

Finally, the acceleration can be computed from

$$\dot{\mathbf{u}}^{n+1} = \frac{1}{\gamma \Delta t} (\mathbf{u}^{n+1} - \mathbf{u}^n) - \frac{1 - \gamma}{\gamma} \dot{\mathbf{u}}^n. \quad (5.39)$$

End-of-step elimination: The first step of the AM projection method with end-of-step elimination involves computing $\tilde{\mathbf{u}}^{n+1}$ from

$$\begin{aligned} \left(1 - \frac{\alpha_m}{\gamma}\right) \dot{\mathbf{u}}^n + \frac{\alpha_m}{\gamma \Delta t} (\tilde{\mathbf{u}}^{n+1} - \tilde{\mathbf{u}}^n) + \mathbf{C} \tilde{\mathbf{u}}^{n+\alpha_f} \\ + \mathbf{b} ((\alpha_f + \delta) \lambda^n + (1 - \alpha_f - \delta) \lambda^{n-1}) = \mathbf{0}. \end{aligned} \quad (5.40)$$

In the second step λ^{n+1} is again computed from (5.37). Substituting the end-of-step velocities \mathbf{u}^n and \mathbf{u}^{n+1} into Equation (5.39) gives an explicit expression for the end-of-step acceleration

$$\begin{aligned} \dot{\mathbf{u}}^{n+1} = \frac{1}{\gamma \Delta t} (\tilde{\mathbf{u}}^{n+1} - \tilde{\mathbf{u}}^n) - \frac{1 - \gamma}{\gamma} \dot{\mathbf{u}}^n \\ - \frac{1}{\alpha_m} \mathbf{b} (\alpha_f \lambda^{n+1} + (1 - 2\alpha_f - \delta) \lambda^n - (1 - \alpha_f - \delta) \lambda^{n-1}). \end{aligned} \quad (5.41)$$

Since the right hand side contains the acceleration $\dot{\mathbf{u}}^n$, it is not possible to use Equation (5.41) to eliminate the end-of-step acceleration in Equation (5.40). Similarly to (5.31), the system of Equations (5.40), (5.37) and (5.41) may be written in matrix form as

$$\tilde{\mathbf{U}}^{n+1} = \mathbf{A}_{\text{AM}} \tilde{\mathbf{U}}^n, \quad (5.42)$$

where $\tilde{\mathbf{U}}^n = \{\tilde{\mathbf{u}}_1^n, \tilde{\mathbf{u}}_2^n, \tilde{\mathbf{u}}_3^n, \Delta t \dot{\mathbf{u}}_1^n, \Delta t \dot{\mathbf{u}}_2^n, \Delta t \dot{\mathbf{u}}_3^n, \Delta t \lambda^n\}^T$, and $\tilde{\mathbf{U}}^{n+1}$ can be expressed analogously. \mathbf{A}_{AM} is the amplification matrix for the generalised- α method.

The role of the factor δ

The factor δ in Equations (5.21) and (5.32) affects the high frequency dissipation of the scheme. A limit analysis of the spectral radius of the amplification matrices \mathbf{A}_{GM} and \mathbf{A}_{AM} , based on a symbolic mathematics software, yields the following limit

$$\lim_{\Delta t \rightarrow \infty} \rho^h = \max(\bar{\rho}_\infty^h, \delta - \bar{\rho}_\infty^h + \delta \bar{\rho}_\infty^h), \quad (5.43)$$

where the parameter $\bar{\rho}_\infty^h$ represents the user-controlled high frequency spectral radius of the applied time integration scheme. Since it is desired that, for the overall method, $\rho^h \rightarrow \bar{\rho}_\infty^h$ for $\Delta t \rightarrow \infty$, Equation (5.43) suggests to choose δ such that

$$\delta - \bar{\rho}_\infty^h + \delta \bar{\rho}_\infty^h = \bar{\rho}_\infty^h, \quad (5.44)$$

which gives

$$\delta = \frac{2\bar{\rho}_\infty^h}{1 + \bar{\rho}_\infty^h}. \quad (5.45)$$

Thus, with Equations (5.12), (2.64) and (5.45) the high frequency damping of the GM and AM projection methods presented above can be fully controlled and $\bar{\rho}_\infty^h$ remains as the only free integration parameter. In the case of the GM projection method it can be used to switch gradually between BE and TR. Similarly, in the case of the AM projection method, it allows for interpolation between BDF2 and TR.

5.1.4 Comparison of schemes

In this section, the projection methods presented in Subsection 5.1.3 are compared to each other, as well as to the monolithic and exact solutions discussed in Subsections 5.1.1 and 5.1.2. First the performance of the schemes is demonstrated for the model problem and subsequently, the schemes are analysed in terms of stability and accuracy.

1D model problem response

In order to show the capabilities of the GM and AM projection schemes to control high frequency damping, the parameters for the model problem are chosen such that both low and high frequency oscillations are present, and no physical damping occurs. The latter is achieved by choosing imaginary damping coefficients in the matrix \mathbf{C} , and the parameters are set as follows: $\xi_1 = 1$, $\xi_2 = 6$, $\xi_3 = 2$, $m = 1$, $c_1 = 0.25i$, $c_2 = 0.32i$, $c_3 = 12i$. By setting the real part of the coefficients to zero, it is ensured that all damping observed in the response of the system is numerical, thus allowing for a straightforward interpretation of the results.

Figure 5.2 shows the response of the component u_1 when using the GM and AM projection and monolithic schemes with different values of $\bar{\rho}_\infty^h$. The periods associated with the low and high frequencies are, respectively, $T_l = 9.725$ and $T_h = 0.385$. The time step size is chosen as $\Delta t = 0.5 > T_h$. It is desired that, in this case, the unresolved high frequency oscillations are damped out while the low frequencies are accurately captured. For $\bar{\rho}_\infty^h < 1$ it can be seen that the AM

projection method more accurately approximates the low frequency response than the GM projection method. Both methods show more numerical dissipation than their monolithic counterparts. As $\bar{\rho}_\infty^h \rightarrow 1$, the response experiences less numerical damping and shows more oscillatory behaviour. The numerical oscillations are damped out at a faster rate for the GM method than for the AM method, however at the cost of more low frequency damping. With $\bar{\rho}_\infty^h = 1$, the TR projection method is recovered, and as expected there is no numerical damping observed for the high or low frequencies.

1D model problem spectral radii

The spectral radius of a scheme's amplification matrix is defined for a $d \times d$ matrix as

$$\rho^h(\mathbf{A}) = \max(|\lambda_1|, |\lambda_2|, \dots, |\lambda_d|), \quad (5.46)$$

where $\lambda_{1,2,\dots,d}$ represent the eigenvalues of the amplification matrix of dimension d and must not be confused with the Lagrange multiplier for the constraint. For a scheme to be unconditionally stable, the spectral radius must not exceed 1 for all positive time step sizes Δt , i.e. $\rho^h(\mathbf{A}) \leq 1 \forall \Delta t \geq 0$. Since $\rho^h(\mathbf{A})$ is highly nonlinear with respect to Δt , only the limits of $\rho^h(\mathbf{A})$ for $\Delta t \rightarrow 0$ and $\Delta t \rightarrow \infty$ can be obtained analytically while, for any given finite value of Δt , the stability check is restricted to the numerical investigation for the given parameters.

The spectral radii for the GM and AM projection methods are compared to their respective monolithic counterparts as well as to the monolithic BE method in Figure 5.3, using the same parameters as in Section 5.1.4. It is visible for both methods that $\rho^h \leq 1$ for all values of $\bar{\rho}_\infty^h$ chosen. It is also evident that $\bar{\rho}_\infty^h$ in both cases defines the limit of the high frequency damping ρ_∞ .

The direct comparison between the GM and AM projection methods is shown in Figure 5.4. Notably, for any value of $\bar{\rho}_\infty^h$ the AM projection method displays less numerical damping in the lower frequency range than the GM projection method. It is also observed that for $\bar{\rho}_\infty^h = 0$ the AM projection scheme is less dissipative than the monolithic BE method. A similar comparison involving only the monolithic counterparts of the methods is presented in Figure 5.5.

Figure 5.6 shows the spectral radii as obtained from modified versions of the proposed GM and AM projection schemes, where $\delta = 1$. Thus, Step 1 of the modified schemes includes a full predictor for the Lagrange multiplier λ . It is evident that the high frequency damping is lost and $\rho_\infty = 1$ is recovered in all cases. However, similarly to their monolithic counterparts, the modified schemes exhibit less damping in the low frequency range.

1D model problem convergence

The convergence of the solution variables as Δt decreases is shown in Figure 5.7. The parameters are set as: $\xi_1 = 1$, $\xi_2 = 1$, $\xi_3 = 1$, $m = 1$, $c_1 = 1i$, $c_2 = 1i$ and $c_3 = 1i$. The errors are obtained by comparison to the exact solution at time instant $t = 30$. With $\bar{\rho}_\infty^h = 0$ and $\bar{\rho}_\infty^h = 0.5$, first order accuracy is observed for both the GM and AM projection methods. However, the AM projection method shows a smaller magnitude of error. Moreover, for $\bar{\rho}_\infty^h = 0.5$, the convergence slope

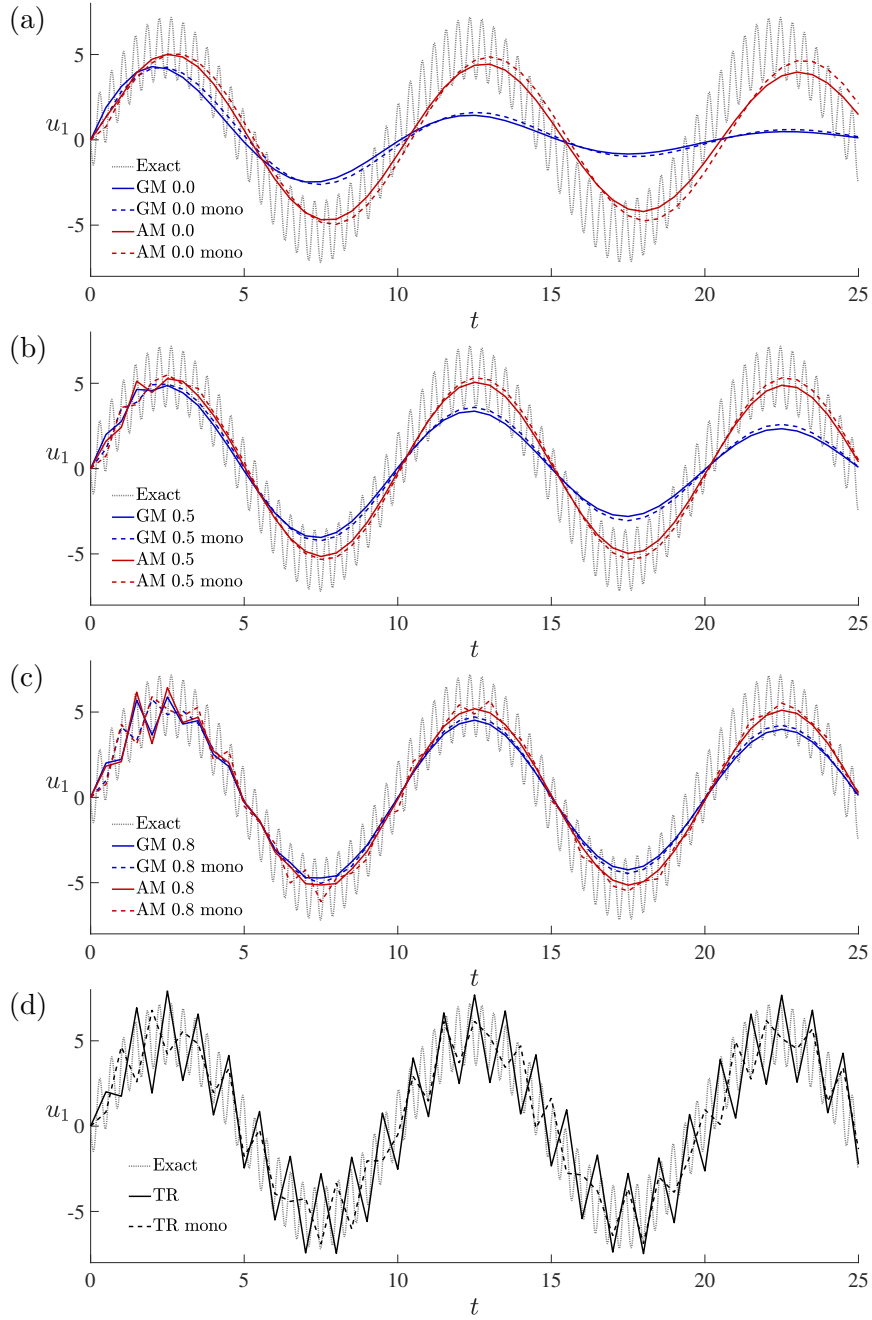


Figure 5.2: 1D model problem: u_1 response for the GM and AM projection methods with (a) $\bar{\rho}_\infty^h = 0$, (b) $\bar{\rho}_\infty^h = 0.5$, (c) $\bar{\rho}_\infty^h = 0.8$, and (d) $\bar{\rho}_\infty^h = 1$, i.e. TR projection method.

of the AM projection method begins to increase towards second order accuracy at larger time steps. For $\bar{\rho}_\infty^h = 1$, the second order accurate TR method is recovered. It can be deduced that increasing $\bar{\rho}_\infty^h$ effectively reduces the magnitude of the error for both methods.

It is pointed out that second order accuracy is achieved for all values of $\bar{\rho}_\infty^h$ with the AM projection method by setting $\delta = 1$ in (5.40). However, as shown in Subsection 5.1.4, this is associated with the loss of high frequency damping.

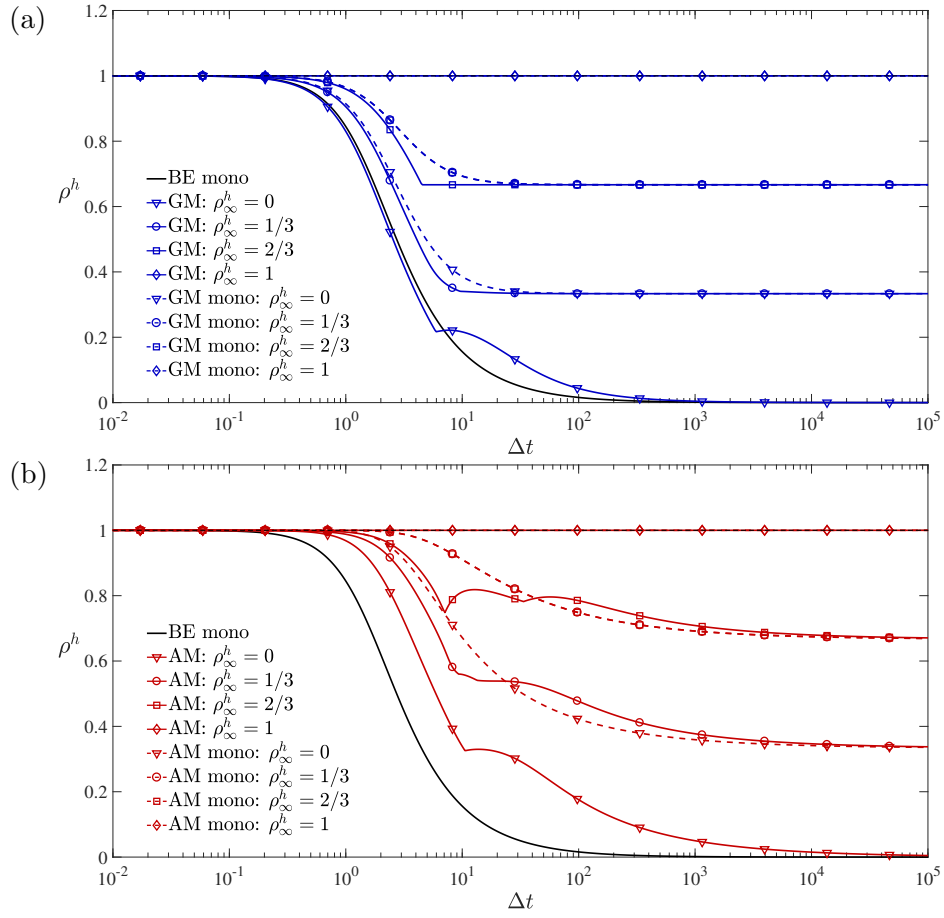


Figure 5.3: 1D model problem: Spectral radius comparison between the GM projection and monolithic methods (a), and the AM projection and monolithic methods (b), using a range of values for $\bar{\rho}_\infty^h$.

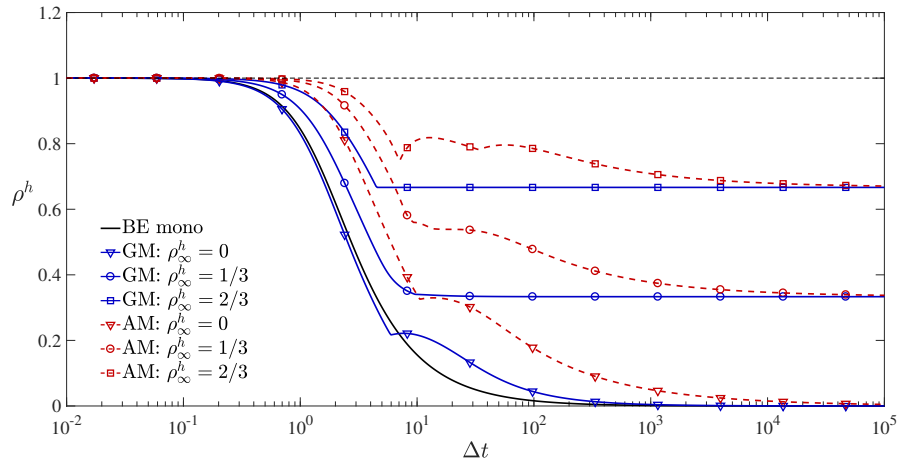


Figure 5.4: 1D model problem: Spectral radius comparison between the GM and AM projection methods.

A further comparison of the GM and AM projection methods is shown in Figure 5.8, where the solution errors are shown for the range $0 \leq \bar{\rho}_\infty^h \leq 1$. Notably for

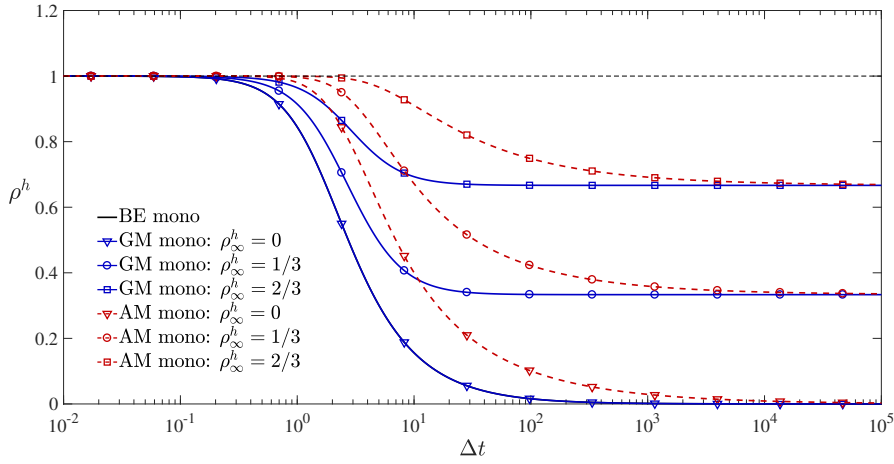


Figure 5.5: 1D model problem: Spectral radius comparison between the monolithic GM and AM methods.

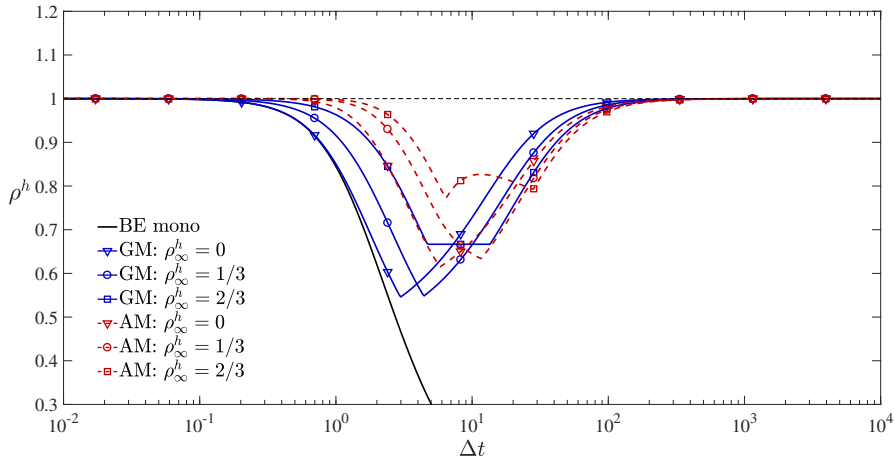


Figure 5.6: 1D model problem: Spectral radius comparison between the modified GM and AM projection methods with $\delta = 1$.

$\bar{\rho}_\infty^h < 0.9$, the AM projection method is an order of magnitude more accurate than the GM projection method.

5.1.5 Conclusions drawn from model problem analysis

Based on the observations made in Subsection 5.1.4, the following conclusions can be drawn:

- (i) The standard projection method based on the backward Euler time integration scheme which does not involve a pressure term in the first step features the same high frequency damping as its monolithic counterpart, i.e. $\rho_\infty \rightarrow 0$ for $\Delta t \rightarrow \infty$.
- (ii) The widely used pressure correction method based on BDF2, which includes a pressure predictor in the first step and which maintains second order accuracy, does not feature any high frequency damping, i.e. $\rho_\infty \rightarrow 1$ for

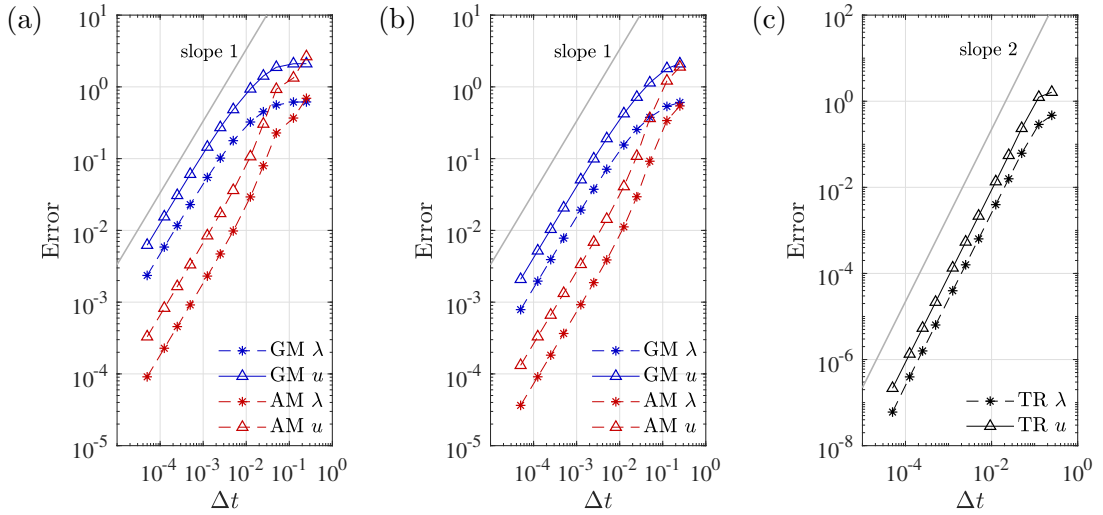


Figure 5.7: 1D model problem: $\text{Error}(\mathbf{u}) = |\mathbf{u} - \mathbf{u}_{\text{ex}}|$ and $\text{Error}(\lambda) = |\lambda - \lambda_{\text{ex}}|$ for (a) $\bar{\rho}_{\infty}^h = 0$, (b) $\bar{\rho}_{\infty}^h = 0.5$ and (c) $\bar{\rho}_{\infty}^h = 1$, at $t = 30$. The terms $(\bullet)_{\text{ex}}$ denote the analytical solution.

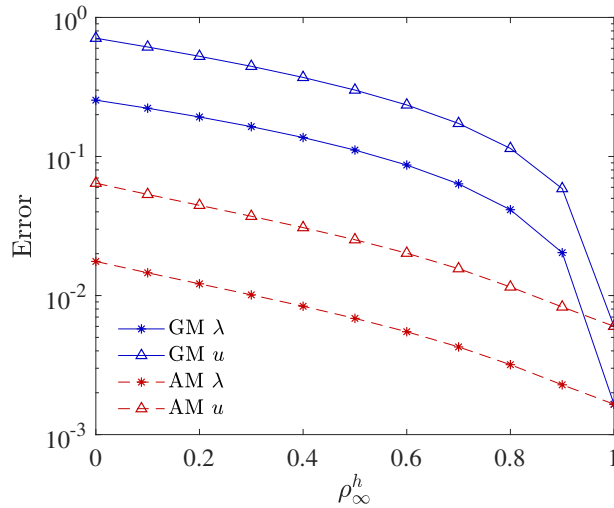


Figure 5.8: 1D model problem: Comparison of errors obtained for different values of $\bar{\rho}_{\infty}^h$. The errors are evaluated at $\Delta t = 0.01$.

$\Delta t \rightarrow \infty$. This is in stark contrast to its monolithic counterpart where $\rho_{\infty} \rightarrow 0$ for $\Delta t \rightarrow \infty$.

- (iii) In the proposed GM and AM projection schemes, the parameters δ and $\bar{\rho}_{\infty}^h$ control high frequency damping according to Equation (5.43).
- (iv) The investigation confirms the well-known fact that overall second order accuracy can only be obtained for $\delta = 1$. Together with Conclusion (iii), this suggests that it is not possible to formulate a second order accurate pressure correction method which possesses any high frequency damping.
- (v) The proposed AM scheme features only first order accuracy, but renders significantly more accurate results than the standard backward Euler projection

method or indeed the proposed GM scheme. The additional computational cost associated with the proposed AM scheme is negligible. Similarly to its monolithic counterpart it provides the desired high frequency damping while preserving the resolved low frequency response.

5.2 Formulations for incompressible fluid flow

In this section the projection methods proposed in Subsection 5.1 will be applied to the incompressible Navier-Stokes equations.

Consider a domain $\Omega \subset \mathbb{R}^d$ ($d \leq 3$) with boundary Γ which is separable into Dirichlet and Neumann subsets, Γ_g and Γ_q . The velocity field \mathbf{u} and pressure field p are described by the following governing equations

$$\rho(\dot{\mathbf{u}} + (\mathbf{u} \cdot \nabla)\mathbf{u}) - \nabla \cdot \boldsymbol{\sigma} = \mathbf{f} \quad \text{in } \Omega \times \mathcal{I}, \quad (5.47a)$$

$$\nabla \cdot \mathbf{u} = 0 \quad \text{in } \Omega \times \mathcal{I}, \quad (5.47b)$$

$$\mathbf{u} = \mathbf{u}_g \quad \text{on } \Gamma_g \times \mathcal{I}, \quad (5.47c)$$

$$\boldsymbol{\sigma} \cdot \mathbf{n} = \mathbf{t} \quad \text{on } \Gamma_q \times \mathcal{I}, \quad (5.47d)$$

$$\mathbf{u}|_{t=0} = \mathbf{u}_0 \quad \text{in } \Omega, \quad (5.47e)$$

where $\mathcal{I} = [0, T]$ is again the time interval under consideration, \mathbf{f} is the body force vector, \mathbf{u}_g is the velocity prescribed on Γ_g , \mathbf{n} is the outward normal to Γ , $\boldsymbol{\sigma}$ is the Cauchy stress tensor, and \mathbf{t} is the imposed boundary traction. Substituting the Cauchy stress tensor for Newtonian fluids,

$$\boldsymbol{\sigma} = -p\mathbf{I} + 2\mu\nabla^s \mathbf{u}, \quad (5.48)$$

into Equation (5.47a) renders

$$\rho(\dot{\mathbf{u}} + (\mathbf{u} \cdot \nabla)\mathbf{u}) - \mu\Delta\mathbf{u} + \nabla p = \mathbf{f}. \quad (5.49)$$

5.2.1 Projection schemes: time discretisation

Analogously to Subsection 5.1.3, GM and AM projection schemes are proposed for the Navier-Stokes Equations (5.47a)-(5.47e). The nonlinearity of the convection term is avoided by extrapolating the convective velocity $\mathbf{u}^{*,n+1}$ from the solution history in an appropriate manner.

GM projection method

The method to be presented is based on the same strategy used in Subsection 5.1.3, specifically Equations (5.30) and (5.28). The first step of the GM projection method with end-of-step elimination involves the computation of the intermediate velocity, $\tilde{\mathbf{u}}$, at time instance t^{n+1} from

$$\begin{aligned} \frac{\rho}{\Delta t} (\tilde{\mathbf{u}}^{n+1} - \tilde{\mathbf{u}}^n) + \rho (\tilde{\mathbf{u}}^{*,n+\gamma} \cdot \nabla) \tilde{\mathbf{u}}^{n+\gamma} + \mu\Delta\tilde{\mathbf{u}}^{n+\gamma} \\ + \nabla ((\gamma + \delta)p^n + (1 - \gamma - \delta)p^{n-1}) = \mathbf{f}^{n+\gamma}, \end{aligned} \quad (5.50a)$$

$$\tilde{\mathbf{u}}^{n+1}|_{\Gamma_g} = \mathbf{u}_D^{n+1}, \quad (5.50b)$$

with

$$\tilde{\mathbf{u}}^{*,n+\gamma} = \gamma \tilde{\mathbf{u}}^{*,n+1} + (1 - \gamma) \tilde{\mathbf{u}}^n, \quad (5.51)$$

$$\tilde{\mathbf{u}}^{n+\gamma} = \gamma \tilde{\mathbf{u}}^{n+1} + (1 - \gamma) \tilde{\mathbf{u}}^n, \quad (5.52)$$

$$\mathbf{f}^{n+\gamma} = \gamma \mathbf{f}^{n+1} + (1 - \gamma) \mathbf{f}^n. \quad (5.53)$$

Here the parameters γ and δ are obtained from Equations (5.12) and (5.45) respectively. The convective velocity extrapolation is expressed as

$$\tilde{\mathbf{u}}^{*,n+1} = 2\tilde{\mathbf{u}}^n - \tilde{\mathbf{u}}^{n-1}. \quad (5.54)$$

Equation (5.50a) resembles Equation (5.30), with λ being replaced by the pressure p and the addition of a convection term. The second order extrapolation in Equation (5.54) is not necessary for $\bar{\rho}_\infty^h < 1$, but crucial to ensure second order accuracy for $\bar{\rho}_\infty^h = 1$ (TR). The second step of the GM projection method is based on

$$\frac{\rho}{\Delta t} (\mathbf{u}^{n+1} - \tilde{\mathbf{u}}^{n+1}) + \nabla (\gamma p^{n+1} + (1 - \gamma - \delta) p^n) = \mathbf{0}, \quad (5.55a)$$

$$\nabla \cdot \mathbf{u}^{n+1} = 0, \quad (5.55b)$$

$$\mathbf{u}^{n+1} \cdot \mathbf{n}|_{\Gamma_g} = 0. \quad (5.55c)$$

Taking the divergence of the terms in Equation (5.55a) and applying Equation (5.55b) yields the following Poisson equation for p^{n+1}

$$-\frac{\rho}{\Delta t} \nabla \cdot \tilde{\mathbf{u}}^{n+1} + \Delta (\gamma p^{n+1} + (1 - \gamma - \delta) p^n) = 0. \quad (5.56)$$

Generalised- α projection method

Following the same strategy as for Equations (5.40) and (5.37) in Subsection 5.1.3, the first step of the AM projection method with end-of-step elimination requires to compute $\tilde{\mathbf{u}}^{n+1}$ from

$$\rho \left(1 - \frac{\alpha_m}{\gamma} \right) \dot{\mathbf{u}}^n + \frac{\rho \alpha_m}{\gamma \Delta t} (\tilde{\mathbf{u}}^{n+1} - \tilde{\mathbf{u}}^n) + \rho (\tilde{\mathbf{u}}^{*,n+\alpha_f} \cdot \nabla) \tilde{\mathbf{u}}^{n+\alpha_f} + \mu \Delta \tilde{\mathbf{u}}^{n+\alpha_f} \quad (5.57a)$$

$$+ \nabla ((\alpha_f + \delta) p^n + (1 - \alpha_f - \delta) p^{n-1}) = \mathbf{f}^{n+\alpha_f} \quad (5.57b)$$

$$\tilde{\mathbf{u}}^{n+1}|_{\Gamma_g} = \mathbf{u}_D^{n+1}$$

with

$$\tilde{\mathbf{u}}^{*,n+\alpha_f} = \alpha_f \tilde{\mathbf{u}}^{*,n+1} + (1 - \alpha_f) \tilde{\mathbf{u}}^n \quad (5.58)$$

$$\tilde{\mathbf{u}}^{n+\alpha_f} = \alpha_f \tilde{\mathbf{u}}^{n+1} + (1 - \alpha_f) \tilde{\mathbf{u}}^n \quad (5.59)$$

$$\mathbf{f}^{n+\alpha_f} = \alpha_f \mathbf{f}^{n+1} + (1 - \alpha_f) \mathbf{f}^n, \quad (5.60)$$

where the parameters α_m , α_f and γ are given in Equation (2.64), and the convective velocity extrapolation is the same as in Equation (5.54).

In the second step the relations

$$\frac{\rho\alpha_m}{\gamma\Delta t} (\mathbf{u}^{n+1} - \tilde{\mathbf{u}}^{n+1}) + \nabla (\alpha_f p^{n+1} + (1 - \alpha_f - \delta) p^n) = \mathbf{0}, \quad (5.61)$$

$$\nabla \cdot \mathbf{u}^{n+1} = 0, \quad (5.62)$$

$$\mathbf{u}^{n+1} \cdot \mathbf{n}|_\Gamma = 0, \quad (5.63)$$

render the following Poisson equation for the pressure p^{n+1}

$$-\frac{\rho\alpha_m}{\gamma\Delta t} \nabla \cdot \tilde{\mathbf{u}}^{n+1} + \Delta (\alpha_f p^{n+1} + (1 - \alpha_f - \delta) p^n) = 0. \quad (5.64)$$

The acceleration is computed from

$$\begin{aligned} \rho \dot{\mathbf{u}}^{n+1} &= \frac{\rho}{\gamma\Delta t} (\tilde{\mathbf{u}}^{n+1} - \tilde{\mathbf{u}}^n) - \rho \frac{1-\gamma}{\gamma} \dot{\mathbf{u}}^n \\ &\quad - \frac{1}{\alpha_m} \nabla (\alpha_f p^{n+1} + (1 - 2\alpha_f - \delta) p^n - (1 - \alpha_f - \delta) p^{n-1}). \end{aligned} \quad (5.65)$$

5.2.2 Finite element method: spatial discretisation

The spatial discretisation is based on the following velocity and pressure interpolation and weighting functions

$$\mathbf{u}^h(\mathbf{x}) = \sum_{A \in \eta} N_A(\mathbf{x}) \mathbf{u}_A, \quad \mathbf{v}^h(\mathbf{x}) = \sum_{A \in \eta} N_A(\mathbf{x}) \mathbf{v}_A, \quad (5.66)$$

$$p^h(\mathbf{x}) = \sum_{\tilde{A} \in \tilde{\eta}} \tilde{N}_{\tilde{A}}(\mathbf{x}) p_{\tilde{A}}, \quad q^h(\mathbf{x}) = \sum_{\tilde{A} \in \tilde{\eta}} \tilde{N}_{\tilde{A}}(\mathbf{x}) q_{\tilde{A}}, \quad (5.67)$$

where η and $\tilde{\eta}$, A and \tilde{A} , N_A and $\tilde{N}_{\tilde{A}}$ represent, respectively, the sets of nodes, the global node numbers and the shape functions for velocity and pressure.

For a compact presentation of the weak forms to be used for the computations in Steps 1 and 2 of the proposed schemes, it is useful to define the following integral forms

$$(\mathbf{u}, \mathbf{v}) = \int_{\Omega} \mathbf{u} \cdot \mathbf{v} \, d\Omega, \quad (5.68)$$

$$a(\mathbf{u}, \mathbf{v}) = \mu \int_{\Omega} \nabla \mathbf{u} : \nabla \mathbf{v} \, d\Omega, \quad (5.69)$$

$$b(\mathbf{v}, q) = - \int_{\Omega} q \nabla \cdot \mathbf{v} \, d\Omega, \quad (5.70)$$

$$c(\mathbf{u}, \mathbf{v}, \mathbf{w}) = \rho \int_{\Omega} (\mathbf{u} \cdot \nabla \mathbf{u}) \cdot \mathbf{w} \, d\Omega. \quad (5.71)$$

GM projection method: The first step requires to solve the weak form of Equation (5.50) for the intermediate velocity: Find $\tilde{\mathbf{u}}^{n+1} \in \tilde{\mathcal{S}}$, such that for all $\mathbf{v} \in \tilde{\mathcal{V}}$

$$\begin{aligned} \left(\rho \frac{\tilde{\mathbf{u}}^{n+1} - \tilde{\mathbf{u}}^n}{\Delta t}, \mathbf{v} \right) &+ a(\tilde{\mathbf{u}}^{n+\gamma}, \mathbf{v}) + c(\tilde{\mathbf{u}}^{*,n+\gamma}, \tilde{\mathbf{u}}^{n+\gamma}, \mathbf{v}) \\ &+ b(\mathbf{v}, (\gamma + \delta) p^n + (1 - \gamma - \delta) p^{n-1}) = (\mathbf{f}^{n+\gamma}, \mathbf{v}). \end{aligned} \quad (5.72)$$

where $\tilde{\mathcal{S}}$ and $\tilde{\mathcal{V}}$ represent the appropriate finite element approximation spaces and the superscript h has been omitted. The quantities $\tilde{\mathbf{u}}^{*,n+\gamma}$, $\tilde{\mathbf{u}}^{n+\gamma}$ and $\mathbf{f}^{n+\gamma}$ are obtained from Equations (5.51)-(5.53). The Dirichlet boundary conditions are applied directly to the intermediate velocity $\tilde{\mathbf{u}}$.

The Poisson Equation (5.56) yields the following weak formulation: Find $p^{n+1} \in \mathcal{P}$, such that for all $q \in \mathcal{P}$

$$(\nabla(\gamma p^{n+1} + (1 - \gamma - \delta)p^n), \nabla q) = \frac{\rho}{\Delta t} b(\tilde{\mathbf{u}}^{n+1}, q), \quad (5.73)$$

where \mathcal{P} represents the appropriate finite element approximation space.

AM projection method: The weak form of Equation (5.57) in the first step reads: Find $\tilde{\mathbf{u}}^{n+1} \in \tilde{\mathcal{S}}$, such that for all $\mathbf{v} \in \tilde{\mathcal{V}}$

$$\begin{aligned} & \left(\rho \left(\dot{\mathbf{u}}^n \left(1 - \frac{\alpha_m}{\gamma} \right) + \alpha_m \frac{\tilde{\mathbf{u}}^{n+1} - \tilde{\mathbf{u}}^n}{\gamma \Delta t} \right), \mathbf{v} \right) + a(\tilde{\mathbf{u}}^{n+\alpha_f}, \mathbf{v}) \\ & + c(\tilde{\mathbf{u}}^{*,n+\alpha_f}, \tilde{\mathbf{u}}^{n+\alpha_f}, \mathbf{v}) + b(\mathbf{v}, (\alpha_f + \delta)p^n + (1 - \alpha_f - \delta)p^{n-1}) \\ & = (\mathbf{f}^{n+\alpha_f}, \mathbf{v}). \end{aligned} \quad (5.74)$$

The weak form of Equation (5.64) is expressed as: Find $p^{n+1} \in \mathcal{P}$, such that for all $q \in \mathcal{P}$

$$(\nabla(\alpha_f p^{n+1} + (1 - \alpha_f - \delta)p^n), \nabla q) = \frac{\rho \alpha_m}{\gamma \Delta t} b(\tilde{\mathbf{u}}^{n+1}, q). \quad (5.75)$$

The acceleration update from Equation (5.65) is obtained from

$$\begin{aligned} (\rho \dot{\mathbf{u}}^{n+1}, \mathbf{v}) &= \left(\rho \frac{\tilde{\mathbf{u}}^{n+1} - \tilde{\mathbf{u}}^n}{\gamma \Delta t}, \mathbf{v} \right) - \left(\frac{1 - \gamma}{\gamma} \rho \dot{\mathbf{u}}^n, \mathbf{v} \right) \\ &- b \left(\mathbf{v}, \frac{1}{\alpha_m} (\alpha_f p^{n+1} + (1 - 2\alpha_f - \delta)p^n - (1 - \alpha_f - \delta)p^{n-1}) \right). \end{aligned} \quad (5.76)$$

It should be noted that, if the product of the mass matrix with the nodal accelerations is employed as history variable, then Equation (5.76) is explicit and its computational cost negligible. This is consistent with Equation (5.74) which also involves the product of the $\dot{\mathbf{u}}$ with the mass matrix.

5.2.3 Stable velocity-pressure interpolations

It is well-known that a pure Galerkin based mixed velocity-pressure finite element formulation for the incompressible Navier-Stokes equations renders spurious oscillations in the pressure field if the same interpolation functions are used for the velocity and the pressure fields. Admissible choices of approximation spaces are required to satisfy the inf-sup condition,

$$\inf_{\mathbf{q}^h \in \mathcal{P}^h} \sup_{\mathbf{v}^h \in \mathcal{V}^h} \frac{(\nabla \cdot \mathbf{v}^h, \mathbf{q}^h)}{\|\mathbf{q}\|_0 \|\mathbf{v}^h\|_1} \geq \alpha > 0, \quad (5.77)$$

where α is a constant, which is independent of the element size. Inequality (5.77) is also known as the LBB compatibility condition [163, 164, 165, 166, 167]. Alternatively, appropriate stabilisation techniques can be employed which are based on variants of the Galerkin method and thereby circumvent the condition. Prominent techniques such as the SUPG/PSPG stabilisation technique or Least-squares finite element method have been widely used and further developed (see, for instance, [168, 169, 124, 170, 171, 172]). It is interesting that, in the context of projection schemes, smooth pressure fields may be obtained even without stabilisation or inf-sup conformity. This is due to the fact that, for large time steps, the incompressibility constraint is far less rigorously enforced. However, it has now become common practice to employ inherently stable velocity-pressure formulations in order to ensure maximum robustness of the overall methodology (see for instance [162, 173]). Similarly to the issue of high-frequency damping addressed in this work, a stable velocity-pressure formulation is crucial to allow for a large degree of independence between spatial and temporal discretisations. Thus, the well-known inf-sup stable Taylor-Hood element (P_2/P_1) based on quadratic velocity and linear pressure triangular elements is employed in the numerical examples in Section 5.3.

5.3 Numerical examples

5.3.1 Lid-driven cavity

As a first demonstration, the benchmark flow problem of a lid-driven cavity is considered. The side length of the square cavity is one unit length and the boundary conditions are shown in Figure 5.9. The no-slip boundary condition is applied to all edges except at the lid boundary, where the normal velocity component is set to zero and the tangential velocity component follows the profile,

$$u_{\text{lid}}(x) = 1 - e^{a(x-1)} - e^{-ax} \quad 0 \leq x \leq 1, \quad (5.78)$$

where a is a dimensionless parameter and x is the horizontal coordinate (adopted from Dettmer *et al.*[81]). The profile (5.78) allows for the control of the sharpness of the singularity in the top corners of the cavity. For this demonstration, $a = 50$ is used. Two Reynolds numbers are tested, $Re = 100$ and $Re = 1000$, which result from using viscosities of $\mu = 0.01$ and $\mu = 0.001$ respectively and a density of $\rho = 1$. Three unstructured meshes are considered: mesh *A* (847 elements, 1782 P_2 nodes), mesh *B* (2061 elements, 4260 P_2 nodes) and mesh *C* (4200 elements, 8597 P_2 nodes). Mesh *A* is shown in Figure 5.9. Initially the fluid is at rest and the velocity at the lid is applied instantaneously. The GM projection scheme with $\bar{\rho}_{\infty}^h = 0$ is used.

The steady state solutions shown in Figures 5.10-5.12 develop quickly and agree well with the reference solutions. The streamlines and pressure contours are shown for $Re = 100$ and $Re = 1000$ in Figures 5.10 and 5.11, respectively. Figure 5.12a shows the horizontal velocity component u and the vertical velocity component v along the vertical and horizontal centrelines of the cavity respectively

for $Re = 100$. Similarly the centreline velocities for $Re = 1000$ are shown in Figure 5.12b.

5.3.2 Lid-driven cavity with dynamic boundary conditions

For the purpose of studying the convergence of the projection schemes, the lid driven cavity problem is considered once more. In order to avoid a steady state solution, the velocity profile in Equation (5.78) is replaced by the time dependent profile,

$$u_{\text{lid}}(x, t) = \frac{1}{2} \sin(\pi x) (1 - \cos(3\pi t)). \quad (5.79)$$

In the convergence analyses to follow, the problem is run until $t = 1$. The viscosity and density are respectively set to $\mu = 0.0025$ and $\rho = 1$ resulting in $Re = 400$, and a mesh with 1140 elements (2365 P_2 nodes) is used. It is demonstrated that, as the time step size Δt is reduced while the spatial discretisation remains unchanged, the velocity and pressure fields converge to an exclusively mesh-dependent approximation of the exact solution. It is shown that, for the same spatial discretisation, the GM and AM projection schemes and the monolithic solver converge to the same response. The reference responses for the Stokes problem in Subsection 5.3.2 and for the Navier-Stokes problem in Subsection 5.3.2 have been computed with the corresponding monolithic AM solvers based on $\Delta t = 0.0001$. The term “error” is used for the deviation between the reference solution and the solutions obtained with the GM and AM projection schemes on the same mesh but for various values of Δt . Similar studies of temporal convergence have been performed in [80, 161, 162, 173] in the context of different methodologies.

Error convergence for Stokes problem

The convergence rates of the L^2 error norms of the velocity and pressure fields are shown for the Stokes flow problem in Figure 5.13, where the GM and AM projection methods are compared. It is clear that for $\bar{\rho}_\infty^h = 0$, the GM and AM projection methods obtain first order convergence rates for both the velocity and

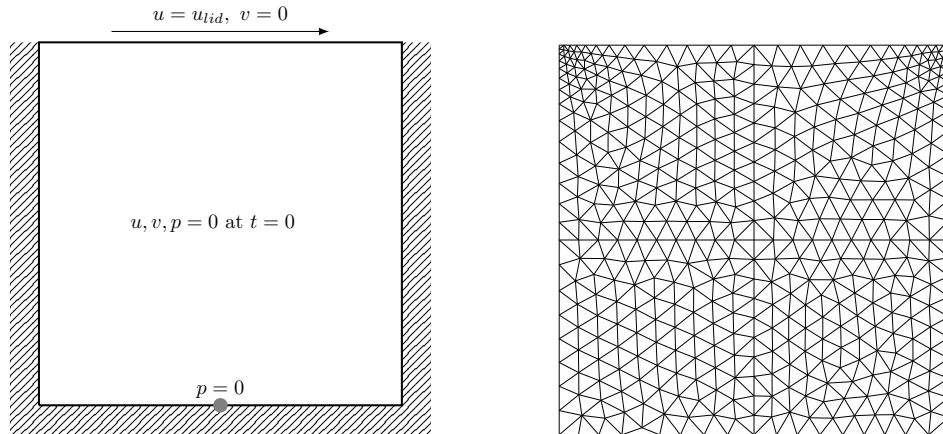


Figure 5.9: Lid-driven cavity: Boundary conditions and mesh A

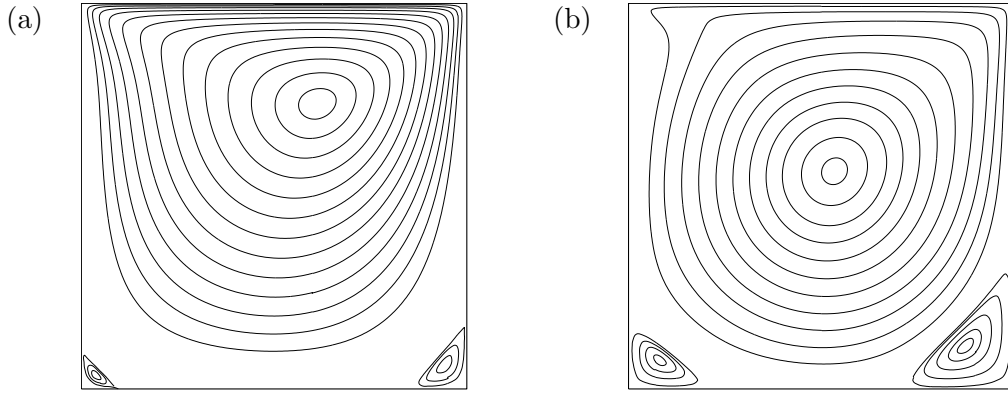


Figure 5.10: Lid-driven cavity: Streamlines for $Re = 100$ (a) and $Re = 1000$ (b).

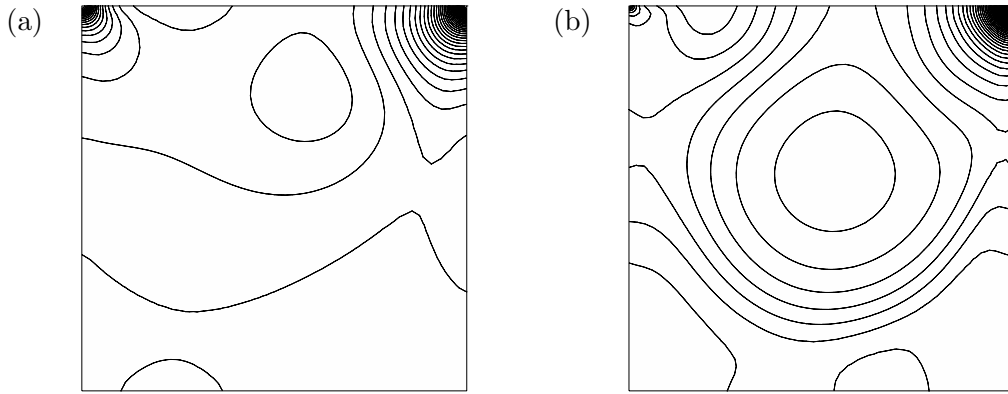


Figure 5.11: Lid-driven cavity: Pressure isolines for $Re = 100$ (a) and $Re = 1000$ (b).

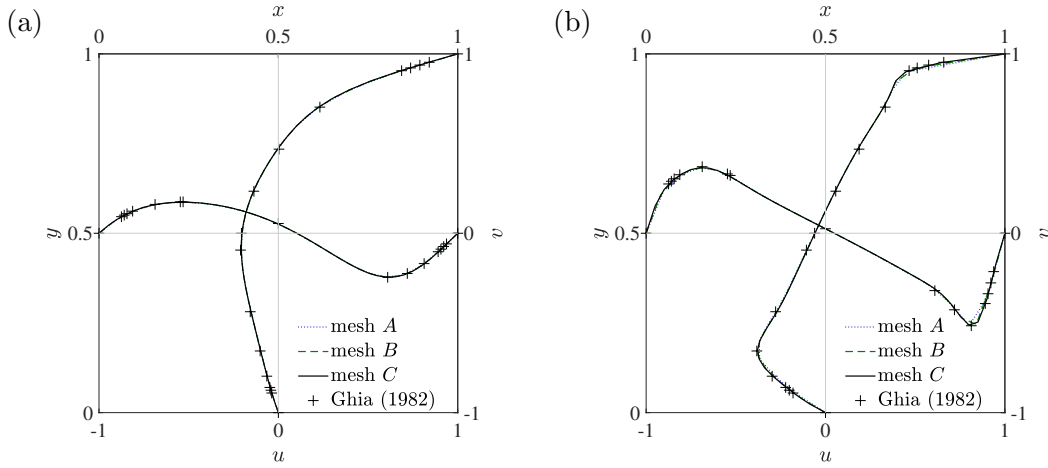


Figure 5.12: Lid-driven cavity: Horizontal velocity u along the vertical centreline and vertical velocity v along the horizontal centreline, for $Re = 100$ (a) and $Re = 1000$ (b).

pressure field errors. Although both methods are first order accurate in time, the AM projection method produces a smaller magnitude of error for both velocity and pressure fields. For $\rho_\infty = 0.5$, both methods again obtain first order accuracy,

although the convergence slope increases towards second order accuracy for larger time steps. Again, the AM projection method performs better in terms of the error magnitude. For $\bar{\rho}_\infty^h = 1$, the trapezoidal method is recovered with second order accuracy. As with the 1D case (Figure 5.7) it can be deduced that increasing $\bar{\rho}_\infty^h$ effectively reduces the magnitude of error for both methods.

Error convergence for Navier-Stokes problem

The L^2 norms of the velocity and pressure field errors are shown for the GM and AM projection methods when considering Navier-Stokes flow in Figure 5.14. It is evident that the convergence slopes closely reflect the observations made for the Stokes flow problem, hence the same accuracy is attained.

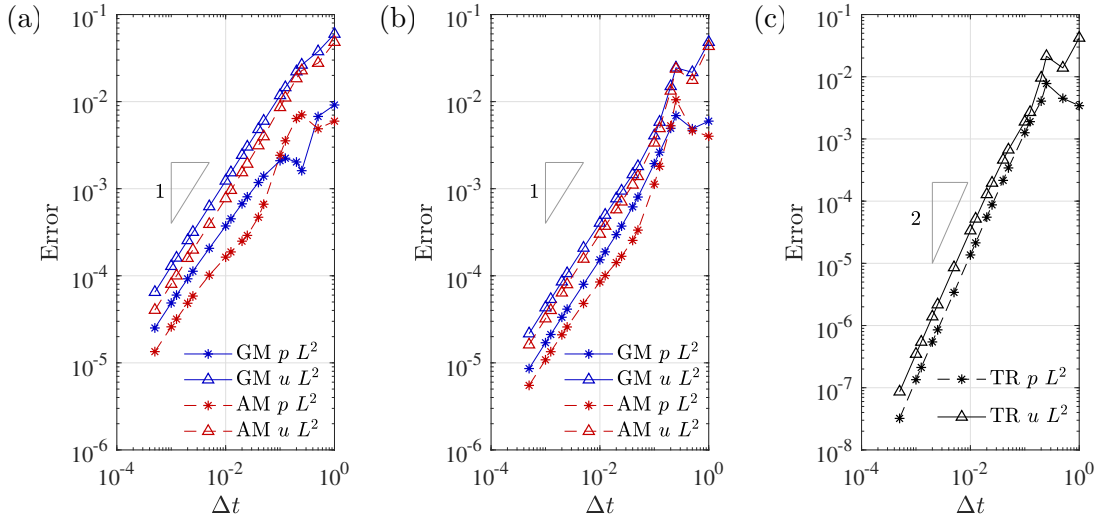


Figure 5.13: Stokes flow cavity model problem: Convergence rates for velocity and pressure field errors with (a) $\rho_\infty^h = 0$, (b) $\rho_\infty^h = 0.5$ and (c) $\rho_\infty^h = 1$.

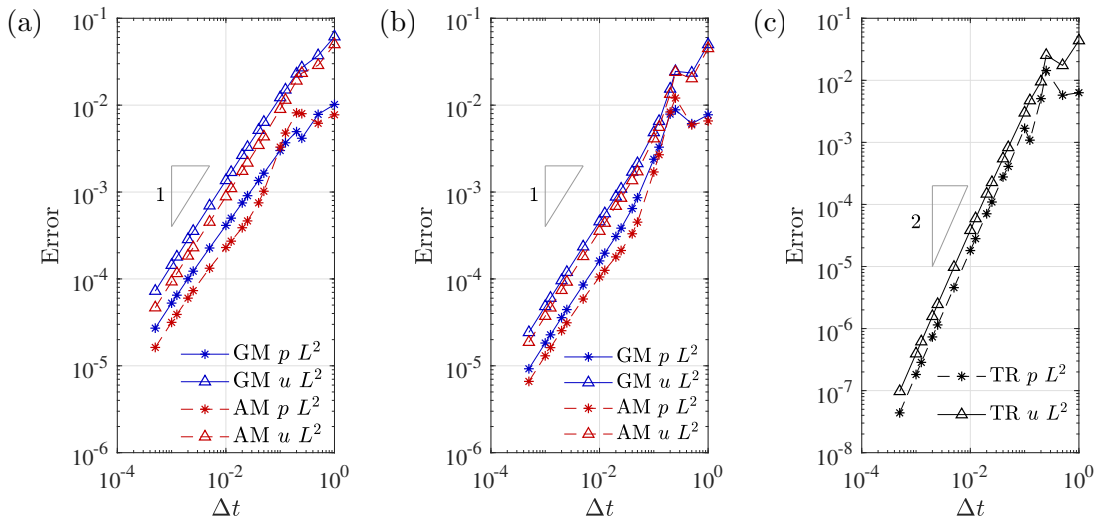


Figure 5.14: Navier-Stokes flow cavity model problem: Convergence rates for velocity and pressure field errors with (a) $\rho_\infty^h = 0$, (b) $\rho_\infty^h = 0.5$ and (c) $\rho_\infty^h = 1$.

5.3.3 Flow around a cylinder

In this example, the well known benchmark problem of flow around a stationary circular cylinder is investigated. The geometry dimensions and boundary conditions for the problem are shown in Figure 5.15. The vertical velocity component v is prescribed as zero on the upper and lower boundaries, while the horizontal component u remains free. Also the pressure is prescribed as zero at the outlet boundary, and u is prescribed uniformly as u_∞ on the inlet boundary, in compliance with the assumption that the flow is uniform far away from the cylinder. In the analyses to follow, the parameters are set as $u_\infty = 1$, $\mu = 0.01$, $\rho = 1$ and $d = 1$, such that $Re = 100$. The mesh employed possesses 1708 elements (3472 P_2 nodes), as shown in Figure 5.15.

For the purpose of this study, several dimensionless quantities are defined. The coefficients of lift and drag, C_L and C_D , as well as the Strouhal number St are evaluated using the expressions

$$C_L(t) = \frac{F_L(t)}{\frac{1}{2}\rho u_\infty^2 d}, \quad C_D(t) = \frac{F_D(t)}{\frac{1}{2}\rho u_\infty^2 d}, \quad St = \frac{fd}{u_\infty}, \quad (5.80)$$

where F_L and F_D are the lift and drag forces respectively, and f is the frequency of the lift force.

Figure 5.16 shows the C_L and C_D evolution with time for $Re = 100$. The C_L amplitude and St number are obtained as $C_L = \pm 0.292$ and $St = 0.165$ respectively, for a time step of $\Delta t = 0.01$. Due to the lack of analytical solutions, a comparison is made to experimental data by Roshko [174] and numerical data by Kadapa *et al.* [175]. The St number agrees well with the experimental data found in [174], where a best-fit line for experimentally obtained data is presented, i.e. $St = 0.212(1 - 21.2/Re)$, which yields $St = 0.167$ for $Re = 100$. An extensive numerical study carried out in [175], compares results obtained for C_L and St coefficients at $Re = 100$ by various authors. The C_L amplitudes range between

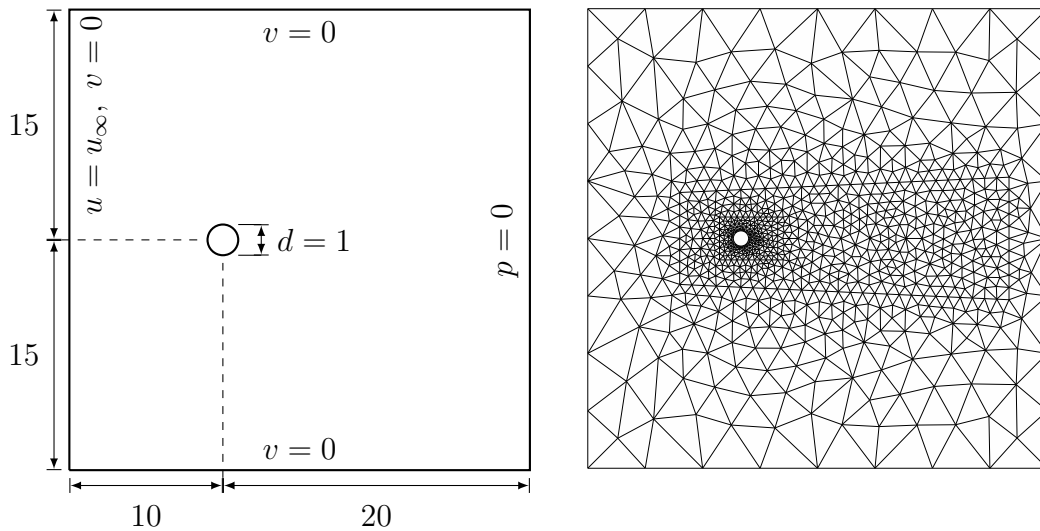


Figure 5.15: Flow around a cylinder: Geometry (not to scale), boundary conditions and mesh.

± 0.250 and ± 0.341 , and St number, between 0.160 and 0.175. Clearly the results of the present study lie within this range.

The variation of the lift amplitude and the Strouhal number with the time step size is displayed in Figure 5.17. The convergence as $\Delta t \rightarrow 0$ is clearly visible. It can also be observed that the AM projection scheme performs significantly better than the respective GM scheme and that both schemes render more accurate results for $\bar{\rho}_\infty^h = 0.5$ than for $\bar{\rho}_\infty^h = 0$.

The temporal C_L amplitude and St errors are shown for the GM and AM projection methods with $\bar{\rho}_\infty^h$ set to 0 and 0.5 in Figure 5.18. The errors are computed by comparing the solutions to that of a reference solution obtained from a monolithic AM solver on the same spatial discretisation with $\bar{\rho}_\infty^h = 0.5$ and $\Delta t = 0.0005$. Thus, similar to Subsection 5.3.2, the term “error” refers to the deviation from the mesh-dependent limit solution, rather than from the exact solution. For the same mesh, the lift coefficients and the Strouhal numbers obtained from the monolithic solver, the GM and AM projection schemes all converge to the same values. The projections methods display first order accuracy, with the AM method achieving a lower magnitude of error than the GM method for the same respective values of $\bar{\rho}_\infty^h$.

Figure 5.19 similarly shows the C_L and St errors when considering the GM and AM projection methods with $\bar{\rho}_\infty^h = 0.9$. Observing the C_L convergence, it is visible that there is an increase of the slope at larger time steps for both methods. In comparison to Figure 5.18, a decrease in the magnitude of error is observed.

Figure 5.20 shows the convergence of the AM projection method for $\delta = 1$ and $\bar{\rho}_\infty^h = 0.9$ in comparison to its monolithic counterpart. It is evident that the solutions for C_L and St become unstable at around $\Delta t \approx 0.04$. This is attributed to the lack of numerical damping of the method, which has been demonstrated in Subsection 5.1.4.

Summarising, the performance of the GM and AM strategies for the flow around the cylinder are consistent with the analysis of the model problem in Section 5.1.

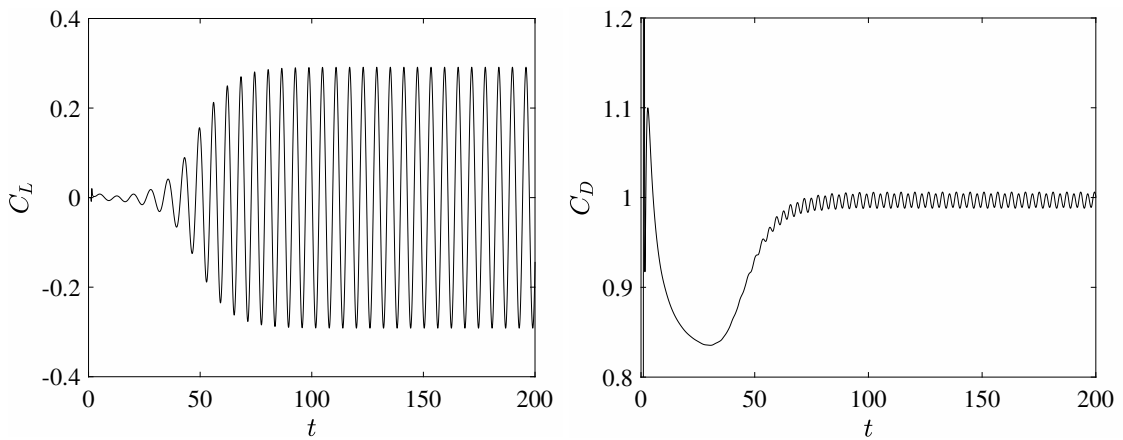


Figure 5.16: Flow around a cylinder: Evolution with time for the lift coefficient C_L (left), and drag coefficient C_D (right), considering the AM projection method with $\rho_\infty = 0.5$, $Re = 100$, $\Delta t = 0.01$, and 1708 elements.

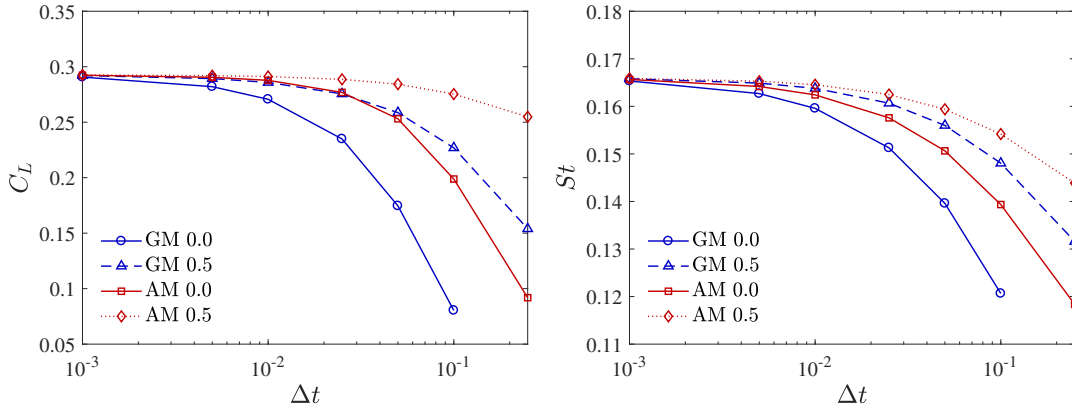


Figure 5.17: Flow around a cylinder: C_L amplitude convergence (left), and St convergence (right), for $Re = 100$.

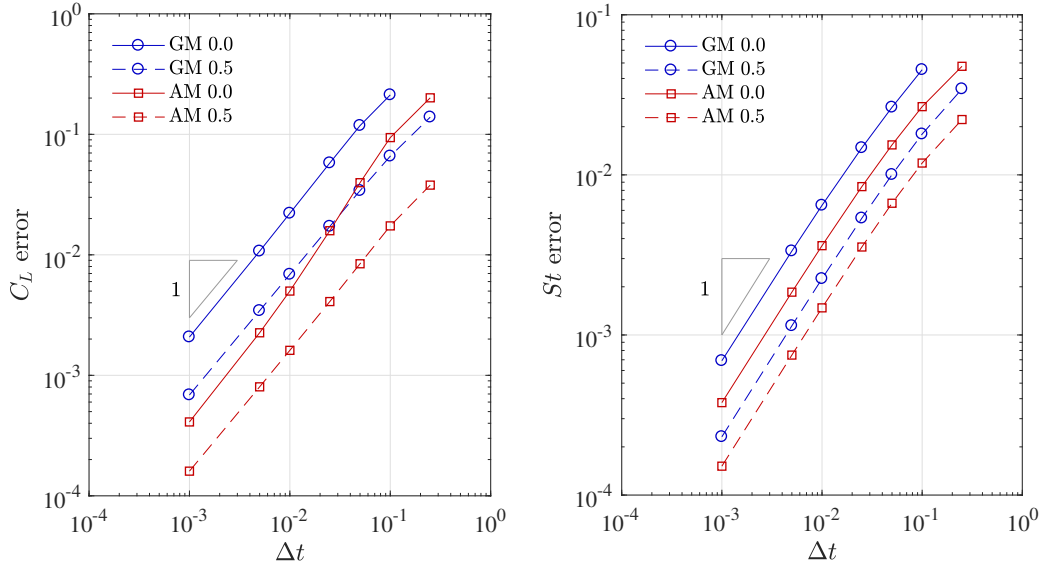


Figure 5.18: Flow around a cylinder: C_L amplitude error convergence (left), and St error convergence (right), for GM and AM projection methods with $\bar{\rho}_\infty^h$ set to 0 and 0.5.

5.4 Concluding remarks

In Section 2 a discrete model problem consisting of point masses and dash-pots has been introduced, which allows for insight into the performance of projection schemes, including aspects which are otherwise difficult to assess, in particular the numerical damping. The investigation performed in Section 2, on the basis of this model problem, suggests that a second order accurate projection scheme cannot possess any high frequency damping.

Also in Section 2, two new methodologies have been proposed which may offer a compromise between accuracy and high-frequency damping. In particular it has been investigated to what extent the properties of the generalised- α method can be maintained when moving from a monolithic scheme to a projection scheme.

In Section 3 the proposed methodologies have been applied to the incompress-

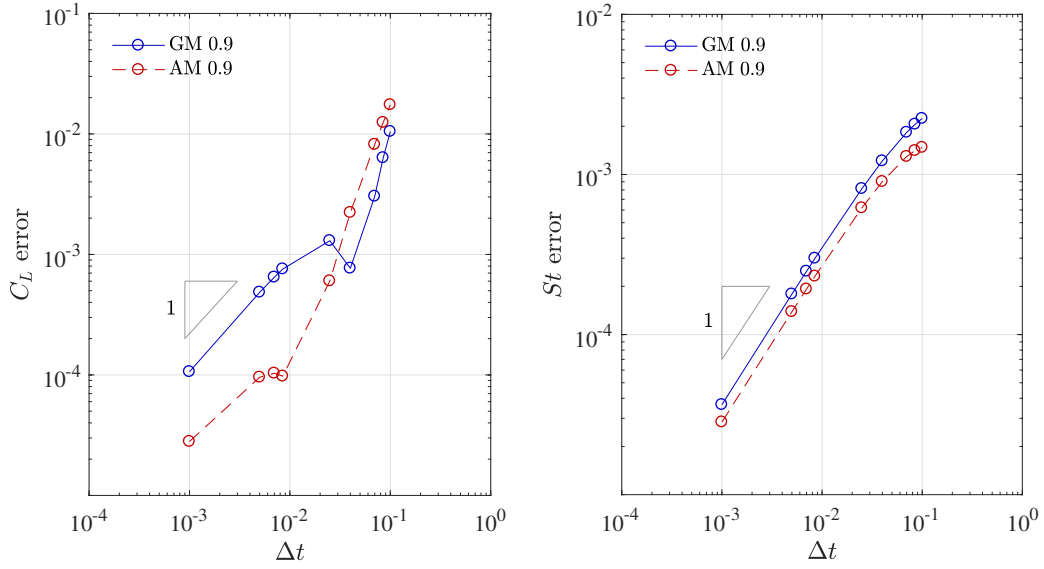


Figure 5.19: Flow around a cylinder: C_L amplitude error convergence (left), and St error convergence (right), with $\bar{\rho}_\infty^h = 0.9$ for the GM and AM methods

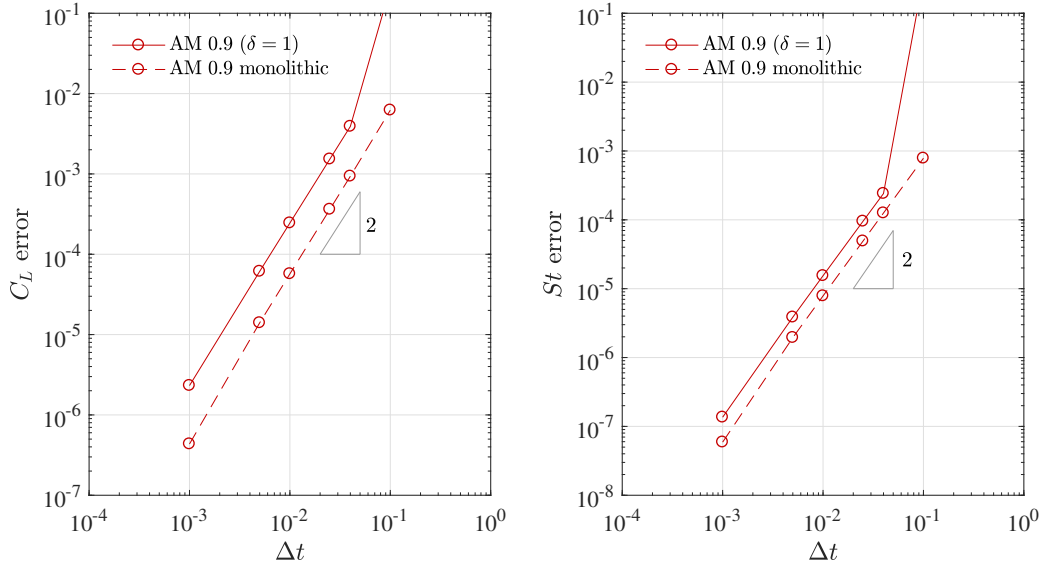


Figure 5.20: Flow around a cylinder: C_L amplitude error convergence (left), and St error convergence (right), with $\bar{\rho}_\infty^h = 0.9$ for the GM and AM methods.

ible Navier-Stokes equations and it has been shown that the additional computational cost of the AM projection scheme is negligible in comparison to the proposed GM or standard BE projection schemes.

Numerical examples based on the lid-driven cavity and the flow around a cylinder have been presented in Section 4. The results obtained are consistent with the conclusions drawn from the model problem and thus confirm its suitability and relevance for studying different types of projection schemes. For the same spatial discretisation, the GM and AM projection schemes and the fully implicit monolithic solver converge to the same response as the time step size is reduced.

The study of the flow around the cylinder includes the presentation of convergence diagrams for the lift coefficient and the Strouhal number which, to the best of our knowledge, have not been shown elsewhere in the context of projection schemes.

For the model problem and for the Navier-Stokes equations, the proposed AM projection scheme consistently outperforms the associated GM projection scheme with the same amount of high-frequency damping by a notable margin (see most notably Figures 5.2 and 5.17). The comparison of the more accurate AM projection scheme to the widely used standard first order schemes based on BE time integration is very favourable.

Chapter 6

Conclusions and Future Work

6.1 Conclusions

Single-component fluid systems for phase transition: In Chapter 2 the Navier-Stokes-Korteweg equations are introduced for the purpose of modelling phase transition phenomena. A low order formulation is proposed with the introduction of an auxiliary variable equation to represent the Laplacian of the density. An efficient solution strategy is presented, wherein the solution variables are solved for non-conservatively. The formulation is demonstrated with highly demanding benchmark problems, both isothermal and non-isothermal in nature. The cavitation phenomenon is successfully exhibited with a nucleate boiling problem.

Binary fluid systems for multiphase flows: A comprehensive study on the Cahn-Hilliard equation is considered in Chapter 3. The objective was to identify a phase dynamics equation which did not have any physical phenomena or effects associated with it, i.e. one which just separated the individual phases. The Cahn-Hilliard equation is observed to have inherent phenomena associated with it, namely the effects of coarsening and shrinkage, which confirms the results of previous studies [63]. The present work provides modifications to the Cahn-Hilliard equation for reducing the mentioned effects, which are demonstrated with numerical examples. It is found that with the proposed modifications a significant reduction in both coarsening and shrinkage are observed.

In Chapter 4 two novel finite element formulations are presented for modelling the Navier-Stokes-Cahn-Hilliard equations; The first uses mixed Taylor-Hood elements, while the second uses linear equal order stabilised SUPG/PSPG elements. The proposed models allow for surface tension effects to be disabled without affecting the phase transport equation. Numerous surface tension dominated benchmark problems are demonstrated, some of which had not been reported in literature at the time of this writing. In addition, several problems with surface tension effects disabled are simulated, and in these instances no additional numerical difficulty is observed.

Increasing computational efficiency with decoupling strategies: The low order formulations presented in Chapters 2, 3 and 4 are by no means computationally inefficient. That being said, there are possibilities of reducing time costs even further, especially in the application of three-dimensional problems. Chapter 5

looks at precisely this, with the focus on decoupling fluid flow equations. The decoupling strategy is based on projection-type fractional step methods. Two projection schemes are proposed: one based on the generalised midpoint rule, and the other on the generalised- α method. The proposed schemes are assessed in terms of accuracy and stability with a unique one-dimensional model problem and various two-dimensional fluid flow examples. Importantly it is confirmed that for a second order accurate scheme, high-frequency damping is sacrificed.

6.2 Suggested future research

The following ideas are presented for future work:

- Understanding the physical relevance of the Navier-Stokes-Korteweg equations, particularly at lower temperatures, i.e. not near critical.
- Demonstrating pressure induced or hydrodynamic cavitation such as observed in orifices or venturis. In the present work, only cavitation through temperature driven nucleate boiling is considered. Setting up boundary value flow problems for flow through an orifice with the compressible Navier-Stokes-Korteweg model can prove challenging.
- The loss of mass on the component level is a hindrance for more complex problems, i.e. the leaking faucet problem. Strategies should be explored to better localising the phase-field variable present in the Cahn-Hilliard and Navier-Stokes-Cahn-Hilliard equations.
- The projection methods discussed in Chapter 5 could be extended to multi-phase flows. Various studies on decoupling the Navier-Stokes-Cahn-Hilliard equations have been made in, for instance, [118, 92, 36], however there are no strategies (at the time of this writing) which allow for the control of high frequency damping.

References

- [1] G. Tryggvason, A. Fernández, A. Esmaeeli, and B. Bunner. *Direct numerical simulations of multiphase flows*, volume 66. 2004.
- [2] T. J. R. Hughes, W. K. Liu, and T. K. Zimmermann. Lagrangian-Eulerian finite element formulation for incompressible viscous flows. *Computer Methods in Applied Mechanics and Engineering*, 29(3):329–349, 1981.
- [3] D. J. Benson. Computational methods in Lagrangian and Eulerian hydrocodes. *Computer Methods in Applied Mechanics and Engineering*, 99(2-3):235–394, 1992.
- [4] J. Donea, A. Huerta, J. Ponthot, and A. Rodriguez-Ferran. Arbitrary Lagrangian-Eulerian Methods. *Encyclopedia of Computational Mechanics*, pages 413–437, 2004.
- [5] W. G. Dettmer and D. Perić. A computational framework for free surface fluid flows accounting for surface tension. *Computer Methods in Applied Mechanics and Engineering*, 195(23-24):3038–3071, 2006.
- [6] P. Bach and O. Hassager. An algorithm for the use of the Lagrangian specification in Newtonian fluid mechanics and applications to free-surface flow. *Journal of Fluid Mechanics*, 152:173–190, 1985.
- [7] B. Ramaswamy and M. Kawahara. Lagrangian finite element analysis applied to viscous free surface fluid flow. *International Journal for Numerical Methods in Fluids*, 7(9):953–984, 1987.
- [8] P. H. Saksono and D. Perić. On finite element modelling of surface tension Variational formulation and applications - Part I: Quasistatic problems. *Computational Mechanics*, 38(3):265–281, 2006.
- [9] P. H. Saksono and D. Perić. On finite element modelling of surface tension: Variational formulation and applications - Part II: Dynamic problems. *Computational Mechanics*, 38(3):251–263, 2006.
- [10] A. Javili and P. Steinmann. A finite element framework for continua with boundary energies. Part I: The two-dimensional case. *Computer Methods in Applied Mechanics and Engineering*, 198(27-29):2198–2208, 2009.

- [11] C. W. Hirt and B. D. Nichols. Volume of fluid (VOF) method for the dynamics of free boundaries. *Journal of Computational Physics*, 39(1):201–225, 1981.
- [12] S. Osher and J. A. Sethian. Fronts propagating with curvature-dependent speed: Algorithms based on Hamilton-Jacobi formulations. *Journal of Computational Physics*, 79(1):12–49, 1988.
- [13] G. Tryggvason. Numerical simulations of the Rayleigh-Taylor instability. *Journal of Computational Physics*, 75(2):253–282, 1988.
- [14] H. Abels, H. Garcke, and G. Grün. Thermodynamically Consistent, Frame Indifferent Diffuse Interface Models for Incompressible Two-Phase Flows with Different Densities. *Mathematical Models and Methods in Applied Sciences*, 22(03):1150013, 2011.
- [15] F. Boyer. A theoretical and numerical model for the study of incompressible mixture flows. *Computers and Fluids*, 31(1):41–68, 2002.
- [16] Lord Rayleigh. XXXIV. On the theory of surface forces. *The London, Edinburgh, and Dublin Philosophical Magazine and Journal of Science*, 30(185):285–298, oct 1890.
- [17] Lord Rayleigh. XX. On the theory of surface forces. II. Compressible fluids. *The London, Edinburgh, and Dublin Philosophical Magazine and Journal of Science*, 33(201):209–220, feb 1892.
- [18] J. D. van der Waals. The thermodynamic theory of capillarity under the hypothesis of a continuous variation of density. *Journal of Statistical Physics*, 20(2):197–200, 1979.
- [19] D. J. Korteweg. Sur la forme que prennent les équations des mouvements des fluides si l’on tient compte des forces capillaires par des variations de densité. *Arch. Neer. Sci. Exactes Ser. II*, (6):1–24, 1901.
- [20] H. E. Stanley. *Introduction to Phase Transitions and Critical Phenomena*. Oxford University Press, Oxford, 1971.
- [21] R. Mendoza, J. Alkemper, and P. W. Voorhees. The morphological evolution of dendritic microstructures during coarsening. *Metallurgical and Materials Transactions A*, 34(3):481–489, mar 2003.
- [22] T. Takaki. Phase-field modeling and simulations of dendrite growth. *ISIJ International*, 54(2):437–444, 2014.
- [23] J. W. Gibbs, K. A. Mohan, E. B. Gulsoy, A. J. Shahani, X. Xiao, C. A. Bouman, M. De Graef, and P. W. Voorhees. The Three-Dimensional Morphology of Growing Dendrites. *Scientific Reports*, 5:1–9, 2015.

- [24] J. W. Cahn and J. E. Hilliard. Free energy of a nonuniform system. I. Interfacial free energy. *The Journal of Chemical Physics*, 28(2):258–267, 1958.
- [25] J. W. Cahn and J. E. Hilliard. Free energy of a nonuniform system. III. Nucleation in a two-component incompressible fluid. *The Journal of Chemical Physics*, 31(3):688–699, 1959.
- [26] D. Jacqmin. Calculation of Two-Phase Navier-Stokes Flows Using Phase-Field Modeling. *Journal of Computational Physics*, 155(1):96–127, 1999.
- [27] C. M. Elliott and S. Zheng. On the Cahn-Hilliard equation. *Nonlinear Analysis*, 96:339–357, 1986.
- [28] J. S. Lowengrub and L. Truskinovsky. Quasi-incompressible Cahn-Hilliard fluids and topological transitions. *Proceedings of the Royal Society A: Mathematical, Physical and Engineering Sciences*, 454(1978):2617–2654, 1998.
- [29] D. M. Anderson, G. B. McFadden, and A. A. Wheeler. Diffuse-Interface Methods in Fluid Mechanics. *Annu. Rev. Fluid Mech*, (30):139–65, 1998.
- [30] G. N. Wells, E. Kuhl, and K. Garikipati. A discontinuous Galerkin method for the Cahn-Hilliard equation. *Journal of Computational Physics*, 218(2):860–877, 2006.
- [31] H. Gómez, V. M. Calo, Y. Bazilevs, and T. J. R. Hughes. Isogeometric analysis of the Cahn-Hilliard phase-field model. *Computer Methods in Applied Mechanics and Engineering*, 197(49-50):4333–4352, 2008.
- [32] J. Liu, L. Dedè, J. A. Evans, M. J. Borden, and T. J. R. Hughes. Isogeometric analysis of the advective Cahn-Hilliard equation: Spinodal decomposition under shear flow. *Journal of Computational Physics*, 242:321–350, 2013.
- [33] S. M. Allen and J. W. Cahn. Ground state structures in ordered binary neighbor interactions. *Acta Metallurgica*, 20:423–433, 1972.
- [34] L. K. Antanovskii. A phase field model of capillarity. *Physics of Fluids*, 7(4):747–753, 1995.
- [35] M. E. Gurtin. Generalized Ginzburg-Landau and Cahn-Hilliard equations based on a microforce balance. *Physica D: Nonlinear Phenomena*, 92(3-4):178–192, 1996.
- [36] J. Shen and X. Yang. A Phase-Field Model and Its Numerical Approximation for Two-Phase Incompressible Flows with Different Densities and Viscosities. *SIAM Journal on Scientific Computing*, 32(3):1159–1179, 2010.
- [37] P. Hohenberg and B. Halperin. Theory of dynamic critical phenomena. *Reviews of Modern Physics*, 49(3):435–479, 1977.

- [38] M. Shokrpour Roudbari, G. Simsek, E. H. van Brummelen, and K. G. van der Zee. Diffuse-interface two-phase flow models with different densities: A new quasi-incompressible form and a linear energy-stable method. *Mathematical Models and Methods in Applied Sciences*, 28(04):733–770, 2018.
- [39] H. Ding, P. D. M. Spelt, and C. Shu. Diffuse interface model for incompressible two-phase flows with large density ratios. *Journal of Computational Physics*, 226(2):2078–2095, 2007.
- [40] X. Xu, L. Zhao, and C. Liu. Axisymmetric Solutions to Coupled Navier-Stokes/Allen-Cahn Equations. *SIAM Journal on Mathematical Analysis*, 41(6):2246–2282, 2010.
- [41] V. Joshi and R. K. Jaiman. A positivity preserving and conservative variational scheme for phase-field modeling of two-phase flows. *Journal of Computational Physics*, 360:137–166, 2018.
- [42] G. Favre and G. Schimperna. On a Navier-Stokes-Allen-Cahn model with inertial effects. *Journal of Mathematical Analysis and Applications*, 475(1):811–838, 2019.
- [43] F. Boyer, C. Lapuerta, S. Minjeaud, B. Piar, and M. Quintard. Cahn-Hilliard/Navier-Stokes model for the simulation of three-phase flows. *Transport in Porous Media*, 82(3):463–483, 2010.
- [44] G. Vilanova, M. Burés, I. Colominas, and H. Gomez. Computational modelling suggests complex interactions between interstitial flow and tumour angiogenesis. *Journal of the Royal Society Interface*, 15(146), 2018.
- [45] G. Lorenzo, T. J. R. Hughes, P. Dominguez-Frojan, A. Reali, and H. Gomez. Computer simulations suggest that prostate enlargement due to benign prostatic hyperplasia mechanically impedes prostate cancer growth. *Proceedings of the National Academy of Sciences*, 116(4):1152–1161, jan 2019.
- [46] L. Gránásy, L. Rátkai, A. Szállás, B. Korbuly, G. I. Tóth, L. Környei, and T. Pusztai. Phase-field modeling of polycrystalline solidification: From needle crystals to spherulites - A review. *Metallurgical and Materials Transactions A: Physical Metallurgy and Materials Science*, 45(4):1694–1719, 2014.
- [47] B. Bourdin, C. Chukwudozie, and K. Yoshioka. A variational approach to the numerical simulation of hydraulic fracturing. *Proceedings - SPE Annual Technical Conference and Exhibition*, 2:1442–1452, 2012.
- [48] D. Santillán, R. Juanes, and L. Cueto-Felgueroso. Phase Field Model of Hydraulic Fracturing in Poroelastic Media: Fracture Propagation, Arrest, and Branching Under Fluid Injection and Extraction. *Journal of Geophysical Research: Solid Earth*, 123(3):2127–2155, 2018.
- [49] J. Bueno, C. Bona-Casas, Y. Bazilevs, and H. Gómez. Interaction of complex fluids and solids: theory, algorithms and application to phase-change-driven implosion. *Computational Mechanics*, 55(6):1105–1118, 2015.

-
- [50] J. S. Langer and L. A. Turski. Hydrodynamic Model of the Condensation of a Vapor near Its Critical Point. *Physical Review A*, 8(6):3230–3243, 1973.
- [51] J. E. Dunn and J. Serrin. On the thermomechanics of interstitial working. *Archive for Rational Mechanics and Analysis*, 88(2):95–133, 1985.
- [52] L. Truskinovsky. Kinks versus Shocks. In J E Dunn, Roger Fosdick, and Marshall Slemrod, editors, *Shock Induced Transitions and Phase Structures in General Media*, pages 185–229, New York, 1993. Springer New York.
- [53] L. K. Antanovskii. Microscale theory of surface tension. *Physical Review E - Statistical Physics, Plasmas, Fluids, and Related Interdisciplinary Topics*, 54(6):6285–6290, 1996.
- [54] D. Jacqmin. An energy approach to the continuum surface tension method. *34th Aerospace Sciences Meeting and Exhibit*, (January), 1996.
- [55] D. M. Anderson and G. B. McFadden. A diffuse-interface description of internal waves in a near-critical fluid. *Physics of Fluids*, 9(7):1870–1879, 1997.
- [56] Lord Rayleigh. VIII. On the pressure developed in a liquid during the collapse of a spherical cavity . *The London, Edinburgh, and Dublin Philosophical Magazine and Journal of Science*, 34(200):94–98, 1917.
- [57] F. Salvatore, H. Streckwall, and T. V. Terwisga. Propeller cavitation modelling by CFD - results from the VIRTUE 2008 Rome Workshop. *Proceedings of the 1st International Symposium on Marine Propulsors*, (June), 2009.
- [58] N. Yilmaz, M. Atlar, and P. A. Fitzsimmons. An Improved Tip Vortex Cavitation Model for Propeller-Rudder Interaction. *Proceedings of the 10th International Symposium on Cavitation (CAV2018)*, pages 76–81, 2019.
- [59] Z. Yu-Kang, H. Jiu-Gen, and F. G. Hammitt. Cavitation erosion of cast iron diesel engine liners. *Wear*, 76(3):329–335, 1982.
- [60] H. Lee and Y. Taenaka. Mechanism for cavitation phenomenon in mechanical heart valves. *Journal of Mechanical Science and Technology*, 20(8):1118–1124, 2006.
- [61] C. C. Coussios and R. A. Roy. Applications of Acoustics and Cavitation to Noninvasive Therapy and Drug Delivery. *Annual Review of Fluid Mechanics*, 40(1):395–420, 2008.
- [62] J. Liu, C. M. Landis, H. Gómez, and T. J. R. Hughes. Liquid-vapor phase transition: Thermomechanical theory, entropy stable numerical formulation, and boiling simulations. *Computer Methods in Applied Mechanics and Engineering*, 297:476–553, 2015.

- [63] P. Yue, C. Zhou, and J. J. Feng. Spontaneous shrinkage of drops and mass conservation in phase-field simulations. *Journal of Computational Physics*, 223(1):1–9, 2007.
- [64] A. Lovrić, W. G. Dettmer, and D. Perić. Low Order Finite Element Methods for the Navier-Stokes-Cahn-Hilliard Equations. pages 1–24, 2019.
- [65] A. Lovrić, W. G. Dettmer, C. Kadapa, and D. Perić. A new family of projection schemes for the incompressible Navier-Stokes equations with control of high-frequency damping. *Computer Methods in Applied Mechanics and Engineering*, 339:160–183, 2018.
- [66] H. Gómez, T. J. R. Hughes, X. Nogueira, and V. M. Calo. Isogeometric analysis of the isothermal Navier-Stokes-Korteweg equations. *Computer Methods in Applied Mechanics and Engineering*, 199(25-28):1828–1840, 2010.
- [67] J. Neusser, C. Rohde, and V. Schleper. Relaxation of the Navier-Stokes-Korteweg equations for compressible two-phase flow with phase transition. *International Journal for Numerical Methods in Fluids*, 79(July):615–639, 2015.
- [68] L. Tian, Y. Xu, J. G. M. Kuerten, and J. J. W. D, Van der Vegt. A local discontinuous Galerkin method for the (non)-isothermal Navier-Stokes-Korteweg equations. *Journal of Computational Physics*, 295:685–714, 2015.
- [69] D. Diehl, J. Kremser, D. Kröner, and C. Rohde. Numerical solution of Navier-Stokes-Korteweg systems by Local Discontinuous Galerkin methods in multiple space dimensions. *Applied Mathematics and Computation*, 272:309–335, 2016.
- [70] J. Liu, H. Gómez, J. A. Evans, T. J. R. Hughes, and C. M. Landis. Functional entropy variables: A new methodology for deriving thermodynamically consistent algorithms for complex fluids, with particular reference to the isothermal Navier-Stokes-Korteweg equations. *Journal of Computational Physics*, 248:47–86, 2013.
- [71] J. Bueno, Y. Bazilevs, R. Juanes, and H. Gómez. Droplet motion driven by tensotaxis. *Extreme Mechanics Letters*, 13:10–16, 2017.
- [72] H. Abels, J. Daube, C. Kraus, and D. Kröner. The Sharp-Interface Limit for the Navier-Stokes-Korteweg Equations. In Christian Klingenberg and Michael Westdickenberg, editors, *Theory, Numerics and Applications of Hyperbolic Problems I*, pages 1–13. Springer International Publishing, 2018.
- [73] C. G. Gal and M. Grasselli. Asymptotic behavior of a Cahn-Hilliard-Navier-Stokes system in 2D. *Annales de l’Institut Henri Poincaré (C) Analyse Non Lineaire*, 27(1):401–436, 2010.
- [74] D. Jamet, O. Lebaigue, N. Coutris, and J. M. Delhayé. The second gradient theory: A tool for the direct numerical simulation of liquid-vapor flows with phase-change. *Nuclear Engineering and Design*, 204(1-3):155–166, 2001.

- [75] T. Ait Ali, S. Khelladi, L. Ramirez, and X. Nogueira. Cavitation modeling using compressible NavierStokes and Korteweg equations. *Computational Methods in Multiphase Flow VIII*, 1:425–435, 2015.
- [76] O. C. Zienkiewicz, R. L. Taylor, and J. Z. Zhu. *The Finite Element Method: Its Basis and Fundamentals*. Elsevier Butterworth-Heinemann, 2005.
- [77] T. J. R. Hughes. *The Finite Element Method: Linear Static and Dynamic Finite Element Analysis*. Prentice Hall, Englewood Cliffs, 1987.
- [78] J. Chung and G. M. Hulbert. A Time Integration Algorithm for Structural Dynamics With Improved Numerical Dissipation: The Generalized- α Method. *Journal of Applied Mechanics*, 60:371–375, 1993.
- [79] K. E. Jansen, C. H. Whiting, and G. M. Hulbert. A generalized- α method for integrating the filtered Navier-Stokes equations with a stabilized finite element method. *Computer Methods in Applied Mechanics and Engineering*, 190:305–319, 2000.
- [80] W. G. Dettmer and D. Perić. An analysis of the time integration algorithms for the finite element solutions of incompressible Navier-Stokes equations based on a stabilised formulation. *Computer Methods in Applied Mechanics and Engineering*, 192(9-10):1177–1226, 2003.
- [81] W. G. Dettmer, C. Kadapa, and D. Perić. A stabilised immersed boundary method on hierarchical b-spline grids. *Computer Methods in Applied Mechanics and Engineering*, 311:415–437, 2016.
- [82] C. Kadapa, W. G. Dettmer, and D. Perić. A stabilised immersed boundary method on hierarchical b-spline grids for fluidrigid body interaction with solid-solid contact. *Computer Methods in Applied Mechanics and Engineering*, 318:242–269, 2017.
- [83] C. Kadapa, W. G. Dettmer, and D. Perić. A stabilised immersed framework on hierarchical b-spline grids for fluid-flexible structure interaction with solid-solid contact. *Computer Methods in Applied Mechanics and Engineering*, 335:472–489, 2018.
- [84] A. De Coninck, B. De Baets, D. Kourounis, F. Verbosio, O. Schenk, S. Maenhout, and J. Fostier. Needles: Toward Large-Scale Genomic Prediction with Marker-by-Environment Interaction. *Genetics*, 203(1):543–555, 2016.
- [85] F. Verbosio, A. De Coninck, D. Kourounis, and O. Schenk. Enhancing the scalability of selected inversion factorization algorithms in genomic prediction. *Journal of Computational Science*, 22(Supplement C):99–108, 2017.
- [86] D. Kourounis, A. Fuchs, and O. Schenk. Towards the Next Generation of Multiperiod Optimal Power Flow Solvers. *IEEE Transactions on Power Systems*, PP(99):1–10, 2018.

- [87] S. Balay, W. D. Gropp, L. C. McInnes, and B. F. Smith. Efficient Management of Parallelism in Object Oriented Numerical Software Libraries. In E. Arge, A. M. Bruaset, and H. P. Langtangen, editors, *Modern Software Tools in Scientific Computing*, pages 163–202. Birkhäuser Press, 1997.
- [88] W. D. Ristenpart, J. C. Bird, A. Belmonte, F. Dollar, and H. A. Stone. Non-coalescence of oppositely charged drops. *Nature*, 461(7262):377–380, 2009.
- [89] J. F. Blowey and C. M. Elliott. The Cahn-Hilliard gradient theory for phase separation with non-smooth free energy Part II: Numerical analysis. *European Journal of Applied Mathematics*, 3(2):147–179, 1992.
- [90] H. Gómez and T. J. R. Hughes. Provably unconditionally stable, second-order time-accurate, mixed variational methods for phase-field models. *Journal of Computational Physics*, 230(13):5310–5327, 2011.
- [91] F. Guillén-González and G. Tierra. On linear schemes for a Cahn-Hilliard diffuse interface model. *Journal of Computational Physics*, 234(1):140–171, 2013.
- [92] C. Liu and J. Shen. A phase field model for the mixture of two incompressible fluids and its approximation by a Fourier-spectral method. *Physica D: Nonlinear Phenomena*, 179(3-4):211–228, 2003.
- [93] João T. Cabral and Julia S. Higgins. Spinodal nanostructures in polymer blends: On the validity of the Cahn-Hilliard length scale prediction. *Progress in Polymer Science*, 81:1–21, 2018.
- [94] J. Zhu, L. Chen, and J. Shen. Morphological evolution during phase separation and coarsening with strong inhomogeneous elasticity. *Modelling Simul. Mater. Mater. Sci. Eng.*, 9(01):499–511, 2001.
- [95] D. Hilhorst, J. Kampmann, T. N. Nguyen, and K. G. Van Der Zee. Formal asymptotic limit of a diffuse-interface tumor-growth model. *Mathematical Models and Methods in Applied Sciences*, 25(6):1011–1043, 2015.
- [96] M. H. Farshbaf-Shaker and C. Heinemann. A phase field approach for optimal boundary control of damage processes in two-dimensional viscoelastic media. *Mathematical Models and Methods in Applied Sciences*, 25(14):2749–2793, 2015.
- [97] Y. Xia, Y. Xu, and C. W. Shu. Local discontinuous Galerkin methods for the Cahn-Hilliard type equations. *Journal of Computational Physics*, 227(1):472–491, 2007.
- [98] H. Gomez and K. G. van der Zee. Computational Phase-Field Modeling. In *Encyclopedia of Computational Mechanics Second Edition*, chapter 11, pages 1–35. John Wiley & Sons, Ltd, Chichester, UK, second edition, 2017.

-
- [99] P. W. Voorhees. Ostwald Ripening of Two-Phase Mixtures. *Annual Review of Materials Science*, 22(1):197–215, 1992.
- [100] R. Folch, J. Casademunt, A. Hernández-Machado, and L. Ramírez-Piscina. Phase-field model for Hele-Shaw flows with arbitrary viscosity contrast. II. Numerical study. *Physical Review E - Statistical Physics, Plasmas, Fluids, and Related Interdisciplinary Topics*, 60(2):1734–1740, 1999.
- [101] T. Biben, K. Kassner, and C. Misbah. Phase-field approach to three-dimensional vesicle dynamics. *Physical Review E - Statistical, Nonlinear, and Soft Matter Physics*, 72(4):1–15, 2005.
- [102] F. Magaletti, F. Picano, M. Chinappi, L. Marino, and C. M. Casciola. The sharp-interface limit of the Cahn-Hilliard/Navier-Stokes model for binary fluids. *Journal of Fluid Mechanics*, 714:95–126, 2013.
- [103] S. Dong and J. Shen. A time-stepping scheme involving constant coefficient matrices for phase-field simulations of two-phase incompressible flows with large density ratios. *Journal of Computational Physics*, 231(17):5788–5804, 2012.
- [104] H. G. Lee, J. S. Lowengrub, and J. Goodman. Modeling pinchoff and reconnection in a Hele-Shaw cell. II. Analysis and simulation in the nonlinear regime. *Physics of Fluids*, 14(2):514–545, 2002.
- [105] J. Kim, K. Kang, and J. Lowengrub. Conservative multigrid methods for Cahn-Hilliard fluids. *Journal of Computational Physics*, 193(2):511–543, 2004.
- [106] X. Feng. Fully discrete finite element approximations of the Navier-Stokes-Cahn-Hilliard diffuse interface model for two-phase fluid flows. *SIAM Journal on Numerical Analysis*, 44(3):1049–1072, 2006.
- [107] Q. Du and J. Zhang. Adaptive Finite Element Method for a Phase Field Bending Elasticity Model of Vesicle Membrane Deformations. *SIAM Journal on Scientific Computing*, 30(3):1634–1657, 2008.
- [108] D. Kay, V. Styles, and R. Welford. Finite element approximation of a Cahn-Hilliard-Navier-Stokes system. *Interfaces and Free Boundaries*, 10(1):15–43, 2008.
- [109] Y. Zhang, H. Wang, and T. Tang. Simulating two-phase viscoelastic flows using moving finite element methods. *Communications in Computational Physics*, 7(2):333–349, 2010.
- [110] K. Bao, Y. Shi, S. Sun, and X. Wang. A finite element method for the numerical solution of the coupled Cahn-Hilliard and Navier-Stokes system for moving contact line problems. *Journal of Computational Physics*, 231(24):8083–8099, 2012.

- [111] Z. Guo, P. Lin, and J. S. Lowengrub. A numerical method for the quasi-incompressible Cahn-Hilliard-Navier-Stokes equations for variable density flows with a discrete energy law. *Journal of Computational Physics*, 276:486–507, 2014.
- [112] J. Giesselmann and T. Pryer. Energy consistent discontinuous Galerkin methods for a quasi-incompressible diffuse two phase flow model. *ESAIM: Mathematical Modelling and Numerical Analysis*, 49(1):275–301, 2015.
- [113] L. F. R. Espath, A. F. Sarmiento, P. Vignal, B. O. N. Varga, A. M. A. Cortes, L. Dalcin, and V. M. Calo. Energy exchange analysis in droplet dynamics via the Navier-Stokes-Cahn-Hilliard model. *Journal of Fluid Mechanics*, 797:389–430, 2016.
- [114] B. S. Hosseini, S. Turek, M. Möller, and C. Palmes. Isogeometric Analysis of the Navier-Stokes-Cahn-Hilliard equations with application to incompressible two-phase flows. *Journal of Computational Physics*, 348:171–194, 2017.
- [115] S. Minjeaud. An unconditionally stable uncoupled scheme for a triphasic Cahn-Hilliard/Navier-Stokes model. *Numerical Methods for Partial Differential Equations*, 29(2):584–618, 2013.
- [116] C. Liu, J. Shen, and X. Yang. Decoupled Energy Stable Schemes for a Phase-Field Model of Two-Phase Incompressible Flows with Variable Density. *Journal of Scientific Computing*, 62(2):601–622, 2015.
- [117] Y. Chen and J. Shen. Efficient, adaptive energy stable schemes for the incompressible Cahn-Hilliard Navier-Stokes phase-field models. *Journal of Computational Physics*, 308:40–56, 2016.
- [118] F. Guillén-González and G. Tierra. Splitting schemes for a Navier-Stokes-Cahn-Hilliard model for two fluids with different densities. *Journal of Computational Mathematics*, 32(6):643–664, 2014.
- [119] X. Yang, M. G. Forest, H. Li, C. Liu, J. Shen, Q. Wang, and F. Chen. Modeling and simulations of drop pinch-off from liquid crystal filaments and the leaky liquid crystal faucet immersed in viscous fluids. *Journal of Computational Physics*, 236(1):1–14, 2013.
- [120] P. H. Chiu. A coupled phase field framework for solving incompressible two-phase flows. *Journal of Computational Physics*, 392:115–140, 2019.
- [121] W. Villanueva and G. Amberg. Some generic capillary-driven flows. *International Journal of Multiphase Flow*, 32(9):1072–1086, 2006.
- [122] X. Xu, Y. Di, and H. Yu. Sharp-interface limits of a phase-field model with a generalized Navier slip boundary condition for moving contact lines. *Journal of Fluid Mechanics*, 849:805–833, 2018.

- [123] H. Yu and X. Yang. Numerical approximations for a phase-field moving contact line model with variable densities and viscosities. *Journal of Computational Physics*, 334:665–686, 2017.
- [124] T. E. Tezduyar, S. Mittal, S. E. Ray, and R. Shih. Incompressible flow computations with stabilized bilinear and linear equal-order-interpolation velocity-pressure elements. *Computer Methods in Applied Mechanics and Engineering*, 95:221–242, 1992.
- [125] T. E. Tezduyar and S. Sathe. Stabilization Parameters in SUPG and PSPG Formulations. *Journal of Computational and Applied Mechanics*, 4(1):71–88, 2003.
- [126] G. Scovazzi. A discourse on Galilean invariance, SUPG stabilization, and the variational multiscale framework. *Computer Methods in Applied Mechanics and Engineering*, 196(4-6):1108–1132, 2007.
- [127] T. J. R. Hughes, G. Scovazzi, and L. P. Franca. Multiscale and Stabilized Methods. In *Encyclopedia of Computational Mechanics Second Edition, Volume 5: Fluids - Part 1*, pages 5–68. 2017.
- [128] W. Ran, S. Fredericks, and J. R. Saylor. Shape oscillation of a levitated drop in an acoustic field. pages 3–4, 2013.
- [129] W. G. Dettmer, P. H. Saksono, and D. Perić. On a finite element formulation for incompressible Newtonian fluid flows on moving domains in the presence of surface tension. *Communications in Numerical Methods in Engineering*, 19(9):659–668, 2003.
- [130] G. B. Foote. A numerical method for studying liquid drop behavior: Simple oscillation. *Journal of Computational Physics*, 11(4):507–530, 1973.
- [131] S. Liu, S. Li, and J. Liu. Jurin’s law revisited: Exact meniscus shape and column height. *European Physical Journal E*, 41(3):1–7, 2018.
- [132] C. Pozrikidis and J. H. Ferziger. Introduction to Theoretical and Computational Fluid Dynamics. *Physics Today*, 50(9):72–74, 1997.
- [133] J. L. Guermond and L. Quartapelle. A Projection FEM for Variable Density Incompressible Flows. *Journal of Computational Physics*, 165(1):167–188, 2000.
- [134] A. J. Chorin. A Numerical Method for Solving Incompressible Viscous Flow Problems. *Journal of Computational Physics*, 2:12–26, 1967.
- [135] R. Temam. *Navier-Stokes Equations: Theory and numerical analysis*. North-Holland Publishing Company, New York, 1977.
- [136] K. Goda. A multistep technique with implicit difference schemes for calculating two- or three-dimensional cavity flows. *Journal of Computational Physics*, 30:76–95, 1979.

- [137] J. van Kan. A second-order accurate pressure-correction scheme for viscous incompressible flow. *SIAM Journal on Scientific and Statistical Computing*, 7(3):870–891, 1986.
- [138] J. L. Guermond and J. Shen. Velocity-Correction Projection Methods for Incompressible Flows. *SIAM Journal on Numerical Analysis*, 41(1):112–134, 2003.
- [139] J. L. Guermond and J. Shen. A new class of truly consistent splitting schemes for incompressible flows. *Journal of Computational Physics*, 192:262–276, 2003.
- [140] J. Blasco, R. Codina, and A. Huerta. A Fractional-Step Method for the Incompressible Navier-Stokes Equations Related to a Predictor-Multicorrector Algorithm. *International Journal for Numerical Methods in Fluids*, 28:1391–1419, 1998.
- [141] P. Nithiarasu, R. Codina, and O. C. Zienkiewicz. The Characteristic-Based Split (CBS) scheme - a unified approach to fluid dynamics. *International Journal for Numerical Methods in Engineering*, 66:1514–1546, 2006.
- [142] R. Temam. *Navier-Stokes equations and nonlinear functional analysis*. Society for Industrial and Applied Mathematics, 1995.
- [143] S. Badia and R. Codina. Algebraic Pressure Segregation Methods for the Incompressible Navier-Stokes Equations. *Archives of Computational Methods in Engineering*, 15:343–369, 2008.
- [144] J. L. Guermond, P. Mineev, and J. Shen. An overview of projection methods for incompressible flows. *Computer Methods in Applied Mechanics and Engineering*, 195:6011–6045, 1998.
- [145] R. Bevan, E. Boileau, R. van Loon, R. W. Lewis, and P. Nithiarasu. A Comparative Study of Fractional Step Method in its Quasi-Implicit, Semi-Implicit and Fully-Explicit Forms for Incompressible Flows. *International Journal of Numerical Methods for Heat & Fluid Flow*, 26(3/4):595–623, 2016.
- [146] J. H. Pyo and J. Shen. Normal mode analysis of second-order projection methods for incompressible flows. *Discrete and continuous dynamical systems-series B*, 5(3):817–840, 2005.
- [147] W. G. Dettmer and D. Perić. A new staggered scheme for fluid-structure interaction. *International Journal for Numerical Methods in Engineering*, 93(1):1–22, jan 2013.
- [148] M. M. Joosten, W. G. Dettmer, and D. Perić. On the temporal stability and accuracy of coupled problems with reference to fluid-structure interaction. *International Journal for Numerical Methods in Fluids*, 64:1363–1378, 2010.

- [149] M. M. Joosten, W. G. Dettmer, and D. Perić. Analysis of the block Gauss-Seidel solution procedure for a strongly coupled model problem with reference to fluid-structure interaction. *International Journal for Numerical Methods in Engineering*, 78:757–778, 2009.
- [150] A. Mini, C. Lerch, R. Wüchner, and K. Bletzinger. Computational Closed-Loop Control of Fluid-structure Interaction (FSCI) for Lightweight Structures. *PAMM Proceedings in Applied Mathematics and Mechanics*, 16:15–18, 2016.
- [151] X. Chen, M. Schäfer, and D. Bothe. Numerical modeling and investigation of viscoelastic fluid-structure interaction applying an implicit partitioned coupling algorithm. *Journal of Fluids and Structures*, 54:390–421, 2015.
- [152] W. G. Dettmer and D. Perić. A computational framework for fluid-structure interaction: Finite element formulation and applications. *Computer Methods in Applied Mechanics and Engineering*, 195(41-43):5754–5779, 2006.
- [153] Y. Bazilevs, K. Takizawa, and T. E. Tezduyar. *Computational Fluid-Structure Interaction: Methods and Applications*. John Wiley & Sons, Inc., 2013.
- [154] C. Kadapa, W. G. Dettmer, and D. Perić. On the advantages of using the first-order generalised-alpha scheme for structural dynamic problems. *Computers & Structures*, 193:226–238, 2017.
- [155] L. J. P. Timmermans, P. D. Minev, and F. N. van De Vosse. An approximate projection scheme for incompressible flow using spectral elements. *International Journal for Numerical Methods in Fluids*, 22:673–688, 1996.
- [156] J. Kim and P. Moin. Application of a fractional-step method to incompressible Navier-Stokes equations. *Journal of Computational Physics*, 59(2):308–323, 1985.
- [157] T. Rüberg and F. Cirak. A fixed-grid b-spline finite element technique for fluid-structure interaction. *International Journal for Numerical Methods in Fluids*, 75(9):623–660, 2013.
- [158] J. C. Pedro, M. K. Banda, and P. Sibanda. Implicit-explicit higher-order time integration schemes for computations of structural dynamics with fluid-structure interaction. *Applications and Applied Mathematics: An International Journal*, 10:287–311, 2015.
- [159] W. G. Dettmer. *Finite Element Modelling of Fluid Flow with Moving Free Surfaces and Interfaces Including Fluid-Solid Interaction*. Phd thesis, Swansea University, 2004.
- [160] X. Zeng, G. Scovazzi, N. Abboud, O. Colomés, and S. Rossi. A dynamic variational multiscale method for viscoelasticity using linear tetrahedral elements. *International Journal for Numerical Methods in Engineering*, 112:1951–2003, 2017.

- [161] J. L. Guermond and L. Quartapelle. Calculation of Incompressible Viscous Flows by an Unconditionally Stable Projection FEM. *Journal of Computational Physics*, 132:12–33, 1997.
- [162] J. L. Guermond and L. Quartapelle. On incremental projection methods. *R. Salvi (Ed.), Pitman, Research Notes in Mathematics Series*, 388:277–288, 1998.
- [163] I. Babuška. Error-Bounds for Finite Element Method. *Numerische Mathematik*, 16:322–333, 1971.
- [164] F. Brezzi. On the existence, uniqueness and approximation of saddle-point problems arising from Lagrangian multipliers. *ESAIM: Mathematical Modelling and Numerical Analysis*, 8:129–151, 1974.
- [165] F. Brezzi and J. Douglas Jr. Stabilized mixed methods for the Stokes problem. *Numerische Mathematik*, 53:225–235, 1988.
- [166] F. Brezzi and M. Fortin. *Mixed and Hybrid Finite Element Methods*. Springer-Verlag, 1991.
- [167] F. Brezzi and R. S. Falk. Stability of higher-order Hood-Taylor methods. *SIAM Journal on Numerical Analysis*, 28:581–590, 1991.
- [168] A. N. Brooks and T. J. R. Hughes. Streamline upwind/Petrov-Galerkin formulations for convection dominated flows with particular emphasis on the incompressible Navier-Stokes equations. *Computer Methods in Applied Mechanics and Engineering*, 32(1-3):199–259, sep 1982.
- [169] T. E. Tezduyar. Stabilized finite element formulations for incompressible flow computations. *Advances in Applied Mechanics*, 28:1–44, 1991.
- [170] T. E. Tezduyar. Stabilization Parameters in SUPG and PSPG Formulations. *Journal of Computational and Applied Mechanics*, 4(1):71–88, 2003.
- [171] G. Lube. Stabilized FEM for incompressible flow: A critical review and new trends. In *European Conference on Computational Fluid Dynamics, ECCOMAS CFD 2006*, 2006.
- [172] T. J. R. Hughes, G. Scovazzi, and L. P. Franca. *Multiscale and Stabilized Methods, Encyclopedia of Computational Mechanics*. Wiley, 2004.
- [173] J. L. Guermond and L. Quartapelle. On stability and convergence of projection methods based on pressure Poisson equation. *International Journal for Numerical Methods in Fluids*, 26:1039–1053, 1998.
- [174] A. Roshko. On the Development of Turbulent Wakes From Vortex Streets. National advisory committee for aeronautics, California Institute of Technology, 1954.

-
- [175] C. Kadapa, W. G. Dettmer, and D. Perić. A fictitious domain/distributed Lagrange multiplier based fluid-structure interaction scheme with hierarchical B-Spline grids. *Computer Methods in Applied Mechanics and Engineering*, 301:1–27, 2015.

Appendices

Appendix A

Formulation and Solution Strategies

A.1 Linearisation and Newton-Raphson procedure

Starting from the weak of the continuous Navier-Stokes-Korteweg Equations (2.55a)-(2.55d), which is rewritten for convenience as: Find $(\rho, \mathbf{u}, \theta, \Upsilon) \in \mathcal{X}$, such that, for all $(q, \mathbf{w}, v, s) \in \mathcal{X}$,

$$\int_{\Omega} q \frac{\partial \rho}{\partial t} - \nabla q \cdot \rho \mathbf{u} \, d\Omega = 0 \quad (\text{A.1a})$$

$$\begin{aligned} \int_{\Omega} \mathbf{w} \cdot \left(\mathbf{u} \frac{\partial \rho}{\partial t} + \rho \frac{\partial \mathbf{u}}{\partial t} \right) - \nabla \mathbf{w} : (\rho \mathbf{u} \otimes \mathbf{u}) - (\nabla \cdot \mathbf{w}) p + \nabla \mathbf{w} : (\boldsymbol{\tau} + \boldsymbol{\kappa}) \\ - \mathbf{w} \cdot \rho \mathbf{b} \, d\Omega = 0 \end{aligned} \quad (\text{A.1b})$$

$$\begin{aligned} \int_{\Omega} v \frac{\partial(\rho \mathcal{E})}{\partial t} - \nabla v \cdot (\rho \mathcal{E} + p) \mathbf{u} + \nabla v \cdot (\boldsymbol{\tau} + \boldsymbol{\kappa}) \mathbf{u} - \nabla v \cdot \mathbf{q} - v (\rho \mathbf{b} \cdot \mathbf{u}) \\ - v \rho r \, d\Omega = 0 \end{aligned} \quad (\text{A.1c})$$

$$\int_{\Omega} s \Upsilon + \nabla s \cdot \nabla \rho \, d\Omega + \int_{\Gamma} s |\nabla \rho| \cos(\alpha) \, d\Gamma = 0. \quad (\text{A.1d})$$

Consider the system of nonlinear equations (A.1a)-(A.1d) represented as

$$\mathbf{R}(\mathbf{U}) = \mathbf{0}, \quad (\text{A.2})$$

where $\mathbf{U} = \{\rho, \mathbf{u}, \theta, \Upsilon\}$. The Newton-Raphson method is implemented to solve the system iteratively. Given solution estimate at the k^{th} iteration, \mathbf{U}_k , The solution at $k + 1$, is evaluated using the linearised approximation:

$$\mathbf{R}(\mathbf{U}_{k+1}) = \mathbf{R}(\mathbf{U}_k) + \Delta \mathbf{R}(\mathbf{U}_k) = 0, \quad (\text{A.3})$$

where $\mathbf{U}_k = \{\rho_k, \mathbf{u}_k, \theta_k, \Upsilon_k\}$, and $\mathbf{U}_{k+1} = \{\rho_{k+1}, \mathbf{u}_{k+1}, \theta_{k+1}, \Upsilon_{k+1}\}$, also

$$\Delta \mathbf{R}(\mathbf{U}_k) = D\mathbf{R}(\mathbf{U}_k)[\delta \mathbf{U}], \quad (\text{A.4})$$

with $\delta \mathbf{U} = \{\delta \rho, \delta \mathbf{u}, \delta \theta, \delta \Upsilon\}$. Here $D\mathbf{R}(\mathbf{U}_k)[\delta \mathbf{U}]$ represents the directional derivative of $\mathbf{R}(\mathbf{U}_k)$ in the direction of $[\delta \mathbf{U}]$.

The residual $\mathbf{R}(\mathbf{U}_k) = \{R_1, R_2, R_3, R_4\}$ is written with all terms expanded and labelled alphabetically as

$$R_1 = \int_{\Omega} \underbrace{q \frac{\partial \rho_k}{\partial t}}_A - \underbrace{\nabla q \cdot \rho_k \mathbf{u}_k}_B d\Omega \quad (\text{A.5a})$$

$$R_2 = \int_{\Omega} \underbrace{\mathbf{w} \cdot \mathbf{u}_k \frac{\partial \rho}{\partial t}}_A + \underbrace{\mathbf{w} \cdot \rho_k \frac{\partial \mathbf{u}_k}{\partial t}}_B - \underbrace{\nabla \mathbf{w} : (\rho_k \mathbf{u}_k \otimes \mathbf{u}_k)}_C - \underbrace{(\nabla \cdot \mathbf{w}) p(\rho_k, \theta_k)}_D \\ + \underbrace{\nabla \mathbf{w} : \boldsymbol{\tau}(\nabla^s \mathbf{u}_k, \nabla \cdot \mathbf{u}_k)}_E + \underbrace{\nabla \mathbf{w} : \boldsymbol{\kappa}(\rho_k, \nabla \rho_k, \Upsilon_k)}_F - \underbrace{\mathbf{w} \cdot \rho_k \mathbf{b}}_G d\Omega \quad (\text{A.5b})$$

$$R_3 = \int_{\Omega} \underbrace{v \frac{\partial}{\partial t} (\rho_k \mathcal{E}(\rho_k, \nabla \rho_k, \mathbf{u}_k, \theta_k))}_A - \underbrace{\nabla v \cdot \rho_k \mathcal{E}(\rho_k, \nabla \rho_k, \mathbf{u}_k, \theta_k) \mathbf{u}_k}_B \\ - \underbrace{\nabla v \cdot p(\rho_k, \theta_k) \mathbf{u}_k}_C + \underbrace{\nabla v \cdot \boldsymbol{\tau}(\nabla^s \mathbf{u}_k, \nabla \cdot \mathbf{u}_k) \mathbf{u}_k}_D \\ + \underbrace{\nabla v \cdot \boldsymbol{\kappa}(\rho_k, \nabla \rho_k, \Upsilon_k) \mathbf{u}_k}_E - \underbrace{\nabla v \cdot \mathbf{q}(\nabla \theta_k)}_F - \underbrace{v (\rho_k \mathbf{b} \cdot \mathbf{u}_k)}_G - \underbrace{v \rho_k r}_{\text{H}} d\Omega \quad (\text{A.5c})$$

$$R_4 = \int_{\Omega} \underbrace{s \Upsilon_k}_A + \underbrace{\nabla s \cdot \nabla \rho_k}_B d\Omega + \int_{\Gamma} \underbrace{s |\nabla \rho_k| \cos(\alpha)}_C d\Gamma, \quad (\text{A.5d})$$

where

$$p(\rho_k, \theta_k) = \frac{8}{27} \frac{\theta_k \rho_k}{1 - \rho_k} - \rho_k^2 \quad (\text{A.6a})$$

$$\boldsymbol{\tau}(\nabla^s \mathbf{u}_k, \nabla \cdot \mathbf{u}_k) = \frac{2}{\text{Re}} \left(\nabla^s \mathbf{u}_k - \frac{1}{3} \nabla \cdot \mathbf{u}_k \mathbf{I} \right) \quad (\text{A.6b})$$

$$\boldsymbol{\kappa}(\rho_k, \nabla \rho_k, \Upsilon_k) = \frac{1}{\text{We}} \left(\left(\rho_k \Upsilon_k + \frac{1}{2} \nabla \rho_k \cdot \nabla \rho_k \right) \mathbf{I} - \nabla \rho_k \otimes \nabla \rho_k \right) \quad (\text{A.6c})$$

$$\rho_k \mathcal{E}(\rho_k, \nabla \rho_k, \mathbf{u}_k, \theta_k) = \frac{8}{27} \frac{\theta_k \rho_k}{\bar{\gamma} - 1} - \rho_k^2 + \frac{1}{2} \rho_k \mathbf{u} \cdot \mathbf{u} + \frac{1}{2\text{We}} \nabla \rho_k \cdot \nabla \rho_k. \quad (\text{A.6d})$$

For brevity the rate $\frac{\partial a}{\partial t}$ will be written as \dot{a} . The linearisation of all the nonlinear terms from Equations (A.5a)-(A.5d) will now be shown:

$$R_{1B} = \int_{\Omega} \nabla q \cdot \rho_k \mathbf{u}_k d\Omega \\ \Delta R_{1B} = \int_{\Omega} \frac{d}{d\epsilon} \bigg|_{\epsilon=0} \nabla q \cdot (\rho_k + \epsilon \delta \rho) \mathbf{u}_k + \nabla q \cdot \rho_k (\mathbf{u}_k + \epsilon \delta \mathbf{u}) d\Omega \quad (\text{A.7}) \\ = \int_{\Omega} \nabla q \cdot (\delta \rho \mathbf{u}_k + \rho_k \delta \mathbf{u}) d\Omega$$

$$\begin{aligned}
R_{2A} &= \int_{\Omega} \mathbf{w} \cdot \mathbf{u}_k \dot{\rho}_k \, d\Omega \\
\Delta R_{2A} &= \int_{\Omega} \frac{d}{d\epsilon} \bigg|_{\epsilon=0} \mathbf{w} \cdot (\mathbf{u}_k + \epsilon \delta \mathbf{u}) \dot{\rho}_k + \mathbf{w} \cdot \mathbf{u}_k (\dot{\rho}_k + \epsilon \delta \dot{\rho}) \, d\Omega \\
&= \int_{\Omega} \mathbf{w} \cdot (\delta \mathbf{u} \dot{\rho}_k + \mathbf{u}_k \delta \dot{\rho}) \, d\Omega
\end{aligned} \tag{A.8}$$

$$\begin{aligned}
R_{2B} &= \int_{\Omega} \mathbf{w} \cdot \rho_k \dot{\mathbf{u}}_k \, d\Omega \\
\Delta R_{2B} &= \int_{\Omega} \frac{d}{d\epsilon} \bigg|_{\epsilon=0} \mathbf{w} \cdot (\rho_k + \epsilon \delta \rho) \dot{\mathbf{u}}_k + \mathbf{w} \cdot \rho_k (\dot{\mathbf{u}}_k + \epsilon \delta \dot{\mathbf{u}}) \, d\Omega \\
&= \int_{\Omega} \mathbf{w} \cdot (\delta \rho \dot{\mathbf{u}}_k + \rho_k \delta \dot{\mathbf{u}}) \, d\Omega
\end{aligned} \tag{A.9}$$

$$\begin{aligned}
R_{2C} &= \int_{\Omega} \nabla \mathbf{w} : (\rho_k \mathbf{u}_k \otimes \mathbf{u}_k) \, d\Omega \\
\Delta R_{2C} &= \int_{\Omega} \frac{d}{d\epsilon} \bigg|_{\epsilon=0} \nabla \mathbf{w} : ((\rho_k + \epsilon \delta \rho) \mathbf{u}_k \otimes \mathbf{u}_k) \\
&\quad + \nabla \mathbf{w} : (\rho_k (\mathbf{u}_k + \epsilon \delta \mathbf{u}) \otimes (\mathbf{u}_k + \epsilon \delta \mathbf{u})) \, d\Omega \\
&= \int_{\Omega} \nabla \mathbf{w} : (\delta \rho \mathbf{u}_k \otimes \mathbf{u}_k + \rho_k \mathbf{u}_k \otimes \delta \mathbf{u} + \rho_k \delta \mathbf{u} \otimes \mathbf{u}_k) \, d\Omega
\end{aligned} \tag{A.10}$$

$$\begin{aligned}
R_{2D} &= \int_{\Omega} \nabla \cdot \mathbf{w} \left(\frac{8}{27} \frac{\theta_k \rho_k}{1 - \rho_k} - \rho_k^2 \right) \, d\Omega \\
\Delta R_{2D} &= \int_{\Omega} \frac{d}{d\epsilon} \bigg|_{\epsilon=0} \nabla \cdot \mathbf{w} \left(\frac{8}{27} \frac{\theta_k (\rho_k + \epsilon \delta \rho)}{1 - \rho_k - \epsilon \delta \rho} - (\rho_k + \epsilon \delta \rho)^2 \right. \\
&\quad \left. + \frac{8}{27} \frac{(\theta_k + \epsilon \delta \theta) \rho_k}{1 - \rho_k} \right) \, d\Omega \\
&= \int_{\Omega} \nabla \cdot \mathbf{w} \left(\left(\frac{8}{27} \frac{\theta_k}{(1 - \rho_k)^2} - 2\rho_k \right) \delta \rho + \frac{8}{27} \frac{\rho_k}{(1 - \rho_k)} \delta \theta \right) \, d\Omega \\
&= \int_{\Omega} \nabla \cdot \mathbf{w} \left(\frac{\partial p}{\partial \rho} \delta \rho + \frac{\partial p}{\partial \theta} \delta \theta \right) \, d\Omega
\end{aligned} \tag{A.11}$$

$$\begin{aligned}
R_{2F} &= \int_{\Omega} \nabla \mathbf{w} : \frac{1}{\text{We}} \left(\left(\rho_k \Upsilon_k + \frac{1}{2} \nabla \rho_k \cdot \nabla \rho_k \right) \mathbf{I} - \nabla \rho_k \otimes \nabla \rho_k \right) \, d\Omega \\
\Delta R_{2F} &= \int_{\Omega} \frac{d}{d\epsilon} \bigg|_{\epsilon=0} \nabla \mathbf{w} : \frac{1}{\text{We}} \left(\left((\rho_k + \epsilon \delta \rho) \Upsilon_k + \frac{1}{2} \nabla (\rho_k + \epsilon \delta \rho) \cdot \nabla (\rho_k + \epsilon \delta \rho) \right. \right. \\
&\quad \left. \left. + \rho_k (\Upsilon_k + \epsilon \delta \Upsilon) \right) \mathbf{I} - \nabla (\rho_k + \epsilon \delta \rho) \otimes \nabla (\rho_k + \epsilon \delta \rho) \right) \, d\Omega \\
&= \int_{\Omega} \frac{d}{d\epsilon} \bigg|_{\epsilon=0} \nabla \mathbf{w} : \frac{1}{\text{We}} \left((\delta \rho \Upsilon_k + \nabla \rho_k \cdot \nabla \delta \rho + \rho_k \delta \Upsilon) \mathbf{I} - \nabla \rho_k \otimes \nabla \delta \rho \right. \\
&\quad \left. - \nabla \delta \rho \otimes \nabla \rho_k \right) \, d\Omega
\end{aligned} \tag{A.12}$$

$$\begin{aligned}
R_{3A} &= \int_{\Omega} v \frac{\partial}{\partial t} \left(\frac{8}{27\bar{\gamma}-1} \frac{\theta_k \rho_k}{\rho_k^2} - \rho_k^2 + \frac{1}{2} \rho_k \mathbf{u} \cdot \mathbf{u} + \frac{1}{2\text{We}} \nabla \rho_k \cdot \nabla \rho_k \right) d\Omega \\
&= \int_{\Omega} v \left(\frac{8}{27(\bar{\gamma}-1)} (\dot{\rho}_k \theta_k + \dot{\theta}_k \rho_k) - 2\rho_k \dot{\rho}_k + \frac{1}{2} \dot{\rho}_k \mathbf{u}_k \cdot \mathbf{u}_k + \rho_k \dot{\mathbf{u}}_k \cdot \mathbf{u}_k \right. \\
&\quad \left. + \frac{1}{\text{We}} \nabla \dot{\rho}_k \cdot \nabla \rho_k \right) d\Omega \\
\Delta R_{3A} &= \int_{\Omega} \frac{d}{d\epsilon} \Big|_{\epsilon=0} v \left(\frac{8}{27(\bar{\gamma}-1)} \left((\dot{\rho}_k + \epsilon \delta \dot{\rho}) \theta + \dot{\theta}_k (\rho_k + \epsilon \delta \rho) \right) \right. \\
&\quad - 2(\rho_k + \epsilon \delta \rho)(\dot{\rho}_k + \epsilon \delta \dot{\rho}) + \frac{1}{2} (\dot{\rho}_k + \epsilon \delta \dot{\rho}) \mathbf{u}_k \cdot \mathbf{u}_k \\
&\quad + (\rho_k + \epsilon \delta \rho) \dot{\mathbf{u}}_k \cdot \mathbf{u}_k + \frac{1}{\text{We}} \nabla (\dot{\rho}_k + \epsilon \delta \dot{\rho}) \cdot \nabla (\rho_k + \epsilon \delta \rho) \\
&\quad + \frac{1}{2} \dot{\rho} (\mathbf{u}_k + \epsilon \delta \mathbf{u}) \cdot (\mathbf{u}_k + \epsilon \delta \mathbf{u}) + \rho_k (\dot{\mathbf{u}}_k + \epsilon \delta \dot{\mathbf{u}}) \cdot (\mathbf{u}_k + \epsilon \delta \mathbf{u}) \\
&\quad \left. + \frac{8}{27(\bar{\gamma}-1)} \left(\dot{\rho}_k (\theta_k + \epsilon \delta \theta) + (\dot{\theta}_k + \epsilon \delta \dot{\theta}) \rho_k \right) \right) d\Omega \\
&= \int_{\Omega} v \left(\frac{8}{27(\bar{\gamma}-1)} \left(\theta_k \delta \dot{\rho} + \dot{\theta}_k \delta \rho + \dot{\rho}_k \delta \theta + \rho_k \delta \dot{\theta} \right) - 2(\rho_k \delta \dot{\rho} + \dot{\rho}_k \delta \rho) \right. \\
&\quad + \frac{1}{2} \mathbf{u}_k \cdot \mathbf{u}_k \delta \dot{\rho} + \dot{\mathbf{u}}_k \cdot \mathbf{u}_k \delta \rho + \frac{1}{\text{We}} (\nabla \dot{\rho}_k \cdot \nabla \delta \rho + \nabla \rho_k \cdot \nabla \delta \dot{\rho}) \\
&\quad \left. + \dot{\rho}_k \mathbf{u}_k \cdot \delta \mathbf{u} + \rho_k (\dot{\mathbf{u}}_k \cdot \delta \mathbf{u} + \mathbf{u}_k \cdot \delta \dot{\mathbf{u}}) \right) d\Omega
\end{aligned} \tag{A.13}$$

$$\begin{aligned}
R_{3B} &= \int_{\Omega} \nabla v \cdot \left(\frac{8}{27} \frac{\theta_k \rho_k}{\bar{\gamma} - 1} - \rho_k^2 + \frac{1}{2} \rho_k \mathbf{u} \cdot \mathbf{u} + \frac{1}{2\text{We}} \nabla \rho_k \cdot \nabla \rho_k \right) \mathbf{u}_k \, d\Omega \\
\Delta R_{3B} &= \int_{\Omega} \frac{d}{d\epsilon} \bigg|_{\epsilon=0} \nabla v \cdot \left(\frac{8}{27(\bar{\gamma} - 1)} (\rho_k + \epsilon \delta \rho) \theta_k \mathbf{u}_k \right. \\
&\quad - (\rho_k + \epsilon \delta \rho)(\rho_k + \epsilon \delta \rho) \mathbf{u}_k + \frac{1}{2} ((\rho_k + \epsilon \delta \rho) \mathbf{u}_k \cdot \mathbf{u}_k) \mathbf{u}_k \\
&\quad + \frac{1}{2\text{We}} (\nabla(\rho_k + \epsilon \delta \rho) \cdot \nabla(\rho_k + \epsilon \delta \rho)) \mathbf{u}_k \\
&\quad + \frac{8}{27(\bar{\gamma} - 1)} \rho_k ((\theta_k + \epsilon \delta \theta) \mathbf{u}_k + \theta_k (\mathbf{u}_k + \epsilon \delta \mathbf{u})) - \rho_k^2 (\mathbf{u}_k + \epsilon \delta \mathbf{u}) \\
&\quad + \frac{1}{2} (\rho_k (\mathbf{u}_k + \epsilon \delta \mathbf{u}) \cdot (\mathbf{u}_k + \epsilon \delta \mathbf{u})) (\mathbf{u}_k + \epsilon \delta \mathbf{u}) \\
&\quad \left. + \frac{1}{2\text{We}} (\nabla \rho_k \cdot \nabla \rho_k) (\mathbf{u}_k + \epsilon \delta \mathbf{u}) \right) d\Omega \\
&= \int_{\Omega} \nabla v \cdot \left(\frac{8}{27(\bar{\gamma} - 1)} \theta_k \mathbf{u}_k \delta \rho - 2\rho_k \mathbf{u}_k \delta \rho + \frac{1}{2} (\delta \rho \mathbf{u}_k \cdot \mathbf{u}_k) \mathbf{u}_k \right. \\
&\quad + \frac{1}{\text{We}} (\nabla \rho_k \cdot \nabla \delta \rho) \mathbf{u}_k + \frac{8}{27(\bar{\gamma} - 1)} \rho_k (\mathbf{u}_k \delta \theta_k + \theta_k \delta \mathbf{u}) - \rho_k^2 \delta \mathbf{u} \\
&\quad \left. + \rho_k (\mathbf{u}_k \otimes \mathbf{u}_k) \delta \mathbf{u} + \frac{1}{2} \rho_k (\mathbf{u}_k \cdot \mathbf{u}_k) \delta \mathbf{u} + \frac{1}{2\text{We}} (\nabla \rho_k \cdot \nabla \rho_k) \delta \mathbf{u} \right) d\Omega
\end{aligned} \tag{A.14}$$

$$\begin{aligned}
R_{3C} &= \int_{\Omega} \nabla v \cdot \left(\frac{8}{27} \frac{\theta_k \rho_k}{1 - \rho_k} - \rho_k^2 \right) \mathbf{u}_k \, d\Omega \\
\Delta R_{3C} &= \int_{\Omega} \frac{d}{d\epsilon} \bigg|_{\epsilon=0} \nabla v \cdot \left(\frac{8}{27} \frac{(\rho_k + \epsilon \delta \rho_k) \mathbf{u}_k \theta_k}{1 - \rho_k - \epsilon \delta \rho} - (\rho_k + \epsilon \delta \rho)^2 \mathbf{u}_k \right. \\
&\quad \left. + \frac{8}{27} \frac{(\mathbf{u}_k + \epsilon \delta \mathbf{u}) \rho_k \theta_k}{1 - \rho_k} - \rho_k^2 (\mathbf{u}_k + \epsilon \delta \mathbf{u}) + \frac{8}{27} \frac{(\theta_k + \epsilon \delta \theta) \rho_k \mathbf{u}_k}{1 - \rho_k} \right) d\Omega \\
&= \int_{\Omega} \nabla v \cdot \left(\left(\frac{8}{27} \frac{\theta_k}{(1 - \rho_k)^2} - 2\rho_k \right) \mathbf{u}_k \delta \rho + \left(\frac{8}{27} \frac{\rho_k \theta_k}{1 - \rho_k} - \rho_k^2 \right) \delta \mathbf{u} \right. \\
&\quad \left. + \frac{8}{27} \frac{\rho_k \mathbf{u}_k}{1 - \rho_k} \delta \theta \right) d\Omega
\end{aligned} \tag{A.15}$$

$$\begin{aligned}
R_{3D} &= \int_{\Omega} \nabla v \cdot \frac{2}{\text{Re}} \left(\nabla^s \mathbf{u}_k - \frac{1}{3} \nabla \cdot \mathbf{u}_k \mathbf{I} \right) \mathbf{u}_k \, d\Omega \\
\Delta R_{3D} &= \int_{\Omega} \frac{d}{d\epsilon} \bigg|_{\epsilon=0} \nabla v \cdot \frac{2}{\text{Re}} \left(\nabla^s (\mathbf{u}_k + \epsilon \delta \mathbf{u}) \right. \\
&\quad \left. - \frac{1}{3} \nabla \cdot (\mathbf{u}_k + \epsilon \delta \mathbf{u}) \mathbf{I} \right) (\mathbf{u}_k + \epsilon \delta \mathbf{u}) \, d\Omega \\
&= \int_{\Omega} \nabla v \cdot \frac{2}{\text{Re}} \left(\nabla^s \delta \mathbf{u} \mathbf{u}_k + \nabla^s \mathbf{u}_k \delta \mathbf{u} - \frac{1}{3} (\nabla \cdot \mathbf{u}_k \delta \mathbf{u} + \nabla \cdot \delta \mathbf{u} \mathbf{u}_k) \right) d\Omega
\end{aligned} \tag{A.16}$$

$$\begin{aligned}
R_{3E} &= \int_{\Omega} \nabla v \cdot \frac{1}{\text{We}} \left(\left(\rho_k \Upsilon_k + \frac{1}{2} \nabla \rho_k \cdot \nabla \rho_k \right) \mathbf{I} - \nabla \rho_k \otimes \nabla \rho_k \right) \mathbf{u}_k \, d\Omega \\
\Delta R_{3E} &= \int_{\Omega} \frac{d}{d\epsilon} \bigg|_{\epsilon=0} \nabla v \cdot \frac{1}{\text{We}} \left(\left((\rho_k + \epsilon \delta \rho) \Upsilon_k + \frac{1}{2} \nabla (\rho_k + \epsilon \delta \rho) \cdot \nabla (\rho_k + \epsilon \delta \rho) \right. \right. \\
&\quad \left. \left. + \rho_k (\Upsilon_k + \epsilon \delta \Upsilon) \right) \mathbf{I} - \nabla (\rho_k + \epsilon \delta \rho) \otimes \nabla (\rho_k + \epsilon \delta \rho) \right) \mathbf{u}_k \\
&\quad + \left(\left(\rho_k \Upsilon_k + \frac{1}{2} \nabla \rho_k \cdot \nabla \rho_k \right) \mathbf{I} - \nabla \rho_k \otimes \nabla \rho_k \right) (\mathbf{u}_k + \epsilon \delta \mathbf{u}) \, d\Omega \\
&= \int_{\Omega} \nabla v \cdot \frac{1}{\text{We}} \left(\left((\rho_k \delta \Upsilon + \Upsilon_k \delta \rho + \nabla \rho_k \cdot \nabla \delta \rho) \mathbf{I} - \nabla \rho_k \otimes \nabla \delta \rho \right. \right. \\
&\quad \left. \left. - \nabla \delta \rho \otimes \nabla \rho_k \right) \mathbf{u}_k + \left(\left(\rho_k \Upsilon_k + \frac{1}{2} \nabla \rho_k \cdot \nabla \rho_k \right) \mathbf{I} \right. \right. \\
&\quad \left. \left. - \nabla \rho_k \otimes \nabla \rho_k \right) \delta \mathbf{u} \right) \, d\Omega
\end{aligned} \tag{A.17}$$

$$\begin{aligned}
R_{3G} &= \int_{\Omega} v (\rho_k \mathbf{b} \cdot \mathbf{u}_k) \, d\Omega \\
\Delta R_{3G} &= \int_{\Omega} \frac{d}{d\epsilon} \bigg|_{\epsilon=0} v ((\rho_k + \epsilon \delta \rho) \mathbf{b} \cdot \mathbf{u} + \rho_k \mathbf{b} \cdot (\mathbf{u}_k + \epsilon \delta \mathbf{u})) \, d\Omega \\
&= \int_{\Omega} v (\mathbf{b} \cdot \mathbf{u}_k \delta \rho + \rho_k \mathbf{b} \cdot \delta \mathbf{u}) \, d\Omega
\end{aligned} \tag{A.18}$$

The linearised terms contribute to $\Delta \mathbf{R}(\mathbf{U}_k)[\delta \mathbf{U}]$, and $\delta \mathbf{U}$ can be solved with

$$\mathbf{K} \delta \mathbf{U} = -\mathbf{R}(\mathbf{U}_k), \tag{A.19}$$

where $\mathbf{K} \delta \mathbf{U} = \Delta \mathbf{R}(\mathbf{U}_k)[\delta \mathbf{U}]$, \mathbf{K} being the tangent stiffness matrix. Completing a single Newton-Raphson iteration, the solution at $k+1$ can now be evaluated as

$$\mathbf{U}_{k+1} = \mathbf{U}_k + \delta \mathbf{U}. \tag{A.20}$$

A.2 Power expenditure term

The power expenditure term can be expressed as

$$\Pi = \frac{1}{\text{We}} \rho \nabla \cdot \mathbf{u} \nabla \rho. \tag{A.21}$$

The residual and stiffness contributions are evaluated as

$$\begin{aligned}
R &= \int_{\Omega} \nabla v \cdot \frac{1}{\text{We}} \rho_k \nabla \cdot \mathbf{u}_k \nabla \rho_k \, d\Omega \\
\Delta R &= \int_{\Omega} \frac{d}{d\epsilon} \bigg|_{\epsilon=0} \nabla v \cdot \frac{1}{\text{We}} \left((\rho_k + \epsilon \delta \rho) \nabla (\rho_k + \delta \rho) \nabla \cdot \mathbf{u}_k \right. \\
&\quad \left. + \rho_k \nabla \rho_k \nabla \cdot (\mathbf{u}_k + \epsilon \delta \mathbf{u}) \right) \, d\Omega \\
&= \int_{\Omega} \nabla v \cdot \frac{1}{\text{We}} ((\rho_k \nabla \delta \rho + \delta \rho \nabla \rho_k) \nabla \cdot \mathbf{u}_k + \rho_k \nabla \rho_k \nabla \cdot \delta \mathbf{u}) \, d\Omega
\end{aligned} \tag{A.22}$$

A.3 Non-conservative Korteweg stress term

The non-conservative Korteweg stress term,

$$\nabla \cdot \boldsymbol{\kappa} = \frac{1}{\text{We}} \rho \nabla \Delta \rho, \quad (\text{A.23})$$

will now be presented in its weak form: Introducing the identities

$$\nabla (\psi \phi) = \psi \nabla \phi + \phi \nabla \psi \quad (\text{A.24})$$

$$\nabla \cdot (\psi \mathbf{A}) = \psi \nabla \cdot \mathbf{A} + \mathbf{A} \cdot \nabla \psi \quad (\text{A.25})$$

$$\begin{aligned} \int_{\Omega} \mathbf{w} \cdot \nabla \cdot \boldsymbol{\kappa} \, d\Omega &= \int_{\Omega} \mathbf{w} \cdot \frac{1}{\text{We}} \rho \nabla \Delta \rho \, d\Omega = \int_{\Omega} \mathbf{w} \cdot \frac{1}{\text{We}} \underbrace{\rho \nabla (\nabla \cdot \nabla \rho)}_{\psi \nabla \phi} \, d\Omega \\ &= -\frac{1}{\text{We}} \int_{\Omega} \mathbf{w} \cdot \nabla \rho (\nabla \cdot \nabla \rho) - \mathbf{w} \cdot \nabla \underbrace{(\rho \nabla \cdot \nabla \rho)}_{\psi \nabla \cdot \mathbf{A}} \, d\Omega \\ &= -\frac{1}{\text{We}} \int_{\Omega} \mathbf{w} \cdot \nabla \rho (\nabla \cdot \nabla \rho) - \mathbf{w} \cdot \nabla (\nabla \cdot (\rho \nabla \rho)) + \mathbf{w} \cdot \nabla (\nabla \rho \cdot \nabla \rho) \, d\Omega \\ &= -\frac{1}{\text{We}} \int_{\Omega} -\nabla (\mathbf{w} \cdot \nabla \rho) \cdot \nabla \rho + \nabla \cdot \mathbf{w} \cdot (\nabla \cdot (\rho \nabla \rho)) - \nabla \cdot \mathbf{w} (\nabla \rho \cdot \nabla \rho) \, d\Omega \\ &\quad - \frac{1}{\text{We}} \int_{\Gamma} \underbrace{(\mathbf{w} \cdot \nabla \rho) \nabla \rho \cdot \mathbf{n} - \mathbf{w} \cdot (\nabla \cdot (\rho \nabla \rho)) \mathbf{n} + \mathbf{w} \cdot (\nabla \rho \cdot \nabla \rho) \mathbf{n}}_{-\mathbf{w} \cdot \rho \Delta \rho} \, d\Gamma \\ &= \frac{1}{\text{We}} \int_{\Omega} \underbrace{\nabla (\mathbf{w} \cdot \nabla \rho) \cdot \nabla \rho}_A + \underbrace{\nabla (\nabla \cdot \mathbf{w}) \cdot (\rho \nabla \rho)}_B + \underbrace{\nabla \cdot \mathbf{w} (\nabla \rho \cdot \nabla \rho)}_C \, d\Omega \\ &\quad + \frac{1}{\text{We}} \int_{\Gamma} \mathbf{w} \cdot \rho \Delta \rho - \mathbf{w} \cdot \nabla \rho (\nabla \rho \cdot \mathbf{n}) - \nabla \cdot \mathbf{w} \rho (\nabla \rho \cdot \mathbf{n}) \, d\Gamma \end{aligned} \quad (\text{A.26})$$

The linearisation of the term is as follows:

$$\begin{aligned} \mathbf{R}_A &= \int_{\Omega} (\nabla \cdot \mathbf{w}) \cdot (\nabla \rho_k \cdot \nabla \rho_k) \, d\Omega \\ \Delta \mathbf{R}_A &= \int_{\Omega} \left. \frac{d}{d\epsilon} \right|_{\epsilon=0} (\nabla \cdot \mathbf{w}) \cdot (\nabla (\rho_k + \epsilon \delta \rho) \cdot \nabla (\rho_k + \epsilon \delta \rho)) \, d\Omega \\ &= \int_{\Omega} (\nabla \cdot \mathbf{w}) \cdot (2 \nabla \rho_k \cdot \nabla \delta \rho) \, d\Omega, \end{aligned} \quad (\text{A.27})$$

$$\mathbf{R}_B = \int_{\Omega} \nabla (\nabla \cdot \mathbf{w}) \cdot (\rho_k \nabla \rho_k) \, d\Omega \quad (\text{A.28})$$

$$\Delta \mathbf{R}_B = \int_{\Omega} \left. \frac{d}{d\epsilon} \right|_{\epsilon=0} \nabla (\nabla \cdot \mathbf{w}) \cdot ((\rho_k + \epsilon \delta \rho) \nabla (\rho_k + \epsilon \delta \rho)) \, d\Omega \quad (\text{A.29})$$

$$= \int_{\Omega} \nabla (\nabla \cdot \mathbf{w}) \cdot (\rho_k \nabla \delta \rho + \delta \rho \nabla \rho_k) \, d\Omega, \quad (\text{A.30})$$

$$\begin{aligned}
\mathbf{R}_C &= \int_{\Omega} \nabla (\mathbf{w} \cdot \nabla \rho_k) \cdot (\nabla \rho_k) + (\nabla \cdot \mathbf{w}) \cdot (\nabla \rho_{k+1} \cdot \nabla \rho_{k+1}) \, d\Omega \\
\Delta \mathbf{R}_C &= \int_{\Omega} \frac{d}{d\epsilon} \bigg|_{\epsilon=0} \nabla (\mathbf{w} \cdot \nabla (\rho_k + \epsilon \delta \rho)) \cdot (\nabla (\rho_k + \epsilon \delta \rho)) \, d\Omega \\
&= \int_{\Omega} (\nabla (\mathbf{w} \cdot \nabla \rho_k) \cdot \nabla \delta \rho + \nabla (\mathbf{w} \cdot \nabla \delta \rho) \cdot \nabla \rho_k) \, d\Omega.
\end{aligned} \tag{A.31}$$

The residual and stiffness contributions are then evaluated with standard Galerkin discretisation as:

$$\begin{aligned}
\mathbf{R} &= \int_{\Omega_e} \mathbf{w}^A \cdot \frac{1}{\text{We}} (\rho \nabla \nabla N^A \nabla \rho_k + \nabla N^A \nabla \rho_k \cdot \nabla \rho_k + \nabla N^A \cdot \nabla \rho_k \nabla \rho_k \\
&\quad + N^A \nabla \nabla \rho_k \nabla \rho_k) \, d\Omega,
\end{aligned} \tag{A.32}$$

and

$$\begin{aligned}
\Delta \mathbf{R} &= \int_{\Omega_e} \mathbf{w}^A \cdot \frac{1}{\text{We}} (\rho_k \nabla \nabla N^A \nabla N^B + \nabla \nabla N^A \nabla \rho_k N^B + 2 \nabla N^A \otimes \nabla N^B \nabla \rho_k \\
&\quad + \nabla N^A \cdot \nabla N^B \nabla \rho_k + N^A \nabla \nabla \rho_k \nabla N^B + \nabla N^B \otimes \nabla N^A \nabla \rho_k \\
&\quad + N^A \nabla \nabla N^B \nabla \rho_k) \delta \rho^B, \, d\Omega
\end{aligned} \tag{A.33}$$

respectively.